

**THÈSE DE DOCTORAT  
DE L'UNIVERSITÉ DE LYON**  
L'Institut National des Sciences Appliquées de Lyon

École doctorale: ELECTRONIQUE, ELECTROTECHNIQUE,  
AUTOMATIQUE

Présentée par

**Frauke ROELLINGHOFF**

Pour obtenir

**LE GRADE DE DOCTEUR**

**Design and Implementation of a  
Prompt-Gamma Camera for Real-Time  
Monitoring of Ion Beam Therapy**

devant le jury composé de :

Joel HÉRAULT      Rapporteur

Frank VERHAEGEN    Rapporteur

Dietmar GEORG

Tony LOMAX

David SARRUT

Julien SMEETS

Denis DAUVERGNE

---

**Proprietary information:** The information contained in this document is the exclusive property of Ion Beam Applications S.A. (IBA) and Institut National des Sciences Appliquées de Lyon (INSA). This information is distributed solely to the members of the jury of the PhD thesis submitted by Ms. Frauke Roellinghoff and bound by the associated non-disclosure agreement. The reproduction, transmission, or use of this information for any other purpose is not permitted without the written permission of IBA and INSA, until the information is made publicly available by IBA and INSA.



# Abstract

Protontherapy is a promising technique for tumor treatment that is becoming more and more widespread. The sharply peaked profile of the dose and the finite particle range allow for very conformal treatment and better sparing of healthy tissue beyond the tumor, but the precise delivery also proves to be the biggest challenge of the technique. Errors in range are a considerable risk in proton therapy and no range monitoring method is currently systematically used for quality control. In this manuscript, an indirect method of measuring the dose distribution, via the detection of secondary prompt gamma radiation emitted along the beam path, is explored.

Two different one-dimensional collimated camera concepts, a multi-parallel-slit camera and a knife-edge slit camera are compared with regards to their potential use. Both systems are optimized via Monte Carlo simulation and measurements are presented for validation. The comparison is made on the basis of the precision with which a shift in the prompt gamma profile falloff edge can be retrieved by comparison with a reference profile as well as the spatial resolution, the cost, weight and bulkiness of the system and guidelines are given for choosing the best configuration for different requirements. Similar values can be obtained for both concepts, reaching a precision for the retrieval of the falloff edge of around 2 mm for a single pencil beam spot of  $5 \times 10^7$  protons.

This study concludes with an outlook on future developments and areas of investigation with the goal of reaching clinical applicability of a prompt gamma detection system.

Keywords: protontherapy; range monitoring; prompt gamma; Monte Carlo



# Résumé

La protonthérapie est une technique prometteuse pour le traitement du cancer, qui se répand de plus en plus. Le pic prononcé de son profil de dose ainsi que la longueur finie du parcours des particules rendent possible un traitement plus ciblé et permettent de mieux éviter d'endommager des tissus sains. Cependant, la précision de l'irradiation s'avère également être le risque principal lors de l'utilisation de cette technique. En effet, une erreur dans la profondeur de pénétration des particules pourrait engendrer des dégâts considérables. A l'heure actuelle, aucune méthode de contrôle n'est systématiquement utilisée pour s'assurer de la qualité du traitement. Dans ce manuscrit, une méthode indirecte de mesure de la distribution de dose, basé sur la détection de gammas prompts émis le long du parcours du faisceau, est étudiée.

Deux concepts de caméra collimatée uni-dimensionnelle sont comparés à l'aune de leur utilisation potentielle : une caméra à fentes parallèles et une caméra "knife-edge". Les deux systèmes sont optimisés par simulations de Monte Carlo et des mesures sont présentés pour valider ces simulations. La comparaison se base sur la précision avec laquelle un décalage dans la chute du profil prompt gamma peut être détecté, la résolution spatiale, le coût et la taille du système. Des recommandations sont émises pour le choix de la meilleure configuration, selon différentes exigences. Des résultats similaires sont obtenus pour les deux concepts, atteignant une précision de environ 2 mm pour un seul point de "pencil beam" correspondant à  $5 \times 10^7$  protons.

L'étude se conclue par un tour d'horizon des pistes de recherche futures qui permettraient d'utiliser un système de détection de gammas prompts dans un contexte clinique futur.

Mots-clés : protonthérapie ; contrôle du range ; gammas prompts ; Monte Carlo



# Foreword

This manuscript is organized in seven chapters. The eighth chapter is a French language summary.

The first chapter sets the context of the work and gives an overview of the existing state of the art as well as an explanation of the purpose of this manuscript. The second chapter describes the properties of proton beams, such as treatment delivery modalities, time structures, beam spot sizes and beam currents in view of their influence on prompt gamma imaging specifically. It also explores the emission profile of prompt gamma and the neutron background, showing what a prompt gamma camera will have to detect.

In the third chapter, a generalized prompt gamma profile is used, independently of an acquisition modality, to establish analysis methods and figures of merit, as well as general observations on desirable profile properties. The next two chapters, four and five, are each devoted to one collimator configuration, parallel-slit and knife-edge. Measurements are presented and optimized solutions are proposed. Chapter six is devoted to the comparison of both configurations with regards to the figures of merit and various practical considerations, as well as observations on the best domain of use for both.

Finally, chapter seven presents a conclusion and an outlook on future work and possible developments and improvements.

## INSA Direction de la Recherche - Ecoles Doctorales - Quinquennal 2011-2015

SIGLE	ECOLE DOCTORALE	NOM ET COORDONNEES DU RESPONSABLE
<b>CHIMIE</b>	<b>CHIMIE DE LYON</b> <a href="http://www.edchimie-lyon.fr">http://www.edchimie-lyon.fr</a>  Sec :Renée EL MELHEM Bat Blaise Pascal 3 <sup>e</sup> etage Insa : R. GOURDON	<b>M. Jean Marc LANCELIN</b> Université de Lyon - Collège Doctoral Bât ESCPE 43 bd du 11 novembre 1918 69622 VILLEURBANNE Cedex Tél : 04.72.43 13 95 <a href="mailto:directeur@edchimie-lyon.fr">directeur@edchimie-lyon.fr</a>
<b>E.E.A.</b>	<b>ELECTRONIQUE, ELECTROTECHNIQUE, AUTOMATIQUE</b> <a href="http://edeea.ec-lyon.fr">http://edeea.ec-lyon.fr</a>  Secrétariat : M.C. HAVGOUDOUKIAN <a href="mailto:eea@ec-lyon.fr">eea@ec-lyon.fr</a>	<b>M. Gérard SCORLETTI</b> Ecole Centrale de Lyon 36 avenue Guy de Collongue 69134 ECULLY Tél : 04.72.18 60.97 Fax : 04 78 43 37 17 <a href="mailto:Gerard.scorletti@ec-lyon.fr">Gerard.scorletti@ec-lyon.fr</a>
<b>E2M2</b>	<b>EVOLUTION, ECOSYSTEME, MICROBIOLOGIE, MODELISATION</b> <a href="http://e2m2.universite-lyon.fr">http://e2m2.universite-lyon.fr</a>  Insa : H. CHARLES	<b>Mme Gudrun BORNETTE</b> CNRS UMR 5023 LEHNA Université Claude Bernard Lyon 1 Bât Forel 43 bd du 11 novembre 1918 69622 VILLEURBANNE Cédex Tél : 06.07.53.89.13 <a href="mailto:e2m2@univ-lyon1.fr">e2m2@univ-lyon1.fr</a>
<b>EDISS</b>	<b>INTERDISCIPLINAIRE SCIENCES-SANTE</b> <a href="http://www.ediss-lyon.fr">http://www.ediss-lyon.fr</a>  Sec : Insa : M. LAGARDE	<b>Mme Emmanuelle CANET-SOULAS</b> INSERM U1060, CarMeN lab, Univ. Lyon 1 Bâtiment IMBL 11 avenue Jean Capelle INSA de Lyon 696621 Villeurbanne Tél : 04.72.68.49.09 Fax :04 72 68 49 16 <a href="mailto:Emmanuelle.canet@univ-lyon1.fr">Emmanuelle.canet@univ-lyon1.fr</a>
<b>INFOMATH S</b>	<b>INFORMATIQUE ET MATHEMATIQUES</b> <a href="http://infomaths.univ-lyon1.fr">http://infomaths.univ-lyon1.fr</a>  Sec :Renée EL MELHEM Bat Blaise Pascal 3 <sup>e</sup> etage <a href="mailto:infomaths@univ-lyon1.fr">infomaths@univ-lyon1.fr</a>	<b>Mme Sylvie CALABRETTO</b> LIRIS - INSA de Lyon Bat Blaise Pascal 7 avenue Jean Capelle 69622 VILLEURBANNE Cedex Tél : 04.72. 43. 80. 46 Fax 04 72 43 16 87 <a href="mailto:Sylvie.calabretto@insa-lyon.fr">Sylvie.calabretto@insa-lyon.fr</a>
<b>Matériaux</b>	<b>MATERIAUX DE LYON</b> <a href="http://ed34.universite-lyon.fr">http://ed34.universite-lyon.fr</a>  Secrétariat : M. LABOUNE PM : 71.70 -Fax : 87.12 Bat. Saint Exupéry <a href="mailto:Ed.materiaux@insa-lyon.fr">Ed.materiaux@insa-lyon.fr</a>	<b>M. Jean-Yves BUFFIERE</b> INSA de Lyon MATEIS Bâtiment Saint Exupéry 7 avenue Jean Capelle 69621 VILLEURBANNE Cedex Tél : 04.72.43 83 18 Fax 04 72 43 85 28 <a href="mailto:Jean-yves.buffiere@insa-lyon.fr">Jean-yves.buffiere@insa-lyon.fr</a>
<b>MEGA</b>	<b>MECANIQUE, ENERGETIQUE, GENIE CIVIL, ACOUSTIQUE</b> <a href="http://mega.universite-lyon.fr">http://mega.universite-lyon.fr</a>  Secrétariat : M. LABOUNE PM : 71.70 -Fax : 87.12 Bat. Saint Exupéry <a href="mailto:mega@insa-lyon.fr">mega@insa-lyon.fr</a>	<b>M. Philippe BOISSE</b> INSA de Lyon Laboratoire LAMCOS Bâtiment Jacquard 25 bis avenue Jean Capelle 69621 VILLEURBANNE Cedex Tél :04.72 .43.71.70 Fax : 04 72 43 72 37 <a href="mailto:Philippe.boisse@insa-lyon.fr">Philippe.boisse@insa-lyon.fr</a>
<b>ScSo</b>	<b>ScSo*</b> <a href="http://recherche.univ-lyon2.fr/scso/">http://recherche.univ-lyon2.fr/scso/</a>  Sec : Viviane POLSINELLI Brigitte DUBOIS Insa : J.Y. TOUSSAINT	<b>M. OBADIA Lionel</b> Université Lyon 2 86 rue Pasteur 69365 LYON Cedex 07 Tél : 04.78.77.23.86 Fax : 04.37.28.04.48 <a href="mailto:Lionel.Obadia@univ-lyon2.fr">Lionel.Obadia@univ-lyon2.fr</a>

\*ScSo : Histoire, Géographie, Aménagement, Urbanisme, Archéologie, Science politique, Sociologie, Anthropologie

# Contents

<b>1</b>	<b>Introduction</b>	<b>1</b>
1.1	Hadrontherapy	1
1.1.1	Range errors	2
1.2	State of the art of range control	4
1.2.1	Overview	4
1.2.2	In-vivo point measurements of the dose	4
1.2.3	Range probes and proton radiography	5
1.2.4	MRI	6
1.2.5	PET	7
1.2.6	Prompt Gamma	8
1.3	Monte Carlo codes	13
1.4	Objective of this study	14
<b>2</b>	<b>The prompt-gamma profile properties</b>	<b>17</b>
2.1	Beam properties	17
2.1.1	Accelerators	17
2.1.2	Beam delivery modalities	18
2.1.3	Properties of pencil beams	20
2.1.4	Beam currents	22
2.2	Particle emission	23
2.2.1	Particle types and energy spectra	23
2.2.2	Spatial distribution	23
2.2.3	Neutron background	27
<b>3</b>	<b>Performance evaluation</b>	<b>29</b>
3.1	Choice of performance criteria	29
3.2	Analysis of prompt-gamma profiles for homogeneous targets	30
3.2.1	Method for obtaining the falloff retrieval precision	30
3.2.2	Methods for fitting the prompt gamma profile	33
3.2.3	Spatial resolution	34
3.2.4	Desirable profile properties	39
3.2.5	Summary	50
<b>4</b>	<b>The parallel-slit camera</b>	<b>53</b>
4.1	Geometrical considerations on the collimator	53
4.2	Experimental data	55
4.2.1	Experimental set-up and data processing	56
4.2.2	Spatial response study with setup A	60
4.3	Monte Carlo simulation	66
4.3.1	Optimization strategy	68
4.3.2	Evaluation of the profiles	69
4.3.3	Estimation of the error of falloff retrieval precision	71
4.3.4	Influence of the setup parameters on the camera performance	72
4.3.5	Performances of the optimized camera	83

4.3.6	Conclusions . . . . .	87
<b>5</b>	<b>The Knife-edge Slit Camera</b>	<b>89</b>
5.1	Concept . . . . .	89
5.2	Monte Carlo simulation . . . . .	93
5.2.1	Summary of the optimization study previously conducted by J. Smeets	93
5.2.2	Parameters chosen before simulation . . . . .	94
5.2.3	Parameters varied through simulation . . . . .	96
5.2.4	Conclusion . . . . .	99
5.3	Experimental data . . . . .	100
5.3.1	Experimental setup and data precessing . . . . .	101
5.3.2	Comparison to simulation . . . . .	104
5.4	Obtainable performances . . . . .	105
5.4.1	Dependence of the performance on energy . . . . .	106
<b>6</b>	<b>Comparison of the knife-edge and multi-parallel-slit cameras</b>	<b>109</b>
6.1	General remarks on geometry . . . . .	109
6.2	Background . . . . .	111
6.3	Spatial resolution . . . . .	111
6.4	Range retrieval performance . . . . .	113
6.5	Measurements . . . . .	116
6.6	Practical considerations . . . . .	117
<b>7</b>	<b>Conclusion and outlook</b>	<b>121</b>
7.1	Choice of camera configuration . . . . .	121
7.2	Possible improvements on current configurations . . . . .	122
7.3	Further study to be conducted . . . . .	122
7.4	Prototypes under development . . . . .	123
7.5	Ideas for integration in clinical workflow . . . . .	123
<b>8</b>	<b>Résumé français</b>	<b>125</b>
8.1	Introduction . . . . .	125
8.1.1	L'hadronthérapie . . . . .	125
8.1.2	Les erreurs de longueur de parcours - erreurs en "range" . . . . .	126
8.1.3	L'état de l'art pour le contrôle du range . . . . .	127
8.1.4	Accélérateurs et modalités de traitement . . . . .	130
8.1.5	L'émission de gammas prompts . . . . .	132
8.2	Remarques communes aux deux géométries . . . . .	132
8.2.1	Evaluation des performances . . . . .	132
8.3	Le collimateur à fentes parallèles . . . . .	142
8.3.1	Le principe géométrique . . . . .	142
8.3.2	Données expérimentales . . . . .	143
8.3.3	Simulations pour l'optimisation du collimateur . . . . .	146
8.4	Le collimateur «knife-edge» . . . . .	148
8.4.1	Optimisation par simulation de Monte Carlo . . . . .	149
8.4.2	Validation expérimentale . . . . .	152
8.5	Comparaison et conclusion . . . . .	154
	<b>Appendices</b>	<b>157</b>
	<b>A NURBS</b>	<b>159</b>

# List of Figures

1.1	Dose profiles of photons and protons in tissue. Several Bragg peaks from protons of different energies are combined into a spread-out Bragg peak. . . .	2
1.2	Different proposed camera concepts for prompt gamma imaging. . . . .	9
1.3	Comparison between profiles obtained with the GATE and MCNPX Monte Carlo codes. . . . .	14
2.1	Illustration of the double-scattering beam delivery modality. . . . .	20
2.2	Illustration of pencil beam scanning. . . . .	21
2.3	Measured spot sizes in air (one sigma) for different beam energies and position around isocenter along the beam trajectory. . . . .	21
2.4	Relative dose measured at the beam isocenter for different proton beam energies with an electronic portal imaging device. . . . .	22
2.5	Spectrum of particles emitted within the target irradiated with a 160 MeV pencil beam. . . . .	24
2.6	Distribution along the beam axis of particles in a PMMA target irradiated with a 160 MeV pencil beam . . . . .	25
2.7	distribution with regards to emission direction of neutrons and photons above 1 MeV. . . . .	26
2.8	Distribution of prompt-gamma emission points in the XY-plane for a perfect pencil beam . . . . .	26
2.9	Neutron distribution with energy greater than 1 MeV along the beam axis direction at different distances in air from the beam axis for a 160 MeV proton beam in PMMA. . . . .	27
3.1	Profile characteristics as defined and used in <a href="#">Smeets [2012]</a> . . . . .	30
3.2	Example of a prostate treatment plan . . . . .	31
3.3	The method for obtaining the falloff retrieval position as applied to a simulated multi-parallel-slit profile and to a profile measured by scanning a single parallel slit. . . . .	32
3.4	Measured prompt gamma profile fitted with two different error functions for the peak and the transition from falloff to background. . . . .	34
3.5	Example application of the 3-straight-line function to a measured profile . . .	35
3.6	Example application of the error function to a measured profile . . . . .	36
3.7	Example application of a cubic spline interpolation to a measured profile . . .	37
3.8	Example application of the NURBS to a measured profile . . . . .	38
3.9	Simulated profile used to get parameters of reference for $P(x)$ . . . . .	42
3.10	Variation of the contrast: example profiles and influence on the FRP. . . . .	43
3.11	Variation of the background: example profiles and influence on the FRP. . . .	43
3.12	Variation of the total number of counts: example profiles and influence on the FRP. . . . .	44
3.13	Variation of the contrast for constant contrast/noise: example profiles and influence on the FRP. . . . .	45
3.14	Dependence of the FRP on the contrast/noise ratio. . . . .	45

3.15	Variation of the falloff width with a constant distance between measurement points of 4 mm. . . . .	45
3.16	Variation of the falloff width and the distance between measurement points at the same time . . . . .	46
3.17	Variation of the slope of the background . . . . .	47
3.18	Variation of the slope of the plateau region . . . . .	48
3.19	Variation of the distance between sampling points for different values of the falloff width. . . . .	49
3.20	Distribution of retrieved falloff shifts with an offset of 1 mm. . . . .	49
3.21	Variation of the offset between the bin center and the center of the falloff. . .	50
4.1	Illustration of the calculation of the detector unit field of view and the detector solid angle. . . . .	54
4.2	Experimental setups from measurements with a single parallel slit. . . . .	56
4.3	Left: two-dimensional plot of the energy deposition in the detector as a function of the TOF information (obtained with the slit facing just before the Bragg peak). Right: TOF spectra after application of the 1 MeV energy threshold with gamma selection windows indicated with red vertical lines. . .	58
4.4	Profiles obtained for different choices of the TOF window length and influence on the contrast and background for $10^9$ protons. . . . .	58
4.5	Profiles obtained for different choices of the energy threshold and influence on the contrast and background for $10^9$ protons. . . . .	59
4.6	Profiles measured with parallel-slit collimators. . . . .	59
4.7	Acquired high-statistics profile without TOF application, profile obtained using TOF and difference between profiles with and without TOF. . . . .	62
4.8	Matching of the reference function with a sample profile and distribution of retrieved falloff positions. . . . .	63
4.9	Objective function used to determine the shift between sample and reference profile for the falloff. . . . .	64
4.10	Retrieval precision ( $1\sigma$ ) with and without TOF, using Poisson generation and data subsampling and corresponding fraction of outliers for the entrance rise and the falloff. . . . .	65
4.11	Visualization of the simulation illustrating the way the phase space can be used repeatedly. . . . .	66
4.12	Illustration of different scoring approaches. Left: monocrystal/barycenter approach, right: pixel approach used in these simulations. . . . .	67
4.13	Parameters of the multislit geometry . . . . .	68
4.14	Influence of the collimator properties: depth, pitch and fill factor. . . . .	69
4.15	Illustration of fitting with a NURBS function and reading the profile properties from the function and its derivative. . . . .	70
4.16	Illustration of a scaled simulated master profile and a corresponding sample profile. . . . .	70
4.17	Reference profiles acquired for the same setup, $5 \times 10^9$ protons each to estimate statistical fluctuations in the reference profiles and the influence on the camera figures of merit. Right: zoom around the falloff region. . . . .	71
4.18	Influence of the spacing and placement of control points: examples. . . . .	73
4.19	Influence of the spacing between two control points. . . . .	74
4.20	Influence of the camera height. . . . .	74
4.21	Influence of the crystal depth. . . . .	75
4.22	Simulated spectrum of counts in the detector for a multi-parallel-slit configuration. . . . .	76
4.23	Influence of the choice of the energy window on the contrast/noise ratio . . .	76
4.24	Influence of the choice of the energy window on the FRP. . . . .	77
4.25	Profiles with different settings for pitch and the derivatives of the fitted NURBS. . .	78
4.26	Influence of the collimator pitch. . . . .	78

4.27	Influence of the crystal pitch on the maximum, correlated signal and background counts as observed per bin . . . . .	79
4.28	Spectra of all recorded counts in the detector for pitch values of 2 mm and 12 mm . . . . .	79
4.29	Influence of the collimator depth. . . . .	80
4.30	Profiles with different settings for collimator depth. . . . .	81
4.31	Influence of the fill factor. . . . .	81
4.32	Influence of the fill factor. . . . .	81
4.33	Influence of the distance between the collimator and the crystals for different collimator depths. . . . .	82
4.34	Influence of inserting tungsten shielding in between the crystals on the FRP. . . . .	83
4.35	FRP for different numbers of protons used for the profile generation. . . . .	84
4.36	Point spread function of perfect and realistic multi-slit cameras. . . . .	86
4.37	Point spread function of a multi-slit collimator for 4.44 MeV photons. . . . .	86
5.1	Parameters for the knife-edge slit camera . . . . .	90
5.2	Illustration of the calculation of the detector unit field of view and the detector solid angle for the knife-edge slit camera . . . . .	90
5.3	Proportion of particles passing through the collimator wall, through the slit edge and through the slit itself for the final knife-edge configuration. . . . .	93
5.4	Distortion due to location-dependent solid angle on the example of a simulated knife-edge profile. . . . .	94
5.5	Influence of the knife-edge collimator thickness . . . . .	97
5.6	Influence of the collimator thickness on the FRP. . . . .	97
5.7	Profiles separated into contributions that came through the slit opening, through the knife edge and through the wall. . . . .	98
5.8	Influence of the collimator angle. . . . .	99
5.9	Influence of the collimator angle on the FRP . . . . .	100
5.10	Influence of the collimator slit opening. . . . .	100
5.11	Influence of the collimator slit opening on the FRP. . . . .	101
5.12	Photograph of the setup of experiments with the knife-edge slit prototype and sketch as seen from above. . . . .	101
5.13	2D view of the image obtained with the HiCam and measured spectrum. . . . .	102
5.14	Acquired profiles for a 160 MeV beam with both an opened and closed collimator after the uniformity correction. . . . .	103
5.15	Comparison of the profiles measured with HiCam for 100 MeV, 160 MeV and 230 MeV beams with the profiles predicted by simulation. . . . .	104
5.16	Achieved falloff precision vs. number of protons for the knife-edge slit camera for the simulated and measured profiles for a 160 MeV beam. . . . .	106
5.17	Possible realistic geometries of the knife-edge collimator. . . . .	107
5.18	Performance of the knife-edge system for different energies and energy-dependent performance for $1 \times 10^8$ protons. . . . .	107
6.1	Camera configurations (to scale) with the prompt-gamma emission distribution within the target. . . . .	112
6.2	Graph showing the trade-off between the falloff width and FRP for different configurations of both cameras. . . . .	115
6.3	Evolution of the FRP for the optimized configurations of the multi-slit collimator and the 220:176 knife-edge collimator when the background is adjusted. . . . .	117
6.4	Measurements using a LYSO-slab prototype detector for the multi-slit configuration (top) as well as two knife-edge slit configurations for beam energies of 100 MeV, 160 MeV and 230 MeV. Simulations using MCNPX. . . . .	118
6.5	Photographs of the setup during the experiment at WPE in october 2013. . . . .	118
6.6	Proposed shielding configuration for a parallel-slit camera. . . . .	119



# List of Tables

1.1	Total number of treatments delivered with various hadrontherapy modalities worldwide as of end of 2012 according to the particle therapy cooperative group (PTCOG).	1
1.2	Estimated range errors listed by source of error with and without the use of Monte Carlo simulations in treatment planning.	3
1.3	Positron emitters relevant for PET used for range monitoring in protontherapy	7
2.1	Typical characteristics of proton pencil beams from different types of accelerators.	23
2.2	Secondary particles leaving the PMMA target (WP3 target) irradiated with a 160 MeV pencil beam in simulation conducted with MCNPX.	24
3.1	Default parameter settings for $P(x)$	42
4.1	Definitions of camera parameters for the multi-parallel slit camera	67
4.2	Values tested in initial exploration of the parameter space.	68
4.3	Optimized configuration for the multi-parallel-slit collimator	72
4.4	Parameters of the optimized multi-slit camera.	84
5.1	Definitions of camera parameters for the knife-edge camera	89
5.2	Attenuation length and effective slit opening for relevant photon energies for lead and tungsten.	95
5.3	Default and final settings for the knife-edge collimator	96
5.4	Values of matching between the NURBS fit of the simulated profiles and the measured profiles.	103
6.1	Table of equations characterizing the properties of the collimators.	109
6.2	Detector unit fields of view for different choices of the collimator angle and slit opening $s$ with the resulting total camera FOV.	113
6.3	Optimized collimator configurations for different trade-offs between the falloff width (FW) and the FRP (for $5 \times 10^7$ protons).	114



# Chapter 1

## Introduction

This chapter gives a brief introduction into the context of the present work in hadrontherapy and an overview of the state of the art in the field and the many developments that have taken in place recently. We then motivate the purpose of the study described in this work.

### 1.1 Hadrontherapy

Next to chemotherapy and surgery, radiation therapy is one of the most common ways in which cancer is treated. Approximately half of cancer patients receive some form of radiation treatment, often in combination with other treatment modalities. Most of this therapy takes place in the form of “conventional” radiotherapy using x-rays, but other particles, such as neutrons, electrons, and heavier charged particles have also been investigated for uses in radiation therapy. Therapy with neutrons, protons, pions and ions is often referred to as a group as hadrontherapy. A list of common modalities and the number of treatments to date is given in table 1.1.

The proposition of the use of protons in radiation therapy dates back to [Wilson \[1946\]](#). While photons are neutral particles whose dose deposit in a target is characterized by a short rise with a peak relatively close to the surface followed by an exponential decline, the dose deposit of charged particles is characterized by a finite range in matter dependent on the starting energy of the particle with a peak in dose deposit towards the end of the range. This form is essentially due to linear energy transfer, which increases as the particle energy decreases, leading to the aforementioned peak, called the Bragg peak. This shape is sometimes also called the inverse depth-dose profile and is the most important asset of radiation with charged particles. The dose profiles of photons and protons are illustrated in [figure 1.1 on the next page](#).

Photon therapy has become more and more conformal to the tumor volume by using sophisticated treatment planning with several beam incidence directions and modulated in-

Particle	Number of treatments
He	2054
Pions	1100
Carbon ions	10756
Other ions	433
Protons	93895
Total	108238

Table 1.1: Total number of treatments delivered with various hadrontherapy modalities worldwide as of end of 2012 according to the particle therapy cooperative group (PTCOG).

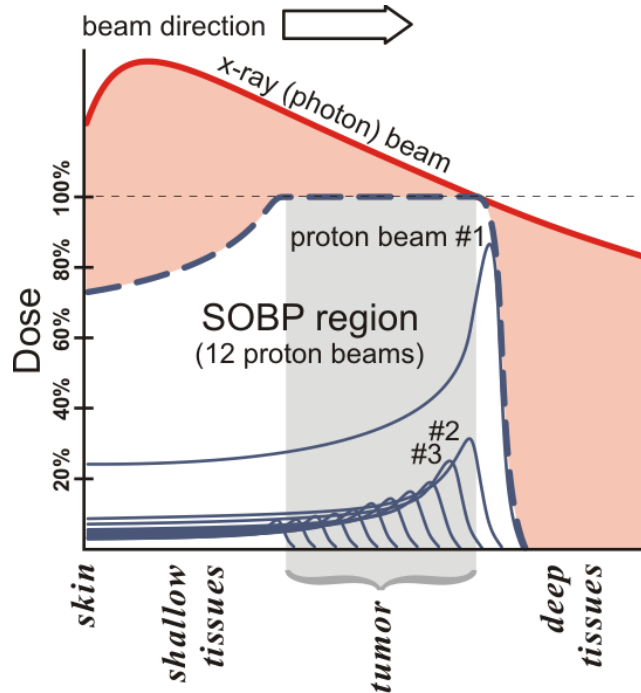


Figure 1.1: Dose profiles of photons and protons in tissue. Several Bragg peaks from protons of different energies are combined into a spread-out Bragg peak. Image credit: Mark Filipak.

tensities (intensity modulated radiation therapy, IMRT, see for example [Lomax \[2008\]](#)). However, it is inherent to the method that a considerable amount of dose will be deposited both before and after the tumor volume. Charged particles open new planning and treatment possibilities due to their finite range. In theory, an organ at risk directly behind the tumor volume to be irradiated can be spared almost completely from radiation.

Today, the most commonly used charged particles for radiotherapy are protons and carbon ions. Carbon ions present the advantage of having a high radiobiological effectiveness (RBE) towards the end of range, making their profile even more peaked in terms of biological dose rather than physical dose. They also present ballistic advantages, being subject to less multiple scattering and less longitudinal straggling. Their main drawback is the production of fragments along the path that have a longer range than the initial carbon ion, leading to a tail dose distribution beyond the Bragg peak.

As the peak of the dose distribution for a single particle energy is too sharply peaked to adequately cover the whole depth of the tumor in almost all cases, dose distributions at different energies are superposed, combining into what is called a spread out Bragg peak (SOBP). In this way, an almost flat dose distribution throughout the depth of the treatment volume can be created.

### 1.1.1 Range errors

While the peaked dose profile is good for conformal treatments, it also significantly increases the risk of deviation from the planned dose distribution. While for photon irradiations, small uncertainties in the depth dose profile lead to small differences in the delivered dose at and around the tumor location, for Bragg-peaked dose profiles a small error can mean the difference between an area receiving the maximum dose and receiving virtually no dose at all. This is problematic both in “undershoot” as well as in “overshoot” cases. In one instance, part of the tumor receives no dose, compromising the effectiveness of treatment, in the other, an organ at risk behind the tumor may receive a very high dose. According to [Knopf and Lomax \[2013\]](#), this risk leads to avoidance of some field directions more vulnerable to range errors in clinical practice, even though treatment with those fields shows better conformality

Source of range uncertainty in the patient	without Monte Carlo	with Monte Carlo
Independent of dose calculation		
Measurement uncertainty in water for commissioning	$\pm 0.3$ mm	$\pm 0.3$ mm
Compensator design	$\pm 0.2$ mm	$\pm 0.2$ mm
Beam reproducibility	$\pm 0.2$ mm	$\pm 0.2$ mm
Patient setup	$\pm 0.7$ mm	$\pm 0.7$ mm
Dose calculation		
Biology (always positive)*	+0.8%	+0.8%
CT imaging and calibration	$\pm 0.5\%$	$\pm 0.5\%$
CT conversion to tissue (excluding I-values)	$\pm 0.5\%$	$\pm 0.2\%$
CT grid size	$\pm 0.3\%$	$\pm 0.3\%$
Mean excitation energy (I-values) in tissues	$\pm 1.5\%$	$\pm 1.5\%$
Range degradation; complex inhomogeneities	-0.7%	$\pm 0.1\%$
Range degradation; local lateral inhomogeneities	$\pm 2.5\%$	$\pm 0.1\%$
Total (excluding *)	4.6% + 1.2 mm	2.4% + 1.2 mm

Table 1.2: Estimated range errors listed by source of error with and without the use of Monte Carlo simulations in treatment planning. Table adapted from [Paganetti \[2012\]](#).

and lower dose to organs at risk in planning.

Range errors can occur due to a variety of causes. A comprehensive list can be found in [Paganetti \[2012\]](#), whose findings are summarized in table 1.2.

Range errors can be subdivided into two main groups. One part has to do with the dose calculation during treatment planning. These are effects such as:

- The underestimation of the RBE in the distal part of the dose profile, leading to an underestimation of the effective biological range.
- Uncertainties of the CT scan itself
- Ambiguity in the conversion between the Hounsfield units obtained with a CT scan and the proton or carbon ion stopping powers needed for treatment planning
- Artifacts in the CT acquisition, due for example to highly heterogeneous tissue or the presence of implants
- Errors and approximations in the dose calculation by the treatment planning software, often due to the incorrect treatment of different tissue material in case of complex heterogeneities or when there is an interface between tissues of different densities right along the beam direction. This type of error can typically be much reduced by the use of Monte Carlo codes for dose calculation instead of using analytical models.

The other group of range errors is due to effects that have to do with differences between the treatment preparation and hence the values used for planning and the treatment delivery itself.

- Errors in the beam modeling, such as inaccuracies in measurement of the beam or changes in beam properties since the last measurement. Also errors in manufacturing

of patient-specific hardware in passive beam delivery, such as range compensators and apertures.

- Setup errors such as mispositioning of the patient, misalignment of patient-specific hardware.
- Intra-fraction organ motion, such as breathing (very location-dependent)
- Inter-fraction anatomical changes such as weight changes, tumor shrinkage and cavity filling. Internal organs may also slightly shift between fractions.

All these different effects can add up to quite sizable range errors. This is usually dealt with by applying safety margins around tumor volume and irradiating a greater volume in order to ensure full dose delivery to the whole tumor. For example, at MGH in Boston, a range margin of  $3.5\%+1$  mm is applied, leading to an intentional overshoot of over 6 mm for a range of 150 mm (160 MeV proton beam). This necessarily leads to irradiation of some additional healthy tissue and limits the ability to use the finite range to shield organs at risk.

Any method to verify the range, ideally during the course of treatment itself in real time, could immensely reduce the risks and lead to a reduction in the margins used, which in turn leads to less dose to healthy tissue. Furthermore, extreme cases in which the errors exceed the margins could be detected and treatment readjusted. Overall, such a technique could potentially provide quality assurance for proton therapy, improve treatment outcomes and reduce side effects of treatment.

To be of interest, such a technique should ideally provide a measurement of the range for typical treatments of the order of 1-2 mm or better, which would already be a considerable improvement over current uncertainties. The performance of the method may vary for different tumor locations and between cases. Its application would be most interesting in those cases which have the highest uncertainties, typically those with complicated heterogeneities or high risk of anatomical changes or organ movement.

## 1.2 State of the art of range control

### 1.2.1 Overview

Several possible avenues of range control are currently being investigated. Although some methods, for example PET scanning, have been tested on patients in clinical settings, there is currently no center using any method to systematically monitor treatments. [Knopf and Lomax \[2013\]](#) gives a very comprehensive overview of the methods currently under investigation.

Methods for range control can be loosely grouped into direct methods (measuring dose) and indirect methods (measuring effects of irradiation correlated to the dose). Different approaches are also made as to the when the measurement is done. Range verification can either be done prior to the treatment (with test beams), during treatment, or after treatment, with different implications for the use of the gathered information.

The state of the art in methods for protontherapy currently being investigated as well as their most important advantages and drawbacks are presented hereafter.

### 1.2.2 In-vivo point measurements of the dose

Point measurements of the dose are a well-established method for dose verification in photon and electron radiotherapy (see [Leunens et al. \[1990\]](#); [Essers and Mijnheer \[1999\]](#); [Ciocca et al. \[2003\]](#)). Usually, a dosimetry device is placed at the location of the entrance of the beam and/or the beam exit (in the case of photon treatments). Unfortunately, dose measurement outside of the patient body cannot be sufficient for range control in proton therapy. Measuring the dose at the patient entrance does not yield much additional information, as the beam energy, beam current and beam position are already well monitored along the beam line and the majority of errors occur after this point. Dose measurement after the patient

during treatment is not possible, as the particles are stopped completely inside the patient (it is possible to use probe beams of higher energy for proton radiography, which is discussed in section 1.2.3).

Implantable MOSFET-based dosimeters that can be read out wirelessly have recently been developed and tested for photon therapy. A similar approach can be used for protontherapy to determine dose deposition inside the patient. Since the dosimeter has to be implanted or otherwise inserted into the patient, the number of measurement points is inherently limited. Additionally, precise placement at a predetermined location is difficult. Determining the precise location by a CT scan after placement is possible. This poses a problem in protontherapy. The spread out Bragg peak is usually planned in such a way that the dose to the tumor volume is uniform, so that the integral dose measurement in this region is constant and insensitive to range errors. Placing a dosimeter at the steep dose falloff at the end of the range, on the other hand, would be very sensitive to range errors. However, it would also be extremely sensitive to the positioning of the dosimeter, working only if it can be placed exactly at the falloff. Two possible approaches are being investigated to overcome these challenges and obtain meaningful data from a point dose measurement.

**Time-dependent dose measurement** While the integral dose within the region covered by the SOBP is quasi-constant, there is a temporal dependency for most treatment delivery methods (for a description of delivery methods, see section 2.1.2 on page 18). For passively scattered fields that use a modulator wheel to modify the beam energy, the time-dependence of the dose deposited at the location of the detector can be predicted and matched to the observed time dependence. Likewise, for pencil beam scanning, the dose at the location of the detector for any spot of the pencil beam can be predicted and matched to the observed dose at the time of delivery of the spot. This method was first tested with a passively scattered beam in a water tank by Lu [2008b] and it was established that the residual range at the position of the detector could be determined with sub-millimeter precision. More recent measurements with a heterogeneous phantom by Bentefour et al. [2012] show that even with range mixing, a reasonable accuracy can still be achieved. The approach has yet to be tested with the more complex heterogeneity effects that can be expected for a real patient.

**Deliberately sloped depth-dose profiles** Lu [2008a] propose a method in which the conventional delivery of a flat SOBP is replaced by a series of partial dose irradiations where the weights of the peaks comprising the SOBP are adjusted to produce a sloped dose encoding the beam range information. Subsequent irradiations have complementary dose slopes to sum up to a uniform dose distribution overall. The ratio of the dose delivered during irradiations with opposite slopes are used to determine the residual range at the location of the detector. This method has been tested for passively delivered fields, but the idea can be applied to pencil beam scanning as well. For example, the ratios between measured doses for each pencil beam layer could be used. This rejoins the above method using time dependency, but timing and synchronization at the layer level is less challenging than at the spot level. The time used for energy switching of the beam could be used to read out the detector.

Although high accuracy can be achieved with these methods, the obvious drawback is the invasiveness of the method, necessitating either implanting a detector or using a device such as a rectal balloon with attached detectors.

### 1.2.3 Range probes and proton radiography

Both range probes and proton radiography are based on using proton beams of sufficient energy that they can pass through the patient and be detected upon exiting. We speak of range probes if this is done with only one or a few pencil beams, leading to a 1D measurement. At its limit, hundreds of range probes are used to obtain a low-resolution proton radiography. The advantage of these methods is that the residual range can be determined with very good accuracy by measuring the complete Bragg peak with a multiple layer ionization chamber

(MOSFET). The concept has been explored by [Romero et al. \[1994\]](#); [Watts et al. \[2009\]](#); [Mumot et al. \[2010\]](#). The latter have shown that Monte Carlo simulations of planning CTs predict accuracy in the measurement of residual range of the order of a millimeter. Additionally, the shape of the Bragg peak is dependent on the material in the beam path and could be used to verify patient alignment in highly heterogeneous environments.

The advantage of this method is that it is fairly simple, provided that protons of the required energy are available, as the technology for measuring the Bragg peak is already available commercially.

Proton radiography is a method that has been investigated since the 1960s. The difference to proton range probing is that a two-dimensional fluence of protons is used to obtain a two-dimensional image. The method has a number of interesting properties ([Koehler \[1968\]](#); [Kramer et al. \[1977\]](#)). Its density contrast is higher than what is usually obtained in x-ray radiography and it directly provides the value of the proton stopping power, which is the relevant value for proton therapy monitoring. Additionally, the dose to the patient is lower than for x-ray radiography (up to two orders of magnitude lower according to [Schneider et al. \[2004\]](#)). To improve the spatial resolution of the method, the entrance and exit coordinates of the individual protons can be measured ([Schneider and Pedroni \[1995\]](#)). Proton radiography is mostly interesting for range control to acquire an image before treatment to verify patient alignment (possibly replacing the x-ray image) and verify that the measured stopping powers match what was used for treatment planning, thus getting rid of errors in Hounsfield conversion, CT artifacts etc, detailed above (see section 1.1.1 on page 2). It could even be possible to base the treatment planification on a proton radiography to obtain a more accurate plan from the beginning and use another radiography image immediately prior to treatment for verification of positioning and to detect any morphology changes. [Schneider et al. \[2004\]](#), achieved a precision of 0.6 mm for the range in animal measurements.

The main challenge to proton radiography at the moment is the availability of adequate proton sources. As most proton accelerators currently used for treatment have maximum beam energies of the order of 230 to 250 MeV, the length of the path through the patient must be less than the range of approximately 33 to 37 cm. This energy is enough to treat almost all tumor sites, but is insufficient for example, for a lateral radiography of a typical pelvis. Moreover, both range probes and proton radiography show the residual range of the beam having traveled across the whole patient, leading to a measurement of accumulated deviations, some of which may be due to something behind the treatment volume that would have no effect on the actual treatment. In theory, 3D expansion of the method is possible. While the dose is relatively low, there is some additional dose delivered to the patient, except if proton radiography is used to replace x-rays.

#### 1.2.4 MRI

The principle of MRI range monitoring is based on the observation that radiation can cause changes in human tissue that are apparent on an MRI scan. Increased intensity on the MRI image has been shown bone marrow in the spine irradiated with photons ([Ramsey and Zacharias \[1985\]](#); [Stevens et al. \[1990\]](#); [Blomlie et al. \[1995\]](#)) and is thought to be due to a reduction in cellularity and an increase in fat and marrow edema. Changes in MRI images of the liver using a reticuloendothelial MR contrast agent are also reported ([Padhani et al. \[1998\]](#)).

More recently, the effect has been studied for proton therapy in view of observing the delivered dose distributions. [Krejcarek et al. \[2007\]](#) have shown on MRIs taken between 10 days and 21 months after radiotherapy, that in patients treated to the thecal sac, there is a sharp demarcation of the hyperintense signal visible in MRI images and the hyperintense regions roughly correspond to the treatment volume. [Gensheimer et al. \[2010\]](#) investigated the possibility of using the effect to the spine for range control. They demonstrated a quantitative link between the visible changes in tissue and the dose delivered. For a data set of ten patients, the dose-signal intensity curve was established. Similarly, a dose-signal intensity relationship was established for the liver by [Yuan et al. \[2013\]](#), demonstrating

Reaction	Threshold energy (MeV)	Half life (min)	Positron energy (MeV)
$^{16}\text{O}(\text{p}, \text{pn})^{15}\text{O}$	16.79	2.037	1.72
$^{16}\text{O}(\text{p}, \alpha)^{13}\text{N}$	5.66	9.965	1.19
$^{14}\text{N}(\text{p}, \text{pn})^{13}\text{N}$	11.44	9.965	1.19
$^{12}\text{C}(\text{p}, \text{pn})^{11}\text{C}$	20.61	20.39	0.96
$^{14}\text{N}(\text{p}, \alpha)^{11}\text{C}$	3.22	20.39	0.96
$^{16}\text{O}(\text{p}, \alpha\text{pn})^{11}\text{C}$	59.64	20.39	0.96

Table 1.3: Positron emitters relevant for PET used for range monitoring in protontherapy

significant correlation in five patients.

MRI techniques have the advantage of providing a good spatial resolution and using technology already commercially available and accessible at treatment centers. In contrast to proton radiography, no additional dose is delivered to the patient. One limitation, of course, is that this method is not applicable to all treatment sites, as it is currently only demonstrated for dose deposits that have edges in the spinal bone marrow and liver. It also has to be kept in mind that the effect occurs in a delayed manner some time after treatment. Effects have usually been detected after a few days (Stevens et al. [1990]) up to several weeks or even months (Krejcarek et al. [2007]; Yankelevitz [1991]). For some treatments, it may therefore be possible to adjust subsequent treatment sessions, but not in all cases, and real-time verification is of course impossible.

### 1.2.5 PET

The PET monitoring method is based on the fact that ions undergo inelastic nuclear collisions that produce radioactive isotopes. Some of these isotopes are beta-plus-emitters, with half-lives of the order of minutes. The photons from the annihilation reaction of the  $\beta^+$ -particles can be detected by positron emission tomography (PET). The most common isotopes useful for PET are listed in table 1.3. Positron emitters are only created up to a certain threshold energy of the proton, causing the distribution of the emitters to drop before the Bragg peak. While the dose distribution and the positron emission are correlated, they are not identical.

PET imaging is probably the most advanced form of range control at this point in time. A recent review article (Studenski and Xiao [2010]) summarizes the current state of development and Knopf and Lomax [2013] gives a very comprehensive overview as well. Various groups have investigated PET for range control in heavy-ion therapy (Parodi et al. [2002]) and proton therapy (Litzenberg et al. [1992]; Vynckier et al. [1993]; Paans and Schippers [1993]; Oelfke et al. [1996]).

The activation depends on the composition of the tissue, especially for proton therapy, in which the projectile itself cannot be activated. This dependence could possibly be used in gaining information about elemental composition of the tissue (Parodi et al. [2005]; Litzenberg et al. [1999]).

There are two basic ways of acquiring a PET image. Either by an in-beam acquisition during the time of treatment, or after treatment in a dedicated PET scanner. A comparison of the two methods can be found in Parodi et al. [2008].

Due to the exponential decrease in activity with time, in-beam PET profits from the highest emission rates. The disadvantage of doing in-beam acquisitions is the limited space available in the treatment area. To accommodate the beam nozzle, the couch robot, the cone-beam CT etc., usually only a dual-head PET acquisition system with a relatively small field of view can be installed. Parodi et al. [2002] and Parodi et al. [2005] showed that a correlation between the distribution of positron emitters and the dose distribution can be found for both carbon ions and protons. For carbon ions, since the projectiles themselves can become activated, the distribution of  $\beta^+$ -emitters is peaked towards the end of the range, while for protons, the distribution of  $\beta^+$ -emitters stops well before the Bragg peak.

Measurements tend to be blinded by the prompt-gamma emission during beam delivery, so [Crespo et al. \[2006\]](#) proposed synchronizing the acquisition with the beam microstructure, only acquiring while no beam is being delivered. As the activity distribution is not equal to the dose distribution, analytical models have been proposed by [Attanasi et al. \[2011\]](#) to give fast feedback by calculating the dose distribution corresponding to the observed activity locally. [Nishio et al. \[2006\]](#) reports on experience with daily PET scans used for treatment replanning upon detection of deviations.

Offline PET acquisitions rely on commercial dedicated PET or PET/CT scanners. The patient is transported to the scanners after treatment, leading to delays between treatment and scan of up to 30 minutes. The improved sensitivity and general performance of these scanners compared to the in-beam dual-head scanners partially compensates for the loss in activity caused by the delay. A further drawback is the occurrence of biological washout, especially in well-perfused areas such as muscle which leads to blurring. Clinical studies have been conducted by [Nishio et al. \[2006\]](#) to study these washout effects. [Parodi et al. \[2007\]](#) obtained 2 mm accuracy comparing measurements to Monte Carlo predictions made with FLUKA and accounting for biological washout. The different half-lives of the relevant isotopes lead to changes in emission rates for different tissues over time.

The advantages of using PET for range control are that it needs no additional dose to the patient and can be done during treatment or in a relatively short time after, providing direct feedback about the treatment. Especially in the case of offline acquisition, commercial scanners may be used which are already available. Imaging of individual pencil beam spots or even individual layers are not possible, as the decay time is of the order of minutes. Furthermore, the emission rates are relatively low, and acquisitions over the course of a whole treatment and several minutes after are probably necessary for a sufficient signal-to-noise ratio. A quantitative evaluation of the dose deposit is quasi impossible due to the washout effects.

### 1.2.6 Prompt Gamma

Prompt gamma range monitoring is based on the gamma rays emitted by excited nuclei from nuclear interactions that, as the name indicates, happen very promptly, typically in time frames well below the nanosecond. The principle is similar to the PET technique detailed above, in that secondary products of interactions of the protons are used to draw conclusions as to the beam path. The time scale, however, is very different and the emission rates for prompt gamma typically exceed the rates of positron emission by an order of magnitude or more ([Moteabbed et al. \[2011\]](#)). The main advantages of prompt-gamma imaging is that it can be truly real-time, with acquisition and evaluation occurring during irradiation. No additional dose to the patient is necessary.

Prompt gamma imaging, differently from PET, cannot rely on coincidence measurements to select valid events and establish a line on which the interaction has taken place. This has two consequences: the detection device must be able to measure the incidence direction of the photon (different methods are detailed below) and the method must contend with a higher background.

Control of the range of protons by means of prompt-gamma detection was first proposed by Stichelbaut and Jongen ([Jongen and Stichelbaut \[2003\]](#)) in 2003. First measurements were made by [Min et al. \[2006\]](#) and demonstrated a clear correlation between the beam path and the prompt-gamma emission. Prompt gamma have also been observed as an unwanted “noise” effect in PET measurements ([Parodi et al. \[2005\]](#)). Since then, the correlation has been confirmed independently by a variety of groups, among them [Testa et al. \[2008\]](#); [Polf et al. \[2009\]](#); [Smeets et al. \[2012\]](#). Note that while the distribution is clearly correlated to the dose, the two are not proportional. This is largely due to the fact that dose deposition mostly occurs through linear energy transfer (LET), which increases as the particle energy decreases, leading to the characteristic Bragg peak, while prompt-gamma emission is due essentially to nuclear reactions, which have cross-sections that are energy- and material-dependent in a different manner. The energy dependence of the cross-sections for the different nuclear reactions leading to prompt gamma vary, but most of them fall off before the proton reaches

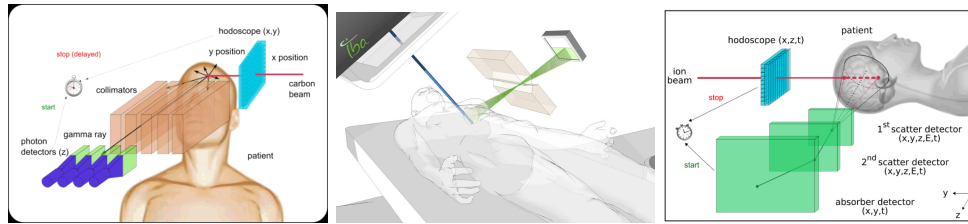


Figure 1.2: Different proposed camera concepts for prompt gamma imaging. Left: parallel-slit camera. Center: knife-edge slit camera. Right: Compton camera.

the low energies of the Bragg peak region (Verburg et al. [2012]), meaning that the prompt-gamma emission in total falls off before the Bragg peak. The distance between the falloff of the prompt-gamma emission profile and the falloff of the dose is approximately 6 mm in water for protons, as given by Polf et al. [2008]. In an homogeneous medium, the distance between the falloff of the prompt-gamma profile and the falloff of the dose profile are constant, but in heterogeneous mediums, it has been shown to vary (Moteabbed et al. [2011]). For carbon ions, this distance is considerably reduced (almost to zero), since carbon-induced fragmentation occurs until the very last hundreds of micrometers of the range.

It has also been shown through simulation (Moteabbed et al. [2011]; Polf et al. [2008]; Smeets et al. [2012]) that the prompt-gamma emission rate per unit length of material depends on the material density and atomic composition. The emission rate was found to be proportional to the material density and CT numbers. De Rydt [2013] presented measurements confirming dependence in the case of Carbon ion beams and Polf et al. [2013] shows spectra of prompt-gamma emission for a selection of material samples irradiated with proton beams.

The prompt-gamma emission has been shown to be isotropic through Monte Carlo simulation (see, for example, Robert et al. [2013] and chapter 2 of this manuscript). For carbon ions this isotropic behaviour has been confirmed experimentally between  $60^\circ$  and  $120^\circ$  by Testa et al. [2009]. The most obvious placement for the camera, then, is in a perpendicular direction to the beam, so that the distal edge of the dose deposition is projected onto the camera perpendicularly, avoiding parallax effects. All of the configurations found in literature cited here use this positioning.

The spectrum of prompt-gamma emission has a continuous component superposed with a number of discrete lines corresponding to specific nuclear de-excitations. It starts at low energies with the main part being contained below 10 MeV and a tail of the distribution going up to even higher energies (a spectrum is shown in figure 2.5 on page 24). Even though the emission rate drops for higher energies, it has been shown repeatedly that the use of higher energy gamma shows better results for correlation with the dose (Min et al. [2006]; Kurosawa et al. [2011], among others). Correspondingly, in most proposed optimized configurations in literature, energy thresholds are used (for example, 3 MeV in Verburg et al. [2013]; Smeets et al. [2012] and 4 MeV in Min et al. [2012]). This is mainly due to the reduced scattering of higher-energy gamma within the target volume.

The systems proposed for the measurement of prompt gamma can be divided into two groups. The first uses physical collimators to produce an image of the prompt-gamma emission profile. This group can be further subdivided into parallel-slit and parallel-hole collimators on the one side and knife-edge and pinhole collimators on the other. The second group uses Compton cameras, sometimes also called electronic collimation. Different approaches have been made to perform 1D imaging of just the proton range (Parallel-slit and knife-edge collimators, some Compton cameras) as well as 2D distribution (parallel-hole, pinhole) and even 3D distribution (Compton cameras). The concepts are illustrated in figure 1.2.

Studies have been conducted for the application to different beam delivery modalities. Details of the available modalities and their impact on prompt-gamma detection are given in section 2.1.2 on page 18. Some groups propose to measure the distal falloff of the SOBP of a

treatment delivered via passive scattering and demonstrate its feasibility through simulation (Polf et al. [2008]; Moteabbed et al. [2011]), but measurements have so far failed to produce a usable falloff (Kurosawa et al. [2011]). Another explored possibility is to image energy layers in passive delivery by synchronizing with the modulator wheel or individual layers in pencil-beam scanning. Others explore the possibility of imaging single pencil beams.

### Parallel-slit collimator based systems

Parallel-hole collimators are well-known from their application in nuclear medicine in the form of single photon emission tomography (SPECT). The high energies of the gamma rays involved in prompt-gamma imaging, however, are out of the scope of camera solutions developed for SPECT. Several groups are currently undertaking efforts to optimize a solution specifically for prompt-gamma range control. With one exception (Lee et al. [2012]), the proposed solutions are parallel-slit collimators instead of parallel-hole collimators, collimating only in one dimension and resulting in a 1D profile permitting measurement of the range only. As the proton range is the most crucial parameter for improving quality control, the other dimension was sacrificed to improve the efficiency of the system.

Several measurements so far have relied on the use of a single slit with parallel edges (Min et al. [2006]; Kurosawa et al. [2011]; Verburg et al. [2013] for protons, Testa et al. [2008] for carbon ions). Measurements with a multi-slit collimator device have so far been performed by Min et al. [2012] for protons and Krimmer and al [2014] for carbon ions.

Several studies have been undertaken for the optimization of the parameters of a multi-slit system. Different figures of merit were used by different groups, explaining divergence in proposed optimal configurations.

In his thesis, Testa [2010] includes a study of several parameters characterizing the performance with regards to efficiency and spatial resolution for variation of parameters such as the collimator thickness and position and the slit and septa widths. The visibility of the collimator slit pattern on the obtained image is also studied for different configurations. While no definitive optimal solution is given, the trends are described for each parameter and mathematical models are proposed, which are further developed in this text.

In recent work by a Korean group, both a two-dimensional parallel-hole system (Lee et al. [2012]) and a parallel-slit system (Min et al. [2012]) have been optimized using MCNPX simulations. As a figure of merit, they use the peak-to-background ratio and the “background fraction”, its inverse, respectively. Lee et al. [2012] find that an optimal peak-to-background is reached with square holes of 4 mm width with septa of 2 mm and a collimator length of 150 mm. Min et al. [2012] find an optimum slit width of 2 mm, observing that the correlated signal steadily increases with larger slit widths, but when the ratio of slit width to septa width becomes too large, the resulting increased septal penetration leads to an increased background. They also observe that large septa widths and deep collimators improve the background fraction, and limit those parameters only due to considerations of the spatial resolution and bulkiness of the system. An absolute range measurement is made by fitting a sigmoidal curve to the obtained profile, using its half-value. Application to clinical cases is proposed on the basis of per-layer measurements in the case of active scanning and measurement of the most distal layer in passive delivery with synchronization with the modulator wheel. It should be noted that while the ratio between correlated signal and background is optimized, the absolute number of counts and corresponding level of noise is not taken into consideration. This configuration is probably indeed most suited for applications to treatment layers and less so for individual pencil beams, where gathering of a sufficient number of counts is an issue.

A comprehensive simulation study of the use of time-of-flight was made by Biegun et al. [2012] for an idealized parallel-slit camera in which no material collimator is used, but photons with certain incidence angles on the detector were selected. The study compares the results of GEANT4 and MCNPX codes and investigates the time shift between different depths inside the patient. Different common beam time structures are investigated with regards to the potential usefulness of time of flight (TOF) where the RF signal of the beam is used as start signal in the TOF measurement. Evaluation was made by looking at the gamma-to-

neutron ratio. TOF was judged useful for beam bunch widths smaller than 5 ns and time between bunches of 10 ns or more.

An interesting approach is proposed by [Verburg et al. \[2013\]](#), proposing the use of profiles generated with only discrete gamma lines. To this end, the energy measurement must be precise. An active shielding system is used to differentiate photons that have deposited their whole energy inside the detector from those who are only scattered. Combining this active shielding with time-of-flight discrimination using the RF signal of the accelerator results in a 90% reduction of the background. The most prominent gamma lines at 4.44, 5.2 and 6.13 MeV are used for imaging and a correlation to the dose profile is observed for each individually. As suggested by [Polf et al. \[2013\]](#), the ratio between different prompt-gamma lines could be used to draw conclusions about the composition of the tissue. Additionally, using a profile of a individual line could be more robust for an absolute measurement of the range if the tissue composition is not well known. A potential limitation of this method is the considerable reduction of the number of counts used for imaging. Using only one line reduces the contrast amplitude of the profile by a factor of roughly ten, and the shape of the profile (in terms of steepness of the falloff, for example) shows no improvement. Potentially, profiles made with single emission lines could be used in combination with the all-energy profile for a more complex analysis. Due to the active shielding used, this type of detector is one of the most expensive proposed solutions.

### Knife-edge Slit Based Systems

Two-dimensional pinhole concepts have been investigated by a few groups. [Kim et al. \[2009\]](#) published measurements conducted with a pinhole collimator made of lead plates at the relatively low proton beam energy of 50 MeV. While a small shift in the center of the imaged distribution was observed for irradiations with different proton beam energies, no falloff edge was observed on the acquired profiles directly and the setup seems rather impractical for range verification. To our knowledge, investigation into the 2D pinhole concept has since been abandoned by the groups working on it.

[Smeets \[2012\]](#) proposes a one-dimensional version of the pinhole concept, a knife-edge slit collimator. Extensive simulations were conducted to optimize the configuration, which will be looked at in more detail in chapter 5. A tungsten collimator configuration with 40 mm thick walls, 6 mm slit opening and distances of 150 mm both between beam line and collimator and collimator and detector has been proposed and validated through measurement. A standard deviation for the accuracy of the range estimation for  $1 \times 10^8$  protons is given as approximately 1.5 mm.

A similar setup is proposed by [Diblen et al. \[2012\]](#), with a slightly smaller slit opening of 5 mm and a slightly more acute angle of the slit edges and distances reduced to 120 mm. A system matrix was established with simulations of a 4.5 MeV point source to use in a 1D maximum likelihood expectation maximization algorithm to reconstruct the emission profile from the measured profile. Such an algorithm could potentially improve the accuracy of the system.

Still another setup was proposed by [Bom et al. \[2012\]](#) with a slit width of 3 mm, a wall thickness of 80 mm and a full opening angle of  $30^\circ$ . The distances were chosen 16 cm between the beam axis and the center of the collimator and 64 cm between the collimator slit and the detector plane. This rather large magnification factor of four and the fact that the camera is rather close to the beam lead to very good spatial resolution of the system compared to other knife-edge solutions. In simulation, the half-height of the prompt-gamma profile falloff could be retrieved with 0.6 mm accuracy for  $1 \times 10^8$  protons. However, to have a reasonable field of view, the detector has to be rather large ( $30 \times 50$  cm in the proposed configuration), so that the probable drawbacks of this solution are its weight, bulkiness and cost.

### Compton camera based systems

In contrast to collimated camera systems, Compton cameras do not use a physical collimator. Instead, they rely on multiple interactions of the photon within the detector to draw conclu-

sions as to the incidence direction of the photon. When a photon undergoes one Compton scattering and one other reaction in the detector and the interaction locations and energy deposits as well as the energy of the photon itself are known, the Compton equations can be used to deduce the scattering angle of the first interaction. The incidence direction of the primary photon then lies on well-defined cone. Usually, several detector planes are used to build Compton cameras, with the initial scattering occurring in one plane and the second interaction in another. As the energy spectrum in prompt-gamma imaging is continuous, the energy of the photon cannot be known a priori. Possible solutions are to maximize the probability of total absorption of the photon by including a relatively thick absorber detector plane or to use a three-interaction Compton camera. With three recorded interactions, the Compton cone can be reconstructed exactly without knowing the initial energy of the photon.

As Compton cameras accept photons from all angles, their efficiency is potentially higher than that of collimated cameras (Kormoll et al. [2011]). However, they require two or three valid interactions and their efficiency is very dependent on the particular configuration chosen, so that general statements as to the gain in counting rate cannot be made. The cross-sections for Compton scattering at the relevant photon energies are relatively low, and a camera model requiring three interactions may have a relatively low rate of valid interactions. A potential problem of Compton cameras is also that there is a high proportion of single interactions which are not useful for imaging but may paralyze the acquisition due to their high rates if the detector is not carefully designed, in a similar way to the observation made above that PET cameras can be blinded during beam delivery due to prompt gamma.

Double scattering Compton camera configurations have been proposed and guidelines for the design discussed (Seo et al. [2007]; Peterson et al. [2010]; Kormoll et al. [2011]; Roellinghoff et al. [2010]; Richard [2012]) and prototypes are under development in Lyon and Dresden. The configuration of a three-interaction Compton camera has also been studied through simulation (Richard et al. [2010]; Mackin et al. [2013]) and the a three-interaction prototype is currently under construction by Llosá et al. [2011].

As the Compton camera only gives the incidence direction of the photons on a cone, several methods have been explored to improve the images obtained with simple backprojection. Frandes et al. [2008, 2010] discussed the use of maximum likelihood methods and did succeed in reconstructing an abrupt edge, but the precise recovery of the Bragg peak has not yet been successful. The combination with a beam hodoscope tagging individual particles was explored by Richard [2012]. Some proposed configurations use electron tracking within the detector (Kurosawa et al. [2011]; Frandes et al. [2008]) to improve the cone backprojection. Another promising avenue is the use of “gamma electron vertex imaging” (Kim et al. [2012]), in which the Compton electron is tracked very precisely through the detector, resulting in a linear backprojection. In simulations, the range could be determined with errors as low as 2-3 mm with the last method.

## Comparisons

Recently, a study comparing geometries of knife-edge slit and parallel-slit collimators was performed by Cambraia Lopes et al. [2012] using Monte Carlo simulations of 200 MeV protons. The knife-edge configuration used was that of Bom et al. [2012] and different multi-parallel-slit configurations were explored, optimized for different distances from the beam line. In a comparison of efficiency for fixed spatial resolution and vice versa, the knife-edge configuration was shown to be advantageous at distances below 45 cm. However, it should be noted that the knife-edge configuration used for the comparison had a large magnification factor, giving it a very good spatial resolution and efficiency by using a very large detector surface. A more equivalent comparison to multi-slit configuration would be one using the same volume of detector material to image the same field of view (FOV) with both cameras, either by modifying the camera height, or by using a converging parallel-slit collimator configuration with an equivalent magnification factor. This would in all likelihood result in a more favorable conclusion for the parallel-slit configuration.

A comparison study between prompt gamma and PET for range verification in four

treatment cases was performed by [Moteabbed et al. \[2011\]](#). The four cases included head and neck, prostate, spine, and abdomen with passive scattering or pencil beam treatment plans. The comparison was made on the base of GEANT4 simulations of the treatment plan in the planning CT and included biological washout models for the PET. The detector response was not included in simulations, and may be somewhat favorable to PET, as 511 keV photons are easier to image than the higher energies used for prompt gamma. Emission rates 10 times higher were observed for prompt gamma than for PET for in-beam imaging, and the difference increased to a factor of 60 to 80 when compared to offline PET due to the decay of the  $\beta^+$  emitters. Both distributions were shown to be correlated to dose distributions, but the distance between the falloff of PET or PG profiles and the Bragg peak varied due to heterogeneities and could be significant (between 0.2 and 9 mm). The prompt-gamma falloff was in average closer to the Bragg peak, an advantage shown mostly in the case of pencil beams.

### 1.3 Monte Carlo codes

To study and optimize different camera configurations, the most practical way is to undertake Monte Carlo simulations. Both the platform GATE based on the code GEANT4 and the code MCNPX were used at different times for results presented in this text, mainly due to practical reasons.

As of yet, no code has been fully validated by comparison with measurements when it comes to prompt-gamma measurements. The MCNPX code has been shown to deviate in the prediction mostly of background counts ([Smeets et al. \[2012\]](#)) and the GATE/GEANT4 V9.1 code has been shown to overestimate prompt gamma emission rates by factors as high as 12 for carbon ions depending on the physics list ([Le Foulher \[2010\]](#)). Modifications have recently been made to the GEANT code that bring simulation results into much closer agreement with measurement, in particular by adjusting the Quantum Molecular Dynamic (QMD) model ([Dedes et al. \[2012\]](#)). In more recent comparisons between GEANT4 and FLUKA codes by [Robert et al. \[2013\]](#); [Biegun et al. \[2012\]](#) in the context of the ENVISION program, GEANT was shown to overestimate gamma emission rates for protons by a factor of two.

For all simulations conducted with GATE, version V6 was used in combination with GEANT4 version 9.4p01 with the physics list and settings proposed by [Grevillot et al. \[2012\]](#) for proton pencil beams. As detailed by [Grevillot et al. \[2012\]](#), we use the standard package for EM interactions and G4HadronElasticProcess combined with the G4HadronElastic model for elastic hadronic interactions. The precompound model for non-elastic hadron interactions. Exceptionally close agreement between simulations using the precompound model and measurements have been shown by [Polf et al. \[2009\]](#) for proton irradiations.

For MCNPX simulations, the setting presented in [Smeets \[2012\]](#) were used. The version used was 2.5. Tabulated cross-sections were used for proton and neutron transport whenever available and the Bertini intranuclear cascade model with default setting wherever not. Proton cross sections were chosen from the la150h library and neutron cross sections from the la150n library.

In order to ensure that the different codes used do not introduce an unfair advantage for one of the camera geometries presented, selected configurations of the multi-slit camera optimization study conducted with GATE were benchmarked against simulations of the same geometry using MCNPX. As shown in [figure 1.3 on the next page](#), rather good agreement was obtained.

To prevent any possible bias, while the optimization study is conducted with different codes to avoid repeating simulations, the final configurations compared in [chapter 6](#) are all made with GATE.

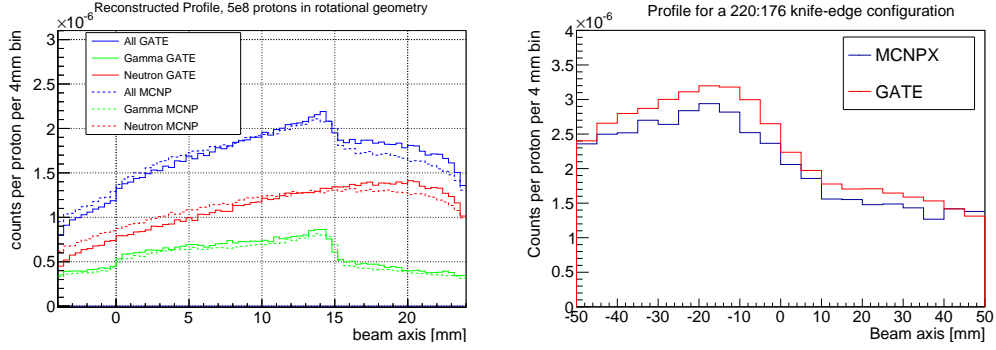


Figure 1.3: Comparison between profiles obtained with the GATE and MCNPX Monte Carlo codes. Left: for a multi-parallel-slit setup (cylindrical configuration, distance beam-collimator 200 mm collimator depth 160 mm, septa width 1 mm, pitch 4 mm, distance collimator-crystal 20 mm). Right: for a knife-edge slit configuration (distance beam-collimator: 220 mm, distance collimator-crystal 176 mm, wall thickness 40 mm, slit opening 6 mm, slit angle 63.4 mm). The energy windows in both cases are set to 3-6 MeV.

## 1.4 Objective of this study

We have seen that developing a method for range control can potentially be a vast improvement to protontherapy and that several avenues are currently being explored to find a solution. Prompt gamma cameras seem to be one viable candidate and the next step towards the application of this method is finding the optimal camera configuration. The focus will be on protontherapy only to limit the scope, but the methods and considerations are of course applicable to carbon ion therapy, once the different emission profiles and rates are taken into consideration.

There is a range of work done on different concepts for prompt-gamma imaging, but for the moment it is rather difficult to compare the different proposed solutions as they are not developed with the same objectives in mind or evaluated with the same figures of merit. In order to make a choice as to what geometry to further develop and make into a prototype, an objective, quantitative mode of comparison is needed.

We will leave aside Compton camera concepts in our comparison, as they are still in a stage of development of finding the right concept and especially the reconstruction algorithms do not seem to be optimized as of yet and ready for a fair comparison. Furthermore, most Compton camera concepts aim at imaging 3D distributions rather than 1D, which is rather difficult to compare. The 2D solutions of parallel-hole and pinhole collimators do not seem to be viable solutions due to very low efficiency.

The objective of this study, then, is to identify optimal solutions for one-dimensional collimated cameras, both parallel-slit and knife-edge and compare the performances of both. The chosen arena of competition is the performance in identifying the falloff location of the prompt-gamma profile for a homogeneous target. Figures of merit are presented that reflect the spatial resolution and the accuracy with which the camera can find the edge of the prompt-gamma profile. A choice is made to use a relative measurement of the position with regards to predictions of simulations rather than an absolute measurement, as the absolute distance between the prompt-gamma profile falloff and the Bragg peak have been shown to vary in heterogeneous media.

As requirements may change for heterogeneous targets and priorities may shift from optimizing one imaging property to another, it is interesting to not only find one optimized solution, but rather understand the underlying parameters and mechanisms that drive the performance. To this end, a study of a generalized prompt-gamma profile is undertaken and mathematical models are proposed to describe the evolution of the camera performance for different parameters. Guidelines are given to construct a camera with the desired trade-off between properties and the limits of achievable performance are highlighted.

Working on both collimated camera concepts in parallel also allows some synergies in the development. For example, basically the same detectors can be installed behind both collimators, a fact which is used in section 6.5 on page 116 where measurements are presented that use the same scintillator detector array behind two prototype collimators and compare the results. An attempt is made to make the comparison between both camera concepts as fair as possible, for example by using similar volumes of scintillators in the detector and the same distances from the target. The two camera concepts have different strong points, which are put forward.



# Chapter 2

## The prompt-gamma profile properties

### 2.1 Beam properties

In this section, we will look at some of the most common techniques used for beam production and delivery and give some typical values for beam properties such as time structure, beam current and spot size, in view of the influence of these parameters on prompt-gamma detection.

#### 2.1.1 Accelerators

There are two basic types of circular particle accelerators used for proton therapy today, cyclotrons and synchrotrons, as well as the mixture of both approaches, the synchro-cyclotron.

In principle, cyclotrons use semi-circular dipoles, called “dees” to generate a uniform magnetic field keeping the accelerated particles on a circular path. In the gap between the dees, an electric field is applied that oscillates in such a way that it accelerates the particles each time they pass the gap. As the energy of the particles increases, the radius of their circular path increases, leading to a spiral motion. Particles are produced by a source in the center of the cyclotron and extracted once they reach the edge. The extraction energy is fixed by the accelerator radius and strength of the magnetic field. An intrinsic limit of the energies obtainable with a cyclotron is the fact that as particles reach relativistic speeds, their rotations are no longer be isochronous and they fall progressively out of step with the radiofrequency used for acceleration.

A synchrotron, on the other hand, uses a modulated magnetic field to keep particles on the same circular path throughout their acceleration. The strength of the magnetic field has to be synchronized with the energy of the particle bunch. Particles are usually injected from a linear pre-accelerator and can be extracted once they reach the desired energy.

Synchro-cyclotrons are a mix of both, using a spiral path and a modulated magnetic field. The main advantage of synchro-cyclotrons is that they can be built smaller than either of the other two.

The consequence of the accelerator type for prompt-gamma imaging lies mainly in the resulting beam time structure. Beam currents are usually given as average currents, but for pulsed beams, the instantaneous current during the pulse can be much larger than the average current. For considerations of the needed detector counting rate capability and dead time, it can be crucial to consider the prompt-gamma detection rate during a pulse as well as the average rate. Additionally, when considering the use of time-of-flight (TOF) discrimination for prompt gamma, the beam microstructure may have an effect on how effective the discrimination is. Slow moving particles such as neutrons emitted in the patient during one bunch may reach the detector at the same time as fast moving particles (prompt gamma) from the next bunch (see section [4.2 on page 55](#) as well as [Biegun et al. \[2012\]](#)).

In cyclotrons, there can in principle be particles on each turn of the spiral simultaneously, so that beam can be continuously injected and extracted. There is, however, a time micro-structure due to the radio frequency (RF) used for the accelerating electric field. In the example of an IBA C230 cyclotron, the RF is 106 MHz, corresponding to one proton bunch every 9.4 ns. The time distribution of protons within the bunch is approximately Gaussian, with the width of the distribution depending on the beam transport system (the longer the beam transport, the more the energy spread of the beam leads to a wider distribution in time). As the energy of the beam is modified with a passive degrader element, the energy spread is larger for low beam energies that had to pass through more degrader material, which leads to more straggling. When the degrader is placed far upstream before the beam transport, this difference in energy spread may lead to differences in bunch length at different energies. At the patient treatment room, bunches are typically around 2 ns long. For most treatment centers, no exact measurement of the bunch width and particle distribution in time are available for the treatment rooms, so that bunch lengths given here are estimations. Other commonly used cyclotrons use similar frequencies of 30-100 MHz and result in similar micro-bunches (see for example [Schippers \[2009\]](#)).

As the magnetic fields are synchronized with the particle energy for synchrotrons and synchro-cyclotrons, particles at different stages of acceleration cannot be in the accelerator at the same time. Each pulse has to be injected, accelerated and extracted before the next can enter. This leads to a beam structure where beam pulses are separated by relatively long intervals.

For a synchrotron, injection and acceleration times are typically of the order of a few seconds, in which time there is no beam to the treatment room. Slow extraction (where only a fraction of the beam is extracted at each turn, so that the accelerator is emptied gradually over many turns) can last up to the order of 10 s, during which time continuous beam is delivered. As an example, the HIT synchrotron in Heidelberg has an injection and acceleration time of 2 s with an extraction of maximum 10 s ([Peters et al. \[2010\]](#)). The extraction can be interrupted as needed, for example to move the pencil beam to the next spot. In a synchrotron, there is also a beam microstructure due to the need to have small ion bunches passing through the acceleration cavities. The filling factor (bunch length divided by the bunch period) is typically around 10%. At maximum energy, the time that a bunch takes to complete one turn is typically one order of magnitude larger than for cyclotrons due to the larger radius used for synchrotrons, leading to a beam microstructure with hundreds of nanoseconds between individual bunches (depending on the extraction energy).

Synchro-cyclotrons have a beam macro-structure due to pulses being accelerated one at a time and a micro-structure due to the RF. As an example, the IBA superconducting synchro-cyclotron S2C2 has a repetition rate of 1 kHz, leading to one pulse every millisecond. The pulse length is currently estimated at 7  $\mu$ s. The beam microstructure is very similar to the one of a cyclotron, with a bunch of the order of one or two nanoseconds every 10.9 ns (all numbers for the S2C2 from [Pearson et al. \[2013\]](#)). As opposed to synchrotrons, cyclotrons have a fixed extraction energy and a fixed bunch frequency at extraction.

For an overview of the values for the different accelerator types, see [table 2.1 on page 23](#).

### 2.1.2 Beam delivery modalities

The modalities of beam delivery can be separated roughly into “passive” and “active” modalities, the main difference being that for active modalities, the beam is scanned across the target, which is not the case in passive delivery. A comprehensive compendium of the methods of beam delivery can be found for example in [Chu et al. \[1993\]](#). The methods currently under widespread use are:

**Single scattering** For this technique, a single scattering foil (often made of lead) is used to widen the beam. Only the central part of the beam, with a nearly flat proton fluence, passes through a compensator and an aperture. This technique is mostly useful for very small volumes, as a large uniform beam is difficult to achieve in this way. The advantages/drawbacks are the same as for double scattering, below.

**Double scattering** A double scattering system combines a first scatterer, used to widen the beam, with a second, non-uniform scatterer that is designed in such a way that the resulting proton fluence is nearly flat at the location of the treated volume. It allows treating volumes much larger than what is possible in single scattering. Figure 2.1 shows an illustration of the principle of double scattering and the resulting dose distribution. A very comprehensive overview of the methods used for double scattering can be found in [Gottschalk \[2004\]](#).

A patient-specific aperture or collimator, often made of brass, is used to limit the lateral extension of the beam in such a way that it is conformal to the volume to be irradiated. A range compensator is used to make the beam conform to the distal shape of the volume to irradiate. A range modulator is used to modify the beam energy so that the volume can be scanned in depth. Usually, a rotating wheel comprising different thicknesses of plastic is used as range modulator, placed inside the beam nozzle either before the scattering elements (“upstream” or “compensated” modulator) or after (“downstream”). It is also possible to use so-called “ridge filters”, which are static devices whose depth varies spatially in fine ripples or points, so that the energy spread of the beam is increased. Ridge filters allow irradiating a range of depths at once.

The main disadvantages of double scattering are that the irradiated volume cannot be completely conformal to the tumor volume; that the modulating and scattering elements relatively close to the patient produce unwanted secondary radiation and that there is a need for patient-specific hardware. In the process of producing a large uniformly flat field, a very significant portion of the protons is stopped in the nozzle. Additionally, the need for the beam to pass through the scatterers makes it impossible to irradiate the patient at the maximum energy produced by the accelerator. The main advantage of double scattering lies in the use for moving tumors by limiting interplay effects between the scanning of the tumor and the movement of the organ. This is done in two ways. Whole layers are irradiated at once, preventing interplay in the directions transversal to the beam. Moreover, the range modulator wheel completes multiple turns during the course of irradiation, which leads to an averaging effect in the depth direction.

From the point of view of prompt-gamma detection, double scattering is far from ideal. [Dowdell \[2011\]](#) studied dose deposit to the patient from neutrons and compared double-scattering and pencil beam scanning under this aspect. He found significantly more neutrons when using double-scattering, especially when measuring far from the beam axis, where our camera would be placed ([Dowdell \[2011\]](#), page 141). [Kurosawa et al. \[2011\]](#) attempted imaging an energy-modulated irradiation with a spread-out Bragg peak of 7 cm depth and observed that the sharp falloff completely disappeared in the acquired profile due to increased background radiation caused by the scattering and modulation system in the nozzle. Furthermore, each irradiated layer comprises a mix of ranges when a compensator is used, so that observing a 1D projection in a direction perpendicular to the beam will not result in a single sharp falloff. It is possible to use a prediction of the profile shape made with Monte Carlo simulations beforehand to compare to the measured profiles, but distinguishing causes of deviation between the two may become much more difficult. The use of ridge filters, of course, makes this even more problematic.

If a profile is to be acquired for each individual layer, the prompt-gamma detection system will have to be synchronized with the modulator wheel.

**Pencil beam scanning** Pencil beam scanning is a method currently being installed in an increasing number of centers. A beam with a small cross-section is scanned across the target using a variable magnetic field in the nozzle. Each layer of the volume to be irradiated is then “painted” with the beam in much the same way one would use a pencil to color an area, hence the name. To change layers, the energy is usually modified by a modulator far upstream, before the beam transport system.

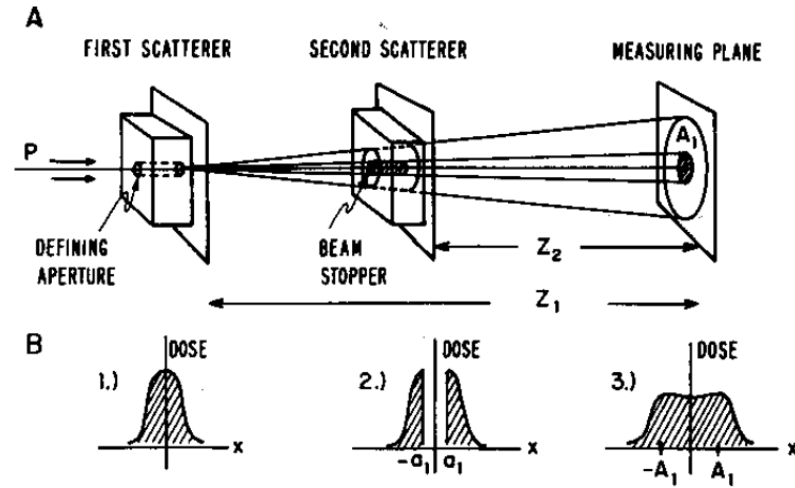


Figure 2.1: Illustration of the double-scattering beam delivery modality. Source: [Gottschalk \[2004\]](#).

During a treatment delivery using pencil beams, one usually starts with the deepest layer, doing a scan of the layer using the scanning magnets, then the energy is reduced to treat the next layer. One can use either discrete spot scanning, where the beam is turned off between each treated spot, raster scanning, where the beam is not turned off between spots, but the time of movement between spots is short compared to the time of irradiation of each spot and finally dynamic spot scanning, where the spot is scanned continuously (see [Paganetti and Bortfeld \[2005\]](#)). Some centers (such as PSI, [Pedroni et al. \[2004\]](#)) use motion of the patient couch for scanning in one dimension.

The advantages of pencil beam scanning are that one can irradiate any given volume very exactly and conform the dose to the proximal shape of the tumor, as well as the quasi-total absence of scattering material in the nozzle close to the patient. As the intensity of each scanned spot can be adjusted individually, pencil beam scanning allows a lot of flexibility in treatment planning, which can be used for intensity-modulated particle therapy (IMPT). The main drawback is the time that it takes to change the beam energy, since the whole beam transport system and the scanning magnets have to be adjusted to each value of the energy. Organ motion may lead to interplay effects with the pencil beam delivery, as shown, for example, by [Bert et al. \[2008\]](#).

In this document, we will always consider pencil beam delivery when developing a prompt-gamma detection system. Apart from the inherent energy spread of the beam, each pencil beam will have only one range (exceptions may occur where a beam is delivered along the interface of tissues of different density, where range mixing is possible). Apart from heterogeneities, the prompt-gamma profile will show a clean falloff and is relatively easy to predict.

The prompt-gamma detection system will have to be synchronized with the beam delivery system so that an individual profile can be acquired for each delivered beam.

### 2.1.3 Properties of pencil beams

As stated, the development of a prompt-gamma detection system in this text is aimed at the use during pencil beam scanning. It is useful to recall the properties of a typical commercial pencil beam delivery system at this point. All simulations in subsequent chapters are made with perfect pencil beams (all protons have exactly the same starting point, energy and direction) to preserve generality for all systems. The influence of realistic beam properties will be discussed here.

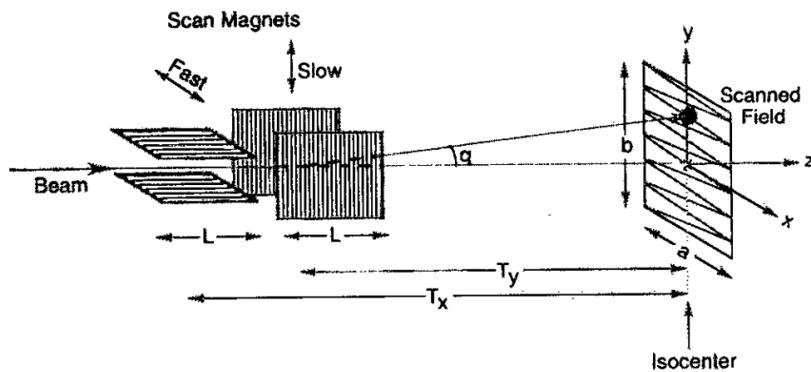


Figure 2.2: Illustration of pencil beam scanning. Source: [Chu et al. \[1993\]](#).

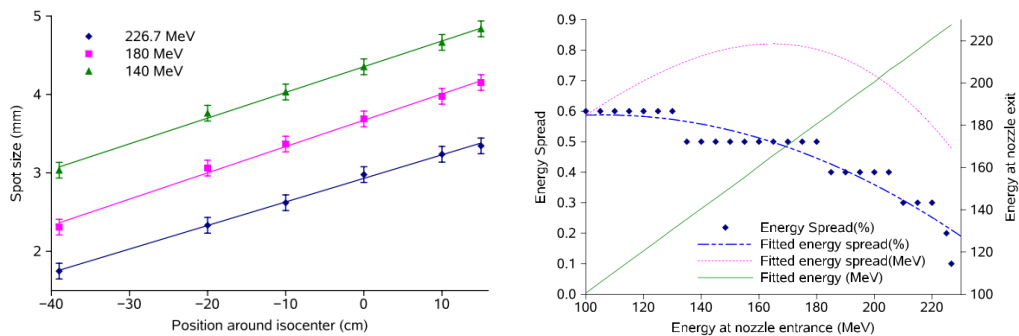


Figure 2.3: Left: measured spot sizes in air (one sigma) for different beam energies and position around isocenter along the beam trajectory. Measurements were made at WPE. Right: Energy spread dependence on the beam energy. Both reprinted from: [Grevillot \[2011\]](#).

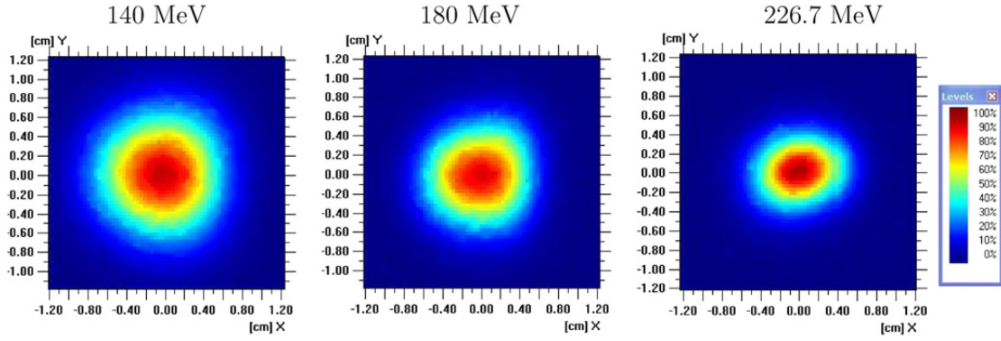


Figure 2.4: Relative dose measured at the beam isocenter for different proton beam energies with an electronic portal imaging device. From: [Grevillot \[2011\]](#).

Realistic beams at nozzle exit have:

- a time spread (discussed above section 2.1.1)
- an energy spread
- a finite size in the transversal plane
- transverse momentum of the particles

Both the energy spread and the size are usually larger for lower energies when the beam is produced with a cyclotron, as they had to pass through more degrader material. The spot size will also vary with the distance from the last beam focusing element, depending on the emittance. Figure 2.3 on the previous page shows the beam size dependence on the beam energy and the distance from the isocenter measured at an IBA treatment center. The spot size is typically around a few millimeters, but it has to be kept in mind that there will be additional scattering and spreading within the target itself, so that the beam width at the Bragg peak is larger. The beam size is relevant for prompt-gamma imaging if it leads to range mixing due to parts of the beam crossing different materials in a heterogeneous environment. Figure 2.4 shows a cross-cut of the dose measured at isocenter for different beam energies.

The energy spread is typically of the order of under one percent of the beam energy. The energy spread of the beam will lead to a larger falloff width of the emitted prompt-gamma profile than what is shown in simulations later on. However, considering the order of magnitude of the energy spread, this is a negligible effect, as the falloff width of a perfect beam is already much larger than the effect of the energy spread on the falloff width (see figure 2.6 on page 25).

#### 2.1.4 Beam currents

The beam current at nozzle exit is important for prompt-gamma detection as it determines the particle flux on the detector and the necessary count rate capability. Beam currents are usually given as average beam currents. For pulsed beams, the beam current during a pulse can be much higher than the stated average. The beam current also depends on the used beam energy and delivery method. The beam transport line is usually optimized for the highest energy of the system and when the energy is reduced upstream, this can lead to higher losses during the transport. In single and double scattering delivery, the beam current is reduced as part of the beam is absorbed by the aperture and compensator.

Table 2.1 gives the highest beam currents at which the example accelerators operate in pencil beam scanning. Even though most treatments will occur at smaller currents, the numbers are meant to give an idea of the order of magnitude of the most challenging conditions a camera may have to deal with during treatment. It is a possibility to reduce the beam current slightly during a few selected spots to facilitate imaging.

	Cyclotron	Synchrotron	Synchro-cyclotron
Example	IBA C230	HIT	IBA S2C2
Energy at extraction	230 MeV	221 MeV	230 MeV
Time macrostructure			
-period	-	~10 s	1 ms
-pulse length	-	~5 s	7 $\mu$ s
Time microstructure			
-period	~10 ns	~100 ns	~10 ns
-bunch length	~2 ns	~10 ns	~2 ns
Mean beam current (at nozzle)	3 nA	up to ~1.5 nA	up to 2 nA
Current during macropulse	-	up to ~3 nA	~300 nA
Duty factor	0.2	0.05	0.0014
Protons per bunch	~200	~2000	~20k

Table 2.1: Typical characteristics of proton pencil beams from different types of accelerators. Sources: [Cee \[2012\]](#); [Pearson et al. \[2013\]](#) and personal communication.

## 2.2 Particle emission

The purpose of this section is to describe the properties of particle emission during proton beam therapy that are most relevant to prompt-gamma imaging. We will not go into the detail of the physics behind dose deposition or neutron and prompt-gamma emission, all of which can be found in pre-existing work, for example [Le Foulher \[2010\]](#), but rather summarize the characteristics of emission that are directly relevant to prompt-gamma imaging.

The target used during simulation was a cylindrical PMMA (PolyMethyl MethAcrylate,  $(C_5H_8O_2)_n$ ,  $1.19 \text{ g/cm}^3$ ) target of 200 mm length and 75 mm radius. This target, along with the proton beam energy of 160 MeV was chosen as a benchmark for different prompt-gamma camera models in the work package 3 of the European FP7 project ENVISION. For the settings of Monte Carlo simulations, see section 1.3 on page 13. Simulations with GATE in this chapter were conducted with  $5 \times 10^6$  protons incident on the target.

### 2.2.1 Particle types and energy spectra

To understand the requirements on a prompt-gamma imaging system and to set up the simulations for optimization, it is useful to first look at the particles that are emitted. Table 2.2 shows a list of the most common particles leaving the target according to Monte Carlo simulations using MCNPX (table reprinted from [Smeets \[2012\]](#)). We can immediately see that the most common particles by far are the neutral particles: neutrons and photons. A second group, electrons and protons, are two orders of magnitude less common and the rest is even more rare. Furthermore, charged particles cannot travel far through collimator material such as tungsten or lead, so that the part that is susceptible to reach the detector is even smaller. This justifies the approach taken during simulations to neglect all particles other than neutrons and gamma leaving the target.

The energy spectrum for the neutrons and photons emitted in the target is shown in figure 2.5 on the next page. The photons have a continuous component and a series of peaks. We can identify several gamma rays listed by [Kozlovsky et al. \[2002\]](#).

### 2.2.2 Spatial distribution

Let us now take a look at the distribution of emission in space. Figure 2.6 shows, on the left, the distribution of emission points of photons and neutrons for a 160 MeV proton beam

Secondary particle	Quantity per proton
Neutron	0.12033(2)
Photon	0.09228(2)
Electron	0.002135(3)
Proton	0.001716(3)
Deuteron	0.0000484(4)
Alpha	0.0000043(1)
Triton	0.00000148(8)
Helium-3	0.00000098(6)

Table 2.2: Secondary particles leaving the PMMA target (WP3 target) irradiated with a 160 MeV pencil beam in simulation conducted with MCNPX. Data table courtesy of [Smeets \[2012\]](#). The uncertainties (2 standard deviations) in parentheses refer to the corresponding last digits.

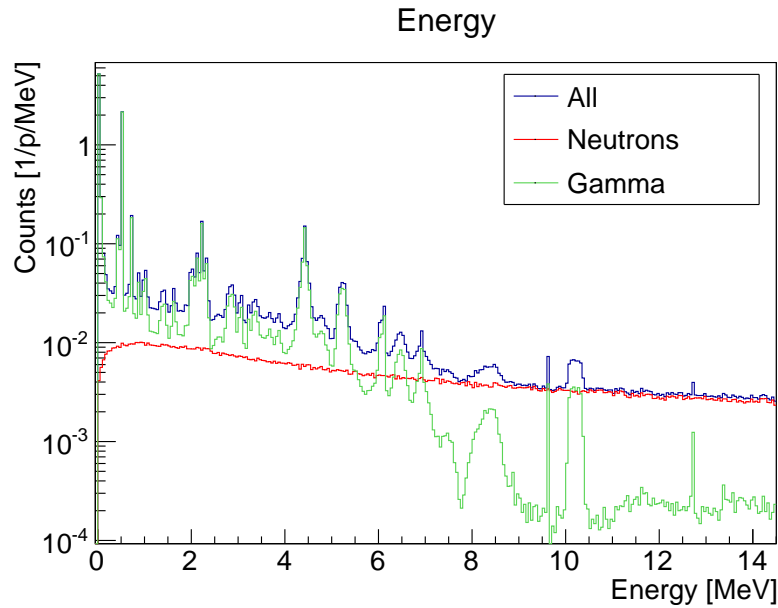


Figure 2.5: Spectrum of particles emitted within the target irradiated with a 160 MeV pencil beam in simulation conducted with GATE (see section 1.3 on page 13 for settings). Photons are shown in green, neutrons in red, and the sum of both in blue.

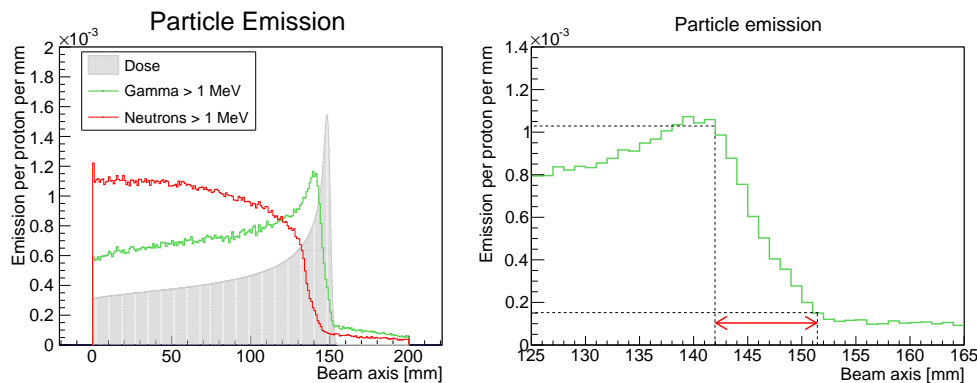


Figure 2.6: Emission of particles in a PMMA target irradiated with a 160 MeV pencil beam in simulation conducted with GATE (see section 1.3 on page 13 for settings). On the left is shown the distribution along the beam axis of neutrons (red) and photons (green) superimposed with the dose profile (the latter is shown in arbitrary units). On the right is shown a zoom of the prompt-gamma emission profile illustrating the measurement of the 95% falloff width of 9.9 mm.

in a PMMA target. Only particles with energies over 1 MeV are shown. For lower energies, probability of scattering in the patient is higher, so that they are less well correlated with the range (see section 4.3.4 on page 75). We can see that the photon emission profile rises slowly over the course of the proton trajectory, peaks just before the Bragg peak and then falls off. The tail of the distribution observed after the Bragg peak is mainly due to neutron interactions in the target. The 95% falloff width of the emission profile is 9.9 mm. The neutrons, on the other hand, show a distribution that decreases along the proton trajectory and falls off well before the Bragg peak.

Figure 2.7 on the next page shows the angular distribution of neutron and photon emission relative to the beam direction. Again, we only look at particles over 1 MeV in energy. We can see that the gamma emission is completely flat and isotropic, while the neutron distribution is sharply forward peaked. For a more detailed look at the angular distribution, the distributions with regards to both the angle and the energy are also plotted in figure 2.7. The emission of photons seems isotropic for all energies (in fact, there is a contribution of low-energy bremsstrahlung photons that is forward-peaked, too small to see in the graph). Meanwhile, the distribution of neutrons is forward-peaked mainly for high energies.

While the cameras discussed in this work are placed in a perpendicular direction from the beam and designed to show a projection of the prompt-gamma profile along the beam axis, it can be useful to have an idea of the emission distribution in the transversal direction also. For the knife-edge slit camera, which accepts photons at angles different from  $90^\circ$  outside of the center of the field of view, a large spread in the transversal direction leads to parallax effects. Furthermore, the beam spread becomes important when considering possible range mixing in heterogeneous targets later on.

Figure 2.8 shows the simulated distribution of prompt-gamma emission points for a perfect pencil beam. The observed broadening towards the Bragg peak is due to the lateral spreading of the proton beam. At the maximum of prompt-gamma emission, just before the Bragg peak, the transversal emission profile has widened to a  $\sigma$  of approximately 2 mm. In addition to this beam spreading in the target, a real proton pencil beam will of course not be perfect, but rather have a finite transversal distribution, transversal momentum, and a mix of proton energies even before impinging on the target. The values of these characteristics depend on the accelerator and beam transport and delivery. The typical spot size for a proton pencil beam is of the order of a few millimeters. A detailed description of the properties of a pencil beam at an IBA center can be found in Grevillot et al. [2011].

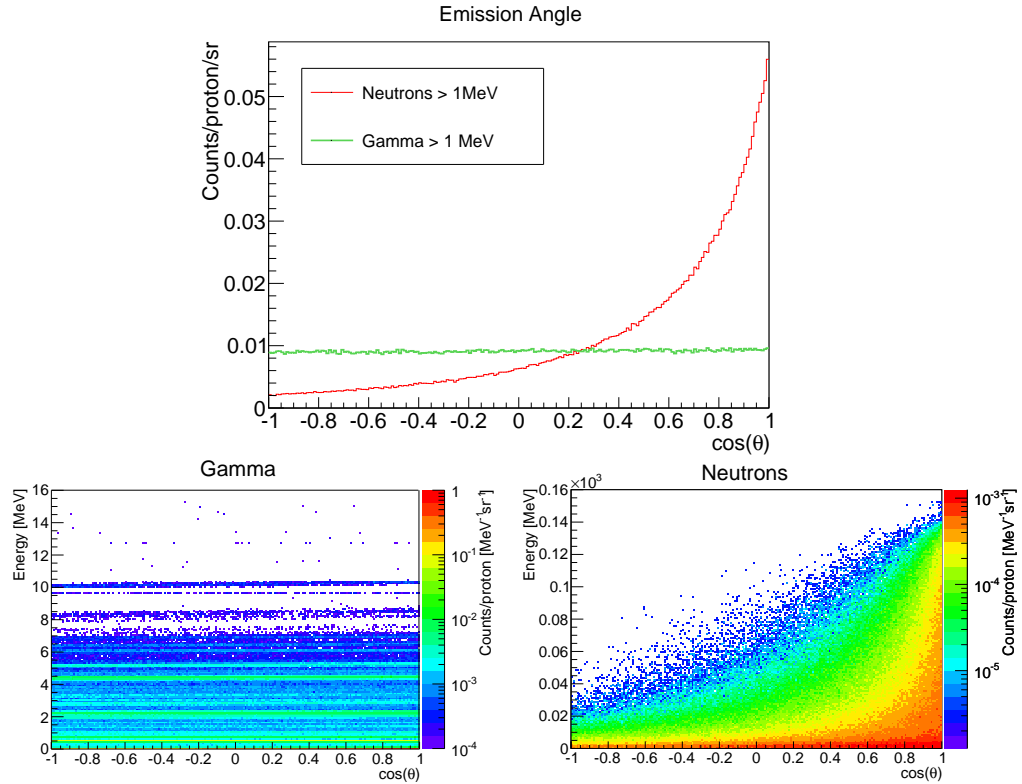


Figure 2.7: Above: different distribution with regards to emission direction of neutrons (red) and photons (green) above 1 MeV.  $\theta$  is the angle between the beam direction and the movement direction of the particle. Below: photon (left) and neutron (right) emission distribution with regards to energy and angle to the beam direction ( $\theta$ ). Photons of all energies are isotropically distributed, while neutrons are forward peaked mainly for high energies. Results shown are for a PMMA target irradiated with a 160 MeV pencil beam in simulation conducted with GATE (see section 1.3 on page 13 for settings).

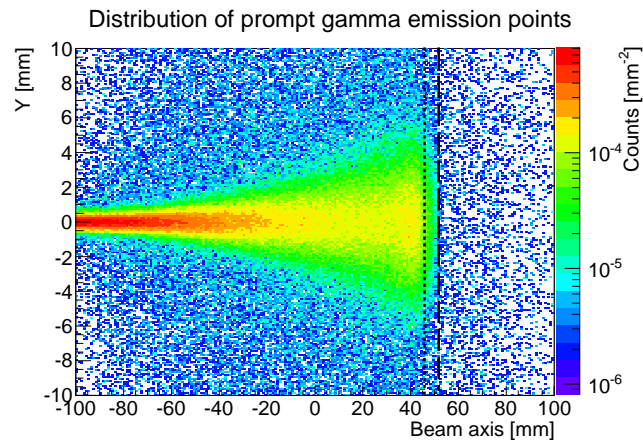


Figure 2.8: Distribution of prompt-gamma emission points in the XY-plane for a perfect pencil beam (spot size at entrance is zero) at 160 MeV in PMMA. Emission rates shown in log scale. The half-value of the prompt gamma profile falloff is shown as a dotted line, the half-value of the dose profile as a dashed line. Transversal dimension of the distribution at the widest part:  $\sigma = 2$  mm.

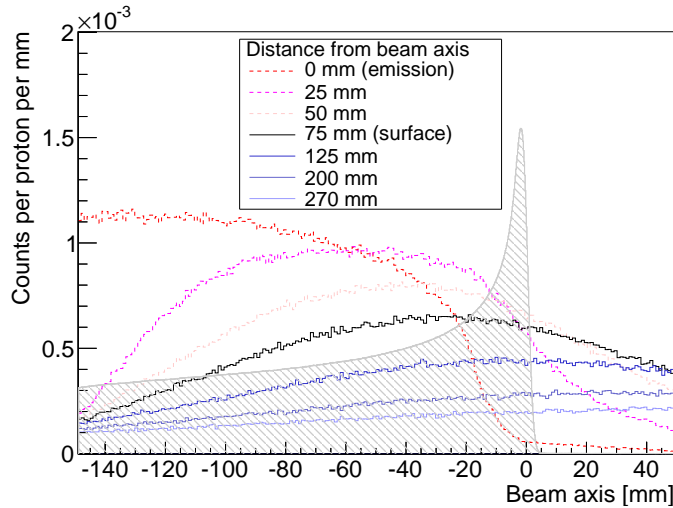


Figure 2.9: Neutron distribution with energy greater than 1 MeV along the beam axis direction at different distances in air from the beam axis for a 160 MeV proton beam in PMMA.

### 2.2.3 Neutron background

As we have seen, neutrons are emitted along most of the range and are sharply peaked in a forward emission direction. Assuming that the neutrons will be largely uncollimated by the collimator setups proposed in this work, it is interesting to look at the distribution of neutrons freely evolving in space. In figure 2.9 are shown the neutron distributions that could be seen at different distances from the beam axis in air. Different distances that are significant for the setups of the camera (see chapters 4 and 5) are represented. The effects of a collimator on the distribution are not taken into account. Due to the distribution of emission directions of the neutrons, their distribution increases along the beam axis direction when measured far from the target. At distances where the camera would typically be placed, we can expect to see a rising neutron background.

In addition to the neutron background coming directly from the target and included in the simulations, there is a contribution of neutrons scattered on material in the room and not included in the simulations. Trial simulations including the walls of the treatment room suggest that the additional contribution is minor, but no simulations have yet been conducted including material that is closer to the target and the camera, such as the patient couch, the nozzle, etc. In pencil beam scanning, the contribution of neutrons emitted in the nozzle is expected to be small compared to what is emitted in the patient (no material in the beam path in the nozzle except for the ionization chamber). Background contributions may vary depending on the experimental setup, the room size etc.



## Chapter 3

# Performance evaluation and analysis methods of the prompt-gamma profile

This chapter focuses on the methods of evaluation of one-dimensional prompt-gamma profiles, independently of the way the profile is obtained. Here, we develop the tools used to analyze the profiles of both parallel-slit and knife-edge cameras and lay the groundwork for understanding how the performance evolves with a changing geometry by looking at generic profiles.

### 3.1 Choice of performance criteria

In order to compare the merits of different camera types and configurations, quantitative criteria have to be chosen to evaluate the performance. Most of the qualities desired in the imaging system are clear-cut and easily observable on the profile itself: large contrast, low background, a narrow falloff width, corresponding to the “peak”, “baseline” and “delta” values in figure 3.1 on the following page. However, modifications of the camera geometry most often result in improvement in one of these criteria and deterioration of another. If so, how should their relative importance be weighted? Is it possible to find one parameter that predicts optimal performance for detecting range errors?

To estimate the ability to measure range errors, we look at the precision with which the falloff position can be retrieved. The measurement of the falloff position can be used in combination with a measurement of the point where the beam enters into the patient to obtain a measured value for the range. The measurement of the entrance point can be made either with the same prompt-gamma camera (in which case a similar precision is expected) or by external means, such as optical patient alignment systems (in which case the precision of the positioning of the camera system itself has to be taken into account). It is assumed that the camera can be aligned very precisely at a perpendicular angle to the beam direction at any time, so that parallax effects do not have to be taken into account. We make the assumption that the camera configuration that is optimal for imaging the falloff will also be optimal for imaging the entrance and only look at the falloff retrieval precision (FRP) and not the entrance position retrieval precision as a figure of merit.

For simplicity and to be able to make the most general statements possible, at first only homogeneous targets are considered. Errors are assumed to take the form of a shift of the profile with regards to the expected profile. The FRP is then expressed as the precision with which such a shift can be measured. The other desired qualities of the profile, such as the contrast, the falloff width and the noise are indirectly factored in to the FRP, as they all influence its value.

By using homogeneous targets, one important aspect of the prompt gamma emission is

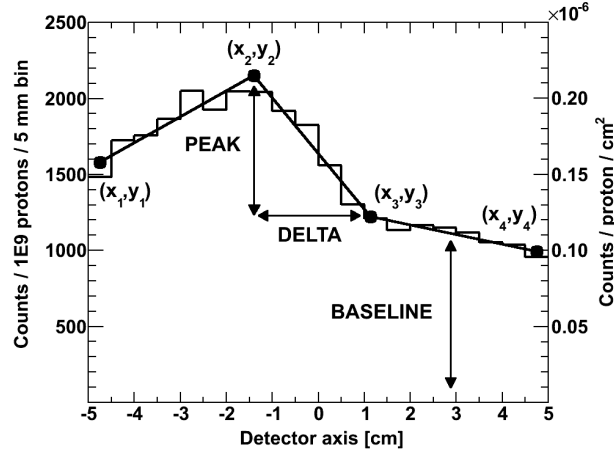


Figure 3.1: Profile characteristics as defined and used in Smeets [2012] : peak, delta and baseline correspond to contrast, falloff width and background respectively. Reprinted from Smeets [2012].

neglected: tissue density and, to a lesser extent, composition variations have an influence on the rate of prompt-gamma emission per proton and unit length (see, for example: De Rydt [2013]). For a real, heterogeneous patient, the entrance rise and the falloff will not be the only variations or edges in the profile. It can then be advantageous to have a good spatial resolution in order to separate the different effects. Therefore, when comparing profiles, the spatial resolution should not be neglected. A final decision on the relative weight of FRP and spatial resolution for performance in clinical conditions can only be made with an extensive study of clinical (heterogeneous) cases and may well depend on the kind of case being targeted.

To accurately estimate the noisiness of profiles, the expected number of counts for a typical profile during measurement has to be known. Figure 3.2 on the next page shows an example of a prostate treatment plan with the pencil beam spots drawn as points plotted according to their beam energy and number of protons to be delivered. This example was taken from Grevillot [2011] and was already used for performance analysis of the knife-edge slit camera in Smeets et al. [2012]. The most interesting spots for range verification are the most distal spots. The beams of distal spots have traveled through the most material, meaning that errors are most likely show up in those spots. Additionally, distal spots are also the ones that are at risk of overshooting and depositing dose in organs at risk behind the tumor volume. Fortunately, these also tend to use the highest numbers of protons. In the example, the distal spots range from about  $5 \times 10^7$  to  $2 \times 10^8$  protons. It seems reasonable to set this as a goal for the number of protons for which the camera must achieve a reasonable FRP.

## 3.2 Analysis of prompt-gamma profiles for homogeneous targets

### 3.2.1 Method for obtaining the falloff retrieval precision

In order to estimate the precision with which the falloff (or entrance) position can be retrieved, we start with the assumption that the expected profile is well known. To get this profile, that we will call “reference profile”, either a high-statistics measurement or a high-statistics Monte Carlo simulation is used (see figure 3.3 on page 32). The number of counts has to be sufficiently high that the statistical fluctuations are small enough to not obscure the shape of the profile. In clinical practice, this reference profile will have to be predicted

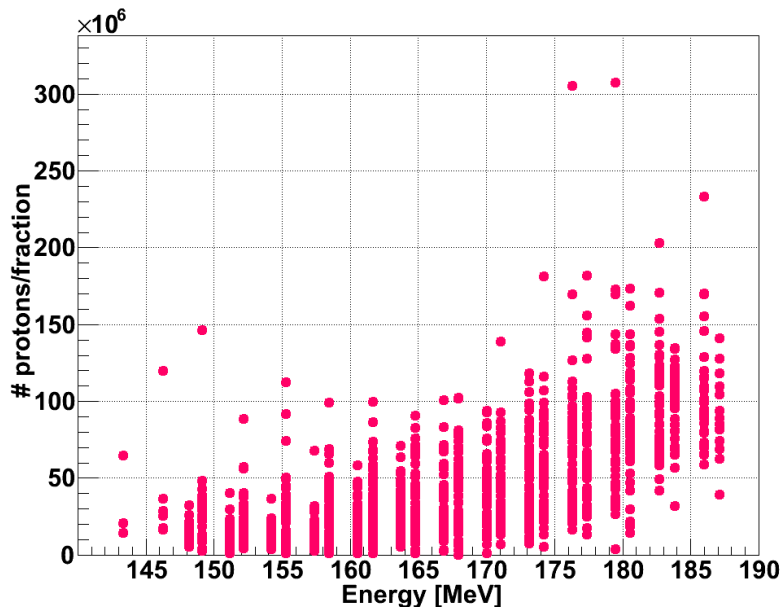


Figure 3.2: Example of a prostate treatment plan: individual pencil beam spots of the treatment are plotted according to the beam energy and the number of protons per fraction delivered to the spot. Source: [Grevillot \[2011\]](#).

by Monte Carlo simulation or analytical models. This type of profile typically consists of a discrete set of points, either corresponding to detector pixels, collimator slits, or measurement points during a scan. To be able to predict the expectation of counts at any one point, the profile is then fitted with a continuous function, the reference function (see section 3.2.2 on page 33). Note that this function is a representation of expected counts for a detector unit placed at a given position (based on the reference profile) and not an emission profile or theoretical model.

Next comes the generation of a “sample” profile. This is a profile that stands for what would actually be measured during irradiation. It corresponds to a given number of protons delivered. It can be generated either by subsampling data gathered for the reference profile or by applying Poisson statistics and a random generator to the reference profile to obtain the appropriate statistical noise (figure 3.3 on the following page, center).

The sample profile is then matched to the reference function by applying a shift along the beam axis. The sections of the function describing the falloff and entrance are used separately. The idea behind this is that when there is an error in range, in the case of a homogeneous target, the profile part around the falloff will shift by an amount corresponding to the range error. Errors in alignment, for example, would result in shifts of both the entrance part and the falloff part. We will concentrate on the part of the falloff here, the same is done analogously for the entrance. The part around the falloff that is used for matching purposes depends on the properties of the profile and is adjusted to the different cases in this manuscript.

To do the matching, several methods can be considered. The method here used is a simple minimization of the  $\chi^2$  (sum of the squares of the differences between sample profile and reference function). Depending on the profile shape and amount of noise, there can be multiple minima in the objective function, one corresponding to the “real” match, the others due to artifacts. Such an artifact could for example be that statistical fluctuations lead to a bump somewhere in the sample profile that matches the peak of the reference profile well by pure chance. The creation of these artifacts is favored by the fact that the contrast in all the profiles studied here is relatively low compared to the unrelated background counts, so that for low statistics profiles, the amplitude of statistical fluctuations (noise) can be of the

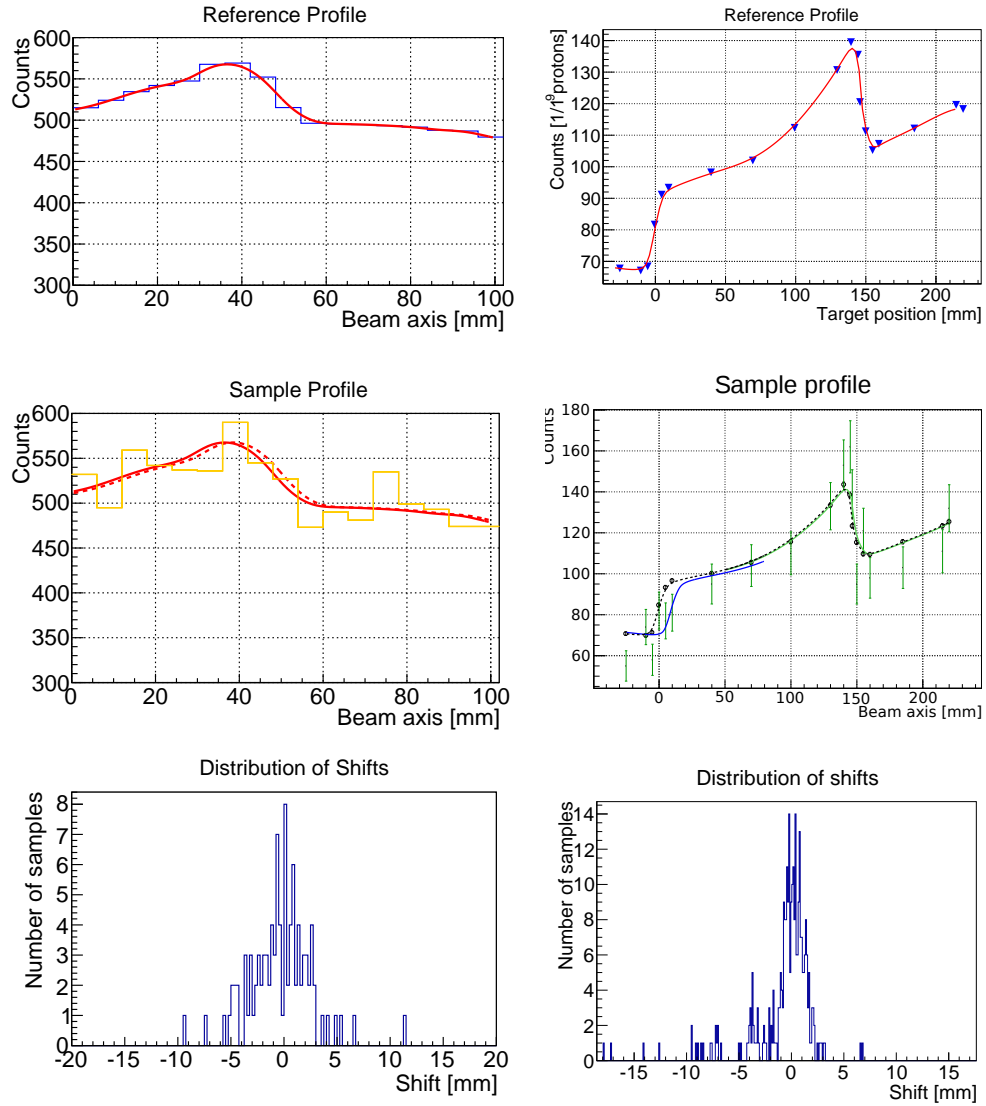


Figure 3.3: The method for obtaining the falloff retrieval position as applied to a simulated multi-parallel-slit profile (left) and to a profile measured by scanning a single parallel slit (right). On the top is shown the high-statistics reference profile fitted with a continuous spline function. In the middle a sample profile generated by applying Poisson noise and the reference function shifted to match. On the bottom the distribution of shifts. The left column corresponds to simulated profiles from section 4.3, while the right column corresponds to measured profiles from section 4.2.

same order of magnitude as the contrast. Since it is impossible to distinguish between the real match and artifacts in the case of a real measurement, the global minimum of the  $\chi^2$  is always taken. And because gradient descent methods are unreliable for finding the global minimum when several minima exist, a grid search method is applied for finding the global minimum.

We have now determined a shift that gives the best match between the sample profile and the reference profile. Since the sample profile represents exactly the same range as the reference profile, the expectation for the shift is zero. When repeated many times with many independently generated sample profiles, the distribution of the obtained shifts gives an idea of how precisely the camera is able to measure a shift (3.3, bottom on page 32). Specifically, the standard deviation of the distribution is a good measure for the precision of the method for determining the falloff position. The mean of the distribution is expected to be zero, otherwise there is a systematic bias in the method.

### 3.2.2 Methods for fitting the prompt gamma profile

For the fitting procedure detailed above to work, the reference profile has to be fitted with a continuous function, the reference function. This function should fulfill several criteria. It should be able to follow the shape of the profile as closely as possible, especially the falloff and entrance part. Ideally, it should include some inherent smoothing of fluctuations in the flat or straight parts of the profile. It should be flexible enough to be applicable to the different profiles observed with different camera geometries and work for both the entrance and the falloff. It should be robust, so that a large number of profiles can be fitted automatically without having to be adjusted or validated by hand. Ideally, it should be continuously derivable, as discontinuities in the derivative can lead to discontinuities in the  $\chi^2$  function used to find the shift.

The first functions tested were simple polynomial functions. They worked well for the falloff itself, but did not fit well if a large part of the plateau and/or background after the falloff was included in the fitting range.

Next, a three-straight-line fit was developed, with each line representing the plateau, falloff and background regions respectively. This method has the advantage of using parameters that directly correspond to interesting properties of the profile, such as slopes, background level, and peak value. The x-values of the first and last points are fixed and the lines must join at interval edges, but the interval edges themselves can slide to best fit the profile. However, the angular nature of the function does not follow the rounded shape of the profile very well and the jumps in the derivative led to problems with the  $\chi^2$ . The obtained FRP is also not very good compared to the other methods. Additionally, the starting point for fitting the reference function to the reference profile has to be well chosen, as this function is not very robust for fitting.

Working with the approximation that the emission profile of prompt gamma is nearly linear before and after the falloff, that the falloff itself is an edge that has been softened by the process of detection, an error function seems a good candidate to model the expected measured profile. It provides the basic advantages of the three-straight-line solution, but avoids its problems by having rounded corners. Indeed, this type of function is used to describe the properties of theoretical profiles in section 3.2.4 on page 39. For the application to the measured or simulated profiles, however, one can observe that the curvatures at the top and bottom of the falloff are not the same, as can be seen, for example, in figure 3.4 on the following page. In the definition of an error function, the curvatures cannot be adjusted separately, as they are controlled by the same parameter. Tests fitting an error function to measured profiles show that it cannot fit the shape at the peak and just after the falloff exactly at the same time.

To follow the profile as closely as possible, different forms of splines were tested (linear interpolation, cubic interpolation among others). Splines have the possible drawback that they follow the noise in the profile and, especially for cubic or higher-order splines, the attempt to pass through points exactly can introduce oscillations. Finally, NURBS were chosen as a robust solution. See figures 3.5 on page 35 to 3.8 on page 38 for an overview of the

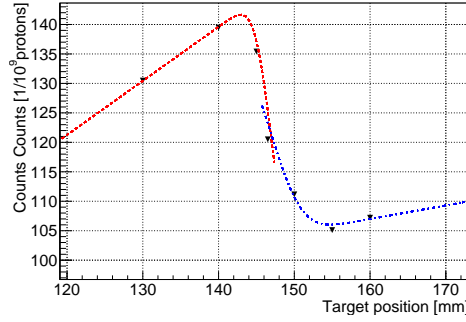


Figure 3.4: Measured prompt gamma profile fitted with two different error functions for the peak and the transition from falloff to background. The curvatures of the best fitting functions for the two parts are different, meaning that an error function cannot properly fit both.

different functions that were tested and appendix [A on page 159](#) for an explanation of NURB splines. NURBS follow the profile shape closely but are not constrained to pass through the points of the profile, so that they have less oscillation and provide some smoothing.

Using splines has one additional advantage that should not be neglected going forward. When studying heterogeneous profiles, additional variations will be introduced in the profile and the shape will no longer necessarily be well described by one function such as polynomial, three-straight-line or error function. Using a spline allows the function to adapt to the profile no matter the shape.

### 3.2.3 Spatial resolution

While most of the optimization focuses on the ideal FRP, the spatial resolution should not be ignored as a figure of merit, as it can be useful to resolve heterogeneities along the beam path.

By definition, the spatial resolution of an imaging system is the ability to distinguish in the image two source points separated by a given distance in the image plane. Oftentimes, the spatial resolution is evaluated by studying the point spread function (PSF) of the imaging system, defined as the response of the system to a point source. In optics, the Rayleigh criterion is used to describe the spatial resolution when Airy discs are used to describe the PSF. It states that the smallest distance for which two points can be separated is that for which the maximum of the PSF of one point coincides with the first minimum of the PSF of the other. In our case, the PSF is better described by a Gaussian shape, for which the Rayleigh criterion does not apply. However, it is possible to define an analogous criterion, where two points can be separated if peaks of the two corresponding PSFs can still be separated, i.e. if there is a minimum between the two. Calculation shows that the minimum disappears when the two points are closer than  $2\sigma$  apart, so that the standard deviation of the Gaussian can be used as a measure for the spatial resolution. For further description of the calculation of spatial resolution, specifically for medical imaging, see for example [Smith \[1997\]](#).

The same information can also be obtained from the response to an infinitely sharp edge. Assuming the PSF has a Gaussian form centered in zero, it can be described by:

$$PSF(x) = G(x) = \frac{1}{\sqrt{2\pi}\sigma} \exp\left(-\frac{x^2}{2\sigma^2}\right) \quad (3.1)$$

Generally, a good representation of edges is found in the error function. The error function is defined as:

$$\text{erf}(x) = \int_0^x \exp(-t^2) dt \quad (3.2)$$

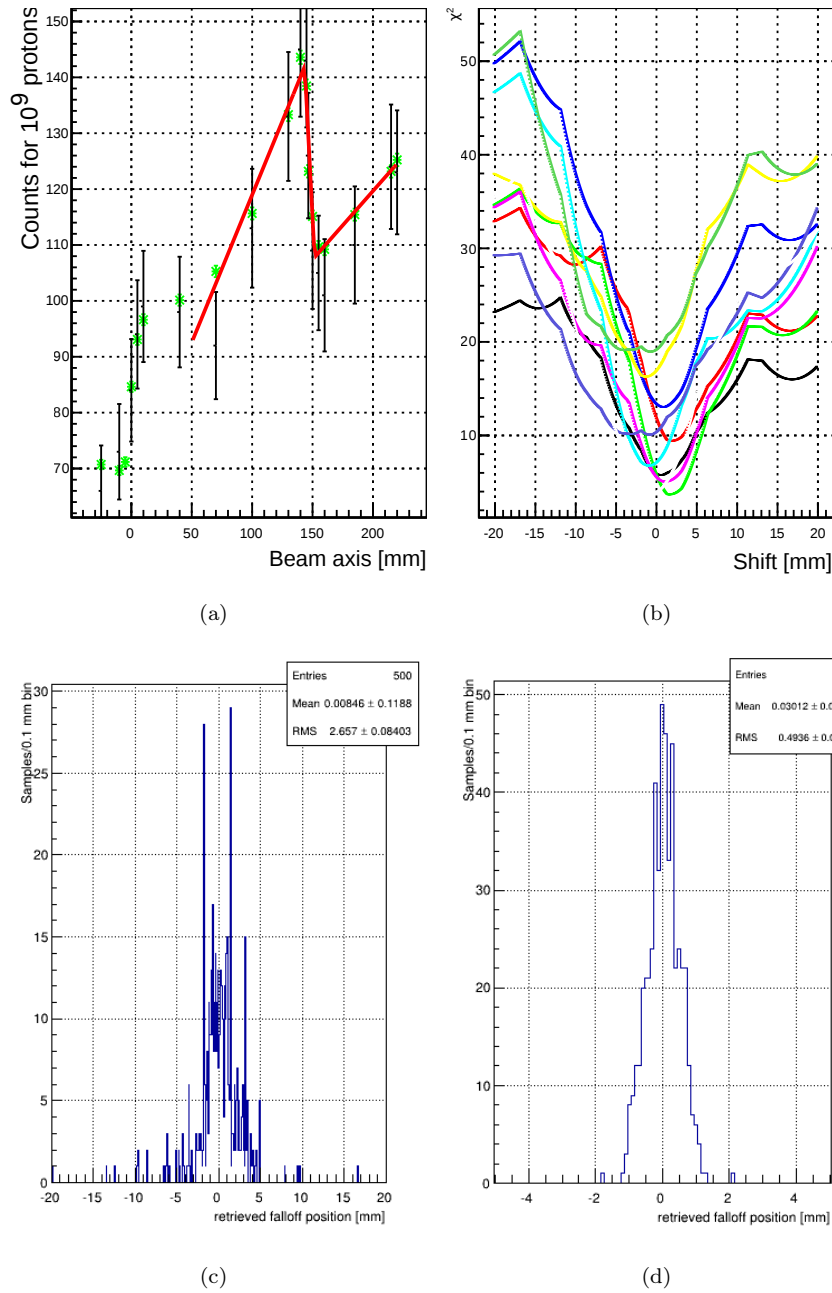


Figure 3.5: Example application of the 3-straight-line function to a measured profile: (a) The reference profile (green) and the function (red) fitted to the sample profile (black). (b) Sample  $\chi^2$  functions for  $1e9$  protons. (c) and (d) Distributions of falloff positions for  $1 \times 10^9$  protons and for  $1 \times 10^{10}$  protons respectively

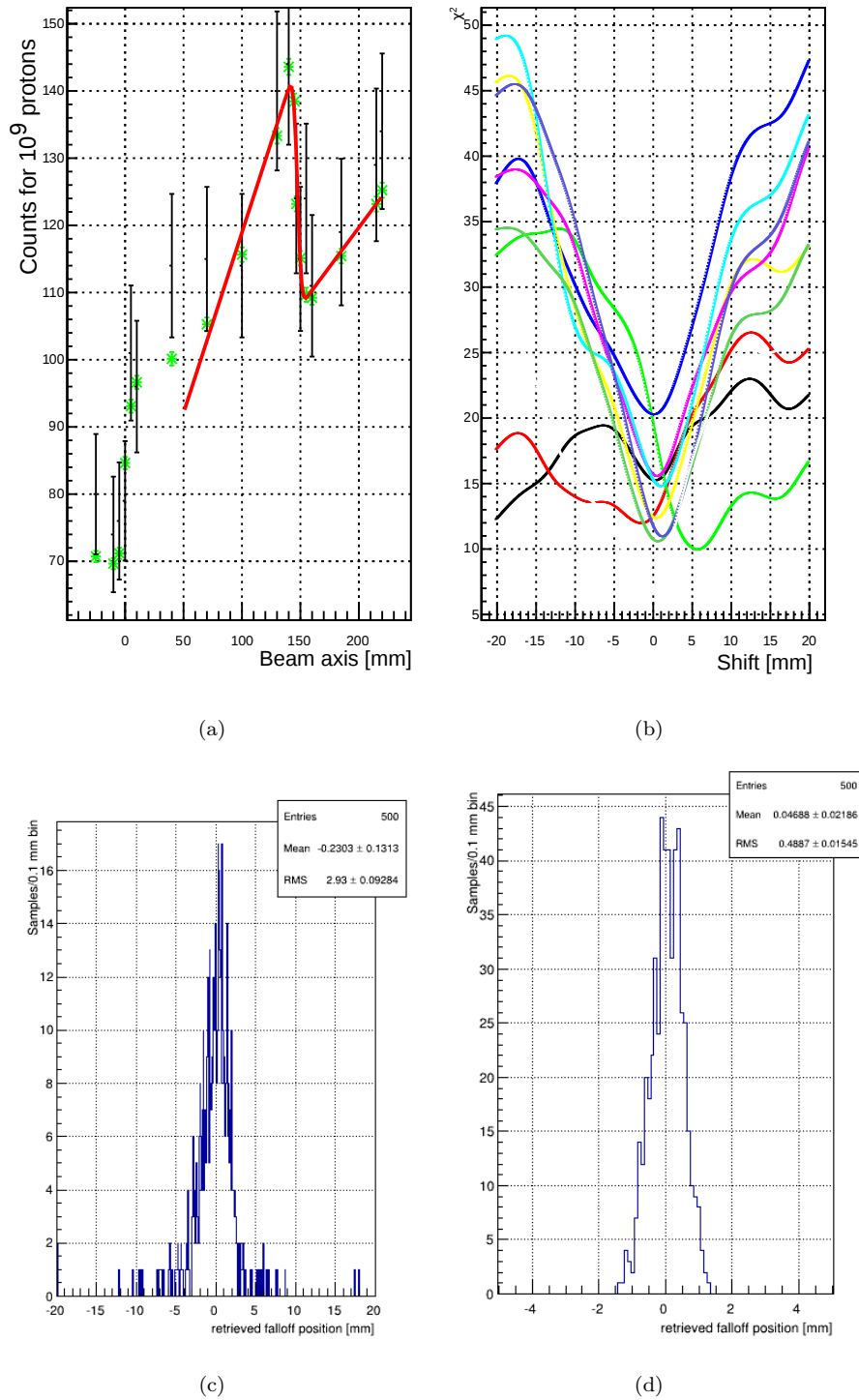


Figure 3.6: Example application of the error function to a measured profile: (a) The reference profile (green) and the function (red) fitted to the sample profile (black). (b) Sample  $\chi^2$  functions for  $1e9$  protons. (c) and (d) Distributions of falloff positions for  $1 \times 10^9$  protons and for  $1 \times 10^{10}$  protons respectively

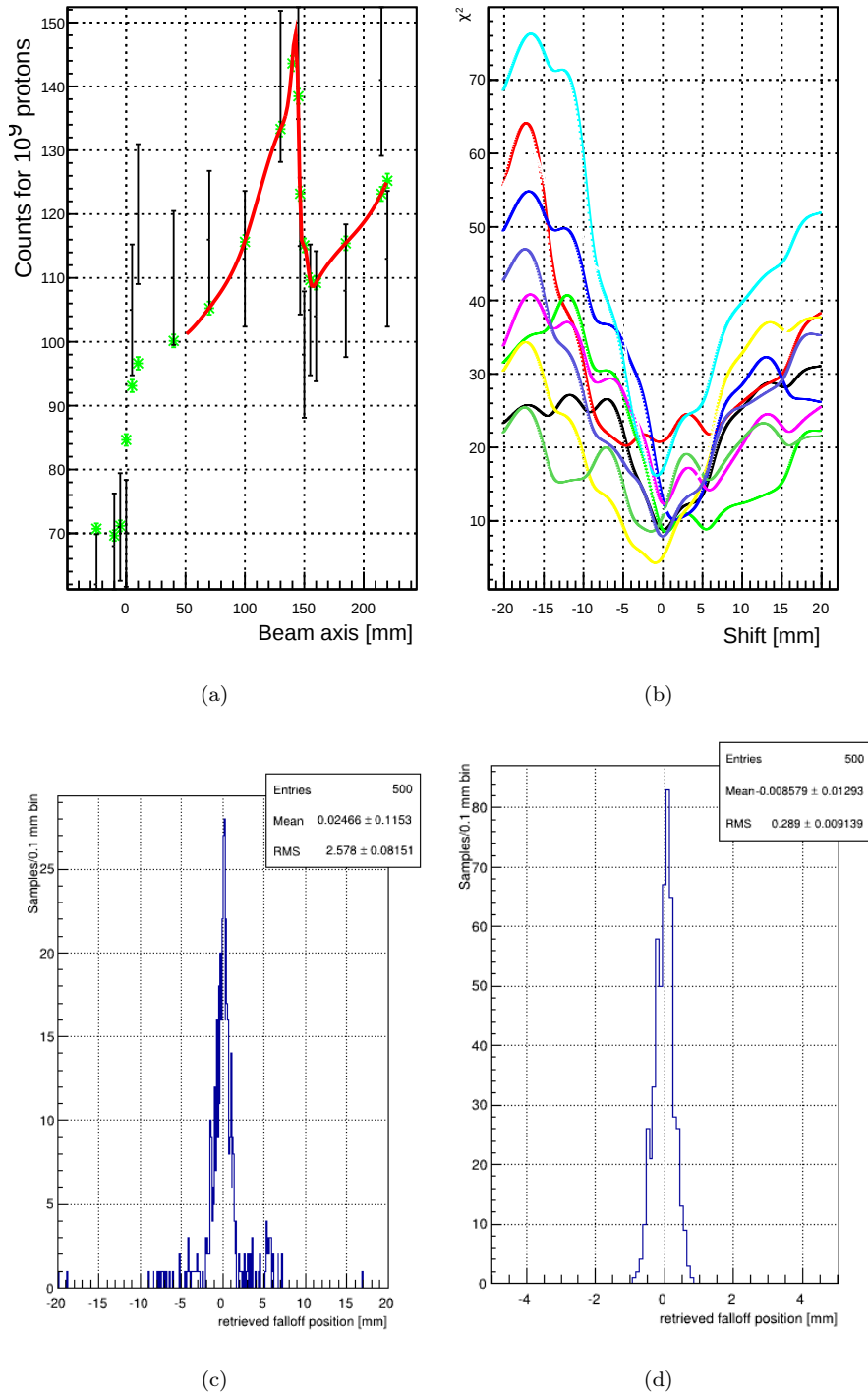


Figure 3.7: Example application of a cubic spline interpolation to a measured profile: (a) The reference profile (green) and the function (red) fitted to the sample profile (black). (b) Sample  $\chi^2$  functions for  $10^9$  protons. (c) and (d) Distributions of falloff positions for  $1 \times 10^9$  protons and for  $1 \times 10^{10}$  protons respectively

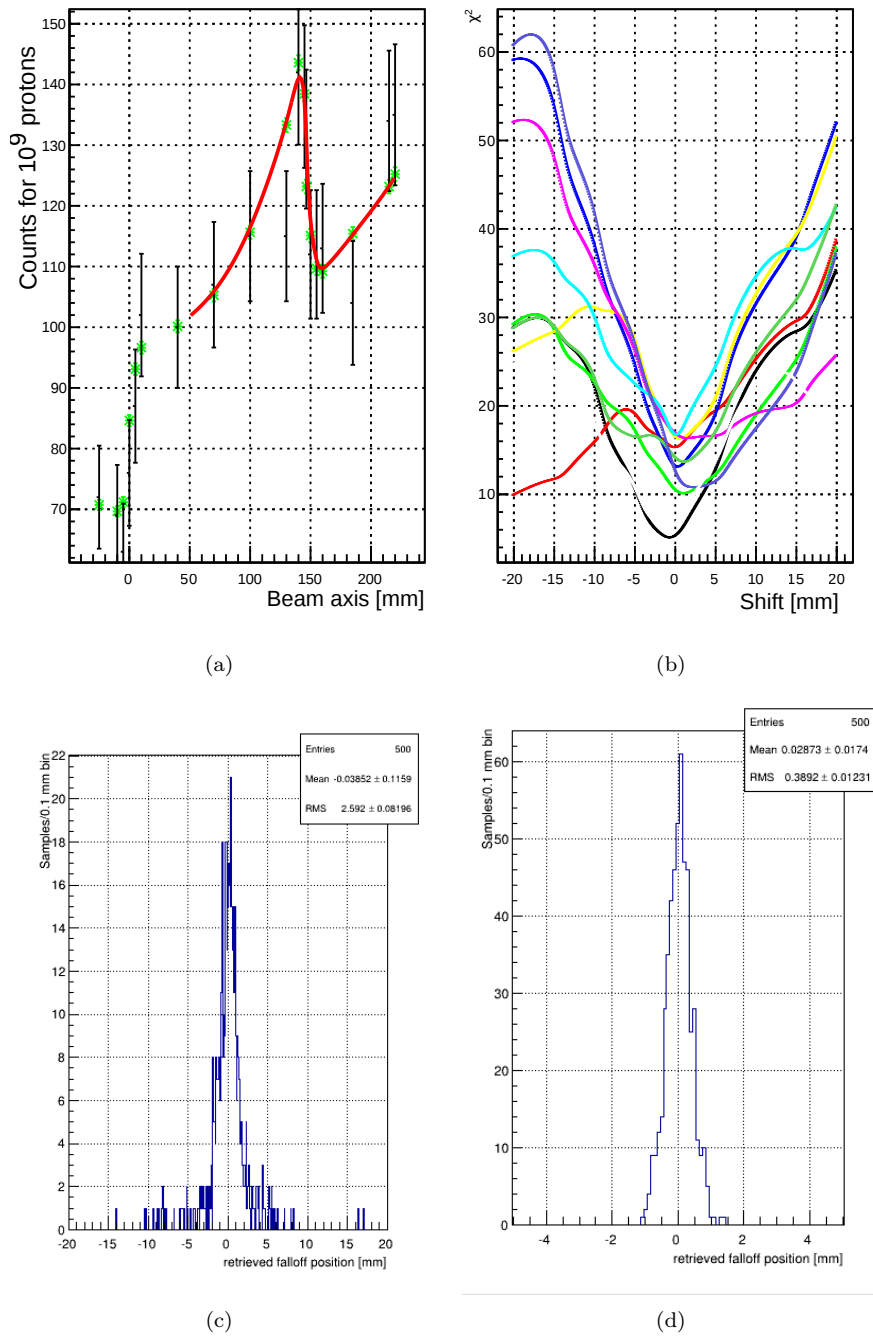


Figure 3.8: Example application of the NURBS to a measured profile: (a) The reference profile (green) and the function (red) fitted to the sample profile (black). (b) Sample  $\chi^2$  functions for  $1e9$  protons. (c) and (d) Distributions of falloff positions for  $1 \times 10^9$  protons and for  $1 \times 10^{10}$  protons respectively

The image of an edge located in zero can be described by:

$$P(x) = a \times \operatorname{erf}(bx) + c = a \frac{2}{\sqrt{\pi}} \int_0^{bx} \exp(-t^2) dt + c \quad (3.3)$$

$$= a \frac{2}{\sqrt{\pi}} \int_0^x \exp(-b^2\tau^2) \frac{\partial t}{\partial \tau} d\tau + c \quad \text{with } t = b\tau \quad (3.4)$$

$$= a \frac{2b}{\sqrt{\pi}} \int_0^x \exp(-b^2\tau^2) d\tau + c \quad (3.5)$$

$$= 2a \frac{1}{\sqrt{2\pi} \left(\frac{1}{\sqrt{2b}}\right)} \int_0^x \exp\left(\frac{-\tau^2}{2\left(\frac{1}{\sqrt{2b}}\right)^2}\right) \quad (3.6)$$

Meaning that parameter  $b$  can be used to describe the width of the PSF in an equivalent way:

$$\sigma \equiv \frac{1}{\sqrt{2b}} \quad (3.7)$$

As can be seen in section 2.2.2 on page 23, the emission profile of the prompt gamma obtained by Monte Carlo simulation falls off shortly before the Bragg peak, with a 95% falloff width of 9.9 mm. The falloff width of the observed profile is a convolution of the emission edge with the PSF, and in the approximation that the PSF is Gaussian, the falloff width of the measured profile will be the root of the sum of the squares of the falloff width at emission and the spatial resolution. Since the falloff width at emission is known, this allows us to obtain the spatial resolution of the camera from the falloff width of the profile.

When considering the theoretical, purely geometrical properties of a collimator/detector configuration, the spatial resolution can be estimated by the field of view that the smallest unit or pixel of the detector has on the source and by the resolution of the detector itself. For a realistic detector, however, we must consider septal penetration and Compton scattering within the collimator material, as they may lead to significant deviations from the geometrical model. These effects are studied individually for both camera types in the corresponding chapters.

### 3.2.4 Desirable profile properties

**An analytical method to study profile properties** When doing optimization of a system by Monte Carlo simulation, each tested configuration can take a lot of calculation time and exploring large parameter spaces blindly is long and inefficient. Therefore, it would be very useful to have analytical calculations that give a first impression of what can be expected and that serve as a guideline during optimization. It is possible to make at least qualitative links between the parameters of a camera geometry and what the expected influence is on the profile properties. For example, it is evident that the acceptance angle of a collimator is instrumental in determining the tradeoff between spatial resolution and signal amplitude. Knowing how these influence the figures of merit in our case already gives a good idea of what kind of collimator is most likely to give good results and points to what region in the parameter space is most interesting.

What we are aiming at is a comprehensive view of how the properties of generic profiles translate into performance of the system with regards to finding the range and to spatial resolution. This description is completely independent of the practical implementation of a camera. Additionally, studying the link between profile properties and performance can allow better separation of effects so that they can be more easily studied and understood. By estimating the importance of some effects beforehand, the number of simulations can be reduced. For example, section 3.2.4 on page 48 presents a study of whether an offset of the slit centers of a multi-slit collimator will have a systematic effect on the measured shift (as observed, for example, by Testa [2010]) and comes to the conclusion that this is only a problem when the field of view through each slit is very narrow. It is therefore not necessary

to study this effect via simulation as long as certain constraints are respected, which reduces the number of simulations considerably.

The profiles that have already been measured or simulated serve as a good starting point to model what a generalized measured prompt-gamma profile can look like and this study gives an idea of the direction to go to improve on the existing systems.

From looking at the simulated emission profile of prompt-gamma and measurements that have been conducted, the essence of finding the range is finding edges in a profile. The edge at the entrance of the target is caused by the sudden and large change in the density of the material that the protons cross (from air to tissue) and the falloff edge is due to protons no longer having the necessary energy to produce the nuclear reactions leading to prompt gamma. There are various effects that contribute to the blurring of the edges, starting with straggling of the protons in the beam, scattering within the target, imperfect collimation and finally effects within the detector itself. The function we are using is meant to approximate all of these effects and give a representation of what the output profile of the detection system could be. A good representation of an edge is the error function, defined in equation (3.2) previously.

Let us consider the parameters that could vary with different implementations of cameras and that could have an impact on the performance:

**The contrast** is defined as the amplitude of the signal component which is correlated to the proton range. It is the difference between the number of counts just before the edge and just after the edge. This value is influenced by the solid angle of the detector, the detector volume and by the acceptance angle of the collimator.

**The background** is defined as all counts that are not correlated to the edge. These are typically neutrons, gamma coming from neutron interactions with the collimator, gamma that have crossed through collimator material without interacting and scattered prompt gamma. The background is influenced by the solid angle, the amount of collimator material and the detector volume.

**The noise** is defined as the statistical fluctuations at each point in the profile. Due to the nature of the measurement, the noise is considered to follow Poisson statistics and be equal to the square root of the number of counts. In all prompt-gamma profiles measured hitherto, the contrast was rather small compared to the background, so the noise is dominated by the amount of background counts. Techniques such as TOF can be used to reduce noise.

**The falloff width** is closely related to the spatial resolution of the system. It is the space over which the falloff occurs. Best spatial resolution is achieved with collimators that have small acceptance angles and for highly pixellated detectors. For all collimated detectors, the falloff width is approximately equal to the convolution of the field of view of a detection unit with the falloff width of the emission profile (see sections 4.1 on page 53 and 5.1 on page 91). To understand this relation between the spatial resolution and the falloff width, consider a scan acquisition of a perfectly sharp emission profile. The measured counts will fall from the maximum to the minimum exactly as the edge is scanned from one side of field of view to the other.

**The slopes** Measurements have shown that the profile is not completely flat before and after the edge. This is due in part to the non-isotropic emission of neutrons, which adds a rising background and to the slight increase in prompt-gamma production towards the end of the proton trajectory. These effects appear as approximately linear increases in beam axis direction. These are not parameters that can be influenced in a straightforward way by the architecture of the camera, since they are inherent to what is emitted. However, they do have to be taken into account since they change the behavior of the profile. The placement of the camera in relation to neutron background does have a slight influence on the slope of the background since the neutron emission is non-isotropic.

**Distance between measurement points** For any type of camera, the profile is generally represented by a discrete set of measurement points. These can be pixels in a crystal or pixels in an image created by Anger logic for a monolithic crystal or measurement positions along a scan for instance. This determines the number of points that define the profile and corresponds to the bin width in histogram representations of the profile. In the case of pixels, the number of pixels is typically anti-proportional to the number of counts per pixel (since the total number of counts is constant). In the case of a scan, this is an independent parameter. It is conceivable to have a variable distance between measurement points, for example taking more points near the falloff. This was the case for some of the measurements relying on a scan of a target with a single slit. For simplicity's sake, this is not an option explored in the present study, but could be an avenue for further improving performance in the future.

**Detector unit** We define as a detector unit the smallest unit of the detector that provides a data point. This can be a crystal in a pixellated scintillator, the crystal of a scanned detector or the binning used for the image of an Anger logic detector.

**Realtive location of measurement points** As the measurement points are discrete, the location of the edge relative to these points can have a systematic effect on the measured position of the edge, as demonstrated by Testa [2010] leading to a “staircase” effect. See section 3.2.4 on page 48 for further explanation.

By introducing a few parameters, the error function can be adjusted to reflect the first four properties as well as a horizontal shift which can be used to represent the shifting of the edge that we are trying to measure.

$$P(x) = -A\text{erf}(B(x - C))(1 + D(x - C)) + (AD + EF)(x - C) + F \quad (3.8)$$

Where:

$A$  controls the amplitude of the edge

$B$  controls the falloff width

$C$  controls the horizontal shift

$D$  controls the slope before the edge

$E$  controls an overall slope

$F$  controls a vertical shift, or background

The parameters describing  $P(x)$  can be linked back to the general properties of a profile as follows:

$$\text{Contrast} = 2A \quad (3.9)$$

$$\text{Background} = F - A \quad (3.10)$$

$$\text{Noise} = 1/2 \left( \sqrt{F + A} + \sqrt{F - A} \right) \quad (3.11)$$

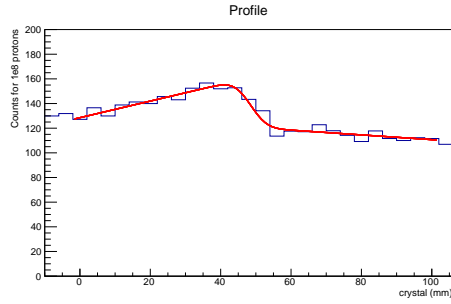
$$\text{Falloff width (95\%)} = \frac{2\sqrt{2}}{B} \quad (3.12)$$

$$\text{Background slope} = E \times F \quad (3.13)$$

$$\text{Slope of correlated signal contribution} = 2A \times D \quad (3.14)$$

The falloff width is defined so that 95% of the total falloff amplitude are contained in the falloff width.

The noise in this case is an approximation of the average noise over the whole profile, using the average of standard deviation of counts just before and just after the falloff. The approximation is valid in cases where the value of the objective  $\chi^2$  function is dominated by



Chosen parameters	
Number of protons	$1 \times 10^8$
Collimator depth	80 mm
Collimator fill factor	0.5
Collimator pitch	4 mm
Dist. Beam-Collimator	200 mm
Dist. Collimator-Crystals	0 mm
Energy window	3-6 MeV

Figure 3.9: Simulated profile used to get parameters of reference for  $P(x)$ . See section 4.3 on page 66 for the definition of configuration parameters.

Parameter	Value
A	20 (Contrast = 40 counts)
B	0.2 (Falloff width = 14 mm)
D	0
E	0
F	140 (Background = 120 counts)

Table 3.1: Default parameter settings for  $P(x)$

contributions from points near the falloff. As the slopes are not taken into account in the calculation of the noise, measurement points far from the falloff may have a different noise level that is not taken into account.

To represent the effects related to the discretization, a profile histogram is drawn from the error function at points distant by  $W$ . The histogram bins also have the width  $W$ . By default, there is a bin center at the origin (which is also the point of inflection of the profile), which can be offset by a parameter  $O$ .

The histogram generated in this way is treated as a reference profile with the generating erf function used as a reference function unless otherwise stated. By definition,  $P(x)$  represents the number of counts per detector unit expected when the detector unit is centered in  $x$ . The influence of each of the profile properties on the FRP is studied in the following sections.

To study the influence of the different parameters on the FRP,  $P(x)$  is used as the reference function and 300 sample profiles are generated using Poisson sampling. The process described above in section 3.2.1 on page 30 is then applied and the FRP is estimated for each setting of the parameters. Each parameter is studied separately, for three different settings of the contrast (except for the contrast itself which is studied for three different settings of the background). To simplify the analysis, profiles are studied with slopes before and after the falloff set to zero.

Since this study is meant to serve as a guideline for optimization of a multi-slit camera in particular, the parameter ranges were based on what had been observed in a first test simulation of a multi-parallel-slit configuration described in figure 3.9.

By default, the parameters are set as in table 3.1 unless otherwise specified.

**Varying contrast for constant background** Let us first take a look at the influence of the amplitude of the contrast on the obtainable FRP while leaving the background constant. For a real detector, the contrast can be changed, for example, by changing the acceptance angle of a collimator. We expect the FRP to improve for higher values of the contrast.

In figure 3.10 on the next page can be seen example profiles for different settings of the

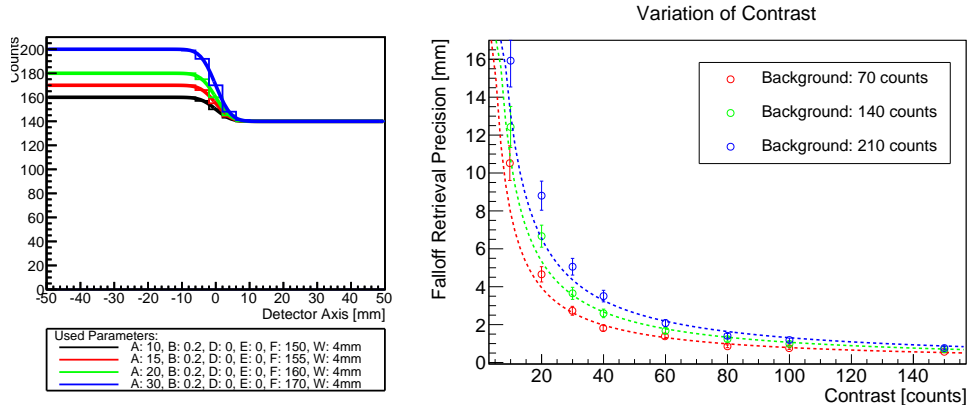


Figure 3.10: Variation of the contrast: example profiles (left) and influence on the FRP (right). The example profiles correspond to points of the green FRP curve. The FRP exhibits behavior consistent with a  $1/x$  dependency on the contrast. Dotted lines in the graph on the right represent fits with  $const. \times 1/x$ .

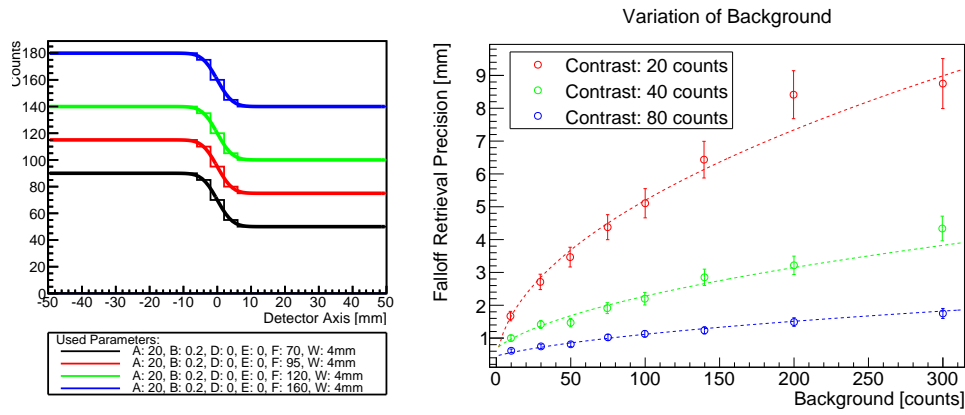


Figure 3.11: Variation of the background: example profiles (left) and influence on the FRP (right). The example profiles correspond to points of the green curve. The FRP exhibits behavior consistent with a  $\sqrt{x + const.}$  dependency on the background, dotted lines present fits with such a function.

contrast as well as the influence on the FRP. For all settings of the background, the data points for the FRP are consistent with a proportionality to the inverse of the contrast. It can be observed that for small values of the contrast, there is a departure from the  $1/x$  behavior, due to increased incidence of outliers (outliers are defined in section 4.2.2 on page 60). This departure from the expected behavior occurs at larger values of the contrast when the background level is higher, since this is an effect that only occurs for small contrast/noise ratios.

**Varying background for constant contrast** A variation of the background can for example be achieved applying background reduction techniques such as TOF.

In figure 3.11, the influence of the background on the profile shape and on the FRP is shown. The background mainly influences the noise on the profile, so it is expected to be proportional to  $\sqrt{x + const.}$  (where the constant relates to the statistical fluctuations of the correlated prompt-gamma signal). Fitting the points with the function (dashed line in the graph) confirms this dependency.

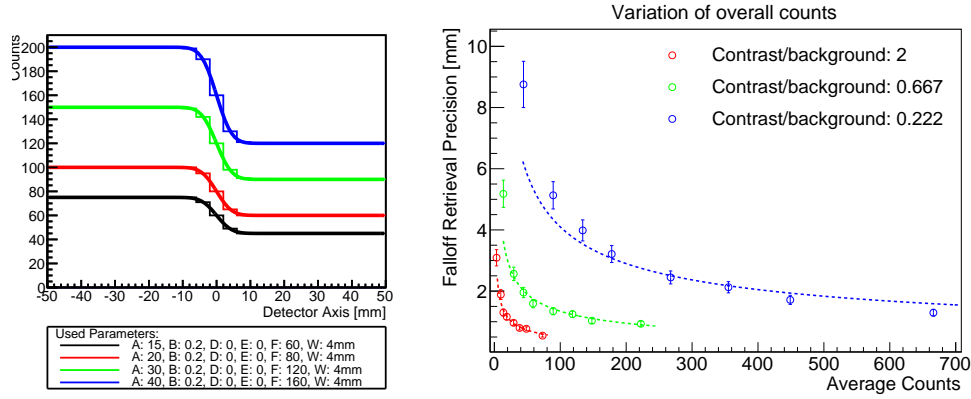


Figure 3.12: Variation of the total number of counts: example profiles (left) and influence on the FRP (right). The example profiles correspond to points of the green curve. The behavior is consistent with the combination of the two previous effects: the total dependency is proportional to  $1/\sqrt{x}$  in the total number of counts.

The influence of the contrast and background can be summarized in one equation:

$$\text{FRP} \propto \frac{\text{Noise}}{\text{Contrast}}$$

**Varying total number of counts** Varying geometrical properties like the detector height or the crystal depth mainly influences the total number of counts (both signal and background) proportionally. As can be seen in figure 3.12, the behavior combines the two previous dependencies on the contrast and background as expected, leading to a total dependency in  $1/\sqrt{x}$ .

**Contrast for constant contrast/noise** From the previous observations, it follows that for a given contrast/noise ratio, the FRP must always be the same, no matter the absolute values of background and contrast. To verify, figure 3.13 on the next page shows the behavior of the FRP for different values of the contrast while keeping the contrast/noise constant.

**The contrast/noise** is not a parameter that is linked to one specific property of collimator geometry. Rather, it provides an indication for the parameter space of the collimator, for it tells us that improving the contrast by a factor  $n$  will have the equivalent effect on the FRP as decreasing the noise by a factor  $n$ .

In figure 3.14 on the facing page are plotted the values obtained for the constants in figure 3.13 as a function of the contrast/noise ratio. As can be expected from the previous observations on the dependence on contrast, the dependence on the total number of counts and the fact that the FRP is constant for a given contrast/noise ratio, the FRP is overall approximately inversely proportional to the contrast/noise ratio.

**Varying falloff width** The falloff width is equivalent to the spatial resolution of the detector. It can be modified, for example, by changing the source field of view of each slit of a multi-parallel-slit camera, or by bringing the camera closer to the target. Note that the distance between measurement points is kept constant.

From figure 3.15 on the next page, it can be seen that the FRP appears to be linear in the falloff width for different values of the contrast. This is valid as long as the falloff width is larger than the distance between measurement points. It is interesting to note that even for the falloff width going to zero, the FRP does not go to zero! This is due to the fact that, although the falloff width diminishes, the distance between the measurement points is kept constant at 4 mm. This means that as the falloff width decreases, there are less measurement

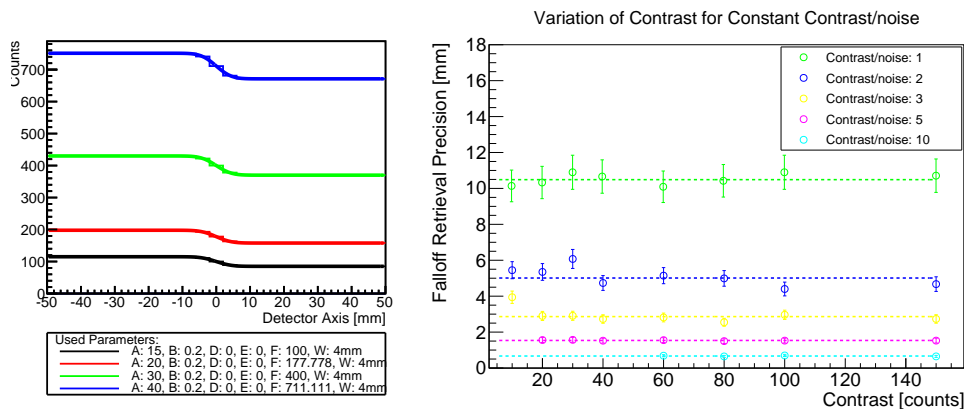


Figure 3.13: Variation of the contrast for constant contrast/noise: example profiles (left) and influence on the FRP (right). The example profiles correspond to points of the yellow curve. The FRP exhibits the expected constant behavior.

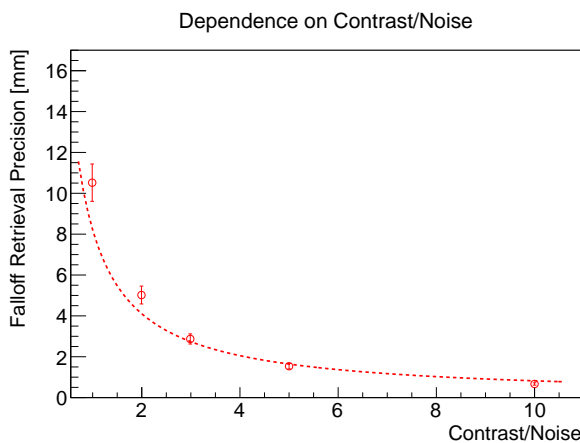


Figure 3.14: Dependence of the FRP on the contrast/noise ratio. The dashed line represents a fit with  $const./x$ , as expected, the FRP is inversely proportional to the contrast/noise ratio.

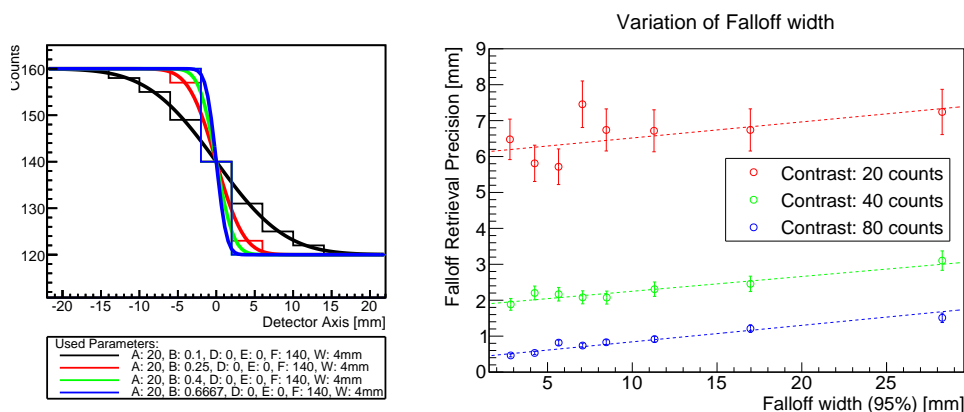


Figure 3.15: Variation of the falloff width with a constant distance between measurement points of 4 mm: example profiles (left) and influence on the FRP (right). The example profiles correspond to points of the green curve. The FRP exhibits linear behavior. The FRP does tend towards zero for very small falloff widths as the FRP is dominated by effects of the binning in this region.

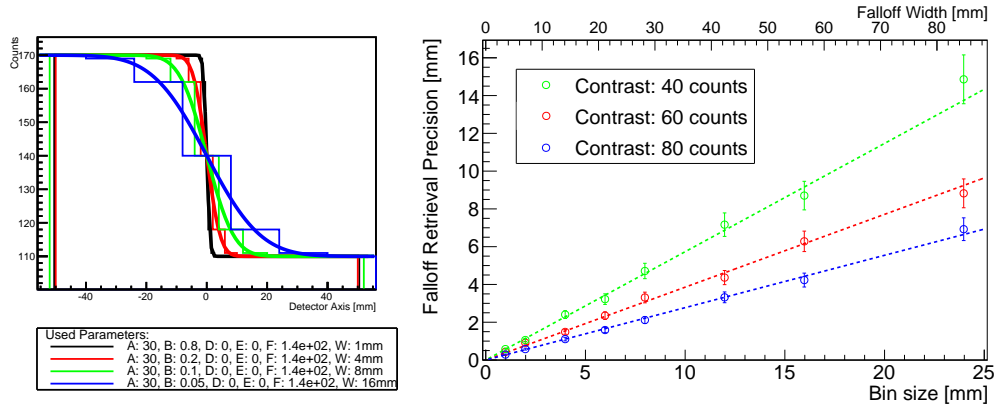


Figure 3.16: Variation of the falloff width and the distance between measurement points at the same time: example profiles (left) and influence on the FRP (right). The example profiles correspond to points of the red curve. The FRP exhibits behavior consistent with being proportional to the falloff width.

points actually seeing the falloff itself. The improvement in FRP due to the improved spatial resolution is partially compensated by this effect. It is further interesting to note that the slope of the FRP with regards to the falloff width is relatively small (0.04 mm change in FRP for 1 mm change in falloff width) and that the slope seems approximately the same for all values of the contrast.

When both the falloff width and the distance between measurement points are adjusted proportionally, as in figure 3.16, the behavior is truly proportional. This is the expected behavior, as adjusting both falloff width and binsize is equivalent to doing a scaling transformation on the detector axis, meaning the FRP will scale as well.

**Varying background slope** As mentioned, the slopes are not a property of the profile that can be easily influenced with camera design choices. However, a study of measured profiles (see section 4.2.2 on page 60) has indicated that there is an influence of the slopes that should not be neglected. The placement of the camera relative to the patient has a strong influence on how it sees the non-isotropic neutron background.

Part of this has to do with how the falloff is retrieved. The assumption used above in section 3.2.1 on page 30 to define shifts in the profile is that the *entire* profile – background included – will shift. To understand what this entails, let us consider a case where there is absolutely no edge and we only see background. In this case, and following our assumptions, the profile will consist of a linear increase in background. When simply applying the method for estimating the FRP described above to this straight line, it turns out that we do indeed obtain a precision, and that this precision improves when the line is steeper, due to the fact that it is perfectly possible to match two straight lines with nonzero slopes horizontally. This would then indicate, that the term of “uncorrelated” counts that we have used for the background is incorrect, since there is apparently information contained in it. This can be interpreted as the amount of background being dependent on where the camera is situated in space compared to the beam path and the material crossed by the beam, so that the level of background measured gives an indication of this relative positioning. The same holds true in an analogous way for the added slope of increasing prompt-gamma emission. The effect becomes apparent for very small contrast/noise ratios and large slopes, when the precision of the edge matching and the background matching are of similar magnitude.

Of course, this poses a problem when considering possible clinical application. A priori, a simple shift of the entire profile with the background will only be observed in some cases, such as misalignment. In most cases, the edge and the background slope will evolve in more complex and different ways. For example, in the abstract case of an overall lower density

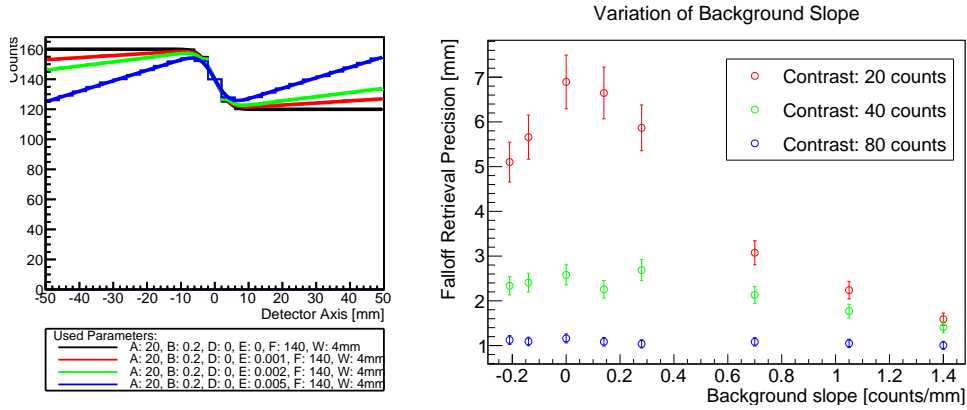


Figure 3.17: Variation of the slope of the background: example profiles (left) and influence on the FRP (right). The example profiles correspond to points of the green curve. For small values of the contrast, the background slope can “help” with matching of the profile and improve the FRP.

of the target, we can expect the falloff edge to shift, but not the background (its slope may be affected). In more realistic clinical cases involving heterogeneities, the evolution of the background is non trivial and will probably have to be predicted by simulation.

In figure 3.17, we can see that for a small contrast (red points), the observed FRP improves significantly for large positive or negative background slopes, with the worst value for the FRP for a completely flat background.

In conclusion, it has to be noted that the background cannot be dismissed as being devoid of information as one would expect at first glance. This can also be observed in the analysis of measurement results with a scanned single-slit camera in section 4.2 on page 55. It is a possibility to imagine a more sophisticated analysis of the profile, in which not only a horizontal shift is considered, but also an adjustment for the background (level and slope). The potential of such a method depends of course on the observed background slope and on the noise present in the profile (more degrees of freedom in matching may lead to a worse match in any one of the free parameters).

**Varying the plateau slope** The same observations made for the slope of the background above are also true for the slope in the plateau region before the falloff: a slope that is non-zero could potentially be used to help with positioning. In figure 3.18 on the next page, the FRP is shown as a function of the plateau slope for different values of the contrast. Only positive values are studied, as we do not expect to ever observe a profile where prompt-gamma emission decreases along the beam path. As for the background slope described above, the FRP again improves significantly for large slopes and small contrasts. However, the maximum is not in zero. This has to do with how the slope and the contrast are described in the formula for  $P(x)$ . When looking at the illustration on the left of figure 3.18 on the following page, we can see that as the slope increases, the maximum of the profile decreases, even though the parameter  $A$  is held constant. This lowering of the effective contrast leads to a worsening of the FRP before the effect of the slope comes in and drives the FRP back down.

**Varying the distance between measurement points** When thinking about the real implementation of a camera, there are different ways to implement a different distance between measurement points. In the example of a parallel-slit camera, the slit width can be increased proportionally or not, the crystal size can be increased or not etc. For simplicity’s sake and to separate this effect from the others, we look at the effect of increasing the distance between the points without changing any other parameter. This corresponds, for

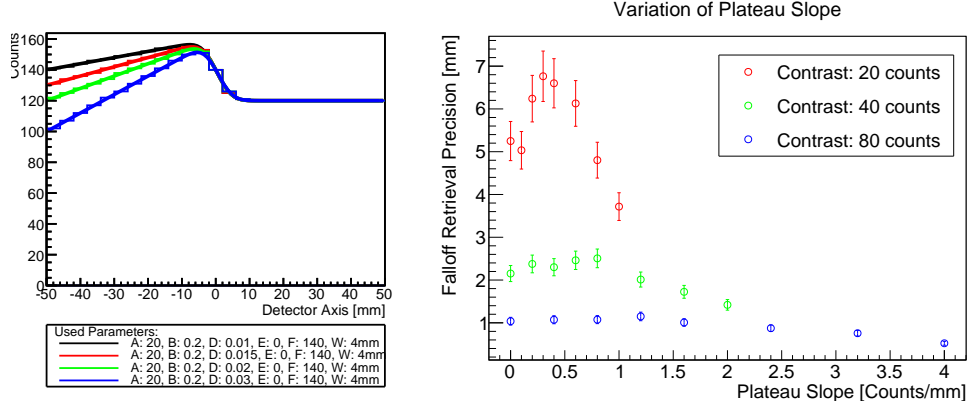


Figure 3.18: Variation of the slope of the plateau region: example profiles (left) and influence on the FRP (right). The example profiles correspond to points of the green curve. For small values of the contrast, the slope can “help” with matching of the profile and improve the FRP.

example, to doing scans with different distances between points or increasing the pitch of a multislit camera without changing the slit width.

The dependency of the FRP on the distance between measurement points appears to follow roughly the square root of the distance between measurement points (figure 3.19). This is easily explained by considering that the total number of counts over the whole profile decreases as the distance between points is increased. It is reasonable to assume that when considering the influence of contrast and noise, one must in fact look at the counts per unit length on the detector.

$$FRP \propto \frac{LN}{LC}$$

where  $LN$  and  $LC$  are the noise and contrast per unit length respectively.

Since the contrast per unit length is proportional to one over the bin size and the noise per unit length, being the square root of the average counts per unit length is proportional to one over the square root of the bin size, it follows that the FRP is proportional to the square root of the bin size.

$$\begin{aligned} LC &\propto 1/w_{bin} \\ LN &\propto 1/\sqrt{w_{bin}} \\ FRP &\propto \frac{LN}{LC} \propto \sqrt{w_{bin}} \end{aligned}$$

There is a deviation from the expected shape as the distance between the measurement points nears the value of the falloff width. This is due to the effective falloff width of the discretized profile no longer being equal to the falloff width of the generating error function, as explained in more detail in the section on the offset, just below.

**Varying the offset between center of falloff and bin center** To understand the possible influence of the offset, let us take a look at the relationship between the falloff width and the field of view of a detector unit. In most parts of this text, we work with the assumption that the two are equal, but this is only true when the distance between measurement points is lower than the falloff width. Indeed, when the field of view is equal to or smaller than the distance between measurement points, the falloff width is ill defined, because it will be contained in a single bin in the profile. However, while the falloff width is ill defined for the discretized profile, it remains defined for the continuous function  $P(x)$  used to generate the profile. Cases where the detector unit field of view is small compared

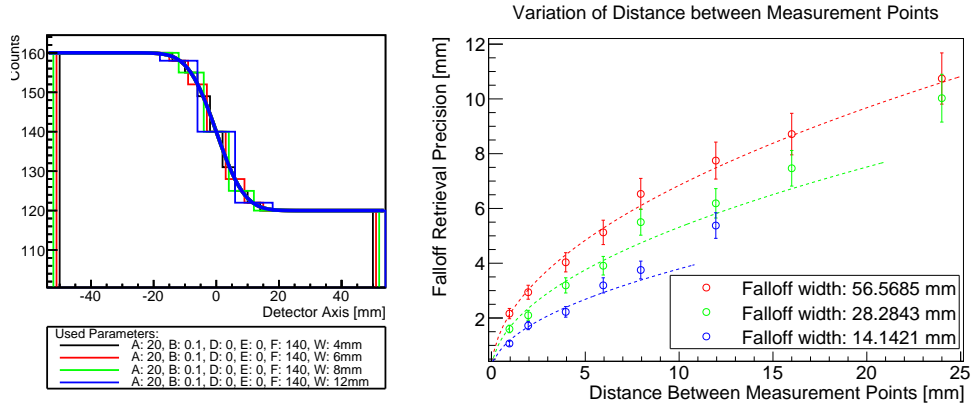


Figure 3.19: Variation of the distance between sampling points for different values of the falloff width: example profiles (left) and influence on the FRP (right). The example profiles correspond to points of the green curve. The FRP exhibits behavior consistent with a  $\sqrt{x}$  dependency. Profiles for which the falloff width would be smaller than the distance between measurement points are not plotted.

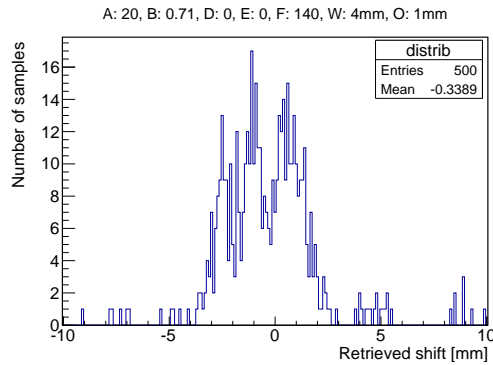


Figure 3.20: Distribution of retrieved falloff shifts with an offset of 1 mm.

to the distance between measurement points are then represented by cases where the falloff of  $P(x)$  is smaller than the bins used for the discretization.

Since all the information on the falloff is contained within one bin, the value of the retrieved shift is determined by a very small number of measurement points. As the noise is of the same amplitude as the contrast, the matching of the reference function to the profile is likely to be highly influenced by statistical fluctuations. This can lead to asymmetry in the distribution of retrieved shifts, depending on where the centers of the bins are located with regards to the falloff. If the bin seeing the falloff is off-center, positive and negative fluctuations will not have the same influence on the measured shift.

Figure 3.20 shows a typical distribution of retrieved offsets for a case where the falloff width and the distance between measurement points are approximately equal. There is an apparent asymmetry in the distribution, which leads to a bias in the retrieved shifts.

While these kinds of falloffs over only one bin are rare in practice (and should be avoided!), even with falloffs over a few bins, asymmetry can lead to small systematic errors in the retrieved shifts. In figure 3.21 on the next page are shown the mean shifts retrieved for different values of the offset and three values for  $B$  (corresponding to FOV of 2, 4 and 8 mm). There is a clear systematic effect for values of the field of view smaller or equal to the bin width of 4 mm, and even for the profile corresponding to a field of view of twice the distance between measurement points, there is an effect of up to 0.5 mm (1/8th of the distance between measurement points). Note: the effect is not of the same amplitude for

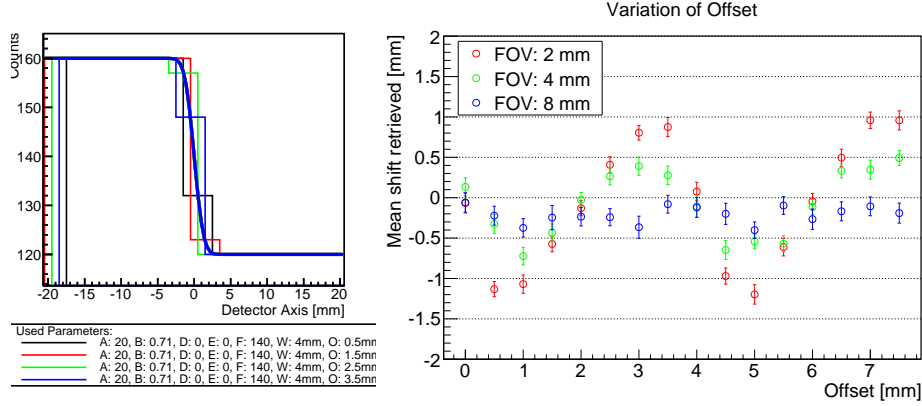


Figure 3.21: Variation of the offset between the bin center and the center of the falloff: example profiles (left) and influence on the mean of retrieved shifts (right). The example profiles correspond to points of the green curve. There is a systematic effect on the mean of retrieved shifts depending on the offset of the bin center. Offsets of up to twice the distance between measurement points (4 mm) are shown to better see the periodicity of the effect.

positive and negative systematic errors because the variance used to draw the entries for each bin for the samples depends on the number of counts in the bin of the reference profile so they are not the same for different positions of the measurement point, which breaks the symmetry between positive and negative shifts. When uniform variance is forced over the whole profile, the effect becomes symmetric.

In conclusion, staircase effects such as this can be minimized by ensuring that the detector field of view is larger than the distance between measurement points and that the falloff is distributed over at least two bins in the profile. This excludes mainly collimator configurations with small acceptance angles that are placed close to the target.

### 3.2.5 Summary

From the above observations, a set of conclusions can be drawn and the most important effects summarized:

- The FRP is anti-proportional to the contrast.
- The FRP is proportional to the noise.
- From the above follows that the FRP is anti-proportional to the contrast/noise ratio.

$$\text{FRP} \propto \frac{\text{Noise}}{\text{Contrast}} \quad (3.15)$$

- The FRP is proportional to the falloff width (FW) if the distance between measurement points is varied proportionally along with the falloff width (“proportional” binsize) and linear in the falloff width if the distance between measurement points is kept constant (constant bin size).

$$\text{FRP} \propto \text{FW} + f \quad (3.16)$$

$$\text{with } f = \begin{cases} 0 & \text{if binsize is proportional} \\ f(\text{binsize}) & \text{else} \end{cases}$$

- The slopes of background and plateau region play a role only if the contrast/noise ratio is small (i.e. smaller than approximately one).

- The distance between measurement points can be neglected if the total number of counts integrated over the profile is constant and if it is smaller than the falloff width.
- Hole-pattern artifact effects can be avoided if the detector unit fields of view overlap.



# Chapter 4

## The parallel-slit camera

This chapter focuses on the parallel-slit camera. The underlying geometrical principles are introduced, measurements with a single-slit simplified prototype are presented and an optimization study is undertaken.

### 4.1 Geometrical considerations on the collimator

A multi-parallel slit collimator is defined by a set of parameters, illustrated in figure 4.1 on the following page and listed below:

$d_1$  Beam-collimator distance

$H$  Camera height

$D$  Collimator depth

$p$  Collimator pitch

$f$  Fill factor (ratio of septa width to pitch)

$s$  Slit width

$d_2$  Collimator-crystal distance

$L$  Total beam-crystal distance

For the gamma of relatively high energy considered here, geometrical considerations are always an approximative endeavor. However, they can be very useful to understand most of the basic effects of varying each parameter. The assumption is made that the prompt-gamma source is a line source that emits isotropically and that the collimator is “perfect”, i.e. completely absorbs any gammas that touch the septa. The most important calculations we will consider are:

**Detector unit field of view:** This is the part of the source that can be “seen” through a single slit. It consists of a part that is directly facing the slit and a part penumbra. The probability of a photon emitted at a given point along a linear source (perpendicular to the slit plane) to reach the detector through a given slit can be described as a trapezoid. We define the detector unit field of view (FOV) as the full width half maximum (FWHM) of this trapezoid as illustrated in figure 4.1:

$$FOV_{d.u.} = s \left( 1 + \frac{d_1}{D} \right) = p(1 - f) \frac{D + d_1}{D} \quad (4.1)$$

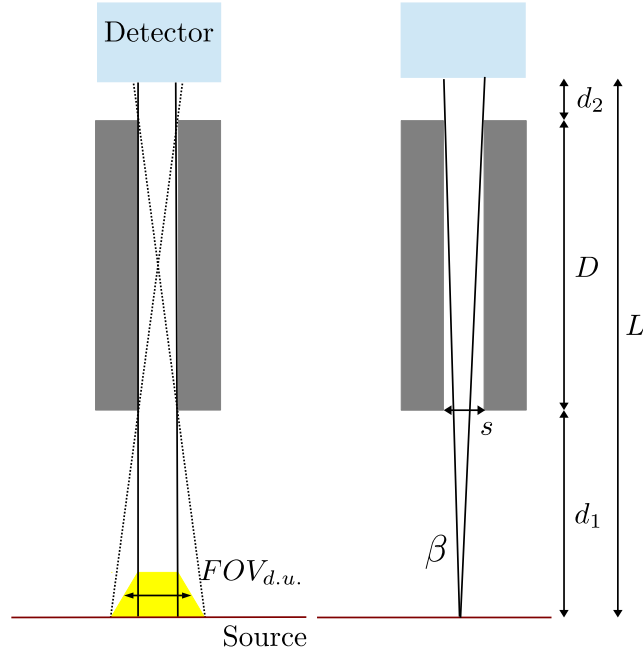


Figure 4.1: Illustration of the calculation of the detector unit field of view and the detector solid angle.

**The collection efficiency** The probability of a photon emitted at a point facing a slit (in the middle part of the trapezoid) to reach the detector is described by the solid angle that the point sees of the detector. The solid angle is composed of the azimuthal angle  $\beta$  and the polar angle. In small angle approximation, we obtain:

$$\Omega_D = \frac{H}{L} \beta = \frac{H}{L} \frac{s}{D + d_1} \quad (4.2)$$

Note that this is true only for cases where the solid angle is limited by the slit width, i.e. the crystal sizes and distances are so that all photons that cross the collimator impinge on detector material. The total collection efficiency (CE) for a photon emitted by the line source through a given slit can then be expressed as the product of the detector unit field of view and the solid angle over  $4\pi$ :

$$CE = \frac{\Omega_D}{4\pi} \times FOV_{d.u.} \quad (4.3)$$

$$= \frac{1}{4\pi} \frac{H}{L} \frac{s}{D + d_1} \times p(1 - f) \frac{D + d_1}{D} \quad (4.4)$$

$$= \frac{Hp^2(1 - f)^2}{4\pi LD} \quad (4.5)$$

Note that the collection efficiency has the unit of a length so that it can be applied to a line source. When it is multiplied by the emission per unit length of the line source, one obtains the number of particles impinging on the detector through one slit.

To obtain the overall collection efficiency per unit length of crystal for the whole collimator (“linear efficiency”, or LE), the above has to be multiplied by the number of crystals and slits per unit length, or, in other words, be divided by the pitch. Note that this is a dimensionless quantity that can be multiplied by the emission per unit length to obtain a number of particles impinging on the detector per unit length or multiplied by the total emission over

the total system field of view to obtain a total number of counts.

$$LE = \frac{Hp(1-f)^2}{4\pi LD} \quad (4.6)$$

These geometrical considerations already give some indication as to what can be expected when each parameter is varied in the course of optimization in section 4.3 on page 66 later on. For example, both the linear collection efficiency and the detector unit FOV go with  $p$ . As the linear collection efficiency determines the contrast and, as we have seen in the previous chapter in equation (3.15) on page 50, the FRP depends on the contrast much more strongly than on the falloff width, we can expect the falloff width to rise with the pitch and the FRP to fall with the pitch. Similarly, a deep collimator will have small falloff width, but a large FRP. The fill factor,  $f$ , goes quadratically into the linear collection efficiency, but only linearly into the detector unit FOV, meaning that we can expect it to have more influence on the FRP than the falloff width. The distance between the source and the collimator,  $d_1$ , is the only parameter that should be chosen as small as possible to improve both the collection efficiency and the detector unit FOV, providing the rationale for choosing it as small as deemed practically possible and fixing it during simulation.

## 4.2 Experimental data

Measurements were conducted at the Westdeutsche Protonentherapiezentrum with a single-parallel-slit collimator. The results have also been presented in Pinto [2014] and Roellinghoff et al. [2014] and part of this section is based on excerpts of the latter, written by the author of this text.

A complete profile was acquired by moving the target incrementally along the beam direction. While this approach approximates the image that can be obtained with a multi-slit detector, there are of course a few significant differences. Most importantly, there are solid blocks of material to both sides of the slit, instead of other slits. This significantly increases the amount of shielding from radiation outside of the acceptance angle of the slit. The amount of shielding material also affects the production of secondary radiation. A comparatively minor effect is that when using only one slit, with one or two small detectors behind it instead of an array of detector crystals, there is no contribution of scattering between crystals. This latter effect has been studied on the basis of experimental data and is being published in a separate work: Krimmer and al [2014].

Another characteristic of this way of acquiring a profile is that the distance between the measurement points can be chosen at will and is not limited to a fixed pitch. The distance can even be chosen to be smaller than the width of the slit itself, which is of course impossible when using a multi-slit configuration. During the experiments presented here, more points were acquired in the region of the falloff, where the count rate varies the most, and less points were acquired in relatively constant regions before and after the falloff. The advantage of such a measurement is that the falloff region can be imaged in detail and without any possible pattern effects of a multi-slit collimator.

These measurements are here presented before the optimization study of a multi-slit collimator. First of all, because they were conducted before the optimization study was complete. Second, because many of the most important considerations for a multi-slit that are developed below, such as the relative widths of slits and septa, have no meaning for a single-slit configuration and, as mentioned, the shielding and rate of background are very different. These measurements are then most useful for three things: first, as a validation of simulations and proof-of-concept for prompt-gamma detection. Second, to give a general idea of the profile that can be expected for a parallel-slit configuration. The methods of falloff position retrieval described in section 3.2 on page 30 are applied to the measured profile to validate that they work on a real, measured profile. Third, the time-of-flight discrimination that was applied allows an evaluation of the possible advantage of using time-of-flight techniques with any type of camera. As the exact time dependence of the beam at

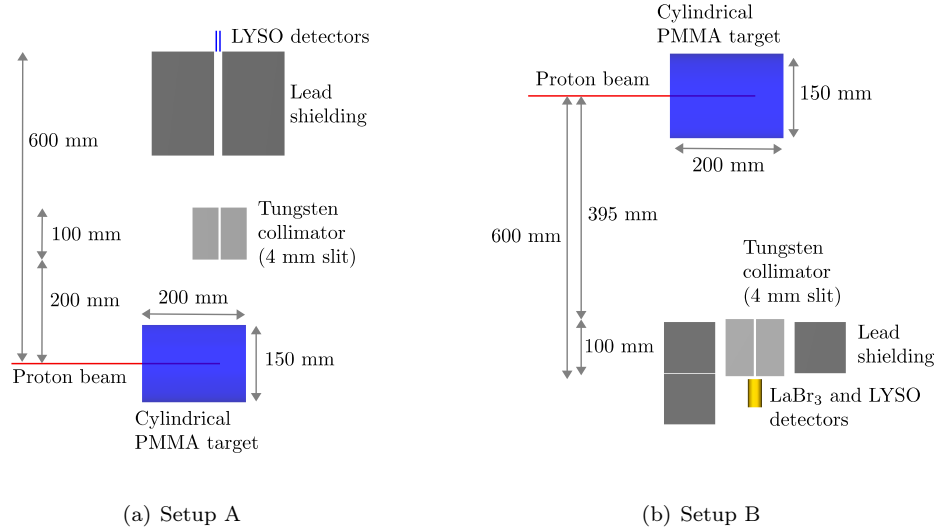


Figure 4.2: Experimental setups from measurements with a single parallel slit. Both setups are shown in the way they would be seen from above and according to their orientation on the patient couch in the gantry treatment room, with the back of the gantry towards the top of the page and the beam coming from the left. The orientation may influence the observed background.

nozzle exit is not very well known (see 2.1.1 on page 17), measurements are crucial in this regard.

#### 4.2.1 Experimental set-up and data processing

We describe here the results from two sets of measurements taken at the Westdeutsche Protonentherapiezentrum in Essen. The setups of the two measurements are shown in figure 4.2 as views from above. We will refer to them subsequently as setup A (on the left) and setup B (on the right). In April 2011, measurements with both setups were conducted, but the scan with setup B did not have enough points near the falloff to be usable for evaluation of the range retrieval precision. Measurements with setup B were repeated in June 2012. In these last measurements, a different beam control mode was used, which lead to occasional and irregular pauses in beam delivery of approximately one second length. These pauses make it impossible to adequately separate the acquired profiles into data packets corresponding to a precise number of delivered protons. Therefore, the analysis was conducted on measurements from 2011 with setup A. The data acquired in 2012 with setup B is shown to demonstrate the effect of the different collimator and shielding configurations.

In both setups, a proton pencil beam impinged centrally on a cylindrical PMMA target. The target had a diameter of 150 mm and a length of 200 mm. A tungsten slit collimator with a 4 mm slit was used in both cases, with additional lead shielding blocks placed to protect the detector from radiation coming from parts of the target not shielded by the collimator. The distances and dimensions are shown in figure 4.2, the only dimension not shown being the height of the collimator and shielding, which was 200 mm. Note that in setup A, there are two LYSO detectors of  $50\text{ mm} \times 40\text{ mm} \times 3\text{ mm}$  behind the slit, one centered and one shifted to the side by 6.6 mm. Due to a technical problem with one of them, the data presented here comes from the one which is actually in the penumbra of the collimator, leading to a systematic underestimation of count rates of correlated gamma by a factor of approximately 0.6. Since the aim of this study is to be a proof-of-concept, the analysis of the data can be carried out nonetheless, and the underestimation can be taken into account when extrapolating to the performances possible with a clinical prototype.

The proton beam used was a 160 MeV pencil beam with a temporal structure of approximately 2 ns long pulses every 10 ns. A hardware energy threshold equivalent to 1 MeV was set. The number of protons delivered during an acquisition was determined by integrating the current measured by an ionization chamber within the beam nozzle.

In order to acquire an image of the whole prompt-gamma emission profile with the single-slit collimator used, the target was moved along the beam axis incrementally and a number of points was acquired for different positions along the profile. The number of protons delivered per acquisition was of the order of  $5 \times 10^{11}$ . This is far above the usual clinical dose for a pencil beam spot, but the purpose of this experiment is to further work with independent subsets of data, and compare them with a high-statistics profile. This approach approximates the profile that could be obtained with a multiple-slit camera.

The time-of-flight technique is used in this context to separate the proton-path correlated prompt-gamma signal from the considerable background of uncorrelated neutrons. The distance of the detector from the target is chosen such that the arrival time of the prompt gamma-rays is well separated from the neutrons set in motion by the same bunch of protons. However, since the proton beam is pulsed with intervals of 10 ns, there is substantial overlap between the neutrons of one bunch and the prompt gamma-rays of the next. For the time measurement, the hit in the detector is used as a start signal and the frequency signal of the cyclotron is used as stop signal, so that the arrival time of the particle is measured in relation to the proton bunches, not individual protons. Consequently, there is an inherent limit to the TOF discrimination linked to the time structure and momentum spread of the beam. The bunch width of the beam determines the minimal achievable size of the TOF window.

The energy threshold has to be chosen so that low-energy photons, which are more likely to be scattered and thus less likely to be correlated to the range are cut. Analysis of the data has shown that as long as low-energy photons are cut, the performances of the system are not very sensitive to this parameter and 1 MeV seems to be a reasonable threshold.

### Choice of time-of-flight windows

As mentioned, these measurements used TOF discrimination to discard part of the neutron background. The TOF measurement was made by using the RF signal of the cyclotron to associate a time stamp relative to the beam pulses with each hit in the detector. Figure 4.3 on the following page shows the time spectrum plotted against the energy spectrum (left) and the time spectrum only (right) for an acquisition looking at a point just before the Bragg peak (at 140 mm inside the target). Peaks corresponding to the arrival of prompt gamma are clearly visible and the distance between peaks corresponds to the 10 ns period of the beam time structure. The centers of the peaks were found by fitting each peak with a Gaussian function and TOF windows were applied around each peak. From simulations (Biegum et al. [2012]), we expect the neutron component to peak several ns after the prompt-gamma peak. However, since the period of the beam time structure is only 10 ns, neutrons from each pulse add up to form a nearly flat background.

TOF windows of different sizes were tested to find the best choice. Figure 4.4 on the next page shows the profiles obtained using TOF windows of different sizes on the left (10 ns corresponds to not using TOF discrimination at all). On the right are plotted the background levels before the target, after the falloff and the contrast. Once again, we can see that the background appears constant through time, as it is proportional to the size of the selection window used. The contrast, corresponding to prompt-gamma signal, on the other hand, seems to be completely contained in a 4 ns time window. Note that the size of the prompt-gamma pulse is a combination of the length of the proton beam pulse (estimated at around two to three nanoseconds) and the timing resolution of the detector.

The 4 ns time window was chosen to include all of the prompt-gamma signal, even though it is not quite the optimal choice with regards to the FRP (reducing the window slightly cuts more of the background than it does of the contrast, leading to a better value of FRP). Optimizing the TOF window for the best FRP or using a detector with better timing resolution (narrower prompt-gamma peak) will increase the effect of TOF techniques.

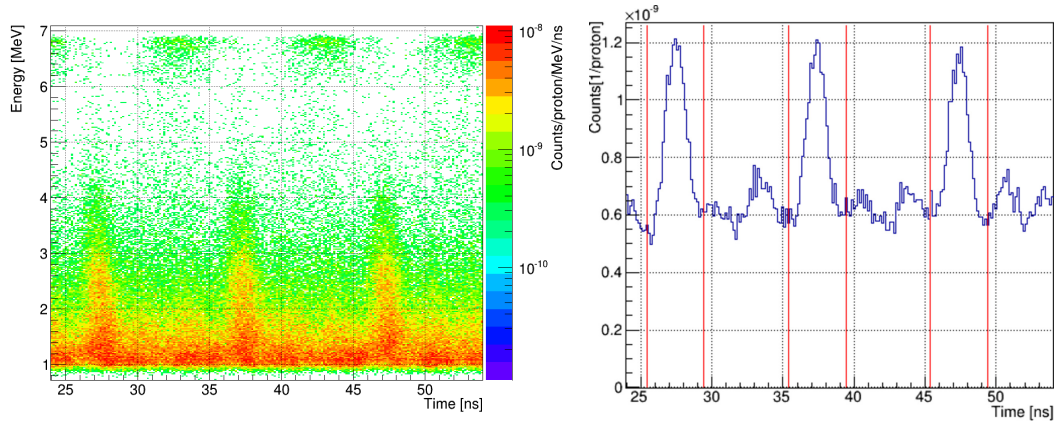


Figure 4.3: Left: two-dimensional plot of the energy deposition in the detector as a function of the TOF information (obtained with the slit facing just before the Bragg peak). Right: TOF spectra after application of the 1 MeV energy threshold with gamma selection windows indicated with red vertical lines.

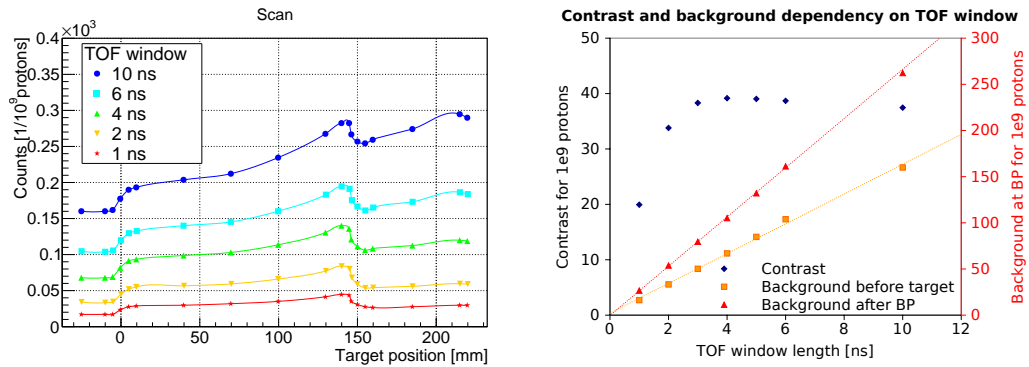


Figure 4.4: Profiles obtained for different choices of the TOF window length (left) and influence on the contrast and background for  $10^9$  protons (right). All prompt-gamma signal seems to be included in TOF windows of 4 ns, after which the contrast stays nearly constant. The background appears to increase linearly.

### Choice of energy threshold

The influence of the lower energy threshold was studied to find the optimal value. Figure 4.5 shows the prompt gamma profile for different values of the threshold as well as the influence on characteristic values such as the contrast, background and contrast/noise ratio. A TOF window of 4 ns was used for all profiles.

Due mainly to scattering within the target, lower-energy photons are less well correlated with the dose profile than higher-energy photons. When the threshold is raised, the background counts decline more rapidly than the correlated counts at first, leading to a maximum of the contrast/noise ratio around 2 MeV. For the subsequent analysis, a threshold of 1 MeV was set in an effort to keep the maximum possible contrast, a choice that was made before the study on optimizing the FRP was complete. An improvement to the FRP may be possible by raising the energy threshold.

### Profiles

Figure 4.6 on the facing page shows the profiles obtained with and without TOF discrimination as well as the difference between the two for the acquisitions with setup A (left) and

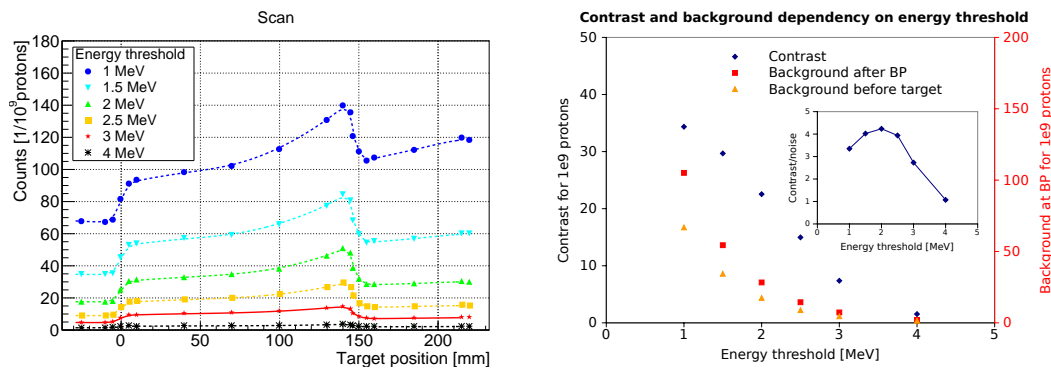


Figure 4.5: Profiles obtained for different choices of the energy threshold (left) and influence on the contrast and background for  $10^9$  protons (right). The inset in the graph on the right shows the influence on the contrast/noise ratio.

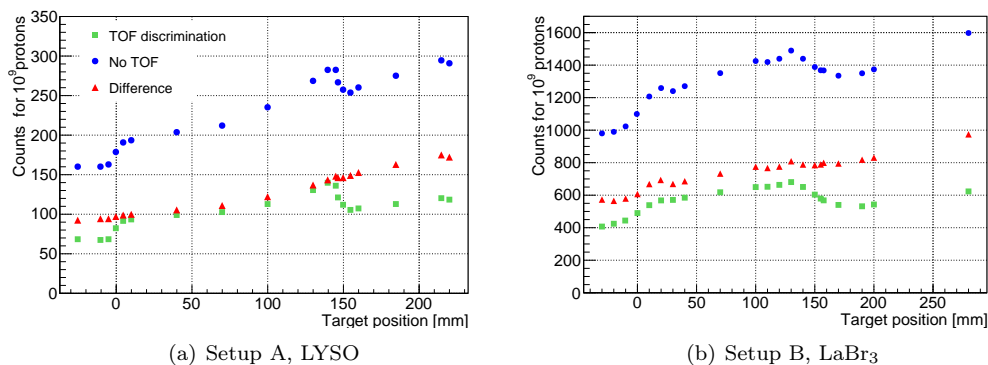


Figure 4.6: Profiles acquired in 2011 with an LYSO detector and setup A (left) and profiles acquired with an LaBr<sub>3</sub> detector and setup B in 2012 (right). Profiles without any TOF discrimination shown as blue circles, with a TOF selection window of 4 ns as green squares, the difference as red triangles. A lower energy threshold of 1 MeV was set in both cases.

setup B (right). First of all, note that the way the collimator was placed, both the source field of view of the detector and the solid angle under which the source saw the detector were larger in setup B, accounting for the very different count rates per proton. One can also observe that the falloff width was larger for setup B, again due to the increased field of view.

We can further see that the TOF discrimination has the same effect in both cases, reducing the background everywhere by a factor 0.4, corresponding to the 4 ns TOF window over the 10 ns period of the beam. Perhaps the most interesting difference between the two measurements is in the apparent sloping of the background. While for setup A, the amount of background nearly doubles between the first measurement point at  $-25$  mm before the target to the last point at 220 mm, for setup B the background only increases by about 50% over the same interval. In general, the observed rise in background is due to the anisotropic emission of neutrons. The difference observed between the two configurations can only be explained by the different shielding used in the two cases, but it is not entirely clear as of yet how such a significant difference came to be. Further simulation and, ideally, measurement should be undertaken to understand these observations.

### 4.2.2 Spatial response study with setup A <sup>1</sup>

From a general point of view, the goal of this type of imaging is to detect deviations between one dimensional profiles acquired during treatment and profiles predicted by simulation (reference profiles). The machine-learning approach proposed by [Gueth et al. \[2013\]](#) used two observables, namely the falloff-position and a correlation value between the measured and simulated profiles. The ability to detect an edge is determined both by the point response function of the system as well as the counting statistics. The current work focuses on the estimation of the performance of such a system, by developing a method to quantify its edge-finding precision.

At first order and especially in homogeneous targets, we can consider that a range error leads only to a shift of the profile. The expected profile is expressed as a function that is then fitted to the measured data points by shifting it along the beam direction. The shift obtained in such a way is a measure of the shift between the predicted ("reference") and measured edges of the profile.

When using a multi-slit camera system (with slit planes perpendicular to the beam direction), the acquired profile is a direct one dimensional projection of the emission profile along the beam path. To obtain the range, there are two positions that need to be measured: the projection of the point where the beam enters into the patient and the location of the Bragg peak. A multi-slit camera can be made large enough for the field of view to encompass both positions and both correspond to sharp edges in the prompt-gamma profile that can be identified. A shift of the entrance rise corresponds to a mispositioning of the patient, while a shift in the position of the falloff can correspond to both mispositioning and/or an error in range. Both shifts are evaluated independently and the difference of the measured shifts is considered to be the error in proton beam range.

To characterize the shape of the prompt-gamma profile, we use a profile acquired with a high number of counts as a reference. In clinical practice, the reference profile would have to be generated via simulation. To approximate the shape of the profile in between data points, a uniform rational third-order b-spline using the data points as control points is used. This spline function is split into two parts, one representing the entrance rise region, the other the falloff region, which are used as reference functions. The reference function represents the expected number of counts that would be observed by the detector if the target was placed at a given position.

For clinical use, a variable of major interest is the precision the camera could achieve for a given number of protons delivered to a dose spot. The data acquired during the experiment can be separated into data packets that correspond to a given number of protons delivered to the target. To do this, half of the data obtained per acquisition is set aside to serve as reference profile. The other half is divided into subsets. Since no absolute time stamp is recorded (only a relative time stamp), the number of hits to the detector corresponding to a given number of protons is estimated using a Poisson distribution and events from the dataset are selected accordingly. All thresholds and windows are applied after the division into subsets.

From each of these packets a sample profile can be generated that corresponds to the type of profile that would be obtained with a multi-slit camera for the irradiation of one spot with this number of protons. To measure a shift between a sample profile and the reference profile, the reference function is shifted with steps of  $2.5\ \mu\text{m}$  along the camera axis and the sum of squares of the differences in each histogram bin is calculated as an objective function at each step. The best match is considered to be the one minimizing the objective function and the shift corresponding to this match is retained as the shift between sample and reference. This procedure is repeated for a number of data packets to obtain a distribution of measured shifts. The standard deviations of these distributions are estimators for the precision with which the camera would be able to measure a shift.

Since the number of data packets using real data is inherently limited to the amount of data acquired and a bias is necessarily introduced when looking at large proton statistics

---

<sup>1</sup>this section is reprinted from [Roellinghoff et al. \[2014\]](#). Some notions have already been discussed in chapter 3, but have been kept for coherence and clarity.

with a small number of data packet samples available, an additional study was undertaken using Poisson statistics to generate artificial subset profiles directly from the reference profile. To generate such sample profiles, the counts for each data point were drawn using a Poisson generator taking the data point of the reference profile scaled to the appropriate proton statistics as parameter.

The precision obtained with this method is mainly determined by the contrast-to-noise ratio of the profile. Since the contrast is proportional to the number of protons used and the standard deviation of the signal is proportional to the square root of the number of protons, it follows that the precision is proportional to the inverse of the square root of the number of protons used. This shows up as a straight line with slope  $-1/2$  in a precision vs. number of protons graph.

It has to be noted that for low proton statistics, the statistical errors of the data points start to be of the same order of magnitude as the signal itself. It happens with increasing frequency that some random fluctuations in the data points will resemble an edge and be picked out by the algorithm. This is reflected in an increasing number of outliers in the distribution of obtained edge (entrance rise or falloff) positions. An outlier in this context is defined as a point that is outside of  $\pm 3\sigma_{extrap.}$  of the mean of the distribution, where  $\sigma_{extrap.}$  is the extrapolation of the standard deviation at high proton statistics to low proton statistics using the straight line behaviour with slope  $-1/2$ . The occurrence of outliers is documented and serves as a criterion for the applicability of the method, but outliers are not removed from the dataset and do go into the calculation of the standard deviations of the distributions.

To reach practical conclusions for clinical use of this type of detector, the edge detection accuracy has to be seen in relation to a realistic dose delivered to a spot of the treatment plan. It has to be noted that the distal spots, which are the most crucial to verify, are usually planned with the highest number of incident protons, and will thus be able to be verified with the highest accuracy. According to the clinical examples used in [Grevillot et al. \[2012\]](#) and [Moteabbed et al. \[2011\]](#), the order of magnitude of protons per spot for the distal layer is around  $10^8$ . The range uncertainty of such spots can be up to 10 mm ([Paganetti \[2012\]](#)). It is reasonable to stipulate that a system that could reach a precision of a few millimeters would bring significant improvement to the accuracy of proton irradiations.

**High-statistics profile** Profiles were then obtained using either all the data (“no TOF”) or just the data falling into the TOF selection windows. The acquisition for each scanned point corresponds to roughly  $5 \times 10^{11}$  protons delivered to the target. In figure 4.7, it is apparent that applying a TOF discrimination reduces the background significantly, while leaving the falloff signal amplitude intact. Most of the background is due to neutrons being emitted by the nuclear reactions along the beam path. The neutron emission is forward peaked and neutrons are not effectively shielded by the collimator, leading to a steady increase in neutron background along the axis. It can also be observed that the background is reduced by approximately 40%, corresponding to the ratio of TOF window size to the cyclotron period. It appears that the uncorrelated counts from different beam pulses overlap in such a way as to form a nearly uniform background over time once energy thresholds are applied. The data points representing the events discarded by TOF (in red) show that almost no correlated signal is lost by applying TOF discrimination and the contrast remains intact.

The rational third-order b-spline mentioned above is used to obtain a continuous approximation of the profile. The function follows the form of the data points very closely, while slightly smoothing the profile.

**Data subsets** The principle for finding range shifts is illustrated in figure 4.8 on the left. The entrance rise and falloff parts of the profile are considered separately and the reference function is shifted horizontally for each to best fit the data points of the sample. The distributions of the measured shifts of the falloff positions for  $10^9$  and  $10^{10}$  protons are illustrated in figure 4.8 on the right. It can be observed that not only the standard deviation of the distributions changes, but also their shape varies significantly. While it nearly follows

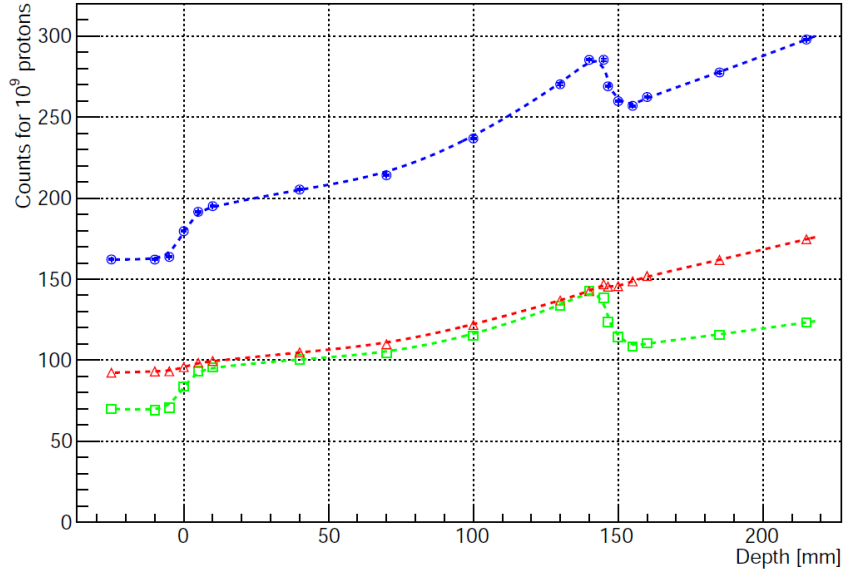


Figure 4.7: Acquired high-statistics profile without TOF application (blue, circles), profile obtained using TOF (green, squares) and difference between profiles with and without TOF (red, triangles) with the corresponding spline functions (dashed lines). The origin of the x-axis corresponds to the target entrance. The error bars of the data points are so small as to be contained in the markers used.

a Gaussian shape in the  $10^{10}$  case, there are more counts outside of  $3 \times \sigma_{extrap}$  in the  $10^9$  case. This is reflected in the fraction of outliers.

Further illustration of the occurrence of outliers can be seen in figure 4.9, that shows typical objective functions obtained for samples corresponding to  $10^8$  incident protons. High statistical fluctuations lead to cases where the objective function has several minima. The existence or absence of multiple minima could be used to estimate the confidence attached to a given shift measurement.

**Precision vs. number of incident protons** In figure 4.10 can be seen the relationship between the number of protons shot to obtain a profile and the obtained precision as well as the fraction of outliers observed. This was calculated both by using subsets of the measured data and using Poisson generation. The error bars result from an estimation of the standard deviation of the values obtained by applying the process 30 times and observing the standard deviation of the results.

For high contrast-to-noise ratios (large numbers of protons), the precision is proportional to the inverse of the square root of the number of protons, as illustrated by the straight line behaviour with slope  $-1/2$  in the log-log plot in figure 4.10. In other words, the precision is mainly dependent on the contrast-to-noise ratio. For low numbers of protons, the outlier occurrence starts to deteriorate the precision and the values deviate from the inverse square root behaviour.

Assuming that the contrast-to-noise ratio is driving the precision, it can be expected that the benefit of TOF discrimination will be proportional to the reduction in statistical noise as well. On average, the variance reduction on data points by applying TOF is 0.45 (figure 4.7 actually shows that the reduction in statistical noise ranges between 0.42 to 0.5 along the profile), it can then be expected that the improvement obtained by applying TOF corresponds to the improvement obtained when using 2.2 times more protons. It is apparent from figure 4.10 that this is not quite the case (it is around 1.7 for both the target entrance and the falloff regions). In fact, it appears that when using a horizontal shift exclusively, the slope of the background actually helps with the positioning. A steeper slope is more beneficial

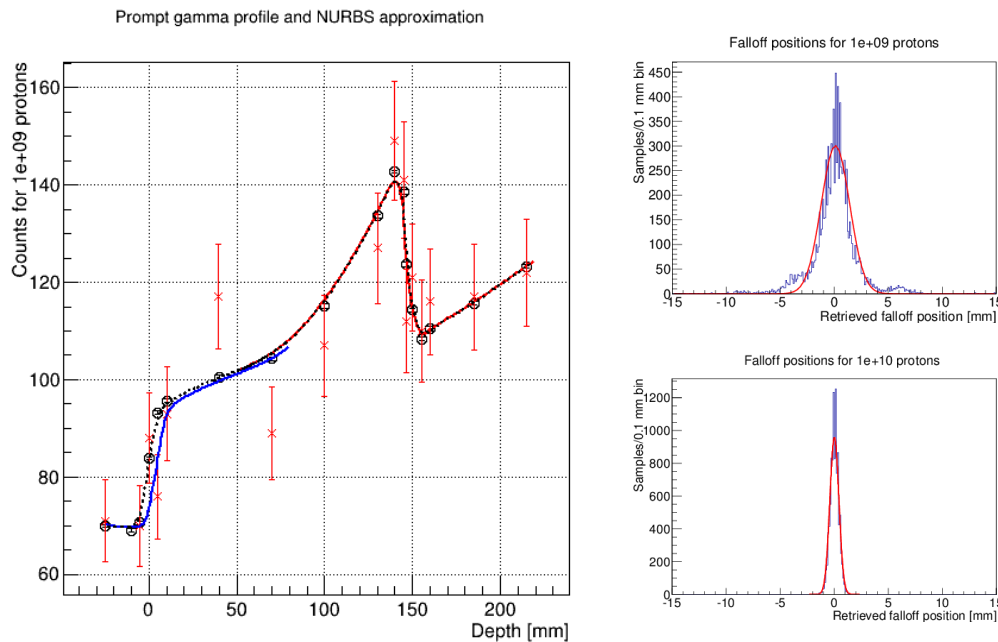


Figure 4.8: Matching of the reference function with a sample profile and distribution of retrieved falloff positions. Left: Reference profile (black circles) and reference function (dotted black) as well as one sample profile (red crosses) obtained for  $10^9$  protons and the function shifted to match the sample profile for the target entrance rise and the falloff (blue and red lines resp.). Right: Distribution of retrieved falloffs for  $10^9$  (top) and  $10^{10}$  (bottom) protons for  $10^4$  Poisson generated profile samples.

and so the reduction in slope by the application of TOF counteracts the improvement in contrast-to-noise ratio. Note that this steep slope corresponds to the particular configuration used in this experiment. Different configurations of shielding will lead to different levels and slopes of background, as was observed in more recent measurements (see figure 4.6 on page 59).

The difference observed between the performance for the entrance rise and the falloff can be explained firstly by the increased contrast of the edge and secondly by the more advantageous shape: in the falloff range, there is a pronounced peak that will lead to an objective function that is steeper around its minimum. It can be observed that the points obtained by subsampling the data are slightly lower than the points generated by Poisson sampling. This results from the way the subsamples are generated, which does not correspond exactly to a Poissonian distribution.

The range deviation can be determined by subtracting the shifts measured for the entrance rise and the falloff. The precision obtainable for this measurement of range is then equal to the square root of the sum of squares of the precisions obtained for the two edges. Interestingly, this is currently dominated by the precision of the entrance rise (for the present setup).

When considering realistic clinical cases of observable shifts, a pure horizontal offset of the whole profile will only happen in some cases, such as mispositioning of the patient. In other cases, the slope of the background may not shift along with the prompt-gamma falloff and thus not contain useful information. These are typically cases where the error relates to deviations from the planned delivery near the end of the range, such as changes in patient morphology, which will impact the position of the falloff primarily, without shifting the background in the same way. The real benefit of TOF application therefore depends on the type of case being studied.

This study shows that not only can the position of the falloff and entrance rise of prompt-

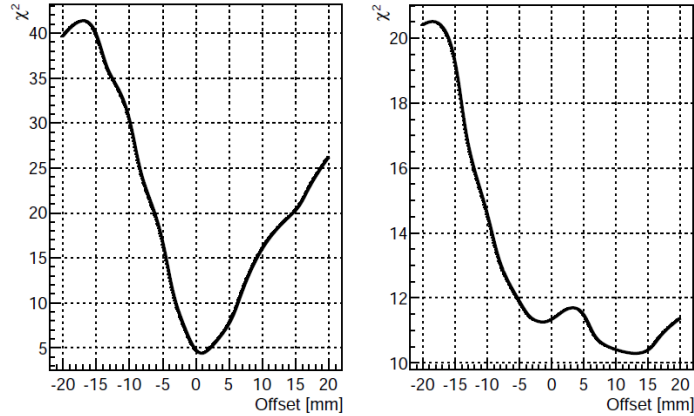


Figure 4.9: Objective function used to determine the shift between sample and reference profile for the falloff: successful case (left) and ambiguous case such as those that lead to outliers (right). Both are obtained for  $10^8$  protons.

gamma emission be seen qualitatively by a prompt-gamma camera, they can be measured quantitatively by comparison with a reference profile. The precision of this quantification depends mainly on the contrast-to-noise ratio of the profile. The precision is inversely proportional to the square root of the number of protons per spot and can be improved either by applying TOF discrimination to the data or by increasing the solid angle and crystal volume of the camera. Since this was a small prototype with suboptimal alignment, it can be easily envisaged to gain an order of magnitude in counting statistics for a realistic clinical camera compared to what is shown here by increasing the solid angle.

Assuming an improved sensitivity over the small-sized prototype of one order of magnitude a distal pencil beam of, for example,  $2 \times 10^8$  protons would correspond to a number of protons of  $2 \times 10^9$  in the current experimental setup. We can therefore consider that this camera design can reach a precision of 2 and 1 mm for the entrance rise and falloff positions respectively and a precision for the total range of 2.2 mm using TOF. As the TOF window and energy threshold have not been optimized with regards to the best achievable FRP, there is some room for improvement in that regard. The analysis shows that the contrast/noise ratio could be improved by 20% each by optimizing the settings of the TOF window and energy threshold, leading to a potential lowering of the FRP by 30% in total.

The scanned single slit camera proposed here gives a good idea of what can be expected for a multi-slit camera model, but a few differences have to be expected, notably the occurrence of septal penetration of prompt gamma and changes in the observed background. The next section of this chapter is dedicated to the optimization of such a multi-slit system and will allow the study of such affects and the verification of the achievable precision.

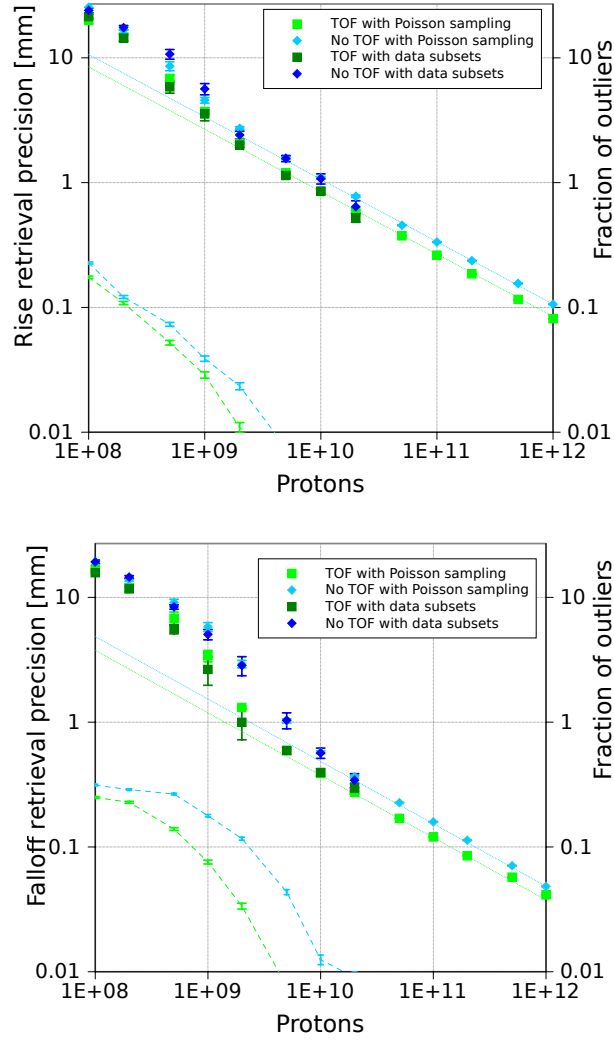


Figure 4.10: Retrieval precision ( $1\sigma$ ) with and without TOF, using Poisson generation and data subsampling (full symbols and dotted lines) and corresponding fraction of outliers (dashed lines) for the entrance rise (above) and the falloff (below).

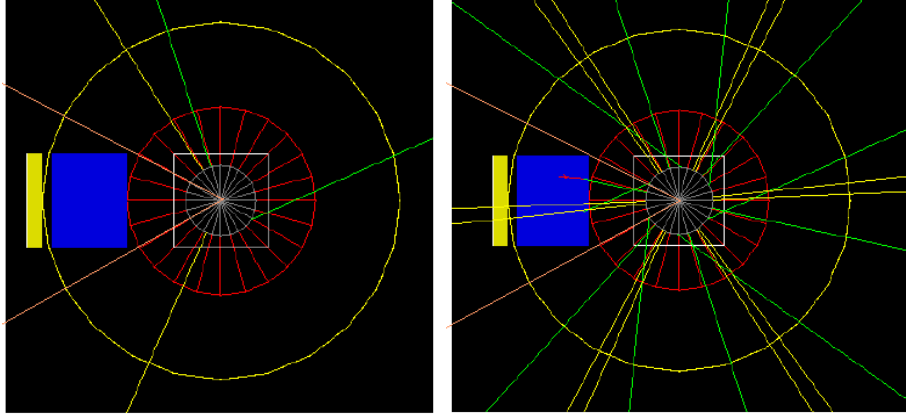


Figure 4.11: Visualization of the simulation illustrating the way the phase space can be used repeatedly. The view is perpendicular to the beam incidence. The target is shown in gray, the collimator in blue and the crystals in yellow. In orange the angle covered by the entrance of the collimator. On the left is shown a single utilization of the phase space (four particles). On the right, the phase space is used six times, each time rotated in regular intervals around the beam axis.

### 4.3 Monte Carlo simulation: optimization of the camera properties

The aim of the simulation was to find the optimal configuration to find the falloff location in a homogeneous target and to be able to compare those simulations with measurements for validation. For ease of comparison, the same cylindrical PMMA target with the beam incident perpendicularly on the middle of one flat surface was used in the measurements and in the optimization of the knife-edge slit camera conducted by J. Smeets ([Smeets \[2012\]](#)). The proton beam used was a perfect pencil beam (no energy or spatial spread and no emittance) of 160 MeV, which is the reference energy used in previous measurements. The perfect beam was used on the assumption that the differences to a perfect beam in terms of prompt-gamma profile are negligible. It also allows to be as general as possible, not modeling a specific beam at a specific site.

To save calculation time, the simulation of the beam hitting the target was conducted only once and the particles exiting the target were saved in a phase space. This phase space was then used in all subsequent simulations of different camera configurations.

The camera is defined to be a set of rectangular-parallelepiped shaped septa which form the collimator, arranged parallel to one another so that the slits are perpendicular to the beam direction. The crystals are also rectangular parallelepipeds and are placed behind the collimator, arranged in the same way as the septa.

Since the camera only covers a very limited solid angle, a great number of particles that are generated never encounter the camera at all. For example, a camera at 200 mm distance with a height of 200 mm only covers 15% of the flat angle in the symmetry plane of the setup. One solution for saving calculation time and memory is to make a cylindrical camera surrounding the target and then correct the results for the solid angle. This was done in the optimization study for the knife-edge slit camera (see section [5.2 on page 93](#)). This can lead to problems due to scattering in the collimator (where a scattered event in the collimator ends up hitting a crystal and being detected in the cylindrical configuration, where there would be no crystal in a parallelepiped configuration). The problem is much more important for a parallel-slit detector than for a knife-edge detector, since particles scattered in a thin septum are more likely to exit the collimator than particles scattered in the solid wall of the knife-edge slit camera. Furthermore, when using a phase space, the gain in calculation time by using a cylindrical configuration is small, since particles emitted in a direction other than

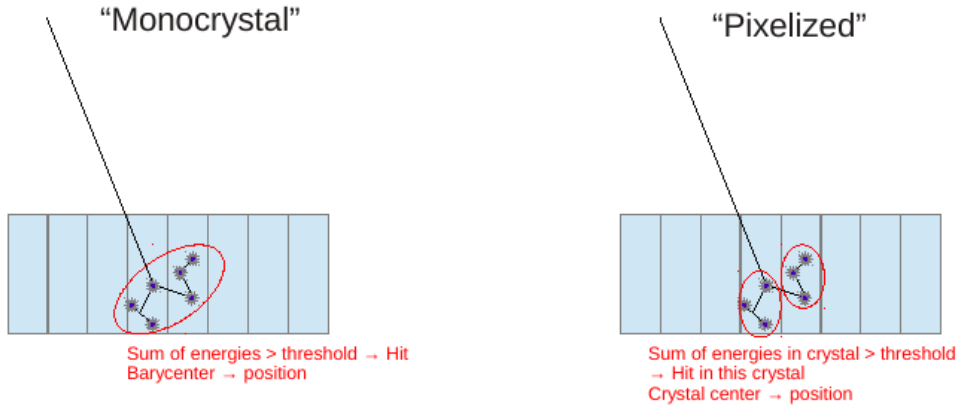


Figure 4.12: Illustration of different scoring approaches. Left: monocrystal/barycenter approach, right: pixel approach used in these simulations.

Symbol	Parameter	Range	
$d_1$	Beam-collimator distance	200 mm	fixed
$H$	Camera height	200 mm	fixed
$D$	Collimator depth	50 mm - 550 mm	
$p$	Collimator pitch	2 mm - 12 mm	
$f$	Fill factor	0.1 - 0.9	
$s$	Slit width		$p(1 - f)$
$d_2$	Collimator-crystal distance	0 mm - 200 mm	
$L$	Total beam-crystal distance		$d_1 + D + d_2$
$d_c$	Crystal depth	31.5 mm	fixed
$w_c$	Crystal width		$p$ or $p(1 - f)$

Table 4.1: Definitions of camera parameters for the multi-parallel slit camera

the direction of the camera encounter no material and typically only take one step in the Monte Carlo. To save memory space for the rather large phase space files, the symmetry of the configuration was exploited to use each phase space multiple times, each time rotated around the symmetry axis. In figure 4.11 on the preceding page can be seen the tracks of four particles coming out of the target. On the left, they are used once (and none hit the camera at all), while on the right the rotational symmetry of the phase space is used to generate each particle six times at regular intervals. This corresponds to placing copies of the same camera six times around the target, but without possible inter-camera scattering.

For scoring in the crystals, it is assumed that detector segments (“crystals”) are read out separately. For each primary particle generated from the phase space, the energy deposits in each crystal are summed and the total energy is counted as one hit in that crystal. The difference between this method of scoring and a monocrystal method in which the barycenters of energy deposition are used is shown in figure 4.12.

The parameters that define the camera setup are illustrated in figure 4.13 on the next page and listed in table 4.1:

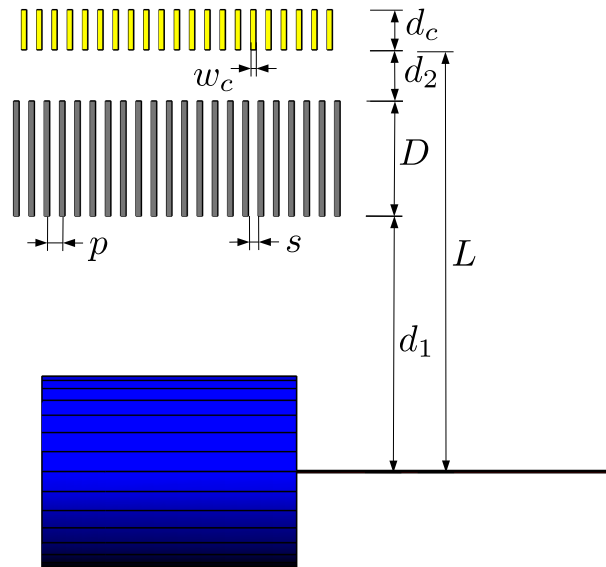


Figure 4.13: Parameters of the multislit geometry

Collimator pitch:	2 mm, 4 mm, 6 mm, 8 mm
Collimator depth:	50 mm, 70 mm, 100 mm, 125 mm, 150 mm
Fill factor:	0.2, 0.35, 0.5, 0.7
Crystal width:	3.9 mm

Table 4.2: Values tested in initial exploration of the parameter space.

### 4.3.1 Optimization strategy

Since there is a large number of parameters describing the camera that have to be optimized and they are a priori interdependent, the parameter space in which the optimum has to be found is multi-dimensional. An attempt was made to use a simplex method for function minimization to find the optimal FRP (method: [Nelder and Mead \[1965\]](#)), but due to relatively small variations of the function around the minimum, such methods quickly get into a region in which the errors of the figure of merit mask any real trend, so that they will no longer work. Therefore, a more systematic approach was chosen.

First of all, certain parameters were fixed: the beam-collimator distance, the camera height, the crystal depth and the total camera field of view. A first large-mesh overview of the parameter space of the defining properties of the collimator (pitch, depth and fill factor) was made to get an idea of the broad trends. The result can be seen in [figure 4.14 on the next page](#). It is reasonable to start with the premise that most parameters' influence is dominated by one or two main effects. If this is the case, we expect to find monotonous trends over large parts of the parameter range rather than multiple quick variations. This leads to a relatively "well behaved" parameter space without many local minima that can be explored using a large mesh. Indeed, when looking at the trends for different parameters,

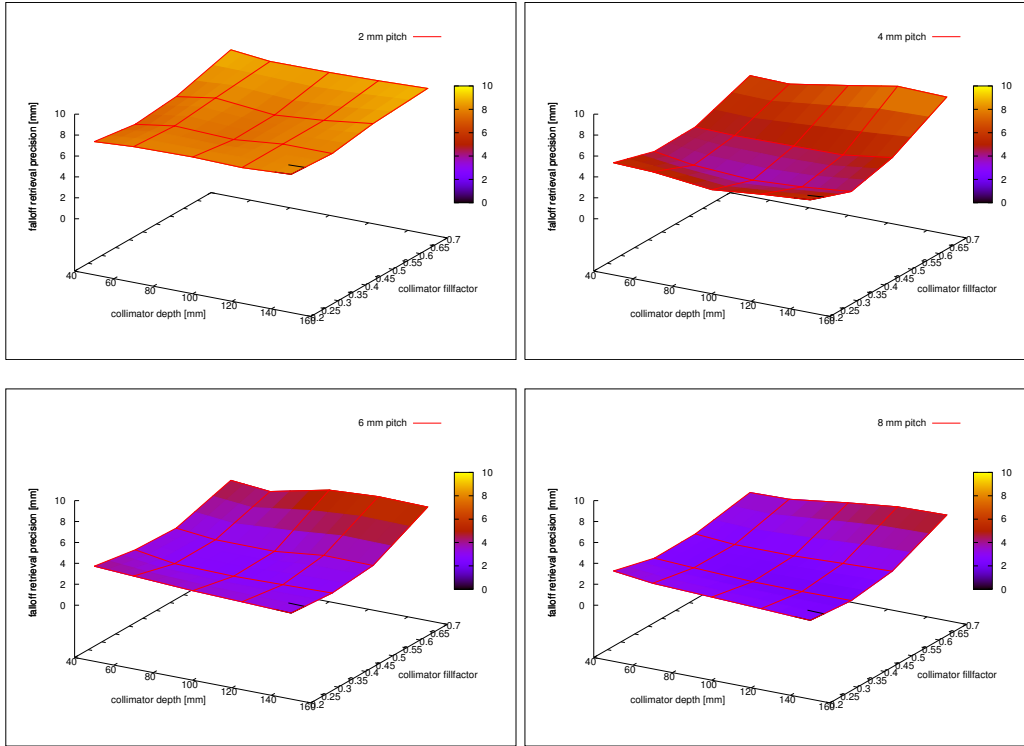


Figure 4.14: Influence of the collimator properties: depth, pitch and fill factor. Simulated configurations are at the crossing of the red mesh, colors show interpolation of the FRP values. Simulation conducted with  $5 \times 10^9$  protons, subsamples corresponding to  $5 \times 10^7$  protons.

generally only one minimum is observed. Furthermore, the minimum seems relatively broad and flat, leading to a sort of optimum region with very similar performances to within the margin of error instead of well defined optimum values.

To get a feeling of the parameter space, all combinations of the values in table 4.2 on the facing page for the collimator parameters were tested.

Once the general area of interest was identified, each parameter was studied separately to understand the effects at play and to choose a value for the final configuration. The distance between collimator and crystal was studied separately, as well as the width of crystals and potential shielding between crystals.

For didactic reasons, we discuss first the observations on separate effects of the individual parameters and return afterwards to the discussion of interdependent effects in subsection 4.3.4 on page 82.

### 4.3.2 Evaluation of the profiles

For the reasoning behind the figures of merit chosen to evaluate the profiles, see section 3.1 on page 29.

The profiles were compared and evaluated in two steps. First, the properties of the profile itself: number of background counts, contrast, contrast/noise ratio and width of falloff (correlated to the spatial resolution). Second, an evaluation of the precision with which the falloff could be retrieved for a profile acquired with a given amount of protons in a spot. Two points of comparison were chosen:  $5 \times 10^7$  and  $5 \times 10^8$  protons in accordance with section 3.1 on page 29.

To evaluate the properties of the profile, it was fitted with a NURBS as described in section 3.2 on page 30. From the NURBS function and its derivative, all of the important properties of the profile can be deduced.

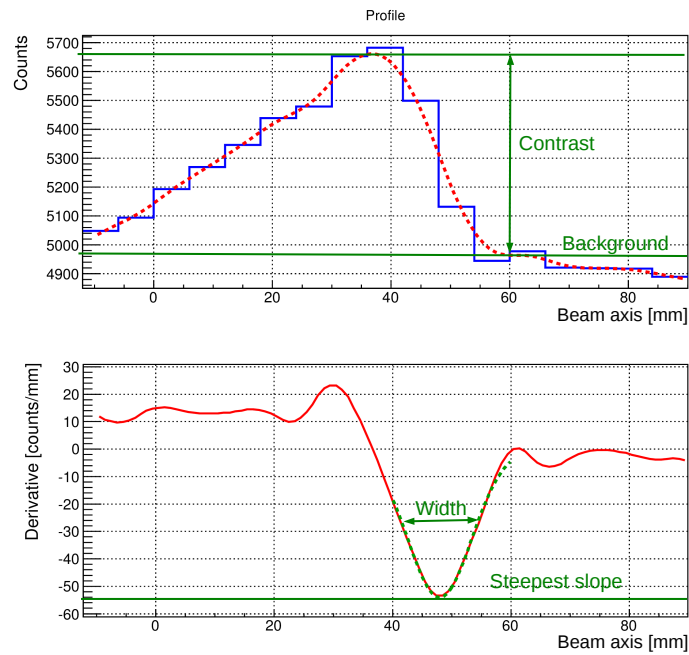


Figure 4.15: Illustration of fitting with a NURBS function and reading the profile properties from the function and its derivative. In all histograms of profiles, the bin width corresponds to the collimator pitch.

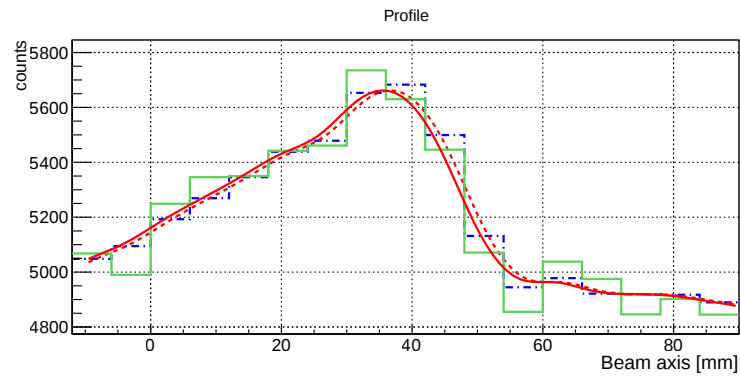


Figure 4.16: Illustration of a scaled simulated master profile (blue, dashed) and a corresponding sample profile (green, solid line) and the corresponding NURBS function, original (red, dashed) and shifted to fit the sample profile (red, solid line).

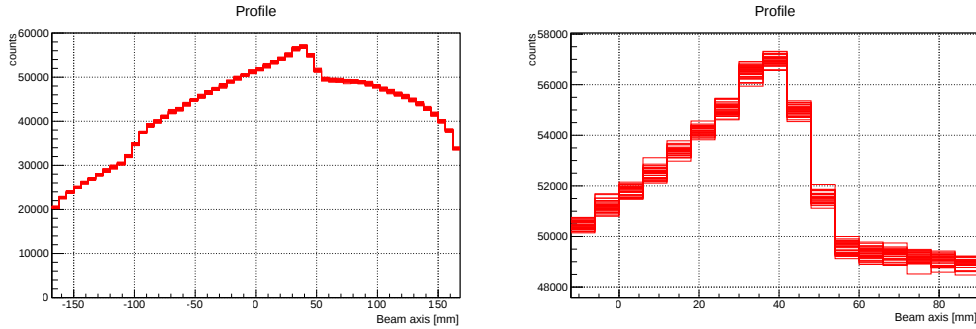


Figure 4.17: Reference profiles acquired for the same setup,  $5 \times 10^9$  protons each to estimate statistical fluctuations in the reference profiles and the influence on the camera figures of merit. Right: zoom around the falloff region.

As can be seen in figure 4.15 on the preceding page, the derivative of the profile is nearly constant far from the falloff and has a characteristic pattern around the falloff. The area around the minimum of the derivative, corresponding to the steepest part of the falloff, can be adequately fitted with a Gaussian. The Gaussian form corresponds to the assumption that the prompt-gamma emission has a sharp edge, the image of which takes the shape of an error function. From the Gaussian can be determined the width of the falloff and the maximum steepness. The FWHM of the Gaussian is used as a measure of the falloff width.

The background level and the contrast can be measured directly from the profile itself. The background is considered to be the level of counts after the dropoff, the contrast is the difference between the number of counts at the maximum and the background counts. To define the place where the dropoff ends and the background begins, we use the Gaussian and consider that two sigma from the center, the background begins. Noise is considered to be the Poisson noise corresponding to the middle point of the falloff, i.e. the square root of the average of maximum counts and background counts. The contrast/noise ratio is calculated by dividing this contrast by this noise.

To evaluate the precision of range retrieval, sample profiles corresponding to  $5 \times 10^7$  and  $5 \times 10^8$  protons respectively were drawn from the simulated profile using a Poisson random generator and the precision was evaluated as described in section 3.2 on page 30. An example of a sample profile is shown in figure 4.16 on the preceding page.

### 4.3.3 Estimation of the error of falloff retrieval precision

In order to distinguish between real effects and statistical variations, it is important to estimate the errors on the evaluation parameters. Simulations were conducted using  $5 \times 10^9$  protons each to obtain a master profile, which lead to counts per bin of the order of tens of thousands in the region of interest around the Bragg peak. Correspondingly, the relative standard error for the number of counts is of the order of less than a percent. However, the contrast being relatively low, the standard error of the contrast is of the order of a few percent. This, in turn, leads to errors in the evaluation criteria, notably the falloff retrieval precision, which are not trivial to predict.

The uncertainty of the calculated falloff retrieval precision comes from two main sources. For one thing, the reference profile itself shows statistical fluctuations due to the finite number of histories in the simulation. This can be estimated using Poisson statistics or by rerunning the simulation several times. The influence of the statistical fluctuations of the reference profile on the figures of merit such as the FRP is non trivial. Since it is impractical to do much longer simulations for the large number of geometries, a study of the typical order of magnitude of the errors was conducted by repeating the simulation of one example configuration 30 times. The result can be seen in figure 4.17. The configuration used corresponds to the optimized configuration shown in table 4.3 on the next page.

Collimator depth	70 mm
Pitch	6 mm
Fill factor	0.35
Beam-collimator distance	200 mm
Collimator-crystal distance	0 mm
Crystal width	3.9 mm

Table 4.3: Optimized configuration for the multi-parallel-slit collimator

The resulting relative statistical error on the FRP is 3.7%. An assumption is made that all profiles show similar behaviour regarding the relative error of the falloff retrieval precision. This error is taken into account in all the error bars of the subsequent figures.

The second type of error is related to the drawing of samples. To obtain the FRP, a certain number of samples is drawn by a Poisson generator and a shift retrieved from each. Since the generation of samples is a random process, there is a fluctuation in the distribution of the retrieved shifts and thus of the properties of the distribution, such as the RMS, which is used as an estimator for the FRP. This error is estimated by repeating the sampling process several times for each configuration.

The NURBS parameters are set to the most simple processing possible (no weights, one control point per bin). It is possible that for certain profiles, different settings could be more advantageous, such as increased smoothing for noisy profiles. To test this, several profiles were taken with spacing between control points different from the bin size. In that case, a gliding average is used to calculate the control points instead of using bin centers. Furthermore, the relative location between control points and bins or control points and the falloff could influence the precision as well, so several configurations were tested (for example, for a spacing of 6 mm, control points can be located at  $x=\{0, 6, 12, \dots\}$  mm or at  $x=\{2, 8, 14, \dots\}$  etc.). Examples are shown in figure 4.18 on the facing page. The variation in precision observed was no higher than the statistical error of the precision in general (see figure 4.19 on page 74), so it seems safe to consider that the method is robust with regards to the spacing and placement of control points.

#### 4.3.4 Influence of the setup parameters on the camera performance

The following optimization is conducted without regard to the possibility of applying time-of-flight selection to the data. An optimization focusing on the best use of time-of-flight was conducted elsewhere (Pinto et al. [2013]). Consequently, a choice was made to place the camera as close to the patient as was thought possible without undue inconvenience to the patient in order to cover a large solid angle with limited crystal volume. This minimum working distance was deemed to be around 20 cm between the beam and the front face of the camera (collimator). Note that this value constitutes an educated guess based on informal conversation with clinicians on what they deem acceptable.

The camera height was fixed at 20 cm. It is assumed that the increase in solid angle linked to the increase in height only leads to an increase in the number of detected particles proportional to the solid angle, at least in first order approximation. This was confirmed by simulation, as can be seen in figure 4.20 on page 74. If the solid angle is indeed the only effect in play, the counts are expected to increase proportionally to  $\arctan(H/2L)$ . The deviation from the theoretical curve at small heights is probably due to decreased total absorption rates in the crystal. The height of 20 cm was chosen as something that seemed reasonable from a practical point of view. Increasing the height or placing several detector heads around the patient is an option to increase the number of counts and is considered to have equivalent influence on the performance as increasing the number of protons.

The depth of crystals was fixed at 31.5 mm, also for practical considerations, as this is the dimension of crystals used for the existing prototype of the knife-edge slit camera,

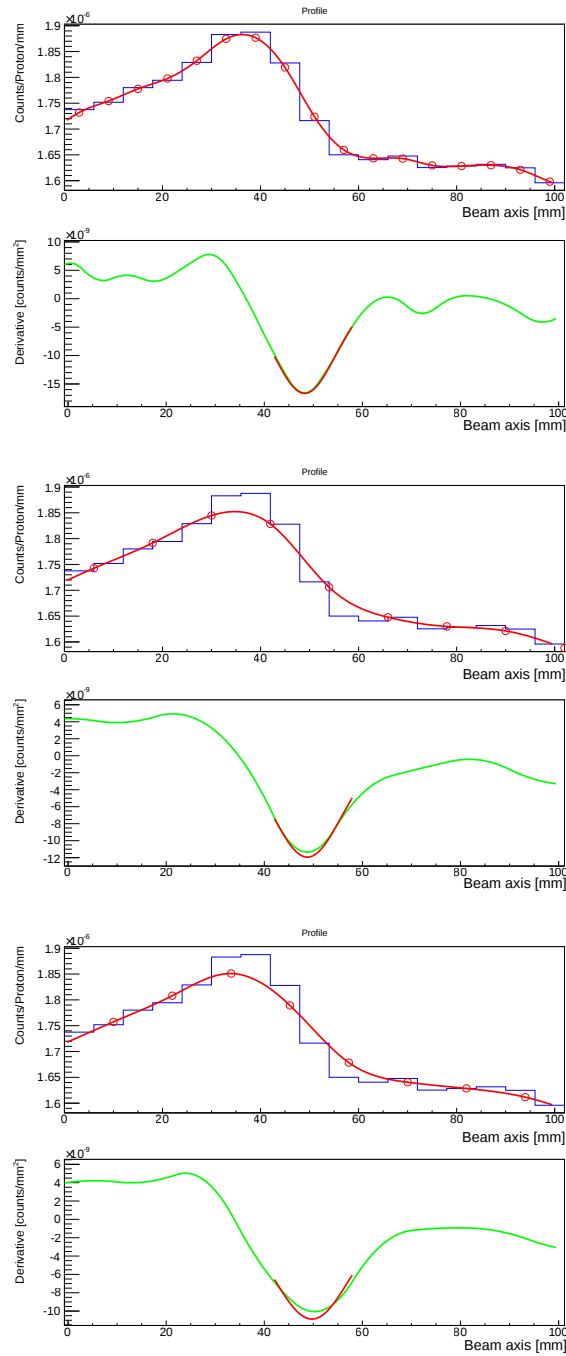


Figure 4.18: Influence of the spacing and placement of control points. The profile is shown in blue, the knots of the NURBS are shown as red circles. Control points are chosen as the center of bins when the spacing is equal to the pitch, or as a gliding average over several bins if the spacing is greater than the pitch. Spacing of 6 mm (equal to pitch) on the top, 12 mm in the middle and bottom. Placement of control points shifted by 2 mm between middle and bottom profiles. The derivative shows that choosing larger spacing leads to smoother profiles and derivatives, but also less steep falloffs.

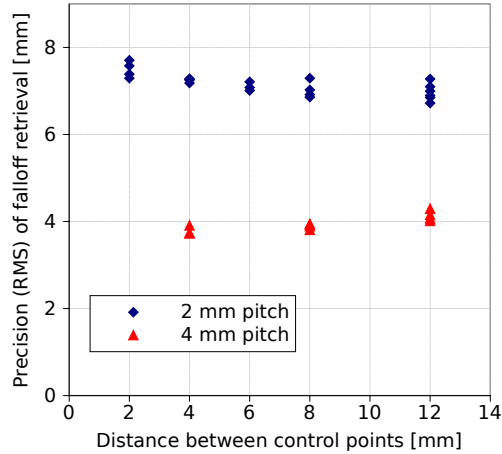


Figure 4.19: Influence of the spacing between two control points. For each spacing, several placements of the control points were tested. Simulation conducted with  $5 \times 10^9$  protons, subsamples corresponding to  $5 \times 10^7$  protons. Other parameters:  $D=100$  mm,  $f=0.35$ , crystal width=3.9 mm. Spacing between control points seems to have no significant influence on the precision.

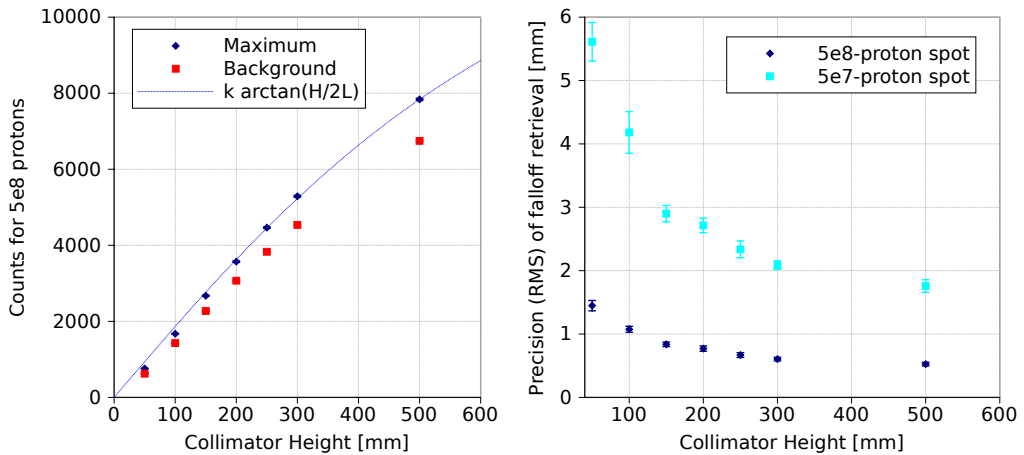


Figure 4.20: Influence of the camera height. Left: comparison of observed count rates to solid angle. The dotted line is proportional to the solid angle, with the factor  $k$  chosen so that it goes through the point at 500 mm height. Right: influence on the falloff retrieval precision. Simulation conducted with  $5 \times 10^9$  protons, subsamples corresponding to  $5 \times 10^8$  and  $5 \times 10^7$  protons. Other parameters:  $D=100$  mm,  $p=6$  mm,  $f=0.35$ , crystal width=3.9 mm. It can be observed that the counts scale as expected with the solid angle and that the behavior of the precision vs. height is the same as when increasing the number of protons in section 4.3.5 on page 83.

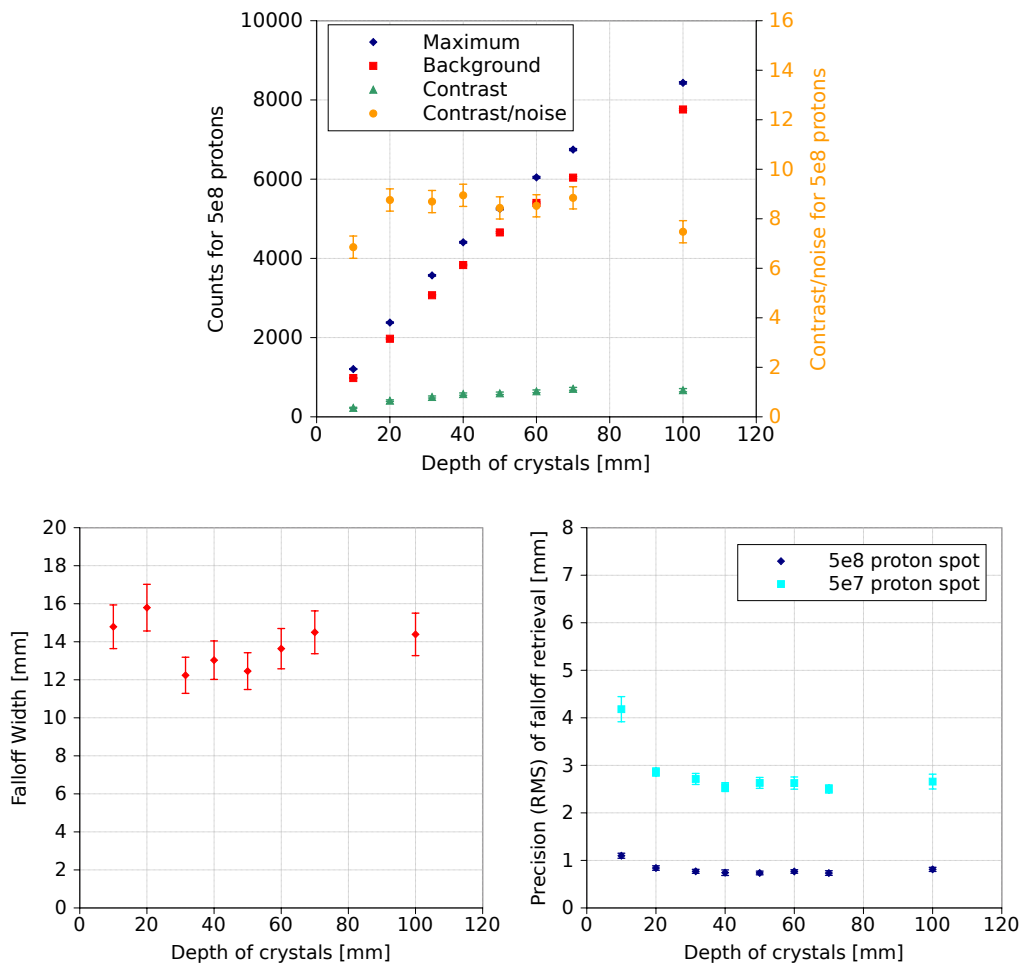


Figure 4.21: Influence of the crystal depth. Above left: observed count rates and contrast/noise. Above right: no significant influence on the falloff width is observed. Below: influence on the falloff retrieval precision. Simulation conducted with  $5 \times 10^9$  protons, subsamples corresponding to  $5 \times 10^8$  and  $5 \times 10^7$  protons. Other parameters:  $D=100$  mm,  $p=6$  mm,  $f=0.35$ , crystal width=3.9 mm. Crystal depths beyond 30 to 40 mm no longer improve the contrast/noise or precision.

which could be reused to test the parallel-slit concept. Additionally, simulations show that increasing the depth of the crystals beyond 30 to 40 mm no longer improves the contrast/noise ratio or the falloff retrieval precision (see figure 4.21).

### Energy window

Energy thresholds were optimized for one configuration at the beginning of the study and kept the same for all configurations. To verify that the choice of thresholds was still adequate for subsequent configurations, different thresholds were re-tested for a few chosen configurations. The analysis showed that the thresholds chosen at the beginning were adequate for all configurations and it is not necessary to re-optimize the energy window for each configuration.

As can be seen in the simulated spectrum of detector counts in figure 4.22 on the following page on the left, the number of prompt-gamma counts decreases rapidly with energy. Above a certain energy, the number of counts due to neutrons surpasses the counts due to gamma by a large factor, meaning that using this region leads to an increase in uncorrelated counts that is larger than the gain in correlated signal, leading to the need for an upper energy limit.

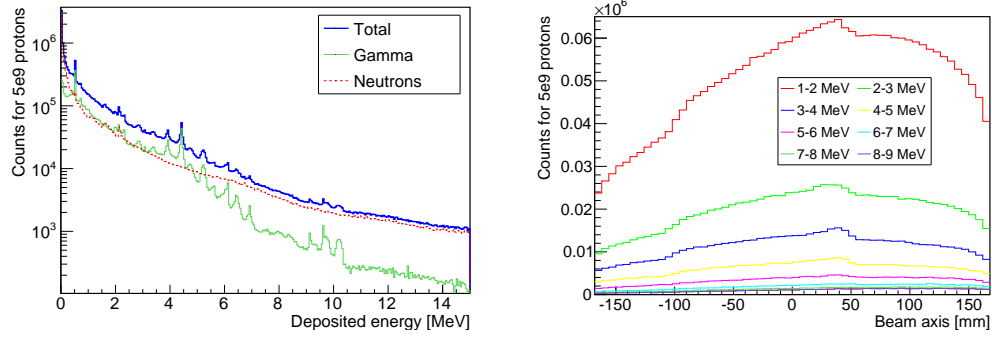


Figure 4.22: Left: Simulated spectrum of counts in the detector for a multi-parallel-slit configuration. The contributions originating from neutrons leaving the target and from gamma leaving the target are detailed. Right: Profiles corresponding to 1 MeV energy windows. The falloff is clearly visible up to windows of 5-6 MeV.

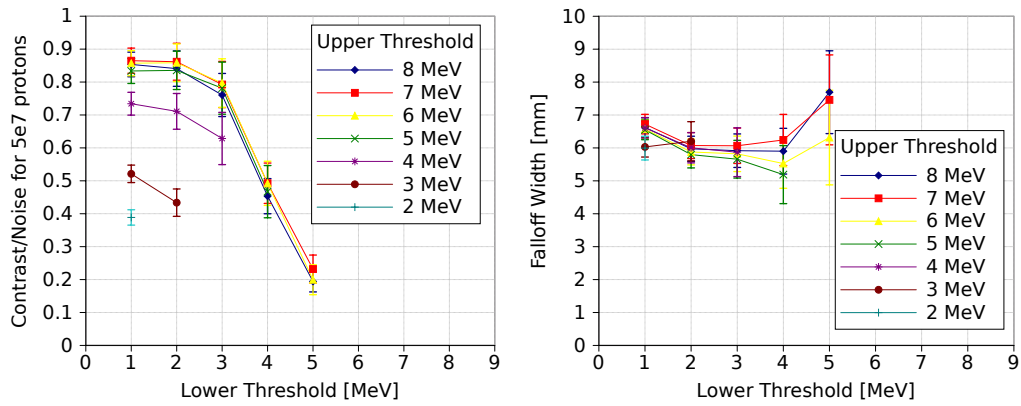


Figure 4.23: Influence of the choice of the energy window on the contrast/noise ratio for  $5 \times 10^7$  protons, and the falloff width. The lower energy threshold is shown on the x-axis, while the upper energy threshold is shown in different curves.

For low energy counts, previous studies (see, for example, [Smeets \[2012\]](#)) have shown that they are less well correlated with the falloff due mainly to scattering. Note that for otherwise equal performance, it is more interesting to use less total counts for practical reasons, such as a less challenging count rate, less dead time, faster data transfer, etc. In the same figure on the right can be seen the profiles corresponding to different 1 MeV-wide energy windows. The falloff is clearly visible for windows up to 5-6 MeV.

Figures 4.23 and 4.24 on the facing page show the performance of the system for different choices of the energy limits. The impact of the chosen thresholds, especially the upper threshold, on the falloff width is small, with best results reached for lower thresholds of 2 to 4 MeV. The influence on the contrast/noise ratio is more pronounced, and directly reflected in the influence on the obtained FRP. It appears that optimal performance is achieved for lower energy limits of 1 to 2 MeV, with 3 MeV still performing rather well. The upper energy threshold must be chosen to be at least 6 MeV, after which the effect of raising the threshold becomes small and is hidden within the error bars. Indeed, looking at the relative order of magnitude of the respective number of counts in each profile, it is clear that higher energy slices contribute less and less counts to the profile and influence the result less.

For the optimization study, a lower energy limit of 2 MeV and an upper limit of 7 MeV were chosen to optimize performance while keeping total count rates low.

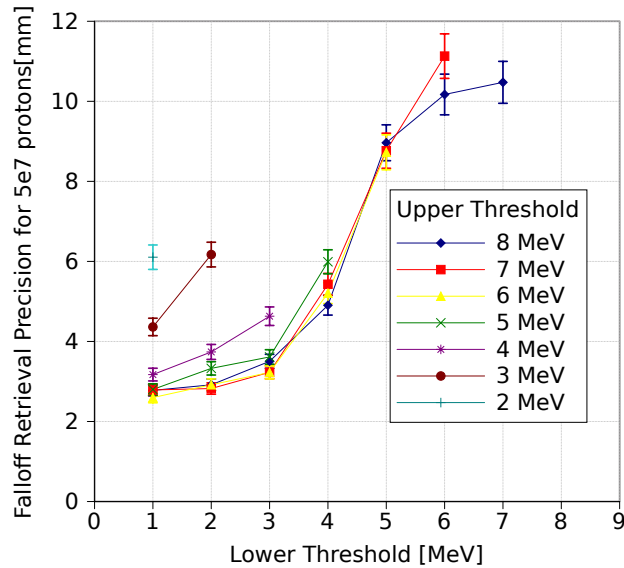


Figure 4.24: Influence of the choice of the energy window on the FRP. The lower energy threshold is shown on the x-axis, while the upper energy threshold is shown in different curves. The optimum is reached for lower thresholds of 1 or 2 MeV and upper thresholds at or higher than 6 MeV.

### Collimator pitch

Changing the pitch is in this case defined as increasing the septa width and the slit width proportionally (leaving the fill factor constant) and also increasing the crystal width, so that there is always one crystal behind each slit. The collimator depth was set to 70 mm and the fill factor to 0.35 according to the optimal values obtained for those parameters. Following the conclusions of section 4.3.4 on page 83, the crystal width was set to be equal to the slit width. The assumption made above that the solid angle is limited only by the slit width is still true since the crystals are just behind the collimator and cover the whole slit.

Figure 4.25 on the following page gives an example of profiles with different values of the pitch and figure 4.26 on the next page illustrates the influence of the pitch on the FRP and the falloff width. The main impact of an increase in pitch can be predicted by looking at the collimator efficiency, equation (4.5). Since the crystal width is increased proportionally to the pitch, the pitch actually goes into the per-slit efficiency quadratically as can be seen in equation 4.5 on page 54. It can be expected that the correlated prompt-gamma signal (contrast) follows the trend of the geometric efficiency, because these are mostly events that were collimated correctly. The neutron background, on the other hand, is expected to not be affected by the collimator as long as the total volume of tungsten is constant (i.e. for constant fill factor) and stay the same per unit length of crystal. The gamma background is dominated by septal penetration (see section 4.3.5 on page 84). In summary, we expect the per bin contrast to rise quadratically with the pitch, while the background should exhibit nearly linear behaviour, as illustrated in figure 4.27 on page 79. As the contrast rises faster than the background (and the noise), the FRP improves when the pitch is larger, as can be seen in figure 4.26.

Additionally, for smaller pitches and crystal widths, it is more likely that a scattered particle will deposit energy in more than one crystal and be counted as two lower energy events, while larger crystals increase the probability of depositing the whole energy in a single crystal. This can be seen looking at the spectra of events in figure 4.28 on page 79, where the spectrum corresponding to a larger pitch shows a distribution towards higher values overall and the peak for 4.44 MeV as well as the two peaks corresponding to the escape of one or two 511 keV annihilation photons are clearly visible, while only the double escape peak is

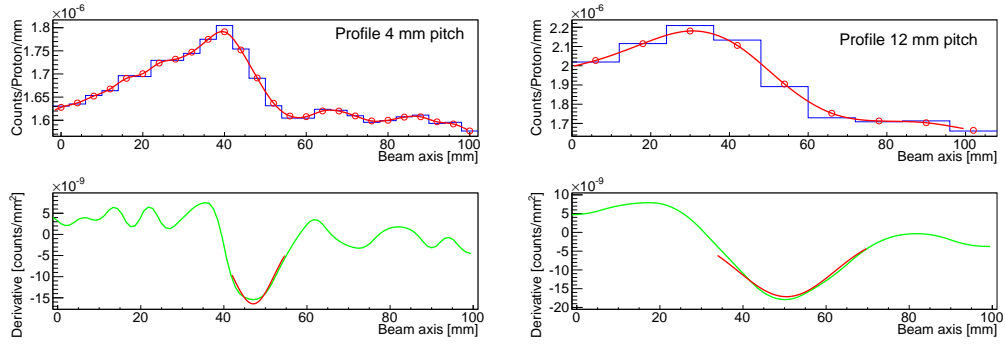


Figure 4.25: Profiles with different settings for pitch and the derivatives of the fitted NURBS. Left: 4 mm pitch, right: 12 mm pitch.

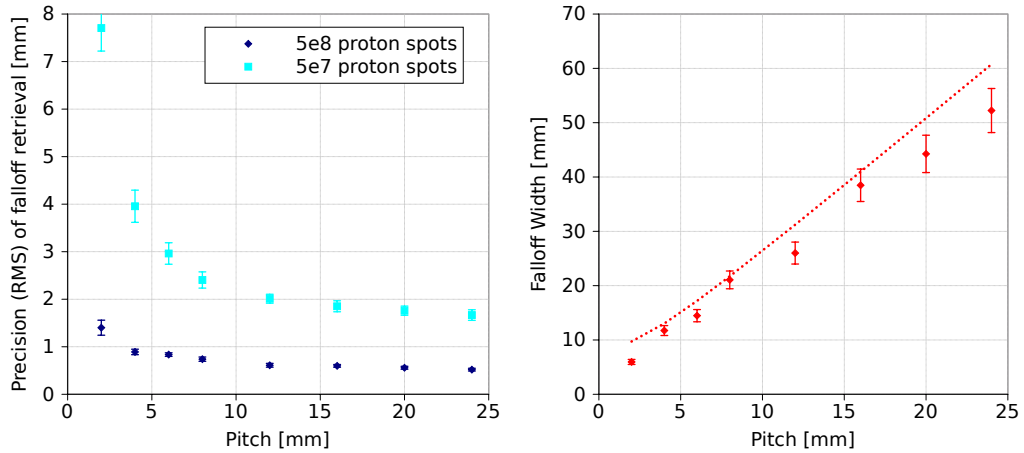


Figure 4.26: Influence of the collimator pitch. Left: influence on the falloff retrieval precision. Right: influence on the falloff width, the expected falloff width based on the detector unit FOV and the emission profile falloff width is drawn as a dashed line. Simulation conducted with  $5 \times 10^9$  protons, subsamples corresponding to  $5 \times 10^8$  and  $5 \times 10^7$  protons. Other parameters:  $D=70$  mm,  $f=0.35$ , crystal width=3.9 mm.

visible in the case of a 2 mm pitch. This effect, however, is small compared to the effect of the pitch described above and can be considered a second-order effect.

As shown in section 4.3.3 on page 71, the number of control points has no measurable effect on the FRP, and likewise a rebinning of the profiles with small pitch shows no significant improvement. The conclusion is that the most important factor determining the FRP is the contrast/noise/cm of crystal, which clearly privileges configurations with large pitch and crystals for the FRP for the reasons cited above.

The pitch is one of the main factors with which one can influence the trade-off between falloff width and falloff retrieval precision. The final decision of where the ideal point in that tradeoff is cannot be made with a study of homogeneous targets, but has to be evaluated through study of examples of real cases with heterogeneous anatomy. For the time being, a pitch of 6 mm seems a reasonable choice, since it is a point where the performance in precision starts to level off.

### Collimator depth

The collimator depth has a great influence on the acceptance angle of the collimator and thus on the falloff width and the efficiency. In essence, depths that are too low will not have

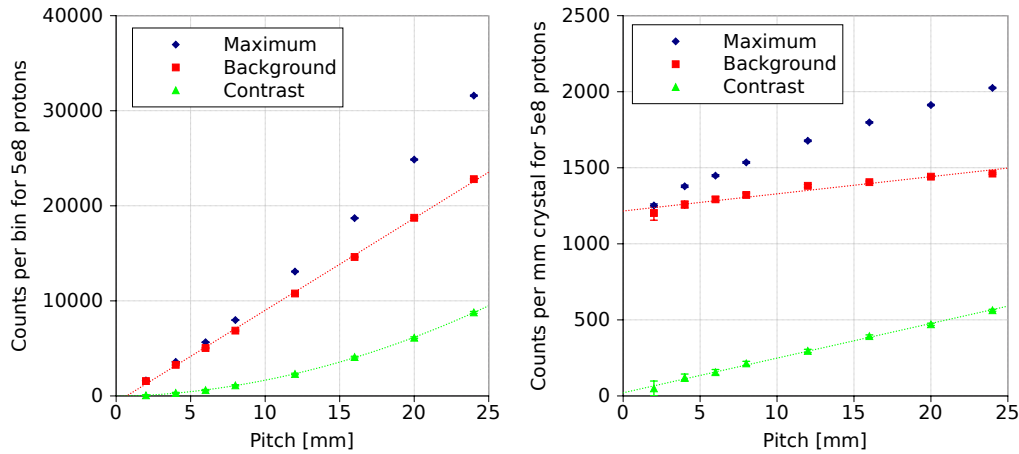


Figure 4.27: Influence of the crystal pitch on the maximum, correlated signal and background counts as observed per bin (binsize equal to the pitch) on the left and per unit length on the right. The correlated prompt-gamma signal exhibits quadratic behaviour in pitch, while the background is nearly linear. Simulation conducted with  $5 \times 10^9$  protons, subsamples corresponding to  $5 \times 10^8$  protons. Other parameters:  $D=70$  mm,  $f=0.35$ , crystal width=3.9 mm.

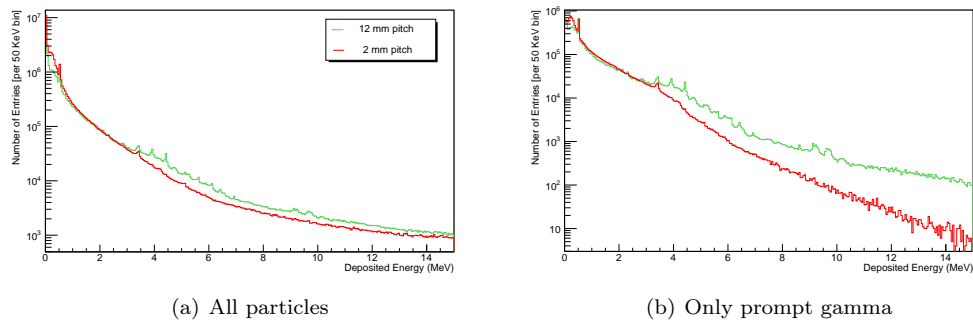


Figure 4.28: Spectra of all recorded counts in the detector for pitch values of 2 mm and 12 mm (recorded counts are all energy deposits by one incident particle in one crystal, particles depositing energy in multiple crystals are counted multiple times). Left: all particles, right: only gamma leaving the target. For the low pitch, there are more counts at low energies as incident particles are more likely to deposit energy in more than one crystal when they are scattered and thus be counted as several separate events. Correspondingly, the energy spectrum is distributed much more toward low values. The peaks at 4.44 MeV with its single and double escape peak are clearly visible in the 12 mm case, while only the double escape peak is visible in the 2 mm case, further indicating a lower probability of an incident particle losing all of its energy in a single crystal.

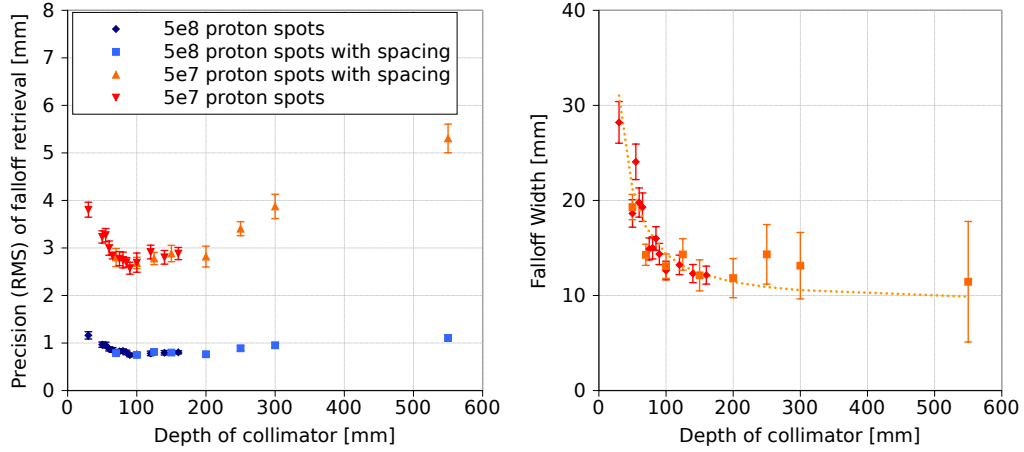


Figure 4.29: Influence of the collimator depth. Left: influence on the falloff retrieval precision. Right: influence on the falloff width. The expected falloff width calculated from the slit field of view and the emission profile falloff width is shown as a dotted line. Two series were made with different spacings between crystals (see section 83) shown in dark/light blue and red/orange respectively. Simulation conducted with  $5 \times 10^9$  protons, subsamples corresponding to  $5 \times 10^8$  and  $5 \times 10^7$  protons. Other parameters:  $p=6$  mm,  $f=0.35$ , crystal width=3.9 mm and 6 mm.

enough collimation, while depths that are too great show good spatial resolution, but the FRP suffers from the reduced efficiency.

For the data series in figure 4.29, the crystals are always right behind the collimator, so a change in collimator depth also means a change in solid angle covered by the crystals. This approach was chosen as the collimator-crystal distance is described as a separate effect later (page 82). A pitch of 6 mm and a fill factor of 0.35 were chosen as they are the default values for these parameters.

As expected, the spatial resolution improves for deep collimators. The falloff width decreases as the depth increases until it asymptotically approaches the falloff width of the emission profile itself. The dotted line in the graph representing the falloff width in figure 4.29 represents the theoretical falloff width as calculated from equation (4.1) combined with the falloff width of the emission profile. The best depth for the FRP is around 100 mm, depths from around 70 mm through 130 mm give similar results to within the margin of error of the method. Figure 4.30 on the next page gives two examples of profiles obtained with different depths of the collimator. It can be seen clearly that the number of counts varies considerably.

### Collimator fill factor

The fill factor is defined as the proportion between the septa width and the pitch. In other words, it is the ratio of tungsten volume to total collimator volume. Using this as a parameter instead of the septa or slit width allows to decouple it from the pitch.

In the case of a perfect collimator, a very small fill factor would be ideal. Considering septal penetration in a real collimator, though, there has to be an optimal fill factor that corresponds to the best tradeoff between low septal penetration and high efficiency.

As can be seen in figure 4.32 on the facing page, the optimal fill factor is around 0.3 to 0.5. The reason can be observed on the bottom of the same figure: as the septa width is decreased, the background strongly increases whereas the contrast starts to deteriorate because of septal penetration. This causes the contrast/noise to drop for small fill factors (figure 4.31 on the next page). Both the FRP and the falloff width increase for low values of the fill factor.

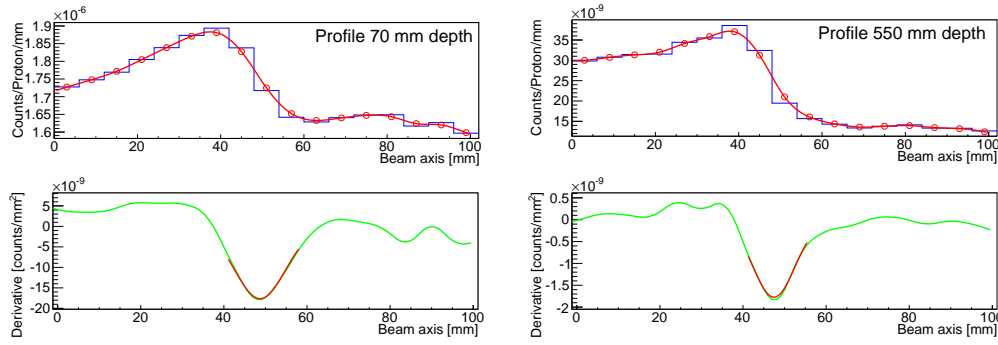


Figure 4.30: Profiles with different settings for collimator depth. Left: 70 mm depth, right: 550 mm depth.

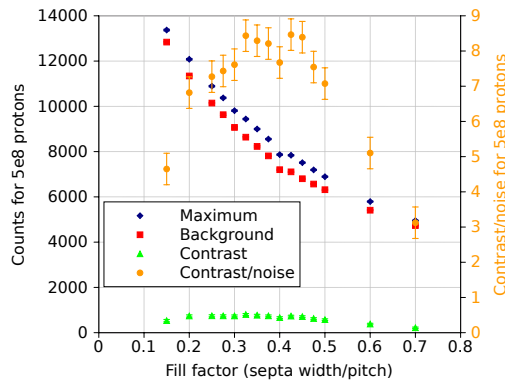


Figure 4.31: Influence of the fill factor. Observed count rates and contrast/noise. Simulation conducted with  $5 \times 10^9$  protons, subsamples corresponding to  $5 \times 10^8$  and  $5 \times 10^7$  protons. Other parameters:  $D=70$  mm,  $p=6$  mm, crystal width=3.9 mm.

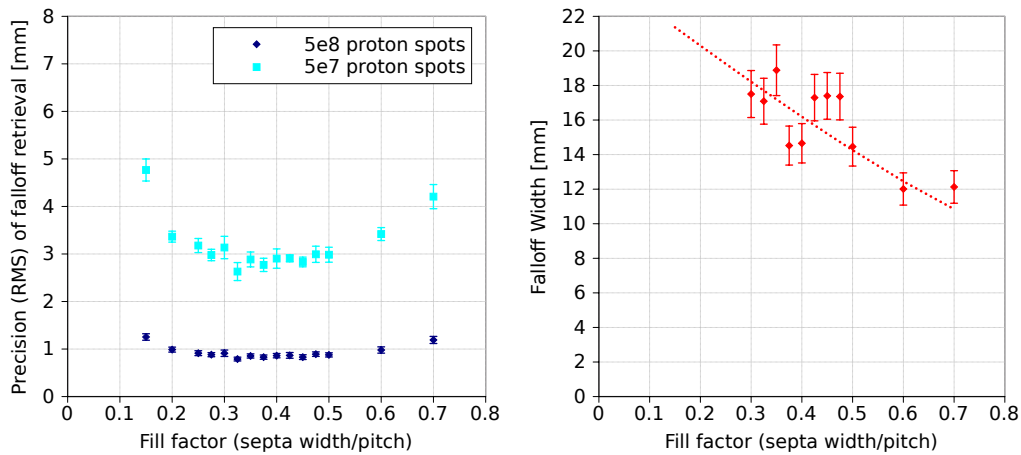


Figure 4.32: Influence of the fill factor. Left: influence on the falloff retrieval precision. Right: influence on the falloff width (the dotted line represents the convolution of detector unit field of view and emission profile falloff width). For fill factors below 0.3, the septal penetration becomes too dominant, so that the method for retrieving the falloff width is no longer accurate. Simulation conducted with  $5 \times 10^9$  protons, subsamples corresponding to  $5 \times 10^8$  and  $5 \times 10^7$  protons. Other parameters:  $D=70$  mm,  $p=6$  mm, crystal width=3.9 mm.

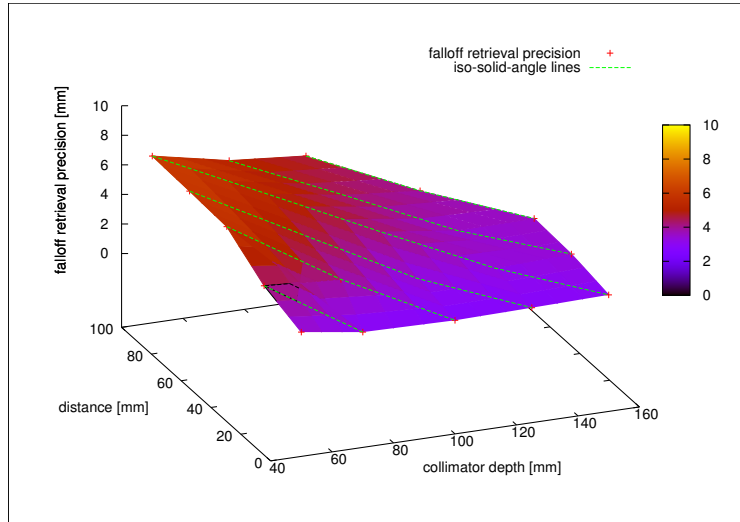


Figure 4.33: Influence of the distance between the collimator and the crystals for different collimator depths. Best results are obtained for smallest distances. Simulated configurations are at the red cross markers, iso-solid-angle lines are shown in green. Colors show interpolation of the FRP values. Simulation conducted with  $5 \times 10^9$  protons, subsamples corresponding to  $5 \times 10^7$  protons.

### Combination of collimator properties

In figure 4.14 on page 69, the FRP for all combinations are plotted as surfaces. Some interdependency between parameters can be observed, but the effects seem to be rather small in the region of the optimum. The following observations can be made:

- The trend of a bigger pitch performing better seems to be the case for all combinations of the other parameters, indicating that the linear collection efficiency, which is proportional to the pitch, has a large influence.
- Large values of the collimator depth and fill factor lead to an increase of the FRP. This can be explained by looking at the efficiency. As expressed in equation 3.15 on page 50, the FRP is inversely proportional to the contrast, and the contrast is determined by the collimator efficiency. As a result, the FRP becomes large very quickly for small values of the efficiency.
- A fill factor of around 0.35 seems to always be a good choice, variations in optimum for different combinations of other parameters are smaller than the mesh of test points.

Overall, it can be seen that the optimum of each parameter does not vary much when the other values are changed and that the effects discussed in the individual sections on the parameters hold true.

### Distance collimator-crystal

The collimator-crystal distance was optimized only once the pitch size and fill factor were fixed. The crystal width was kept equal to the pitch, so that the crystals touch each other. This is different from what was used before. When the crystals are directly behind the collimator, it is sufficient that they cover the area directly behind the slits to collect all that comes through the slit. As they are placed farther away, they need to be larger to cover also the penumbra of the collimator in order not to lose correlated signal. To make sure the observed effects are not due to the solid angle, the collimator depth was also varied.

For all simulated collimator depths, the best FRP is achieved when the crystals are directly behind the collimator, as illustrated in figure 4.33. Indeed, when looking at the

geometrical considerations described in section 4.1 on page 53, one can see that increasing the distance offers no obvious benefit, while it has the drawback of decreasing the solid angle.

### Spacing and shielding between crystals

Since the crystals are directly in front of the collimator, there are some parts of the crystals that are in the penumbra from the septa. It is therefore logical to use a configuration in which the width of the crystals corresponds to the width of the slits instead of the pitch, so that only the space behind the slits is filled with crystal. A comparison between the two solutions is made to be certain that the reduced crystal size performs as well as a full crystal.

The comparison was made for a collimator depth of 70 mm with a fill factor of 0.35 and a pitch of 6 mm.

Crystal width	6 mm	3.9 mm
Precision for $5e8$ p <sup>+</sup>	$0.85 \pm 0.03$	$0.78 \pm 0.05$
Precision for $5e7$ p <sup>+</sup>	$2.89 \pm 0.15$	$2.79 \pm 0.19$
Falloff width	7.4	6.0

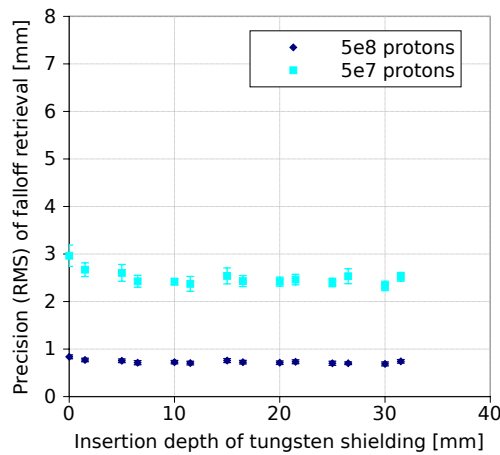


Figure 4.34: Influence of inserting tungsten shielding in between the crystals on the falloff retrieval precision. The x-axis represents the depth of insertion of the tungsten shielding between the crystals. The width of tungsten shielding is equal to the septa width. Other parameters:  $D=70$  mm,  $p=6$  mm,  $f=0.35$ , crystal width=3.9 mm.

As can be seen from the values of the table above, there seems to be a small gain in precision and spatial resolution by reducing crystal size, even though it is not much above the standard error of the method (for  $5 \times 10^8$  protons). However, there is a guaranteed reduction in cost and weight of the system by using smaller crystals, so this is the preferred configuration.

Once the crystal width is reduced, the option presents itself to apply shielding in between the crystals, or to insert them (partially) into the collimator. This was done while keeping the crystals at the same distance from the beam, to keep the solid angle constant. In other words, the collimator septa are extended in between the crystals.

As can be seen from figure 4.34, a small amount of shielding seems to yield a very slight advantage, but increasing it further has almost no effect. Considering the added complication in the manufacturing of the camera and the added weight in tungsten, this tweak is probably not worth it.

### 4.3.5 Performances of the optimized camera

The final configuration chosen can be found in table 4.4.

Collimator depth	70 mm
Pitch	6 mm
Fill factors	0.35
Beam-collimator distance	200 mm
Collimator-crystal distance	0 mm
Crystal widths	3.9 mm

Table 4.4: Parameters of the optimized multi-slit camera.

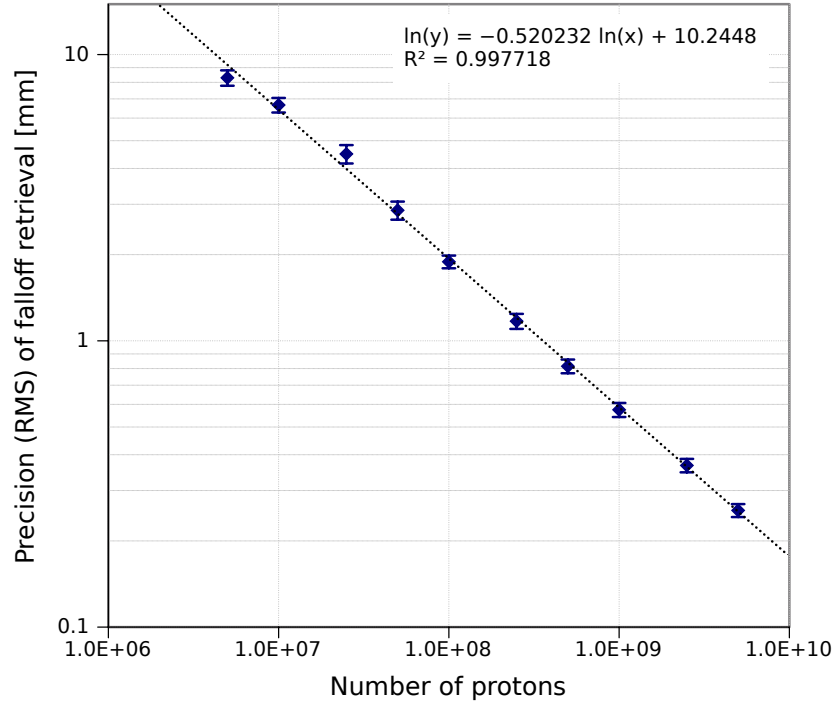


Figure 4.35: FRP for different numbers of protons used for the profile generation.

For those parameters where an optimum of the FRP was observed (depth, fill factor and collimator-crystal distance), a value in the acceptable region was chosen, while also minimizing weight and bulk. For the pitch, an intermediate value was chosen that can be adjusted to privilege either FRP or spatial resolution depending on the results obtained for heterogeneous targets.

Analysis of the profiles was made for a range of proton numbers per spot, as shown in figure 4.35. As expected, the data shows linear behaviour in the log/log plot, corresponding to the FRP being anti-proportional to the square root of the number of protons. This illustrates the effect of the statistical noise on the performance. Note that due to the relatively large falloff width, no outlier component can be seen even at low statistics ( $1 \times 10^7$  protons), unlike what was observed with the small-angle device used for experiments in section 4.2 on page 55. The precision is about 2 mm for  $1 \times 10^8$  protons, which confirms the expectations drawn from the experimental study.

### Spatial resolution and septal penetration

While we have explored the dependence of the falloff width of the profiles on the different parameters during the course of the collimator optimization and seen that it is well predicted by the detector unit field of view, looking at the PSF of the collimator for photons yields

some additional information that cannot be gathered from looking at the profiles alone. For one, the PSF directly shows the effect of septal penetration of the collimator and allows to assess whether septal penetration should be taken into account when estimating the spatial resolution of a system. Second, we study whether the spatial resolution is dependent on the relative position of source and collimator (point source in front of a slit or septum).

We call septal penetration the proportion of radiation that travels through one or more collimator septa and impinges on the detector. Usually, this is something that one tries to limit as much as possible in collimator design. [Gunter \[2004\]](#) gives an empiric criterion for acceptable septal penetration in square-hole collimators:

$$\mu Df > 12.57$$

where  $\mu$  is the attenuation coefficient of the collimator material. Unfortunately, at the gamma energies involved here, it becomes very impractical to try to satisfy the criterion. The necessary collimator depths are well above 200 mm, which is very far from the optimum and very impractical. Additionally, considering the neutron background present in any case, limiting the septal penetration of photons may not be as high a priority in our case as in the development of collimators for nuclear medicine.

Let us consider the possible effects of septal penetration on our profile. Photons that are just outside of the acceptance angle of the collimator slits may cross a part of a single septum. If this is a significant contribution, it will increase the spatial resolution of the collimator compared to a perfect collimator without septal penetration. Indeed, this is the case for the knife-edge slit camera, as described in [section 5.1 on page 92](#). Photons that impinge with angles further and further outside of the acceptance angle will cross two, three, four,... septa until, for photons far outside the acceptance angle, the effect becomes approximately continuous and a photon will “see” a mean thickness of collimator material divided by the cosine of its incidence angle. This mean thickness corresponds to the depth of the collimator times the fill factor and we will call it the effective thickness  $T_e$  of the collimator:

$$T_e = Df \tag{4.7}$$

The effective thickness is the thickness of a solid block of collimator material that would have the same effect.

We can then separate the point spread function of a collimator for a photon source into three contributions:

- Photons that pass through slit openings without touching the septa.
- Photons that pass through a small number of septa. This contribution is difficult to model and is usually studied by Monte Carlo or ray tracing.
- Photons that are very far outside the acceptance angle and cross a large number of septa. These can be modeled using an effective thickness of material  $T_e$ .

[Figure 4.36](#) shows the point spread function of the multi-slit camera to a photon point source to demonstrate the effect of septal penetration. It was obtained via Monte Carlo simulation of a 4.44 MeV point source facing one of the collimator slits. Both the optimized configuration with a fill factor of 0.35 and a configuration with a very small fill factor of 0.15 are shown. The red curves correspond to a theoretical model of what would be observed with a solid block of material of thickness  $T_e$ . We can see the three contributions mentioned above clearly. The photons that pass through the slit are the same for the perfect and realistic collimators and form a peak in the center. Photons passing through one, two or three septa form an oscillating pattern next to the central peak. Beginning at four septa, the PSF becomes indistinguishable from what would be observed for a solid block of material. From comparison with the PSF of the perfect collimator, we can observe that fortunately, the effect of septal penetration does not seem to influence the width of the central peak, meaning

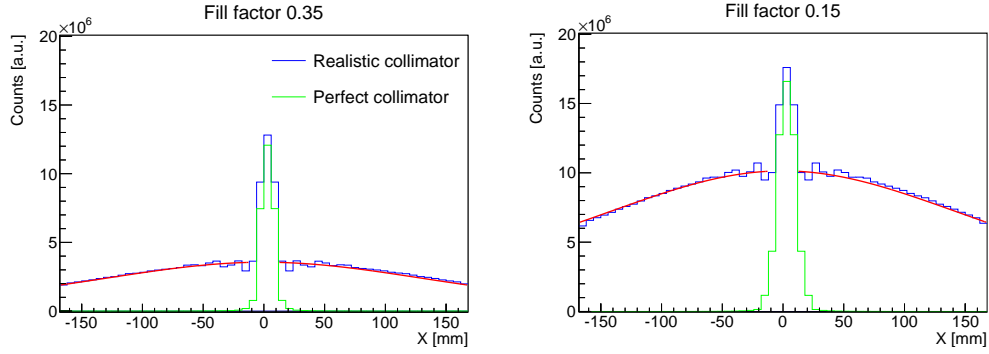


Figure 4.36: Point spread function of perfect and realistic multi-slit cameras for 4.44 MeV photons obtained with a point source facing a slit opening. The red curve corresponds to a theoretical model of what would be observed with a solid block of detector of thickness  $T_e = Df$ . The parameters of the collimator are  $D = 70$  mm,  $p = 6$  mm,  $d_1 = 200$  mm,  $d_2 = 0$  mm,  $w_c = 3.9$  mm,  $f = 0.35$  (left) and  $f = 0.15$  (right).

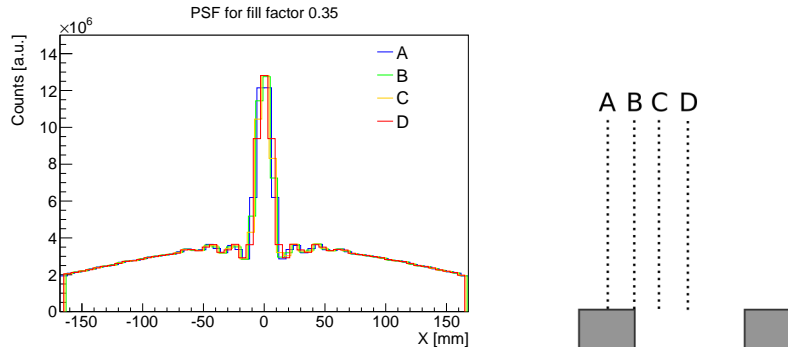


Figure 4.37: Point spread function of a multi-slit collimator for 4.44 MeV photons. The collimator was displaced so that the point source faced a slit opening, a septum, and two intermediate points respectively. The source positions are illustrated to the right. The parameters of the collimator are  $D = 70$  mm,  $p = 6$  mm,  $d_1 = 200$  mm,  $d_2 = 0$  mm,  $w_c = 3.9$  mm and  $f = 0.35$ .

that considerations of the spatial resolution of the detector do not need to be adjusted for septal penetration within the range of parameters studied here.

We can also observe that for the smaller fill factor, the level of background from septal penetration is increased very significantly. While the central peak also increases, the background hides a large part of the peak. This confirms nicely what was observed in section 4.3.4 on page 80 and explains why the contrast decreases for small fill factors, as can be observed in figure 4.32 on page 81.

To investigate whether the part of the collimator that the source is facing plays a part in either the septal penetration or the width of the central peak, four different source positions were tested for the optimized collimator configuration. One was facing the center of a septum, one the center of a slit and two were equidistant intermediate positions. As can be seen in figure 4.37, the general shape both the central peak and the background are not affected by translating the source. We have already shown in section 3.2.4 on page 48 that the relative positioning between the falloff position and the measurement points does not have an effect on the FRP provided that the field of view is larger than the pitch. We can now conclude that we do not expect it to have a significant effect on the spatial resolution either.

### Mass of the system

With a fill factor of 0.35, a depth of 70 mm and a height of 200 mm and assuming pure tungsten of a density of  $19 \text{ g/cm}^3$ , the collimator mass per cm of field of view is  $0.94 \text{ kg/cm}$ . The tungsten alloy used will probably have lower density of down to  $17 \text{ g/cm}^3$ . The crystal mass (assuming LYSO with a density of  $7.3 \text{ g/cm}^3$ ) for the depth of 31.5 mm and with spacing is  $0.30 \text{ kg/cm}$ . Together, this amounts to  $1.24 \text{ kg/cm}$ , so for a field of view of, for example, 10 cm around the Bragg peak, the total mass would be 12.4 kg, not including shielding. A camera that could cover the whole range for the maximum energy of 230 MeV should have a length of around 40 cm (covering 30 cm of range plus 5 cm margin on each side to see the edges) would weigh 49.6 kg.

### 4.3.6 Conclusions

In this chapter, measurements using a scanned system with a single parallel-slit were shown, demonstrating that a parallel-slit camera is able to detect the prompt-gamma falloff for a proton beam. The performance of this system was assessed and can be used as a reference point for what can be expected of a real parallel-slit camera. Next, simulations were conducted to optimize a multi-slit configuration with regards to the performance in falloff retrieval precision, confirming the extrapolated values from the single-parallel-slit measurement. The final optimized configuration is one with a relatively “light” collimator with a small fill factor of 0.35 and relatively low depth (70 mm) compared to what was proposed by other groups (see section 1.2.6 on page 10). This result is a direct consequence of the fact that the FRP is mainly driven by the contrast/noise ratio, which privileges configurations with high count rates and low noise. It was also shown that the FRP continually improves for ever larger values of the pitch, while the spatial resolution deteriorates. A reasonable compromise between the two is set at 6 mm, but may have to be adjusted once studies of heterogeneous targets indicate the best tradeoff.



# Chapter 5

## The Knife-edge Slit Camera

### 5.1 Concept

A “knife-edge” collimator designates the one-dimensional version of a pinhole collimator. There is one single slit, and the edges of the collimator walls on both sides are tapered so that particles from different angles are accepted through the slit and projected onto the image plane.

Whenever profiles are shown or analyzed in this section, the profile is projected into the source plane. This allows for direct comparison between configurations with different magnifications as well as a fair comparison with the parallel-slit camera.

If a perfect collimator (completely absorbing material) is considered, the imaging properties are described by the slit opening of the collimator ( $s$ ) and the distances between object and collimator and collimator and image plane ( $d_1$  and  $d_2$  resp.). Note that the angle of the collimator edges also limits the total field of view of the camera (that we shall call “total camera FOV”, as opposed to “detector unit FOV”). The ratio between  $d_2$  and  $d_1$  is the magnification factor of the image. For a real collimator with finite attenuation of radiation, the thickness of the collimator and the angle of the edges come into play.

The parameters defining the geometry of a knife-edge camera are illustrated in figure 5.1 on the following page and summarized in table 5.1:

Note that while the nomenclature of the multi-slit camera is transferred as much as possible, the distances  $d_1$  and  $d_2$  are here measured from the center of the collimator instead of the surface, because this is much more convenient for the calculations of the field of view and collection efficiency, below.

Symbol	Parameter	Relation
$d_1$	Patient-collimator center distance	
$d_2$	Collimator center-crystal distance	
$H$	Camera height	
$T$	Collimator wall thickness	
$s$	Slit opening	
$\alpha$	Collimator angle	
$L$	Total beam-crystal distance	$d_1 + d_2$
$M$	Magnification factor	$d_2/d_1$
$d_c$	Crystal depth	
$w$	Crystal width	

Table 5.1: Definitions of camera parameters for the knife-edge camera

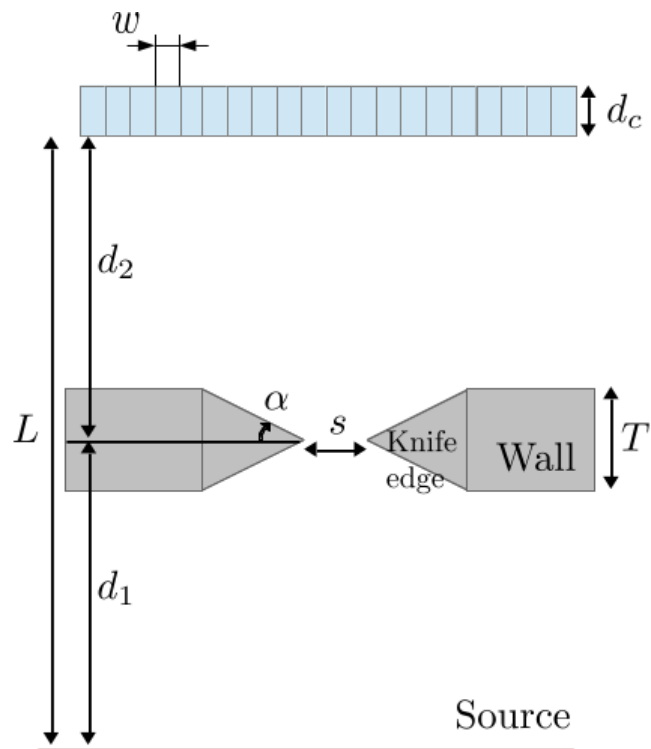


Figure 5.1: Parameters for the knife-edge slit camera

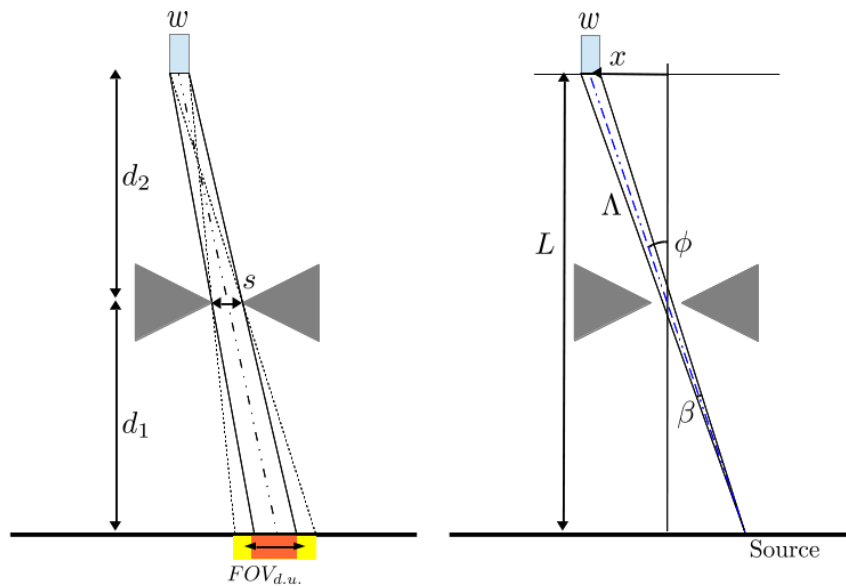


Figure 5.2: Illustration of the calculation of the detector unit field of view and the detector solid angle for the knife-edge slit camera

**Geometrical Considerations** The source field of view of a detector unit through the slit of a knife-edge camera is defined as the part that can be seen from every point on the crystal (orange in figure 5.2 on the facing page) plus half of the two penumbras (in yellow). Since both penumbras are the same size, this is equal to the central part plus one penumbra and a simple geometrical relation yields:

$$FOV_{d.u.} = s \left( 1 + \frac{d_1}{d_2} \right) = \frac{sL}{d_2} \quad (5.1)$$

As always, the FOV of a detector unit has a direct influence on the spatial resolution of the system. If a point source moves through the FOV, the signal on the detector unit is reduced to half exactly when the point source reaches the edge of the FOV, meaning that the size of the FOV is at the same time the FWHM of the PSF of the collimator. The terms FOV of a detector unit and spatial resolution of the collimator are thus interchangeable. Note that this is only true for a magnification factor of one and/or when using the projection of the profile into the source plane. All mentions of falloff width and spatial resolution in this text are understood to be in the source plane.

The total camera field of view is defined as the space that can be seen with the complete camera and is limited by the collimator angle:

$$FOV_{total} = \frac{2d_1}{\tan(\alpha)} + s \quad (5.2)$$

The solid angle under which a point of the source sees a crystal of the detector depends on the location of the point source, since the distance between source and crystal changes significantly over the field of view of the camera. We consider the solid angle for a point of the source that is within the central part of the field of view of the crystal at location  $x$  on the detector plane (the origin of the detector plane facing the center of the slit). Following the drawing in figure 5.2 on the preceding page, the flat angle  $\beta$  in the plane transversal to the slit with which a point source sees the crystal is (under small angle approximation):

$$\beta = \frac{w \cos(\phi)}{\Lambda} = \frac{wL}{\Lambda^2} \quad (5.3)$$

with  $\Lambda$  the distance between the source point and the crystal:

$$\Lambda^2 = L^2 + x^2 \left( 1 + \frac{d_1}{d_2} \right)^2 = L^2 \left( 1 + \frac{x^2}{d_2^2} \right) \quad (5.4)$$

The solid angle  $\Omega_D$  can then be expressed as:

$$\Omega_D = \frac{HwL}{\Lambda^3(x)} = \frac{wH}{L^2 \left( 1 + \frac{x^2}{d_2^2} \right)^{3/2}} \quad (5.5)$$

The collection efficiency of a single crystal through the slit can then be defined in analogy to section 4.1 on page 53 as

$$CE = FOV_{d.u.} \times \frac{\Omega_D}{4\pi} \quad (5.6)$$

$$\begin{aligned} &= \frac{sL}{d_2} \frac{1}{4\pi} \frac{wH}{L^2 \left( 1 + \frac{x^2}{d_2^2} \right)^{3/2}} \\ &= \frac{swH}{4\pi d_2 L} \frac{1}{\left( 1 + \frac{x^2}{d_2^2} \right)^{3/2}} \end{aligned} \quad (5.7)$$

The linear collection efficiency per unit length of detector can be obtained by dividing by the crystal width  $w$ :

$$LE = \frac{sH}{4\pi d_2 L} \frac{1}{\left( 1 + \frac{x^2}{d_2^2} \right)^{3/2}} \quad (5.8)$$

Both the crystal field of view and the linear efficiency can also be expressed in terms of magnification factor  $M = \frac{d_2}{d_1}$  and total distance instead of using the distances  $d_1$  and  $d_2$ :

$$FOV_{d.u.} = s \left( 1 + \frac{1}{M} \right) \quad (5.9)$$

$$LE = \frac{sH \left( 1 + \frac{1}{M} \right)}{4\pi L^2} \frac{1}{\left( 1 + \frac{x^2}{L^2} \left( 1 + \frac{1}{M} \right)^2 \right)^{3/2}} \quad (5.10)$$

and in case of a magnification factor of one, as proposed by [Smeets \[2012\]](#), it simplifies to:

$$FOV_{d.u.} = 2s \quad (5.11)$$

$$LE = \frac{sH}{2\pi L^2} \frac{1}{\left( 1 + 4 \frac{x^2}{L^2} \right)^{3/2}} \quad (5.12)$$

**Effective Slit Opening** At the particle energies that occur in prompt-gamma imaging, a non-negligible amount of particles will cross the collimator slit edges. This effect can be approximated by introducing an effective slit opening that can be used in the evaluation of the field of view and the efficiency in place of the geometrical slit opening. It is usually defined for a pinhole collimator as the diameter of an ideal pinhole that lets pass the same amount of particles as the real pinhole. Several analytical approximations can be found in literature for pinhole configurations, notably expressions proposed by ([Anger \[1967\]](#)), ([Paix \[1967\]](#)) and ([Metzler \[2005\]](#)). The first two have to be adapted if they are to be used for a knife-edge collimator instead of a pinhole collimator.

[Metzler \[2005\]](#) proposes a method to estimate the effective slit opening specifically to calculate the spatial resolution accurately. His expressions are based on one-dimensional cuts through the pinhole geometry and can be applied directly to a knife-edge geometry without modification. Their approach is for a point source and dependent on the location of the source within the FOV. For a source in the center, it simplifies to:

$$s_e = s + \frac{\ln 2}{\mu \tan(\alpha)} \quad (5.13)$$

with  $\mu$  the linear attenuation length of the radiation in the collimator material and  $\alpha$  the collimator angle defined above.

The effective slit width can be simply inserted into the equations (5.1) to (5.12) above instead of  $s$  to describe penetration effects. The effective collection efficiency then describes the efficiency including photons that crossed the edges of the collimator and the effective field of view includes effects of broadening by those same photons.

Since the attenuation length is dependent on the energy and we have a continuous energy spectrum, the model can only be an approximation. Fortunately, the attenuation length is nearly constant for the energies we are interested in, varying by less than 2% over the relevant energy window of 3-6 MeV (see the table of values in section 5.2.2 on page 95). It therefore suffices to take any value of  $\mu$  within the energy window. The attenuation coefficient for 4 MeV photons is used for all theoretical curves of the field of view in the rest of this chapter.

To predict the falloff width of the profiles, the initial falloff width of the emission profile described in section 2.2.2 on page 23 has to be included. The approximation is made that both combine as if they were Gaussian, that is:

$$\begin{aligned} FW &= \sqrt{FW_{emission}^2 + FOV_{d.u.,eff.}^2} \\ &= \sqrt{FW_{emission}^2 + \left( \left( s + \frac{\ln(2)}{\mu \tan(\alpha)} \right) \left( 1 + \frac{d_1}{d_2} \right) \right)^2} \end{aligned} \quad (5.14)$$

Figure 5.3 on the next page shows a Monte Carlo simulation of the proportions of particles detected after crossing the collimator wall, after crossing the tapered knife edge or passing

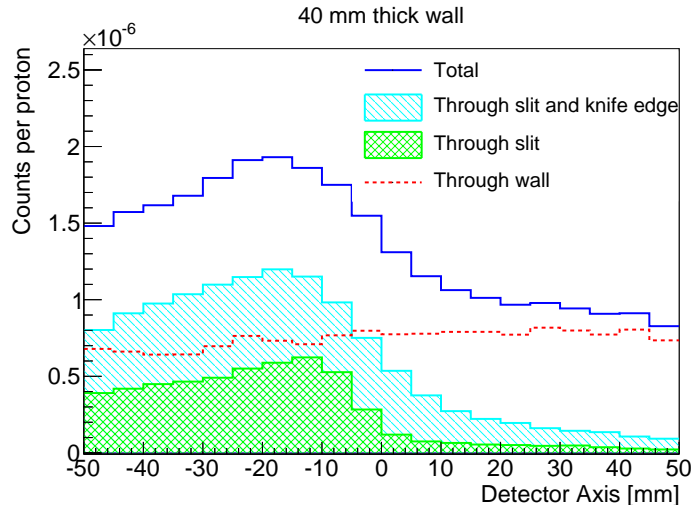


Figure 5.3: Proportion of particles passing through the collimator wall, through the slit edge and through the slit itself for the final knife-edge configuration (table 5.3 on page 96).

through the slit. The results for the final detector geometry are shown. Note that the counts through the knife edge show a correlated falloff, but with a larger falloff width. The combination of counts through the slit opening and through the collimator knife edge corresponds to the effective collection efficiency. The falloff width of just the counts that went through the slit corresponds to  $FOV_{d.u.}$ , each combined with the falloff width of the emission profile. The particles crossing the collimator wall have a nearly flat profile, with a slight increase towards positive values.

**Image distortion** Since particles have to travel a longer way to get to the edges of the image than the center, there is also some distortion of the image, or, in other words, the collection efficiency depends on the location of the source in the image (see equation (5.8) above). It would be theoretically possible to adjust for this distortion by either arranging the detector in a curved way or by increasing the crystal sizes towards the edges to compensate for the smaller solid angle. However, this effect does not seem to be crucial to the performance studied here, so the simplest possible option is chosen so as to not complicate the manufacturing of a prototype. In figure 5.4 on the following page is shown an example of the effect of distortion on a simulated profile.

**Expectations for the optimization** Several conclusions can be drawn from the geometrical considerations as to what can be expected of the influence of each parameter and we will reference the corresponding equations as the effects appear in the simulation study. It should be noted from the beginning that both the spatial resolution and the collection efficiency are proportional to the slit opening. When using the effective slit opening  $s_e$ , we can then expect the geometrical slit opening  $s$  and the collimator angle  $\alpha$  to have a major influence on the collection efficiency and spatial resolution. The collimator thickness  $T$ , meanwhile, does not appear in the equations. We expect it to influence mainly the background.

## 5.2 Monte Carlo simulation

### 5.2.1 Summary of the optimization study previously conducted by Smeets [2012]

An extensive simulation study using the Monte Carlo code MCNPX was undertaken by Smeets [2012] to optimize the knife-edge configuration for the application to protontherapy.

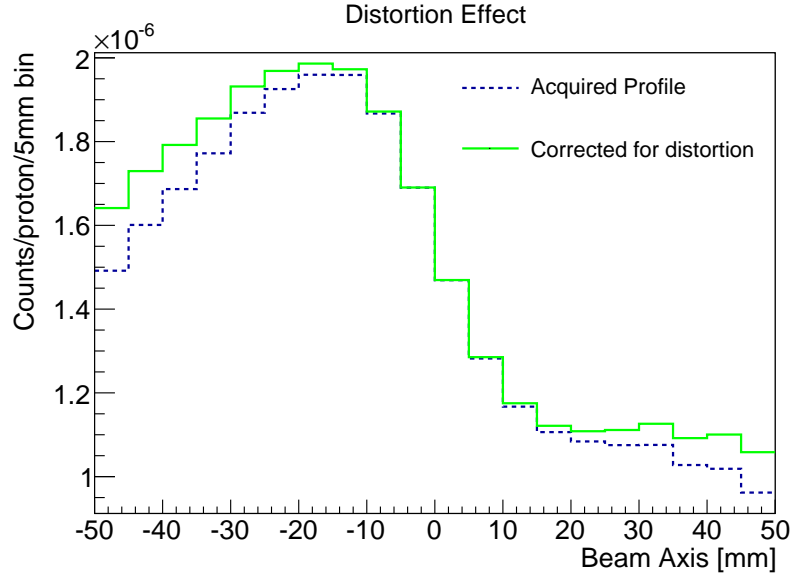


Figure 5.4: Distortion due to location-dependent solid angle on the example of a simulated knife-edge profile. Acquired distorted profile shown in blue, dashed, corrected profile in green. The correction factor is:  $\left(1 + 4\frac{x^2}{L^2}\right)^{3/2}$ .

The profiles were fitted with a three-line function and evaluated on the basis of the contrast, background and falloff width (called “PEAK”, “BASELINE” and “DELTA” resp. in [Smeets \[2012\]](#)). Optimal parameters were chosen on the basis of reasonable trade-offs between these figures of merit and using practical considerations such as collimator mass and expected count rates.

In order for the two camera systems to be comparable, the analysis described in chapter 3 was applied to the simulated profiles obtained by J. Smeets. The choice of parameters for the collimator configuration was evaluated in terms of contrast/noise ratio, FRP and falloff width.

## 5.2.2 Parameters chosen before simulation

Not all of the parameters of the knife-edge slit camera were re-examined. Some, such as the camera height and crystal depth, have easily predictable behaviour analogous to what was observed for the multi-parallel slit collimator in section 4.3.4 on page 72.

### The camera height

The camera height influences almost exclusively the number of counts that are acquired per delivered proton due to the increased solid angle. Increasing the height has the same effect as increasing the number of delivered protons by the same factor. This effect is the same as described in section 4.3.4 on page 72 for the multi-parallel slit collimator.

### The crystal properties

Crystal depth, like height, mostly affects the count rate per proton and the conclusions drawn in section 4.3.4 on page 72 (see also figure 4.20 on page 74) for the parallel-slit collimator apply.

This system was designed with a segmented crystal in mind and the width of segments is a possible parameter. Unlike the parallel-slit system, where matching each crystal with a slit imposes the segmentation, there is no default value for a knife-edge camera. From section 3.2.4 on page 47, we know that as long as the falloff width and total number of counts

Energy	Lead (11.4 g/cm <sup>3</sup> )		Tungsten (17.0 g/cm <sup>3</sup> )	
	$\mu$	$s_e$ for 63.4°	$\mu$	$s_e$ for 63.4°
3 MeV	0.048 mm <sup>-1</sup>	25.34 mm	0.069 mm <sup>-1</sup>	22.18 mm
4 MeV	0.048 mm <sup>-1</sup>	25.42 mm	0.068 mm <sup>-1</sup>	22.25 mm
5 MeV	0.049 mm <sup>-1</sup>	25.25 mm	0.070 mm <sup>-1</sup>	22.12 mm
6 MeV	0.050 mm <sup>-1</sup>	24.98 mm	0.071 mm <sup>-1</sup>	21.92 mm

Table 5.2: Attenuation length and effective slit opening for relevant photon energies for lead and tungsten calculated with equation (5.13). The geometrical slit opening is 6 mm.

are not impacted, the width of segments has practically no influence on the performance. The segments have to be small enough that the falloff is spread over several segments (ideally at least three or four). We also know from section 4.3.4 on page 72 on the multi-slit system, that segments that are too small lead to more inter-segment scattering, but that this is a minor effect. In conclusion, within the limits imposed by these effects, the size of segments can be chosen freely, knowing that considerations of detector electronics may influence the choice. Larger segments mean less channels, which is simpler and less expensive. On the other hand, if the count rate capability is a limitation, smaller segments may be advantageous.

### The collimator material

The collimator material has to have a high density and good attenuation. Typically, either tungsten or lead are used. Unlike the parallel-slit camera, where density is crucial to achieve low septal penetration while keeping the septa as thin as possible (to have high efficiency), one can compensate for lower density with a knife-edge camera by increasing the thickness. Note however, that the effective slit opening is increased for lower density material if the angle is kept the same, as can be seen in table 5.2. If the effective slit opening is to be conserved, the angle has to be adjusted, compromising the total camera field of view.

Another important difference between tungsten and lead is their different cross-section to neutrons. Lead is more transparent to neutrons, meaning more neutrons impinging on the detector, but at the same time less secondary photons from neutron reactions in the material. Smeets [2012]’s simulations indicate that passing from a 40 mm thick tungsten collimator to a lead collimator of equivalent thickness (60 mm), the total number of neutrons impinging directly on the detector is increased by 14%, while the number of photons impinging on the detector is reduced by 16% for a 160 MeV beam. These are photons that were produced by neutron reactions in the collimator. Smeets [2012] also shows that the two effects nearly cancel out in the final profile of the optimized configuration, so simulations do not indicate a clear choice for the collimator material. It is reasonable to use the higher-density material providing a better compromise between total camera FOV and effective slit opening.

### The distances

The distances of the system and their interplay with the other camera properties were not studied via Monte Carlo simulation. However, some theoretical observations are possible. From equations (5.1) and (5.8), it is interesting to note that if  $d_2$  is held constant, the  $FOV_{d.u.}$  diminishes for small  $d_1$  and the collection efficiency increases (due to  $L$  decreasing with  $d_1$ ). It is therefore clear that this distance has to be chosen as small as possible, to improve both the spatial resolution (as a direct consequence of the smaller  $FOV_{d.u.}$ ) and the contrast (due to better collection efficiency). The distance between the collimator and the detector  $d_2$ , on the other hand, leads to a trade-off between efficiency and spatial resolution.

These considerations, of course, leave aside the important effect of the background. It is reasonable to expect the background to be reduced significantly with distance, due to three effects:

Symbol	Parameter	Value
$d_1$	Patient-collimator distance	150 mm
$d_2$	Collimator-crystal distance	150 mm
	Collimator material	tungsten
$T$	Collimator wall thickness	40 mm
$s$	Slit opening	6 mm
$\alpha$	Collimator angle	63.4°
$d_c$	Crystal depth	10 mm
$w$	Crystal width	5 mm

Table 5.3: Default and final settings for the knife-edge collimator

- Particles that cross the collimator without interaction will see the detector under a reduced solid angle, leading to an effect  $\propto 1/L^2$
- Particles that interact in the collimator, with reaction products going towards the detector, will be affected by both the solid angle between target and collimator and between collimator and detector.
- the neutron emission is forward peaked, meaning that as the camera is moved farther from the target perpendicularly to the beam, less neutrons are emitted in its direction.

It is not entirely clear at this point how big the reduction in background is. Additionally, increasing the distance will not only decrease the background, but also the collection efficiency and thus the contrast. It is not clear whether the reduction in background could lead to improvements in the FRP enough to compensate for the loss in contrast. Simulations, or, ideally, measurement of the background are necessary to draw conclusions on this point.

### 5.2.3 Parameters varied through simulation

We show here the effect of the collimator parameters thickness, slit angle and slit opening, one by one, while keeping the others fixed to their final chosen values. MCNPX was used for the simulations. For all simulations, the used values, unless otherwise stated are described in table 5.3.

The simulations were conducted in a cylindrical setup where there is a camera ring all around the target in order to increase the solid angle and save simulation time. [Smeets \[2012\]](#) estimated that the difference between this kind of setup and a rectangular setup due to scattering effects is 8% after correction for the solid angle.

#### The collimator thickness

When considering the collimator thickness, it is interesting to note that, for a perfect collimator (all particles that touch the material are completely absorbed), the thickness has no influence on either the detector unit field of view (5.1), and thus on the spatial resolution and falloff width, or the collection efficiency (5.8). Therefore, the thickness only comes into play when there is a significant amount of particles penetrating the material. Those particles are uncollimated and contribute to the background, indicating that a thicker collimator is preferable from this point of view.

Figure 5.5 on the next page shows the evolution of profiles and maximum counts, background, contrast and contrast/noise ratio with regards to the collimator thickness. It can be observed that the background diminishes in an exponential fashion, as would be expected due to the increased attenuation. The apparent increase in contrast, however, is not so trivial to explain, as we would expect the correlated signal counts that passed through the slit opening to not be influenced by the thickness.

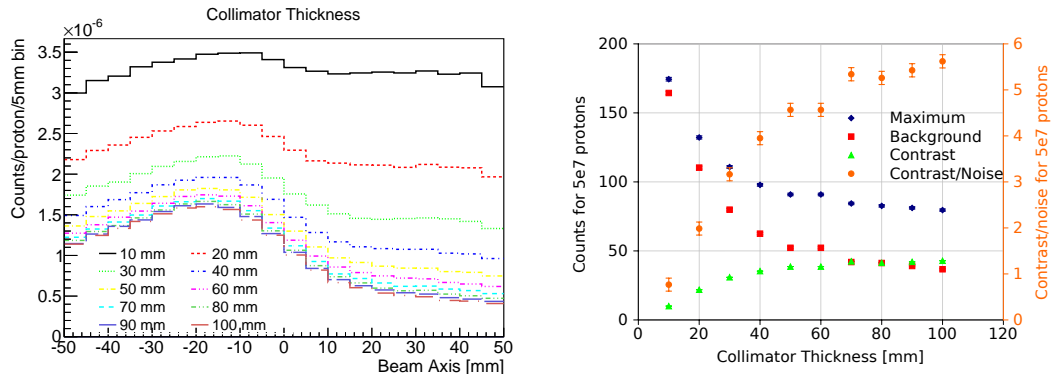


Figure 5.5: Left: Simulated profiles for different thicknesses of the knife-edge collimator. Right: Influence of the collimator thickness on maximum counts, background, contrast and contrast/noise ratio.

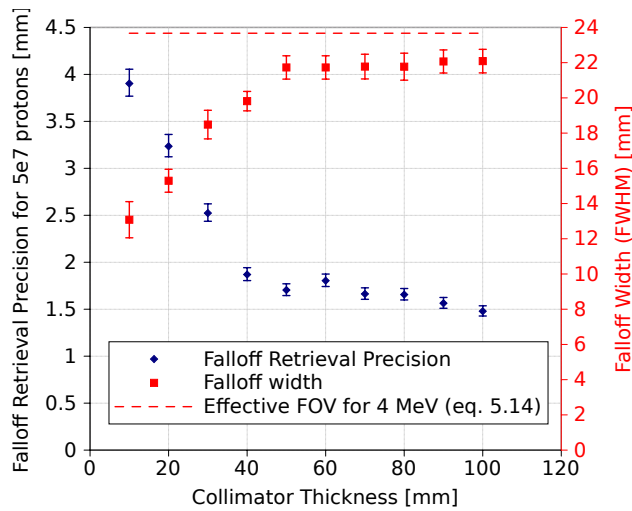


Figure 5.6: Influence of the collimator thickness on the FRP (blue, left axis) and falloff width (red, right axis). The effective falloff width given by equation (5.14) using the effective slit opening for 4 MeV photons is shown as a dashed line.

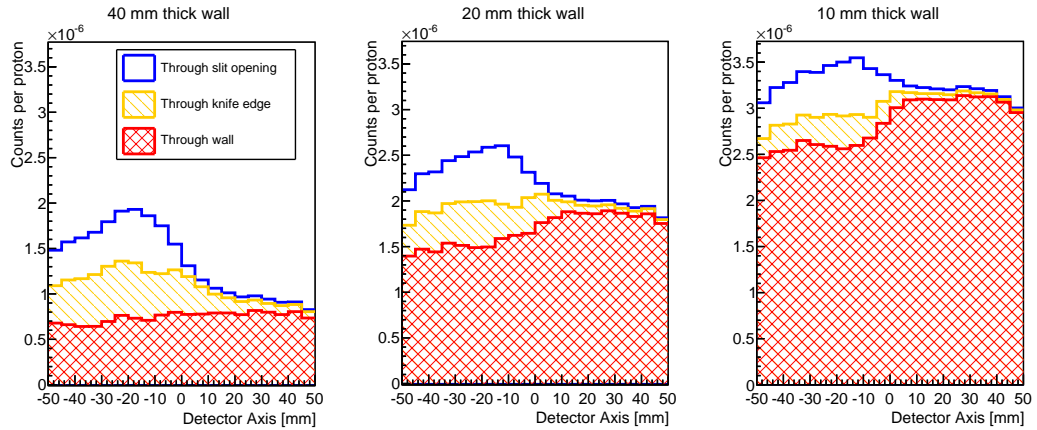


Figure 5.7: Profiles separated into contributions that came through the slit opening, through the knife edge and through the wall for three different values of the collimator thickness. For thin walls, the contribution through the collimator wall shows a correlation with the emission profile opposite to the image projected through the slit.

To explain this phenomenon, it is useful to look at the profiles separated into contributions that came through the slit opening, through the knife edge and through the wall, as in figure 5.7. The part corresponding to particles that came through the slit stays the same for different thicknesses, as expected. As to the particles that came through the wall, there are more for thinner collimators, as can be expected. For thin collimators we can additionally observe that this background contribution is not constant, but rather resembles a direct projection of the emission profile. This can be explained by the fact that the length of collimator material that particles have to cross to get through the wall depends on the incidence angle. Photons that impinge perpendicularly to the wall have the smallest distance to travel through the collimator wall and the highest probability to get through the wall. Parts of the detector that are facing the proton track will then receive more photons through the wall than parts of the detector that are far away. This leads to a sort of projection of the emission profile onto the detector. As this projection is opposite to the projected image through the slit, the two partially cancel out, which decreases the contrast. When comparing with the evolution of the profiles in figure 5.5 on the previous page on the left, it appears that the peak stays in the same place, while the transition from falloff to background changes with the thickness, as if the background was hiding the lower part of the falloff.

This effect of the background also has an influence on the observed falloff width. It appears as though the falloff width decreases for thin collimators, but this is really just another effect of the two opposing projections. For wall thicknesses above 40 mm, where the background is nearly flat, the falloff width is approximately constant and corresponds well to what is predicted by equation (5.14) (dashed line in the graph).

### The knife-edge angle

The collimator slit angle, like the collimator thickness, does not influence either spatial resolution or collection efficiency in the case of a perfect collimator. The main influence of the angle will be in the number of gamma that cross the slit edge. As seen in figure 5.3 on page 93, these are gamma that are correlated with the falloff, but have a larger falloff width. Correspondingly, in figure 5.8 on the next page, we can see that decreasing the angle (“sharper” knife edge) leads to a larger contrast as more correlated counts are accepted. The background counts are nearly stable (the observed dependency is due to the fact that the background is measured at  $2\sigma$  of the falloff, as described in section 4.3.2 on page 69, so that this value includes some correlated signal).

Figure 5.9 on page 100 shows that the increased contrast due to counts through the slit

edge leads to better FRP for smaller angles, while the falloff width increases due to the larger effective slit opening.

The angle also limits the total field of view of the camera. For the distance of 150 mm from the source used in these simulations, the respective fields of view are:

Angle	50.2°	56.3 °	63.4°	71.6°	80.5°
Total camera FOV	250 mm	200 mm	150 mm	100 mm	50 mm

All in all, the choice of the slit angle does not seem to be critical for the performance of the camera. Very large angles limit the field of view and lead to worse FRP, while very small angles lead to bad spatial resolution. The compromise of 63.4° proposed by J. Smeets appears adequate.

### The collimator slit opening

The slit opening is the one parameter that plays a role even for a perfect collimator. It goes linearly into both equation (5.1) and (5.8), so that we may expect both the contrast and the falloff width to depend linearly on the slit opening. This corresponds to an increasing proportion of photons that are transmitted through the slit opening and contribute to the correlated signal part.

As can be seen in figure 5.10 on the following page, the contrast does indeed increase approximately linearly with the slit opening, while the background stays stable. Looking at the FRP and the falloff width in figure 5.11 on page 101, as expected the FRP improves for larger slit opening, while the falloff width broadens. Both the expected falloff width of a perfect collimator and the falloff width estimated using the effective slit opening (5.14) are drawn in the figure and it appears that the effective slit opening describes the observed effect well, although it slightly overestimates the falloff width, especially for large slit openings.

In an analogous way to what was discussed in section 4.3.4 on page 77 regarding the pitch of the parallel-slit collimator, the slit opening can be used to adjust easily the trade-off between FRP and falloff width so that the camera can be modified according to the needs. One could even imagine a camera with an adjustable slit opening that can be chosen according to the best tradeoff for the specific treatment being imaged.

### 5.2.4 Conclusion

In summary, the effects of the collimator parameters on the performance of the system are well described by the geometrical considerations. None of the parameters have a true

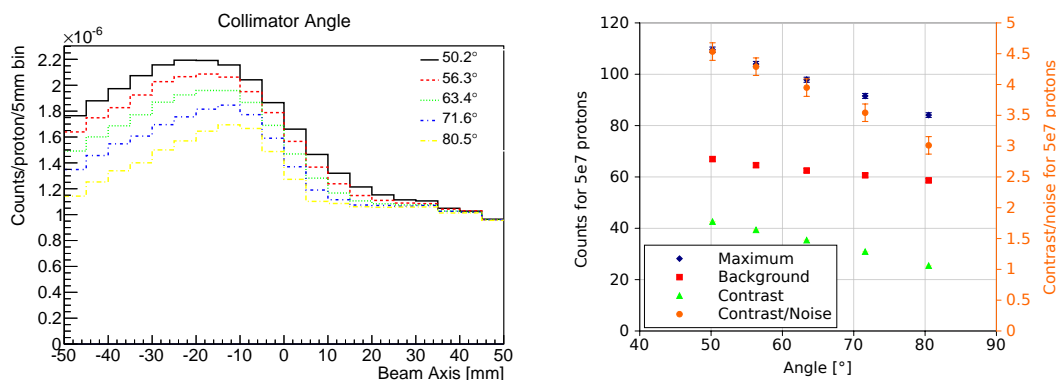


Figure 5.8: Left: Simulated profiles for different angles of the knife-edge collimator. Right: Influence of the collimator angle on maximum counts, background, contrast and contrast/noise ratio.

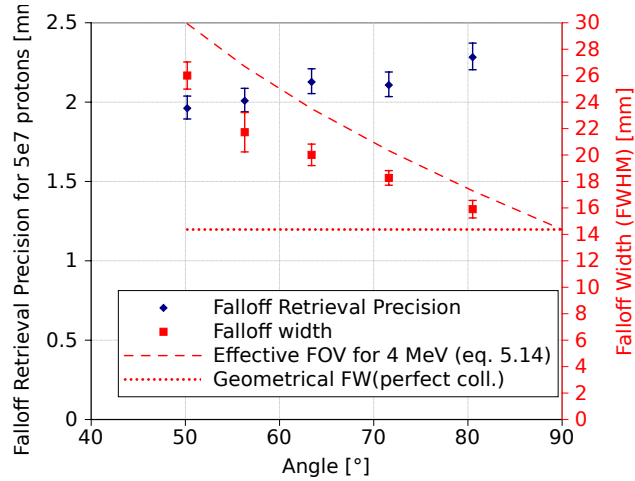


Figure 5.9: Influence of the collimator angle on the FRP (blue, left axis) and falloff width (red, right axis). The effective geometrical field of view using the effective slit opening for 4 MeV photons and adjusted for the emission falloff width as described in equation (5.14) is shown as a dashed line.

optimum of the FRP in the considered range, but rather monotonous tendencies. The choices are then determined by a trade-off between the FRP and the spatial resolution and/or by practical considerations. The slit opening and the angle present such trade-offs, with the FRP being best for large effective slit openings, while the reverse is true for the spatial resolution. For the thickness, in theory the FRP continues to improve indefinitely with the thickness, but mass and bulkiness limit what is practically feasible. The values proposed by Smeets [2012] all seem reasonable compromises in this light.

### 5.3 Experimental data

To validate the knife-edge slit configuration obtained through simulation, experiments were conducted on a proton beam at the Westdeutsche Protonentherapiezentrum Essen (WPE) in 2011 and 2012. A detailed description of the experiments can be found in Smeets et al. [2012] and Smeets [2012], chapter 5 and detailed descriptions of the detector used can be found in Peloso et al. [2010] and Perali et al. [2012]. The data used for the evaluation of the FRP

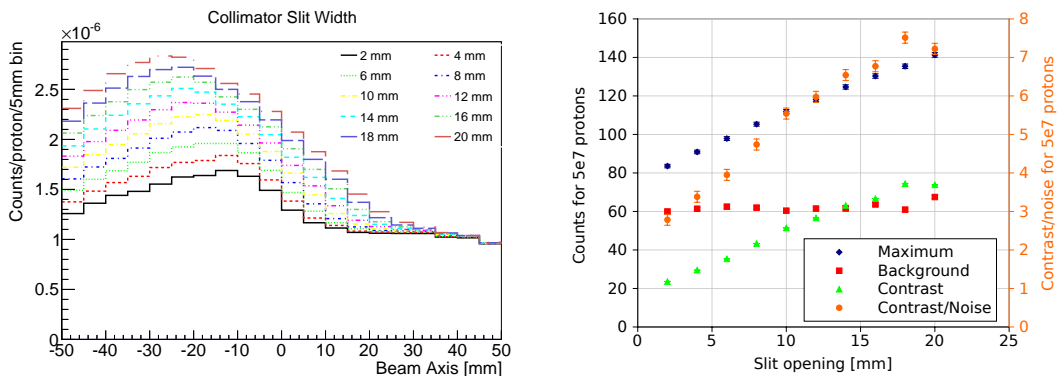


Figure 5.10: Left: Simulated profiles for different slit openings of the knife-edge collimator. Right: Influence of the collimator slit opening on maximum counts, background, contrast and contrast/noise ratio.

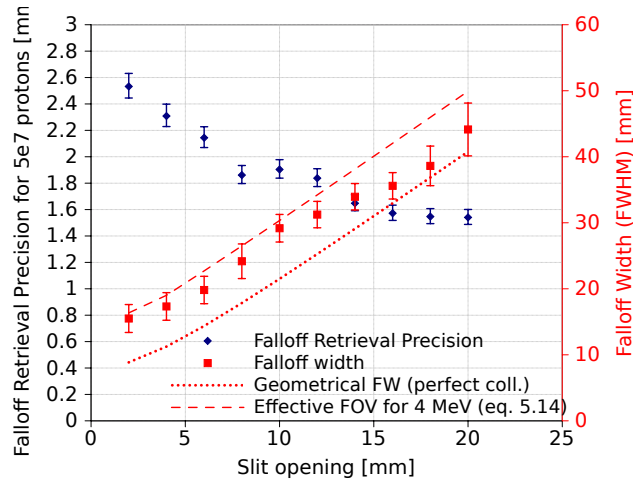


Figure 5.11: Influence of the collimator slit opening on the FRP (blue, left axis) and falloff width (red, right axis). The effective geometrical field of view using the effective slit opening for 4 MeV photons and adjusted for the emission falloff width as described in equation (5.14) is shown as a dashed line.

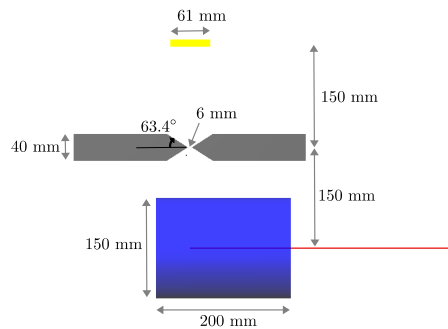
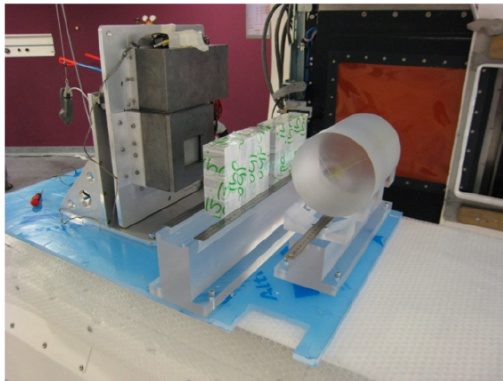


Figure 5.12: Photograph of the setup of experiments with the knife-edge slit prototype and sketch as seen from above.

were obtained in March 2012, and described in Smeets [2012], section 5.7. Compared to the measurements made in 2011 and used in Smeets et al. [2012], these acquisitions benefit from improved beam stability during measurement, while the setup and data processing remain the same.

We will only briefly recall the used setup and data processing procedures in the following pages.

### 5.3.1 Experimental setup and data processing

The setup of the knife-edge slit experiment corresponds to the final optimized setup obtained by simulations, with the caveat that the detector used was smaller and used a monolithic crystal with Anger logic instead of a segmented crystal. Figure 5.12 shows a photograph of the setup. The nozzle can be seen in the background behind the PMMA target. The collimator is wrapped in white and green tape and the camera is encased in a lead box to shield it from ambient radiation. The small window in the lead box corresponds to the surface of the detector. On the right is shown a sketch of the view from above with the dimensions of the setup. Since the detector was smaller than in simulations, the collimator

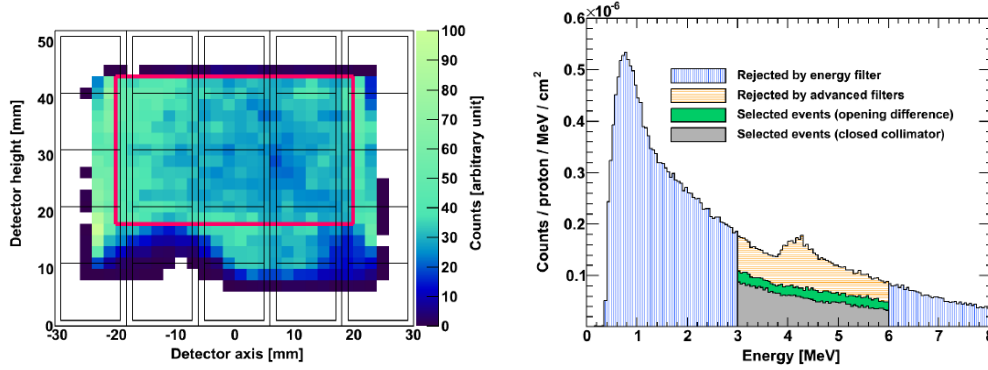


Figure 5.13: 2D view of the image obtained with the HiCam (left) and measured spectrum (right). The advanced filters correspond to the saturation, basic, zeta and pile-up filters.

blocks were only 160 mm high, since this is sufficient to completely shield the detector from the target.

In addition to the measurements with the optimized geometry, measurements were also done with a completely closed collimator wall by joining the right-angled faces of the collimator blocks. This allows making a measurement of only the background, which can be useful for comparison with simulations.

Contrary to simulations, the detector used a monolithic, 10 mm thick LYSO crystal, with resulting scintillation light collected by silicon drift detectors (SDD) and using a center of gravity method to obtain the image. The area of the detector was only 54 mm  $\times$  61.5 mm, so that the height and field of view were reduced. To obtain complete profiles, three separate acquisitions were made with the camera in three positions (offset by  $\pm 40$  mm), the acquisitions were then combined into a single profile. Due to the failure of one SDD at the time of measurement, an area of the detector was dead and the area used had to be further restricted to just 26 mm  $\times$  40 mm. The used area is represented by the red rectangle in figure 5.13 on the left.

Beam energies of 100 MeV, 160 MeV and 230 MeV were tested to get an idea of the energy dependence. For each beam energy, the collimator slit and camera were centered facing the expected range in the target. The number of protons was recorded by a large parallel-plate ionization chamber intercepting the beam in the nozzle. Since the camera could not function with the high count rates that occur at clinical beam currents, the beam current was lowered down to the order of 10 pA for 230 MeV, two orders of magnitude below the maximum current used for treatment.

To get usable profiles, several corrections and filters had to be applied to the data. Most of them have to do with the Anger logic necessary to reconstruct the image. Again, a detailed description can be found elsewhere, we will just list the main principles:

- Saturation filter: Events are discarded if one SDD reaches the ADC dynamic range limit.
- “Basic” and “Zeta” filters: when the great majority of the collected charge is distributed on a small number of SDDs, the center of gravity reconstruction is considered to be inaccurate and the event is rejected.
- Pile-up filter: events are discarded when the charge distribution appears as if there were two separate locations of energy deposit.

To compensate for the events discarded by the filters, a correction factor is applied to the remaining events. To adjust for the dead time of the electronics, a correction factor of 1.37 was also applied.

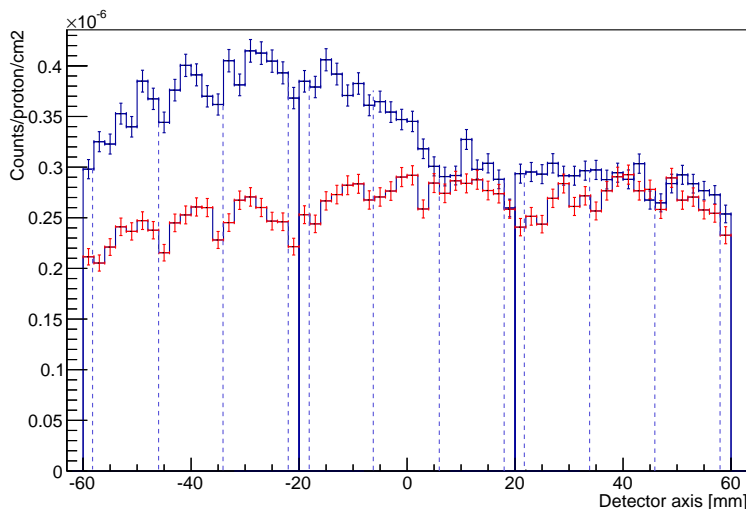


Figure 5.14: Acquired profiles for a 160 MeV beam with both an opened and closed collimator after the uniformity correction. Superposed as solid vertical lines are the edges of the camera, where the acquisitions from the three different camera positions are joined. Superposed as dashed vertical lines are the edges of the SDDs. The statistical errors on each bin are also shown.

Beam energy	100 MeV	160 MeV	230 MeV
x-offset [mm]	1.33	4.01	0.01
factor	1.00	1.10	1.16
y-offset [counts/p/cm <sup>2</sup> ]	0.07E-6	0.17E-6	0.26E-6

Table 5.4: Values of matching between the NURBS fit of the simulated profiles and the measured profiles.

As the response of the detector was not completely uniform in space, a uniformity correction had to be made. For this purpose, both a “flood” acquisition without collimator and an acquisition with a closed collimator wall were made, on the principle that those images are expected to lead to nearly flat profiles, where any non-uniformity could be easily identified and correction factors for each pixel generated. Figure 5.14 shows the profiles for a 160 MeV beam with both an opened and closed collimator after the uniformity correction. Superposed as solid vertical lines are the edges of the camera, where the acquisitions from the three different camera positions are joined. Superposed as dashed vertical lines are the edges of the SDDs. Even though the profile has been corrected for uniformity, a significant and systematic decrease in counts at the camera edges and the SDD edges is still visible, indicating that the uniformity correction that was applied is not sufficient. Usable profiles can be obtained by using larger bins and/or by smoothing algorithms (only the former is used in the subsequent analysis).

In figure 5.13 on the preceding page on the right can be seen the energy spectrum corresponding to counts within the useful field of view. Note that the peaks observed in the simulated spectra are not visible due to the insufficient energy resolution of the camera. The bump visible just over 4 MeV is in fact an effect of saturation of electronics and is eliminated by applying the filters listed above.

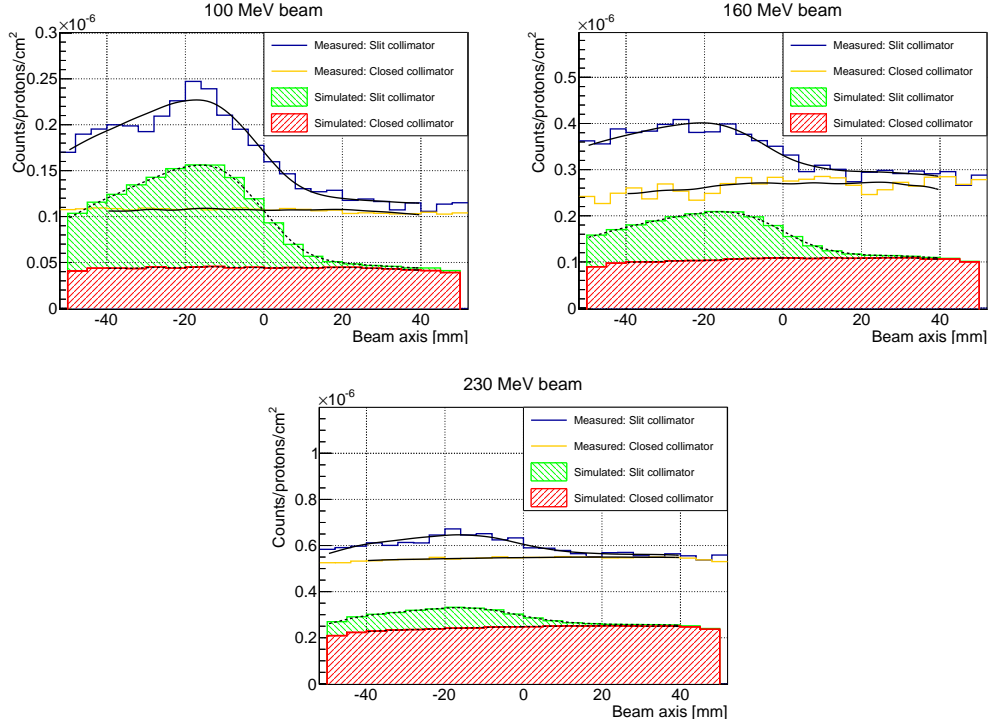


Figure 5.15: Comparison of the profiles measured with HiCam for 100 MeV, 160 MeV and 230 MeV beams with the profiles predicted by simulation. Superposed as black dashed lines are NURBS fits of the simulated profiles and as black solid lines the same NURBS fits adjusted with a factor and x- and y-offsets to the measured profiles.

### 5.3.2 Comparison to simulation

In figure 5.15 are shown the measured profiles for beam energies of 100 MeV, 160 MeV and 230 MeV with both open and closed collimator. The profiles are shown in units of counts/proton/cm<sup>2</sup> to eliminate the influence of the different solid angle. The measured profiles shown have far more counts than the simulated profiles. To investigate the origin of the additional counts, the NURBS fits  $f$  of the simulated profiles of the open collimator were adjusted to match the measurements by applying an x-offset  $o_x$ , a y-offset  $o_y$  and a multiplication factor  $m$  as follows:  $f_{adj}(x) = m \times f(x + o_x) + o_y$ . The values obtained can be found in table 5.4. Note first of all that after the adjustments, the shape of the profiles matches extremely well, indicating that the overall shape and the falloff width were predicted very accurately by the simulations. The x-offset is most likely due to mispositioning of the target during the experiment.

One difference between the simulated configuration and the camera used during measurement is the different scoring system used. For the simulations, each crystal segment was considered separately. A particle that scatters in the detector and deposits energy in two different crystals would be considered as two separate hits that have to clear the energy threshold individually. In the setup during experiment, since a monocrystal with center-of-gravity reconstruction was used instead, those scatter events are treated as a single hit of the detector. Simulations were conducted comparing the total number of hits within the energy window in a segmented configuration to the number of hits in the energy window for a monocrystal. The results can be found tabulated in Smeets [2012] in table 6.17 on page 130. The expected additional counts are 10%, 8% and 4% for 100 MeV, 160 MeV and 230 MeV beams respectively, making it unlikely that this is the origin of the observed factor, as it is an effect that should decrease with the beam energy rather than increase. Another possible source of error that could lead to a factor is a systematic error on the calibration of the

ionization chamber measuring the number of protons. The energy calibration of the detector is also a possible source of systematic errors. To give an idea of the order of magnitude of such an effect, simulations indicate that lowering the energy thresholds by 10% can lead to an increase of the contrast by 8% and an increase of the background by 17%, which could contribute to the factor, but is not sufficient to explain the y-offset.

We currently do not know to what the observed y-offset is due. We can observe the same effect for both the open- and closed-collimator profiles, indicating that the simulations significantly underestimate the closed collimator contribution (i.e. the background), while much more accurately estimating what passes through the slit and thus the contrast. The natural radioactivity of the LYSO scintillator is well below the threshold and not active enough to lead to enough pile-up to be significant. The y-offset increases with the energy, just as the closed collimator contribution also increases with the energy. This is coherent with what was observed during a spectrometry measurement using an NaI detector described in [Smeets et al. \[2012\]](#), where signal coming through a closed wall of shielding was significantly underestimated by simulation with MCNPX, while the difference between a wall with an opening and the closed wall was accurately predicted. Interestingly, however, new measurements with a new knife-edge prototype (see section 6.5) do not seem to show such large discrepancies with simulations. The cause for the discrepancies with the HiCam measurements is still not clear. Further measurements with the dedicated prototype with different configurations of shielding may shed some light on this matter.

## 5.4 Obtainable performances

The parameters chosen for an optimal configuration are given in table 5.3 on page 96.

It should be noted that these values were not chosen because they represent an optimum of the FRP (no such optimum exist within the studied ranges of the parameters), but rather reasonable seeming trade-offs between the three factors of merit FRP, falloff width and total camera FOV.

The performance of the system in terms of FRP is shown in figure 5.16. Shown in blue is the performance obtained with simulated profiles, in orange that of the measured profiles. The latter have been corrected for the reduced camera size. As was the case for the profiles obtained with the multi-slit configuration, the FRP is anti-proportional to the square root of the number of protons for both simulated and measured profiles. The difference between the two is due to the increased background observed during measurement.

After considering feedback from clinicians, it seems unlikely that the camera could be as close as 150 mm to the beam in all treatment cases. A distance of at least 200 mm between the beam and the front of the collimator seems more feasible. To this end, a prototype with  $d_1 = 220$  mm and  $d_2 = 176$  mm is being considered. The magnification factor is reduced in an effort to keep the total distance between beam and detector, and thus the collection efficiency, high. The performances of both setups will be compared to the multi-parallel slit collimator in the next chapter.

**Mass of the system** With a thickness of 40 mm and a height of 200 mm and using the density of pure tungsten of  $19 \text{ g/cm}^3$ , the collimator wall would weigh 1.5 kg/cm ( $1.4 \text{ kg/cm}$  if using a tungsten alloy density of  $17 \text{ g/cm}^3$ ). What this means for the total mass of the camera depends on the way the collimator walls are configured. If straight walls are used as in the simulations, the total wall length needed to shield the detector at the maximum beam energy of 230 MeV will be around 300 mm, leading to a total mass of 45.6 kg.

On the other hand, it is possible to use bent or angled walls, as shown, for example, by [Bom et al. \[2012\]](#). This would have the advantage that photons from the target would impinge on the wall at greater angles with regards to the surface normal of the wall, so that the same attenuation can be achieved with a thinner wall. Figure 5.17 on page 107 shows a classic straight configuration in gray and an angled wall configuration hatched. Straight lines drawn from the entrance of the target give an idea of the necessary wall length and the angles of incidence. For a conservative estimate of the possible reduction in wall thickness

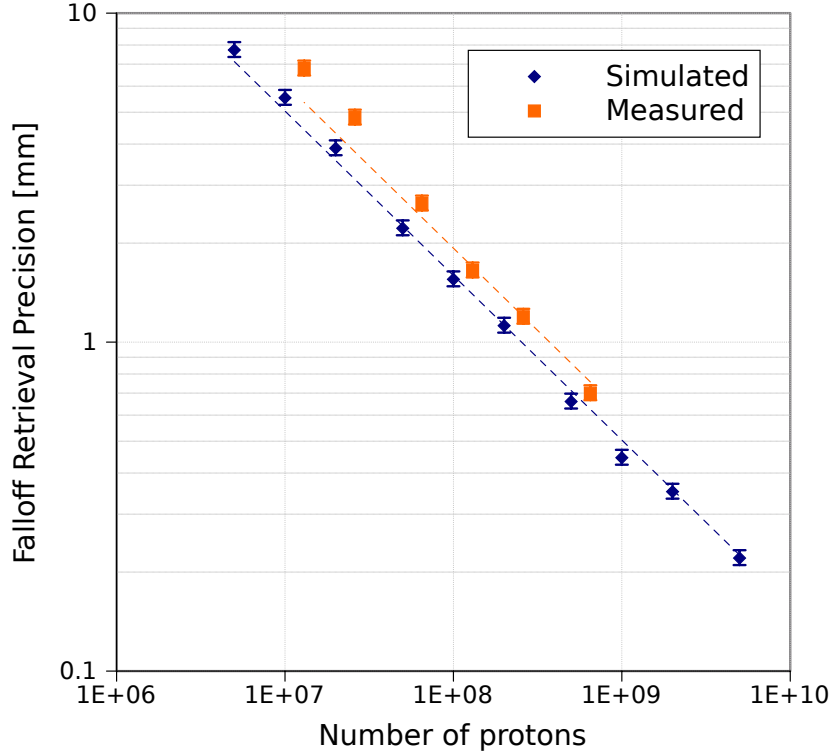


Figure 5.16: Achieved falloff precision vs. number of protons for the knife-edge slit camera for the simulated and measured profiles for a 160 MeV beam. The measured data was corrected for the smaller solid angle by plotting points at the equivalent number of protons in the reference geometry.

that becomes possible in this way, we can impose that the minimum thickness of collimator material that a particle must cross from anywhere along the proton path to anywhere on the detector must at least be 40 mm. In the case illustrated in figure 5.17, this corresponds to the dotted line and allows a reduction by 20% in the thickness of the angled wall part. Since the large majority of photons impinge with significantly larger angles, it is likely that a reduction by 50% or even more is possible without detrimental effects on the profile, although this should be verified by Monte Carlo simulation.

For a best guess at the minimum realistic mass, we can take a configuration in which only the side facing the nozzle (“proximal wall”) is angled (the other side needs less shielding, so it is not clear whether an angled wall is advantageous). The distal wall would be straight, 100 mm long and weigh 15 kg. The proximal wall could be angled after about 50 mm and the thickness of the angled part be reduced to 20 mm, leading to a mass of 21 kg. The total mass of the collimator in this case is 36 kg, a reduction of almost 10 kg compared to the simple straight-wall approach. Since the geometry shown is a 5:4 projection, only 80 mm of crystal would be needed, leading to a mass in LYSO crystals of 3.7 kg.

#### 5.4.1 Dependence of the performance on energy

FRP can be expressed in the form  $FRP = C(E)/\sqrt{N}$  with  $N$  being the number of protons and  $C(E)$  a coefficient depending on the camera configuration and the beam energy. In figure 5.18 on the facing page, we can see plotted the FRP for different energies. The values were obtained via simulated profiles using the optimized configuration of the camera. It is then possible to obtain a value for  $C(E)$  by fitting. The results for three beam energies are shown on the right. It is clear that the performance worsens significantly with energy, though it is not possible to determine the form of dependence from just three points.

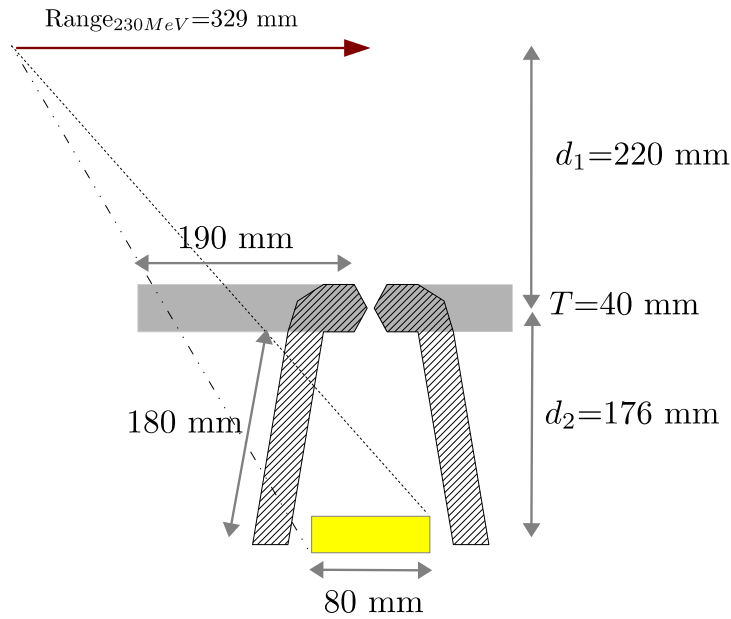


Figure 5.17: Possible realistic geometries of the knife-edge collimator. The classic straight configuration is shown in gray, while a possible angled wall configuration is shown hatched. Straight lines from the entrance of the target show how far the shielding must go and give an idea of the minimal angle of incidence of particles on the shielding.

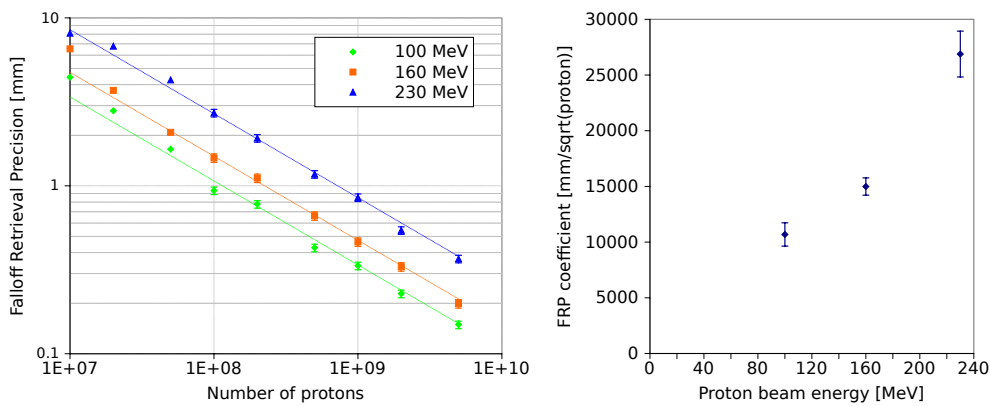


Figure 5.18: Performance of the knife-edge system for different energies (left) and energy-dependent performance for  $1 \times 10^8$  protons (right).



## Chapter 6

# Comparison of the knife-edge and multi-parallel-slit cameras

After having established common criteria for performance evaluation and general guidelines for the optimization in chapter 3, those same guidelines and performance criteria were applied to optimize both the parallel-slit and knife-edge slit collimators in chapters 4 and 5 respectively. This chapter aims at summarizing what we have learned about both geometries and systematically comparing their properties and performances. As the optimizations were conducted for homogeneous targets and it is not yet clear whether adjustments may be necessary for heterogeneous targets, we also focus on the range of achievable performances for each camera type and their limitations. Finally, a set of measurements conducted using the same detector in exactly the same experimental conditions with both a knife-edge and a multi-parallel-slit collimator are presented.

### 6.1 General remarks on geometry

First, let us consider the purely geometrical properties of the collimators. The equations detailed for each collimator type in sections 4.1 on page 53 and 5.1 on page 91 respectively are summarized in table 6.1.

There is an obvious symmetry between the properties of the detectors. The equations for the detector unit FOV are the same, with the collimator-detector distance  $d_2$  of the knife-edge collimator taking the place of the collimator depth of the multi-slit design. The collection efficiency is also expressed nearly the same way and can be separated into a common factor and a collimator specific factor. The collimator specific factor for the parallel-slit design

	Multi-parallel slit	Knife-edge
Effective slit width ( $s_e$ )	$s$	$\left(s + \frac{\ln(2)}{\mu \tan(\alpha)}\right)$
Det. unit FOV	$s \left(1 + \frac{d_1}{D}\right)$	$s_e \left(1 + \frac{d_1}{d_2}\right)$
Lin. collection efficiency	$\frac{Hs}{4\pi LD}(1 - f)$	$\frac{Hs_e}{4\pi Ld_2} (1 + x^2/d_2^2)^{-3/2}$
Effective thickness ( $T_e$ )	$Df$	$T$

Table 6.1: Table of equations characterizing the properties of the collimators. With  $s$ : slit width,  $H$ : height,  $d_1$ : distance source-collimator,  $d_2$ : distance collimator-detector,  $L$ : total distance between source and detector,  $D$ : depth of collimator (parallel slit),  $f$ : fill factor (parallel slit),  $\alpha$ : angle of the knife-edge slit collimator edge,  $x$ : coordinate on detector plane (knife-edge),  $\mu$ : attenuation length in tungsten.

depends on the fill factor, while the knife-edge slit camera has a source-location dependent factor. It is very interesting to note that for an ideal collimator with infinitely thin septa, and neglecting the location dependence for the knife-edge design, both give exactly the same result for both detector unit FOV (and hence spatial resolution) and linear collection efficiency if the collimator-detector distance  $d_2$  of the knife-edge slit camera and the collimator depth  $D$  of the parallel-slit camera are chosen equal.

Consequently, the difference between both designs is due to the ways in which an imperfect collimator with finite septa and wall thickness influences the result. Let us look, one by one, at the effects of implementing a realistic collimator as opposed to a perfect collimator:

**Finite septa for the parallel-slit collimator** The thickness of septa of the parallel-slit collimator directly impacts the linear collection efficiency by the factor  $(1 - f)$ , limiting the contrast of the profile. For a realistic collimator, there is also a certain amount of septal penetration. Unlike what can be observed for the knife-edge slit camera, the septal penetration has little effect on the spatial resolution of the parallel-slit camera for the configurations studied in chapter 4, as evidenced by the fact that the falloff width observed by Monte Carlo simulation is well predicted by the theoretical calculation of the FOV without any correction for septal penetration (see for example figures 4.29 on page 80 and 4.32 on page 81). There is no need to introduce an effective slit width or effective FOV as was done for the knife-edge geometry. However, there is a significant contribution of photons crossing the collimator that contribute to the background. On average, the thickness of tungsten that a straight path through the collimator crosses is determined by the ratio of the volume of tungsten to the total volume of the collimator. We have introduced in section 4.3.5 on page 84 an effective thickness of the collimator,  $T_e = fD$ , which is the thickness of an equivalent solid block of tungsten. This effective thickness is the determining parameter for both the penetration of photons through the collimator and the interaction of neutrons with the collimator (described in section 6.2 on the next page).

The optimal choice of the fill factor is described in section 4.3.4 on page 80 and does indeed represent a tradeoff between unacceptable septal penetration for thin septa and low contrast for thick septa.

In some cases, the septa can also cause a dependency on the relative position of the falloff and the septa, due to shadows of the septa. As shown in section 3.2.4 on page 48, this is only the case when the detector unit field of view is smaller than the pitch, or in other words for

$$FOV_{d.u.} < p \quad (6.1)$$

$$p(1 - f) \left( 1 + \frac{d_1}{D} \right) < p \quad (6.2)$$

$$f > d_1 / (D + d_1) \quad (6.3)$$

The periodic pattern can then be avoided by choosing  $f$  appropriately.

**Thickness of the knife-edge collimator wall** As discussed earlier in section 5.2.3 on page 96, the collimator thickness has no influence on the spatial resolution or collection efficiency per se. It does, however, have a significant influence on the amount of background. Both the penetration of photons through the collimator and the interaction of neutrons with the collimator are determined by the thickness almost exclusively.

**Angle of the knife-edge collimator** The choice of the angle of a knife-edge collimator, described in section 5.2.3 on page 98, has two consequences. It limits the total camera field of view and it determines the amount of penetration through the knife edges. Penetration through the knife edges, as opposed to penetration through the collimator wall or the septa of the parallel-slit collimator, does contribute to the contrast. Compared to a perfect collimator, this contributes to an increase in collection efficiency (and thus contrast) and in a larger falloff width. Both of these effects have been described in

section 5.1 on page 91 by introducing an effective slit opening. Using the effective slit opening in the calculation of the detector unit FOV and collection efficiency leads to an effective detector unit FOV and effective collection efficiency. It is interesting to note that due to the effective slit opening, even if the collimator is completely closed, the collection efficiency and detector unit FOV do not go to zero. This limits the spatial resolution achievable for a given total camera FOV.

To illustrate the effects, figure 6.1 shows both camera concepts with perfectly thin septa/walls and in a realistic configuration. Three examples of detector unit fields of view are drawn for each of the configurations. Within the target is drawn the distribution of prompt-gamma emission points. As the septa width increases (the pitch is held constant), the field of view of each slit decreases as well as the collection efficiency. For the knife-edge slit collimator, using finite walls does not change the field of view or collection efficiency of each detector unit. However, the total camera field of view (shown in red) is decreased and the camera can no longer see, for example, the entrance of the target.

## 6.2 Background

Excluding background due to the room environment, the background can essentially be decomposed into three contributions: prompt gamma that crossed the collimator septa or wall; neutrons that went through the collimator and particles that are scattered or react producing secondaries within the collimator. The first depends on the attenuation provided by the collimator, which in turn depends on the (effective) thickness. The direct neutron counts depend on the solid angle under which the neutrons “see” the detector, the position of the detector with regards to the forward peaked neutron emission and the amount of collimator material. And the last depends on the solid angle of the collimator, the amount of collimator material (i.e.  $T_{(e)}$ ), the self attenuation of the collimator (again,  $T_{(e)}$ ) and lastly the solid angle of the detector from the collimator.

While more simulations and especially experimental data are needed to make quantitative statements about the background, qualitative comparative statements between the two camera geometries are possible.

One advantage of the knife-edge geometry is that the thickness  $T$  does not influence any other properties of the collimator and can be chosen freely to minimize the background. Meanwhile, the effective thickness of the parallel-slit collimator,  $T_e = Df$  is conditioned by the depth and fill factor, which also impact the collection efficiency and detector unit FOV, so that it cannot be chosen freely without impacting those other parameters. Concretely, trying to decrease the prompt-gamma part of the background by increasing the depth or fill factor will necessarily also decrease the contrast.

## 6.3 Spatial resolution

The spatial resolution of the system is potentially important to be able to distinguish fluctuations due to inhomogeneities. When trying to achieve very good spatial resolution (i.e. a very small detector unit FOV), the parallel-slit camera has the clear advantage. Indeed, the spatial resolution can be reduced to any desired small value by, for example, choosing a very small pitch. This will, of course, impact the collection efficiency and thus the contrast and FRP as can be deduced from the equations in table 6.1 on page 109. Roughly, reducing the pitch by a factor of two will reduce the falloff width by a factor of two and also reduce the contrast by a factor of two.

For the knife-edge slit camera, improving the spatial resolution is not as trivial. Looking at the equation for the effective detector FOV in table 6.1 on page 109, there are three possibilities to get a smaller detector unit FOV:

- Changing the magnification factor  $d_2/d_1$ . Assuming that the distance  $d_1$  is determined by practical limits (such as the body of the patient), the distance  $d_2$  would have to



$\alpha$	d.u. FOV		total FOV	
	$s = 6$ mm	$s = 0$ mm	$d_1 = 150$ mm	$d_1 = 220$ mm
50.2	28.9 mm	16.9 mm	250 mm	367 mm
56.3	25.5 mm	13.5 mm	200 mm	293 mm
63.4	22.1 mm	10.1 mm	150 mm	220 mm
71.6	18.7 mm	6.7 mm	100 mm	146 mm
80.5	15.4 mm	3.4 mm	50 mm	74 mm

Table 6.2: Detector unit fields of view for different choices of the collimator angle  $\alpha$  and slit opening  $s$  with the resulting total camera FOV (at 150 mm and 200 mm distance). The detector unit FOV for  $s = 0$  mm corresponds to the best achievable spatial resolution for the angle assuming a magnification factor of one.

be increased, leading to a significant loss in collection efficiency. Additionally, we can see from the equation for the detector unit FOV ( $s_e (1 + d_1/d_2)$ ), that no matter the choice of  $d_1$  and  $d_2$ , the detector unit FOV can never be smaller than the effective slit opening  $s_e$ , limiting the gain achievable in this way.

- Reducing the geometrical slit opening. This is fairly straightforward, but limited. When using a collimator with an angle of  $63^\circ$  and closing the collimator completely, the effective field of view is still 10 mm. To go below this value, there is only one last option:
- Increasing the collimator angle. Once the collimator is completely closed ( $s = 0$ ), the effective slit opening and thus the effective detector unit FOV scales with  $1/\tan \alpha$ . Note that since the collection efficiency also scales in the same way, improving the spatial resolution by a factor of two also reduces the collection efficiency by a factor of two.

Additionally, increasing the angle has an impact on the total camera FOV. The impact of the angle on both the detector unit FOV and total camera FOV is listed in table 6.2. Assuming that there is a hard limit to the size of the total FOV that one does not want to go below (because a certain region of the tumor has to be within it, for example), improving the spatial resolution further becomes very difficult. If the detector unit FOV is to be decreased while maintaining the total camera FOV, the only option is to increase the distances at the same time. Once the collimator is completely closed, to decrease the detector unit FOV further by a factor of two while keeping the total camera FOV,  $s_e$  has to be divided by two, and  $d_1$ ,  $d_2$  and  $L$  multiplied by two (see equation (5.2)). From the equation for the collection efficiency  $\frac{Hs_e}{4\pi Ld_2} (1 + x^2/d_2^2)^{-3/2}$ , it follows that this leads to a total decrease in collection efficiency by a factor of eight at the center of the camera FOV. In other words, instead of having a 1:1 tradeoff between spatial resolution and efficiency, the tradeoff becomes a much less favorable  $n:n^3$

This introduces a practical lower limit of the spatial resolution for the knife-edge camera. For the moment, it seems likely that what can be achieved is sufficient. For retrieving the falloff, it seems unlikely that a spatial resolution smaller than the falloff width of the emission profile should prove to be necessary. A very good spatial resolution could be useful to see, for example, abrupt changes in density.

## 6.4 Range retrieval performance

In sections 4.3.5 and 5.4, we looked at the FRP achievable with each of the optimized configurations. However, since the trade-off decision between FRP and falloff width taken was not the same in both cases, it is misleading to compare the FRP of the optimized

Multi-parallel slit collimator configurations						
$p$ [mm]	$f$ [mm]	$D$ [mm]	$d_1$ [mm]	$d_2$ [mm]	FW [mm]	FRP [mm]
2					5.96	7.71
4					11.73	3.96
6					14.47	2.96
8					21.06	2.40
12	0.35	70	200	0	26.00	2.01
16					38.48	1.85
20					44.25	1.76
24					52.24	1.67
30					51.59	1.47

Knife-edge collimator configurations						
$s$ [mm]	$\alpha$ [°]	$T$ [mm]	$d_1$ [mm]	$d_2$ [mm]	FW [mm]	FRP [mm]
2					15.50	2.53
6					19.82	2.14
8	63.4	40	150	150	24.17	1.86
14					33.94	1.65
20					44.13	1.54
0					19.29	3.29
3					22.63	2.29
6	63.4	40	220	176	28.73	2.05
12					39.79	1.62
24					68.88	1.56

Table 6.3: Optimized collimator configurations for different trade-offs between the falloff width (FW) and the FRP (for  $5 \times 10^7$  protons). All simulations conducted with GATE. The 150:150 configuration of the knife-edge slit camera only used a 1 cm thick crystal.

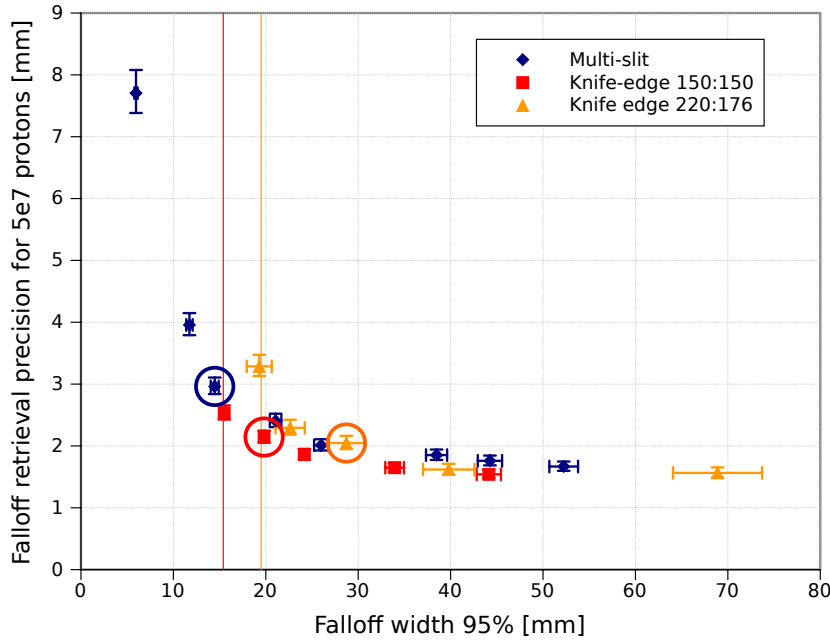


Figure 6.2: Graph showing the trade-off between the falloff width and FRP for different configurations of both cameras. The parallel-slit camera is shown in blue diamonds, the optimized knife-edge configuration in red squares. In orange triangles is shown a modified knife-edge configuration with  $d_1 : d_2 = 220 \text{ mm} : 176 \text{ mm}$  to have the same beam-collimator entrance distance as the multi-slit collimator. The optimized configurations are circled and the intrinsic limit of the knife-edge collimator is indicated with a vertical line. All simulations are carried out with GATE to exclude possible bias due to differences in the Monte Carlo code.

configurations only. Rather, we will look at a series of configurations for each of the collimator concepts and see how they perform with regards to both FRP and falloff width.

As was shown in section 4.3.4 on page 77, for the multi-slit camera, there is no optimum of the FRP with regards to the collimator pitch in the investigated range of the parameters. Rather, the FRP continues to improve even for a very large pitch. We made the choice to use a pitch of 6 mm for the optimized configuration exclusively on the basis that it seemed a reasonable choice for the trade-off between FRP and falloff width. We can then use the pitch as a variable that allows us to obtain different configurations with different trade-offs without compromising the optimization. We can then very simply obtain the configurations that have the best FRP for any given value of the falloff width. The same is true for the slit opening parameter of the knife-edge collimator, which can also be used for trade-off adjustment.

The parameters used for the configurations of both multi-parallel-slit and knife-edge collimators and the obtained falloff width and FRP are shown in table 6.3. The values of the FRP are plotted against the values of the falloff width for each configuration in figure 6.2. For the knife-edge collimator, both the optimized configuration of  $d_1 : d_2 = 150 : 150 \text{ mm}$  and a  $220 : 176 \text{ mm}$  configuration are shown. The latter was included because the collimator entrance is at 200 mm distance from the beam, which is considered more clinically feasible and is incidentally the same beam-collimator entrance distance chosen for the multi-slit camera. Note that the 150:150 configuration of the knife-edge camera uses an only 10 mm deep crystal, as this was what was used during optimization, while the other two configurations use a 31.5 mm deep crystal. The fairest comparison is between the 220:176 configuration of the knife-edge and the multi-slit configuration, as they use the same crystals and the same distance from target.

The first conclusion from the figure is that the performances are remarkably similar. The 150:150 knife-edge is a little bit better than the other two as it benefits from the increased solid angle being closer to the beam. There is a region between about 20 and 30 mm falloff width where all perform very similarly, giving results just above 2 mm FRP. Going towards smaller values of the falloff width (better spatial resolution), it can be seen how the knife-edge performance in FRP degrades more rapidly than the performance of the multi-slit camera. The values with the smallest falloff width shown for the knife-edge camera use a geometrical slit opening of 0 mm. As discussed above, decreasing the falloff width further becomes difficult and compromises the FRP even more. On the other hand, if the FRP is prioritized and a large falloff width acceptable, the knife-edge seems to perform slightly better in that region.

The optimized configurations, shown circled, are all for slightly different trade-offs. As stated, a final evaluation of the best trade-off can only be made through a study of heterogeneous targets.

Some measurements, as in section 5.3 on page 100 suggest that the background may be much higher in reality than what is predicted in simulations, roughly by a factor of two. More recent measurements, such as those shown in the next section, do not show such an increase in background, and it has not yet been clarified to what the observations were due. To estimate the possible influence of such an increased background on the comparison between the cameras, the background obtained by simulation in the optimized configurations was artificially increased. Based on the observations during measurement, we take the background value just after the falloff and add a supplementary background to the whole profile proportionally to that value. Since the origin of the background increase is not known, it is not clear whether the effect on both cameras will be the same. Figure 6.3 on the facing page shows the evolution of the FRP of the optimized configurations of the multi-slit collimator and the 220:176 knife-edge collimator when the background is adjusted. As expected, the FRP is proportional to the noise according to equation (3.15) on 50. The degradation with added background is more pronounced in the case of the multi-slit camera. The falloff width is not affected by the increase in background.

## 6.5 Measurements

Measurements have recently been conducted, again at the WPE, with a new detector prototype consisting of an array of 100 mm high, 31.5 mm deep and 4 mm wide LYSO slabs read out by SiPMs. For a detailed description of the prototype, see [Perali et al. \[2013\]](#).

Preliminary analysis has been performed on the profiles and a first comparison to simulations is possible. Acquisitions were made both with knife-edge slit configurations of 150:150 mm and 220:176 mm with the optimized collimator configuration as well as a multi-slit configuration using septa 1.57 mm thick and arranged to correspond to the pitch of the detector crystals, which was 4 mm. The multi-slit collimator was 100 mm deep. The collimator entrance was placed at 200 mm from the target and the detector was aligned right behind the collimator. This latter configuration was chosen as the tungsten plates used were already available, it does not correspond to the exact optimized configuration, but is fairly close.

Figure 6.4 on page 118 shows the results of the measurements. The profiles have not yet been corrected for dead time, which is estimated at a few percent, as an exact model of the dead time behaviour is still under development. The knife-edge profiles were corrected for uniformity using acquisitions with the closed collimator wall, as before in measurements for the knife-edge camera in section 5.3 on page 100. For the multi-parallel slit camera, making a uniformity correction is somewhat more complicated. There was some variation in the thickness of the tungsten plates used as septa and the LYSO crystals of the detector were in a closed box, meaning that alignment between slits and crystals could not be verified exactly. Consequently, there was some variation in the acceptance of each individual slit, leading to the necessity to make a uniformity correction that accounts for the collimator. To this end, an acquisition of the center of the plateau region, which is relatively flat was

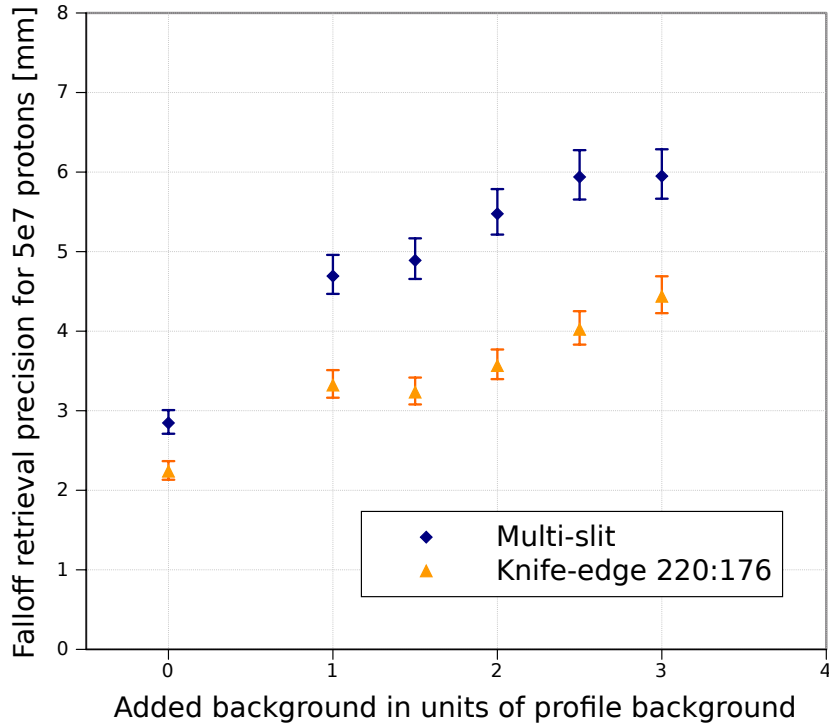


Figure 6.3: Evolution of the FRP for the optimized configurations of the multi-slit collimator and the 220:176 knife-edge collimator when the background is adjusted. The added background is given as a factor of the background of the simulated profile.

made at 230 MeV. This acquisition was used to correct for irregular responses of the detector segments.

Surprisingly, in contradiction to previous measurements, these recent results show an overestimation of the measurements by the simulations. For all collimator configurations, measurements nearly match simulations at 100 MeV, but seem to have at once less contrast and less background at higher energies than predicted. According to first estimations, the dead time of acquisitions is not high enough to account for this difference. In any case, the large additional background compared to simulation observed in previous measurements was not observed in this case.

Generally speaking, these results are rather encouraging, as they show that measurements with a dedicated prototype generate results in line with the predictions of simulation, meaning that our predictions for the performance are close to what can be obtained in reality.

## 6.6 Practical considerations

In sections 4.3.5 on page 83 and 5.4 on page 105, we discussed the mass of the camera geometries. On a per-unit-length of collimator basis, the optimized multi-slit collimator is significantly lighter with only 0.94 kg/cm as opposed to 1.5 kg/cm of the optimized knife-edge collimator due to the smaller effective thickness. For the total system mass, we have to distinguish between a configuration of the parallel-slit camera where the whole proton ranged is imaged, totaling 49.6 kg and a configuration only imaging 100 mm of the target to be comparable to the total camera FOV of the knife-edge slit. For the latter, some shielding has to be added to attenuate photons coming from the beginning of the target. A reasonable approach is to impose that particles impinging through the shielding must always travel at least through the effective thickness  $T_e$  of tungsten before reaching the detector. This can be achieved by adding a wedge as shielding next to the collimator and crystals. The thickness

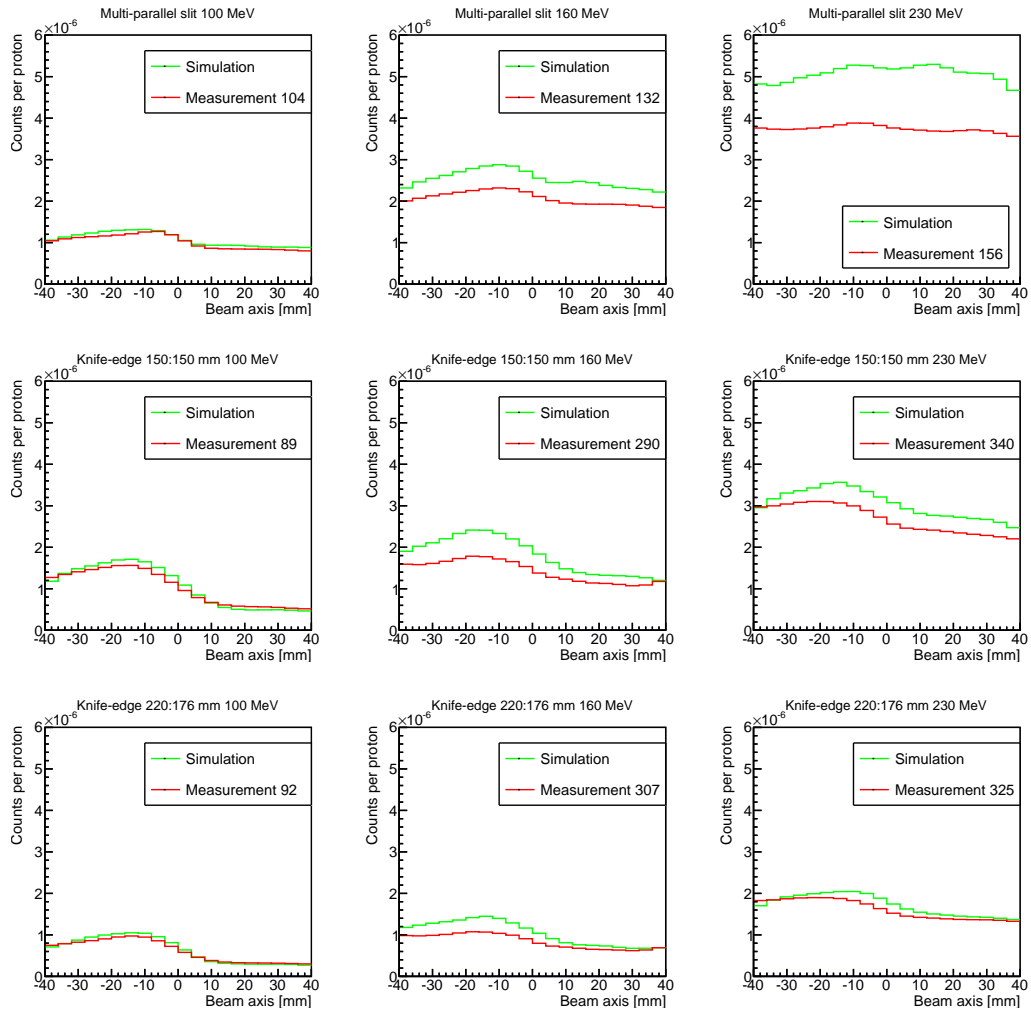


Figure 6.4: Measurements using a LYSO-slab prototype detector for the multi-slit configuration (top) as well as two knife-edge slit configurations for beam energies of 100 MeV, 160 MeV and 230 MeV. Simulations using MCNPX.

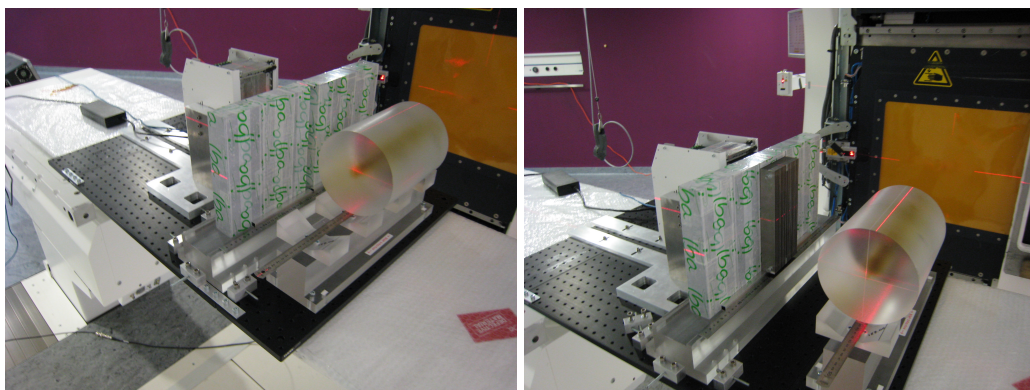


Figure 6.5: Photographs of the setup during the experiment at WPE in October 2013. Left: Knife-edge camera in 150:150 configuration. Right: multi-parallel-slit camera.

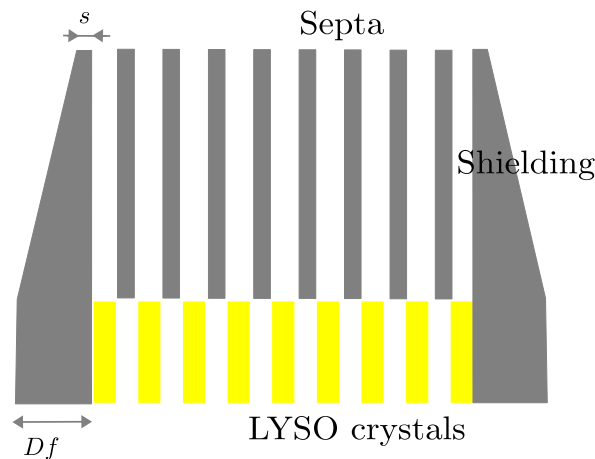


Figure 6.6: Proposed shielding configuration for a parallel-slit camera.

of the wedge is equal to the septa thickness  $s$  at the entrance of the collimator and equal to the effective thickness  $T_e$  next to the crystals. The mass of such a shielding wedge is 6.5 kg. The total mass of two wedges plus enough septa to cover 100 mm equals 25.4 kg of tungsten. The minimal mass of the equivalent knife-edge configuration covering 100 mm of the target was estimated at 36 kg, meaning the parallel-slit collimator is significantly lighter.

Similar considerations can be made for the bulkiness of the camera. The parallel-slit camera has the advantage of having the detector right next to the collimator, leading to a very compact design. The geometry shown in figure 6.6 has the dimensions of 10.2 cm  $\times$  15 cm  $\times$  20 cm (depth  $\times$  length  $\times$  height), while the knife-edge camera comes in at about 22.8 cm  $\times$  12 cm  $\times$  20 cm. If the multi-parallel-slit camera is to be used to image the whole proton range, of course it would have to be much larger, to be able to be used up to proton energies of 230 MeV. Alternatively, two small detector heads of 10 cm FOV each could be used, one for the entrance region and one for the falloff.

Another possible technical challenge is the positioning of the camera head. If only the falloff is imaged, the camera needs to be positioned very exactly, since the error of camera positioning will directly go into the error on range measurement. The beam entrance position will have to be estimated via an optical system. The accuracy of currently available systems of this type is below one millimeter. Additionally, the error on the relative positioning between the two imaging systems (optical and prompt gamma) will have to be taken into account. One possibility of having a good precision in relative positioning would be if part of the camera were visible on the cone-beam CT image of the patient, in which case very precise estimation of the position is possible.

Additionally, for small total camera fields of view, the camera may have to be repositioned during treatment so that the falloff stays in the center of the image as the energy and thus the range change. This is especially true for the knife-edge camera due to the distortion of the image near the edges and the large falloff width. The multi-parallel-slit camera, of course, can be built with any desired total camera field of view, so that it would not have to be moved during treatment (at the expense of being heavier and bulkier, of course). In the short term, it may be more practical to have such a bulky but immobile system for a first prototype, since this requires little engineering effort and almost no modifications to the treatment room. In the long term, once a sophisticated positioning system has been developed and integrated into the gantry, a less bulky system may be more convenient.

Our last consideration shall be for the camera cost. The main contributions to the cost are the scintillator material, the collimator material, the electronics and the positioning system.

Since the detector behind both configurations is the same, the scintillator material and electronics cost are also comparable. The collimator material cost follows the considerations made above for the collimator mass (although the fabrication of individual collimator septa may be more expensive than blocks used for the collimator wall). The positioning system for the knife-edge camera and the small parallel-slit camera has the same requirements and will thus probably cost the same. This means that the knife-edge camera and the small parallel-slit camera have nearly the same cost. The large multi-slit configuration with view of the whole trajectory is, of course, significantly more expensive (the cost scales approximately with the size of the field of view, which is four times larger).

# Chapter 7

## Conclusion and outlook

The study of the two collimated camera types, through simulation and measurement, has shown promising results for the application in range control in protontherapy. Both configurations have been optimized, and, in the previous chapter, the relative merits were discussed. The development of a collimated prompt gamma camera is now ripe for the next step in development. Prototypes are being developed to validate the projected performance through measurement. The study of heterogeneous targets is necessary to predict the performance for real patients and make a decision between the two configurations based on their different assets. And finally, it is time to give some thought to the integration into the workflow of proton therapy treatments.

### 7.1 Choice of camera configuration

Optimization studies of both camera configurations have shown that there is no clear-cut overall winner in the comparison of the two cameras. Figure 6.2 on page 115 in the previous chapter shows that performances are remarkably similar for optimized configurations for the falloff retrieval precision and spatial resolution. While the parallel-slit camera can more easily be configured to have very good spatial resolution, the knife-edge slit camera has a slight advantage when a very good falloff retrieval precision is required. So depending on the priorities set, either camera can be a good solution. Other considerations such as weight, size and cost also prove to be quite similar in both cases, as detailed in section 6.6 on page 117.

The parallel-slit camera offers the possible advantage that the field of view can be extended at will, making it possible to image the whole trajectory of protons including the entrance into the target. Due to this and to the fact that there is no distortion towards the edges of the field of view, the camera would not necessarily have to be moved during the course of treatment, a clear advantage for a first clinical prototype that should be as simple as possible. Less distortion also means that effects due to heterogeneities near the edges of the field of view could be more easily identifiable, especially if a configuration with good spatial resolution is chosen.

A possible risk of the multi-slit configuration lies in the fact that the geometry has not been validated for higher-energy proton beams and measurements (section 6.5 on page 116) seem to indicate that the performance is less than ideal. As the multi-slit configurations have tendentially a higher background than comparable knife-edge slit configurations, this could indeed prove problematic for high proton energies, which already suffer from high background. This is an area that merits further investigation.

The knife-edge slit camera has been tested up to beam energies of 230 MeV and the performance seems adequate. In case that investigations into the occurrence of the higher-than-expected background indicate that this contribution is coming from the target or nozzle, the wall thickness can be more easily adjusted to be optimal for the real background, as the wall thickness does not otherwise influence the properties of the image.

## 7.2 Possible improvements on current configurations

During simulations, some choices were made to limit the considered configurations to limit the parameter space and some possible tweaks to the geometry were not investigated. Any of these could lead to possible improvements to performance.

- Time of flight techniques were not considered in the optimization process. It has been shown that there is potential for improvement in performance by using such techniques (Roellinghoff et al. [2013]; Biegun et al. [2012]; Verburg et al. [2013]). An optimization study of the parallel-slit collimator using time of flight is being done separately (Pinto et al. [2013]). Recent improvements in detector timing resolution have shown that time of flight discrimination could work even at small distances (work to be published by the group of D. Schaart, P. Lopes).
- Introducing a magnification factor for the knife-edge slit camera could lead to better spatial resolution and better falloff retrieval precision. So far, only 1:1 configurations and in one case, a 5:4 configuration have been shown here. The drawback is the need for a larger detector to cover the whole field of view, making the camera more expensive and much more bulky.
- Similarly, a converging collimator configuration could be tested for multi-parallel slits. This would introduce a magnification improving the spatial resolution. The drawback is again, the use of more detector material. Furthermore, using a converging collimator introduces a dependency of the image on the position of the pencil beam being scanned across the target. This complicates reconstruction and introduces an element of error which is otherwise nicely avoided in parallel-slit configurations.
- Individual photon energy lines could be used in addition to the profiles to possibly gain in precision and gather additional information about elemental composition. This is not possible with the prototype being currently developed, as the energy resolution is too poor.
- More complex electronics could be devised which discard events where coincident counts occur in several detector segments on the basis that these are most likely scatter events. This could be used in combination with the previous point as a version of the active shielding proposed by Verburg et al. [2013] without additional detector material.
- A more sophisticated method than simple backprojection could be used to obtain emission profiles from measured profiles, such as MLEM methods suggested by Diblen et al. [2012]. This could be especially interesting in heterogeneous cases, where not only range errors, but also lateral errors could potentially be identified by using prompt gamma emission probabilities for each voxel of the patient based on the CT scan in the algorithm.

## 7.3 Further study to be conducted

Some further study needs to be conducted for the development of a clinical prototype to insure the best possible performance.

The inconsistency of the observed background in different experiments should be investigated, as the inability to predict the background correctly could compromise the validity of predictions of performance. Ideally, systematic measurements should be made that explore different possibilities for the origin of such background. First insights could be gained by simply mapping the amplitude of background at different positions in the treatment room with regards to the target, the nozzle and the collimator. The dependence on the distance of all of those could give some valuable clues as to the origin of additional background not predicted by simulation. The amount of shielding and other material in the room could also play a role and could be investigated by placing different amounts of material such

lead blocks, tungsten, PMMA, aluminum and wood (the last three were used for support of setup elements in different experiments) near the experimental setup. A simple repetition of the spectrometry acquisition could also add a data point. If new experiments are unable to reproduce the background observed during past experiments, indicating that previous observations were in some way due to the camera not being optimal for the experiment, this would be a welcome result in that it means that Monte Carlo simulations are more precise than previously thought.

Complete analysis of new measurements presented in section 6.5 on page 116 including dead time effects and improved uniformity correction is under way. This is an important step in validating the new prototype before the application to clinical cases.

The next logical step in camera optimization is the simulation of heterogeneous targets. Such a study is currently under way and first results indicate that there is a strong dependence of camera performance on the individual case being studied. It is therefore necessary to study a large library of cases that could potentially benefit from prompt gamma imaging and evaluate the performance. The cases in such a library could be weighted with regards to the current uncertainty involved and the potential benefit of using prompt gamma imaging, such as better protection of organs at risk in proximity to the irradiated volume. It could be interesting to evaluate camera geometries besides the optimized configuration to evaluate whether it is advisable to prioritize spatial resolution or collection efficiency in heterogeneous cases.

On a more practical note, reliable ways to perform calibration and assessment of the camera have to be found. This regards energy calibration, dead time evaluation and uniformity of crystal response. It has to be studied how much all of these vary in time (due, for example, to temperature issues, radiation damage,...) and how often recalibration will have to be performed. A study of the effects of calibration errors on the prediction of range errors would be valuable.

## 7.4 Prototypes under development

A complete prototype of the knife-edge slit camera of the geometry described in section 6.5 on page 116 is nearly completed. This development is being undertaken by IBA and XGLab/Politecnico di Milano. It is more completely described in (Perali et al. [2013]). The prototype will be tested on heterogeneous targets and in clinical settings to validate the simulation study on heterogeneous targets.

A multi-slit camera with the ability to use time-of-flight discrimination, is also under development in Lyon and will be tested on proton and carbon ion beams. To be able to use TOF, the camera will be placed farther away from the target. An increased depth of 17 cm will be used in order to reduce background due to prompt gamma and, in combination with the neutron background reduction by TOF, achieve a low background and noise level. The collimator will be made out of modular tungsten sheets of 1.5 mm thickness that can be configured with either a pitch of 3.5 mm or 7 mm, each time with a fill factor of 0.42.

## 7.5 Ideas for integration in clinical workflow

Once a prompt gamma camera is functional and validated, attention has to be turned to its use. The use envisaged for the camera here, to image individual spots, means that a lot of information will be gathered for each treatment, that has to be condensed and put into a form that can be used to evaluate the quality of the treatment and potentially make decisions such as interrupting treatment, changing the treatment plan, etc.

Use of a prompt gamma camera is possible in a variety of ways. There is the possibility of choosing a few pencil beams ahead of time that will be delivered as a first step of treatment and allow validation before giving the bulk of the dose. The same can also be done during the course of normal treatment, with the possibility of interruption if warranted. A more

complete analysis could be conducted post-treatment, in which case subsequent treatment fractions can be replanned accordingly.

We have already mentioned the importance of evaluating heterogeneous targets. In some cases, the calculation of a shift may not be sufficient to describe variations in the profile. A simple shift, as assumed in this manuscript, will only occur if the tissue around the Bragg peak is relatively homogeneous. In other cases, it may be necessary to predict possible scenarios due to various errors ahead of time and go towards a method of matching the profile to those scenarios.

The list of possible scenarios can be extensive, taking into account all of the sources of range errors mentioned in section 1.1.1 on page 2. As a reference profile based on the CT scan is needed for each scenario and for multiple pencil beams, the calculation time can be considerable. A dedicated Monte Carlo code or (semi-)analytical methods could accelerate this process considerably (see, for example, Sterpin et al. [2013]). Even with such methods, the number of profiles to be generated is still substantial, so it could be worthwhile to develop ways of choosing certain reference pencil beams based on the probability of being sensitive to errors (for example, proximity to an interface between tissue materials). The list of scenarios can comprise some that are standard, possibly automatically adapted to the tumor location (translation, rotation, variations in stopping power of the material) and also some that may require input from a clinician (marking cavities that could potentially be filled).

Once such a library of scenarios has been built for a treatment, for each acquired pencil beam a “quality of match” and a corresponding confidence level can be calculated for each scenario. The information of all pencil beams (or all pencil beams that were chosen ahead of time for their sensitivity) can be combined to make a ranking of the likelihood of each calculated scenario. It then has to be analyzed whether there is reason to believe that a deviation from the treatment plan has occurred. This is the case if the likelihood of the “perfect” scenario (treatment as planned) is low and the likelihood of another scenario is significantly higher, with consistent information from the different pencil beams. In this case, the information can be presented to the clinician in a concise form, by giving the likelihood of a deviation from the plan and the most likely alternate scenario. Depending on the magnitude of the deviation, a recommendation to interrupt and/or replan the next fraction can be issued.

The possibility of using machine learning to improve the rate of adequate recommendations has been explored by Gueth et al. [2013]. Especially in the case of a (semi-)analytical or simplified Monte Carlo simulation used to calculate the scenarios, the algorithm could be trained on mock measurements simulated with a more complete Monte Carlo code and/or on irradiations of an anthropomorphological phantom with deliberate errors in delivery.

# Chapitre 8

## Résumé français

### 8.1 Introduction

#### 8.1.1 L’hadronthérapie

Avec la chimiothérapie et les interventions chirurgicales, la radiothérapie est la méthode la plus répandue pour le traitement du cancer. Environ la moitié des patients reçoivent quelque forme de radiothérapie, souvent en combinaison avec une autre modalité de traitement. La plus grande partie de ces thérapies sont sous forme de radiothérapie «conventionnelle» utilisant des rayons x, mais l’utilisation d’autres particules, tels que les neutrons, électrons et particules chargés plus lourds a aussi été étudié. La thérapie utilisant des neutrons, protons, pions ou ions s’appelle l’hadronthérapie. Une liste des particules les plus utilisées et le nombre de traitements à ce jour sont donnés en tableau 8.1.

L’idée d’utiliser des protons pour la radiothérapie remonte à [Wilson \[1946\]](#). Les profils de dépôt de dose des protons sont bien différents de ceux des photons. Alors que les photons sont des particules neutres dont les profils sont caractérisés par une courte montée suivi d’un pic et un déclin exponentiel, les particules chargés comme les protons ont une longueur de parcours constante et le dépôt de dose a un fort pic vers la fin du parcours. Cette forme du profil de dose et l’avantage principal de la thérapie avec des particules chargés.

Des développements dans la radiothérapie photons comme le Intensity Modulated Radiation Therapy (IMRT) ont permis à la radiothérapie conventionnelle de mieux s’adapter à la forme de la tumeur. Cependant, avec cette méthode, une dose importante est forcément déposé avant et après le volume à irradier. L’utilisation de particules chargées ouvre de nouvelles possibilités de planification de traitement dû à leur parcours fini. En théorie, un organe à risque se trouvant juste derrière la tumeur peut alors éviter presque complètement le rayonnement.

De nos jours, les particules les plus utilisées pour la radiothérapie sont les protons et les

Particule	Nombre de traitements
He	2054
Pions	1100
Ions carbone	10756
Autres ions	433
Protons	93895
Total	108238

TABLE 8.1 – Nombre total de traitements délivrés avec différentes modalités d’hadronthérapie dans le monde avant fin 2012, selon le Particle Therapy Cooperative Group (PTCOG).

Source of range uncertainty in the patient	without Monte Carlo	with Monte Carlo
Independent of dose calculation		
Measurement uncertainty in water for commissioning	$\pm 0.3$ mm	$\pm 0.3$ mm
Compensator design	$\pm 0.2$ mm	$\pm 0.2$ mm
Beam reproducibility	$\pm 0.2$ mm	$\pm 0.2$ mm
Patient setup	$\pm 0.7$ mm	$\pm 0.7$ mm
Dose calculation		
Biology (always positive)*	+0.8%	+0.8%
CT imaging and calibration	$\pm 0.5\%$	$\pm 0.5\%$
CT conversion to tissue (excluding I-values)	$\pm 0.5\%$	$\pm 0.2\%$
CT grid size	$\pm 0.3\%$	$\pm 0.3\%$
Mean excitation energy (I-values) in tissues	$\pm 1.5\%$	$\pm 1.5\%$
Range degradation; complex inhomogeneities	-0.7%	$\pm 0.1\%$
Range degradation; local lateral inhomogeneities	$\pm 2.5\%$	$\pm 0.1\%$
Total (excluding *)	4.6% + 1.2 mm	2.4% + 1.2 mm

TABLE 8.2 – Estimated range errors listed by source of error with and without the use of Monte Carlo simulations in treatment planning. Table adapted from [Paganetti \[2012\]](#).

ions carbone. Les ions carbone ont l'avantage d'avoir une efficacité biologique relative plus élevée vers la fin du parcours, rendant le pic du profil encore plus marqué. L'inconvénient est la production de fragments qui ont un parcours plus long. Le profil du dépôt de dose présente une queue après le pic de Bragg.

Comme le pic de la distribution de dose est trop fin pour couvrir toute la profondeur d'une tumeur dans la quasi-totalité des cas, des distributions de dose à différentes énergies sont superposés, formant ainsi ce qu'on appelle "a spread out Bragg peak" (SOBP). De cette manière, une distribution de dose presque uniforme peut être atteinte sur toute la profondeur de la tumeur.

### 8.1.2 Les erreurs de longueur de parcours - erreurs en "range"

Bien que la forme du profil, présentant un pic de Bragg, ait des avantages pour les traitements, elle augmente de manière significative le risque de déviation par rapport à la distribution de dose prévue. Alors que pour les irradiations avec des photons, des petites incertitudes dans la profondeur mènent à des petites différences en dose délivrée, pour des profils comprenant un pic de Bragg, une petite erreur peut entraîner d'importantes différences, avec une dose maximale délivrée dans une région et presque pas de dose délivrée dans une autre. Ceci est problématique dans le cas d'un «overshoot» aussi bien que dans le cas d'un «undershoot». Dans le premier cas, un organe à risque peut recevoir un très haute dose; dans l'autre, une partie de la tumeur peut ne pas recevoir de dose, compromettant ainsi l'efficacité du traitement.

Il existe tout une variété de cause pouvant entraîner des erreurs en range. Une liste complète peut être trouvée dans [Paganetti \[2012\]](#), dont les résultats sont résumés dans le tableau 8.2.

Les erreurs en range peuvent être divisées en deux groupes principaux. Une partie de ces erreurs est due au calcul de dose lors de la planification du traitement. Ce sont des effets

comme :

- La sous-estimation de l'efficacité biologique relative (EBR) dans la partie distale du profil de dose, conduisant à une sous-estimation du range biologique effectif.
- Des incertitudes dans le scan CT.
- Une ambiguïté dans la conversion entre les unités Hounsfield obtenues par scan CT et le pouvoir d'arrêt des protons utilisé pour la planification.
- Des artefacts dans l'image de scan CT, dus par exemple à du tissu très hétérogène ou à la présence d'implants métalliques.
- Des erreurs et/ou approximations dans le calcul de dose par le logiciel de planification.

L'autre groupe d'erreurs en range est dû à des différences entre la préparation du traitement et le traitement lui-même :

- Des erreurs de modélisation du faisceau, comme par exemple des erreurs de mesure des propriétés du faisceau ou un changement depuis la dernière mesure. Également des erreurs de fabrication de matériel spécifique au patient, comme les compensateurs.
- Des erreurs d'installation du patient.
- Un mouvement des organes intra-fraction, comme la respiration (très dépendant de l'emplacement).
- Des changements anatomiques entre fractions, tels que les changements de poids, réduction de la tumeur et remplissage de cavités. Les organes internes peuvent également légèrement basculer entre les fractions.

Tous ces différents effets peuvent s'additionner à des erreurs en range considérables. Ceci est habituellement traité en appliquant des marges de sécurité autour du volume de la tumeur, menant à l'irradiation d'un volume plus grand, afin d'assurer l'irradiation complète de la tumeur.

Une méthode de vérification du range, idéalement en temps réel lors du traitement même, pourrait réduire les risques et conduire à une réduction des marges utilisées, ce qui mènerait également à moins de dépôt de dose dans des tissus sains. En outre, les cas où l'erreur dépasserait les marges pourraient être détectés et le traitement interrompu et corrigé. Afin d'être utile, une telle méthode devrait être capable de fournir une mesure du range avec une incertitude de 1-2 mm voir mieux.

### 8.1.3 L'état de l'art pour le contrôle du range

Plusieurs solutions possibles pour le contrôle du range sont actuellement à l'étude. Bien que certaines, comme la TEP, aient été testées sur des patients en environnement clinique, il n'y a actuellement aucun centre utilisant une méthode systématique pour contrôler les traitements. [Knopf and Lomax \[2013\]](#) donne une vue d'ensemble très compréhensive de l'état de l'art des différentes méthodes.

Les méthodes du contrôle du range peuvent être de deux types : les méthodes directes (mesure de la dose) et les méthodes indirectes (mesure d'autres effets corrélés à la dose). Des approches différentes s'appliquent aussi au timing de la mesure. Le contrôle du range peut avoir lieu soit avant le traitement (avec des faisceaux tests), pendant le traitement ou après le traitement, ce qui a différentes implications sur l'utilisation de l'information recueillie.

**Mesure de la dose in-vivo** Une méthode bien établie pour la vérification de la dose en radiothérapie avec des photons ou électrons consiste à effectuer des mesures ponctuelles de la dose. Normalement, un dispositif de densimétrie est placé à l'endroit où le faisceau entre dans le patient et/ou à la sortie. Malheureusement, les mesures de la dose en dehors du corps du patient ne sont pas suffisantes pour le contrôle du range en protonthérapie. Des dosimètres implantables basés sur la technologie MOSFET et pouvant être lus à distance ont récemment été développés pour la radiothérapie conventionnelle. Une approche similaire peut être utilisée en protonthérapie. La dose intégrée dans le SOBP est constante, donc un détecteur placé dans cette zone sera insensible aux erreurs en range. Le placement près du Pic de Bragg le plus distal est sensible aux erreurs en range, mais aussi très sensible aux erreurs de positionnement du dosimètre.

Deux approches possibles sont en cours d'investigation pour surmonter ces défis. Pour des faisceaux utilisant un diffuseur passif, la mesure de la dose peut être synchronisée avec la roue du modulateur, le profil temporel de dose apportant les informations nécessaires. Cette méthode a été testée par Lu [2008b] et le range a pu être mesuré avec une précision en dessous du millimètre. Lu [2008a] proposent également une méthode où le SOBP plat habituel est remplacé par une paire de SOBP avec des pentes complémentaires. La pente de la dose encode alors l'information sur le range du faisceau.

Bien qu'une bonne précision puisse être atteinte avec cette méthode, l'inconvénient évident est son caractère invasif, nécessitant l'implantation d'un détecteur ou l'utilisation d'un dispositif tel qu'un ballonnet rectal.

**Radiographie protons** La radiographie protons est basée sur l'utilisation de faisceaux de protons suffisamment énergétiques pour traverser le patient et être détectés en sortie. Dans la version la plus simple, seuls quelques points faisceau sont utilisés («range probes»). Ceci a été testé par Romero et al. [1994]; Watts et al. [2009]; Mumot et al. [2010]. Ces derniers ont montré par simulation Monte Carlo que des précisions dans la mesure du range de l'ordre du millimètre étaient possibles.

L'obtention d'une image bi-dimensionnelle par radiographie est une idée poursuivie depuis les années 60. La méthode présente un nombre de propriétés intéressantes (voir Koehler [1968]; Kramer et al. [1977]). Son contraste en densité est meilleur que pour la radiographie avec rayons X et elle fournit directement l'information sur le pouvoir d'arrêt des protons. De plus, la dose délivrée au patient est moindre.

La radiographie protons est intéressante pour le contrôle du range et, plus particulièrement, pour les acquisitions d'image pré-traitement utilisée pour vérifier, d'une part, l'alignement du patient et, d'autre part, pour vérifier que les pouvoirs d'arrêt mesurés correspondent à la planification. Dans certains cas cependant, les faisceaux protons d'énergie suffisante ne sont pas disponibles.

**IRM** Le principe du contrôle du range par imagerie IRM consiste en l'observation des changements que la radiation peut entraîner dans le tissu humain, ceux-ci apparaissant sur un scan IRM. Avec la radiothérapie conventionnelle, on observe une intensité accrue de l'image IRM de la moelle osseuse dans la colonne vertébrale (Ramsey and Zacharias [1985]; Stevens et al. [1990]; Blomlie et al. [1995]). Plus récemment, l'effet a été étudié pour la protonthérapie en vue de l'observation des distributions de doses délivrées. Krejcarek et al. [2007] ont montré que chez les patients traités au sac dural, l'IRM prise entre 10 jours et 21 mois après la radiothérapie présente une démarcation nette de l'hypersignal visible, correspondant au volume irradié. Gensheimer et al. [2010] ont étudié la possibilité d'utiliser l'effet de la colonne vertébrale pour le contrôle du range en protonthérapie.

**TEP** La méthode de contrôle de dose par TEP est basée sur le fait que les ions du faisceau subissent des collisions nucléaires inélastiques produisant des isotopes radioactifs. Certains de ces isotopes sont des émetteurs  $\beta+$ , avec des demi-vies de l'ordre de quelques minutes. Les photons produits par l'annihilation de la particule  $\beta+$  peuvent être détectés par la tomographie d'émission de positons (TEP). Les émetteurs  $\beta+$  ne sont produits que jusqu'à

une certaine énergie des protons, ce qui fait que la distribution de l'émission chute avant le pic de Bragg. Bien que la distribution de la dose et des émissions de positons soient corrélés, ils ne sont pas identiques.

Il y a deux façons principales d'acquérir une image TEP. Soit par une acquisition «en ligne» en cours du traitement, ou alors après le traitement par un scanner TEP dédié. Une comparaison des deux méthodes peut être trouvée dans [Parodi et al. \[2008\]](#). Le fait que le TEP en ligne profite des taux d'émission les plus élevés s'explique par la décroissance exponentielle. L'inconvénient est l'espace limité disponible dans la salle de traitement. Afin d'accommoder la nozzle, le système de positionnement du patient, le cone-beam CT etc, normalement seul un système TEP à deux têtes avec un champ de vue relativement petit peut être installé. [Parodi et al. \[2002\]](#) et [Parodi et al. \[2005\]](#) ont montré qu'une corrélation entre la distribution d'émetteurs de positons et la distribution de dose peut être trouvée expérimentalement.

L'acquisition TEP «off-line» utilise des scanners TEP ou TEP/CT industriels. Le patient est transporté vers les scanners après le traitement, ce qui cause un délai entre le traitement et le scan pouvant aller jusqu'à 30 min. L'amélioration de la sensibilité et de la performance de ces scanners, comparés aux scanners dual-head, peut partiellement compenser la perte en activité causée par le délai. L'effet du «washout» biologique limite la précision.

### Gammas prompts

Le contrôle du dépôt de dose par gammas prompts est basé sur les rayons gammas émis par des noyaux excités par des réactions nucléaires, dans des temps très inférieurs à la nanoseconde. Le principe est similaire à la technique TEP détaillé ci-dessus, mais l'échelle de temps est très différente et le taux d'émission de gammas prompts dépasse celui des positons, typiquement d'un ordre de grandeur ou plus.

Cette technique a été proposée pour la première fois par ([Jongen and Stichelbaut \[2003\]](#)) en 2003. Les premières mesures ont été faites par [Min et al. \[2006\]](#), qui ont démontré une corrélation entre le passage du faisceau et l'émission gammas prompts. Depuis, plusieurs groupes ont indépendamment vérifiés cette corrélation, parmi eux [Testa et al. \[2008\]](#); [Polf et al. \[2009\]](#); [Smeets et al. \[2012\]](#). Il faut noter que, bien que les distributions soient clairement corrélés, elles ne sont pas proportionnelles.

Des simulations de Monte Carlo ont démontré que l'émission de gammas prompts est un procédé isotrope (voir, par exemple [Robert et al. \[2013\]](#) et chapitre 2). Le spectre de gammas prompts a une composante continue, superposé à un nombre de lignes discrètes correspondant à des désexcitations nucléaires spécifiques. Le spectre commence à de faibles énergies et la plus grande partie est contenue en-dessous de 10 MeV, avec une queue de la distribution allant jusqu'à des énergies plus élevées.

Les systèmes de détections proposés pour la mesure de gammas prompts peuvent être divisés en deux groupes. Le premier utilise des collimateurs physiques pour produire une image du profil d'émission. Ce groupe peut être divisé davantage entre les collimateurs à fentes parallèles ou trous parallèles d'une part, et les collimateurs knife-edge et pinhole d'autre part. Le deuxième groupe utilise des caméras Compton, aussi appelés collimation électronique.

**Caméras collimatés** Plusieurs mesures ont reposé sur l'utilisation d'une seule fente à bords parallèles ([Min et al. \[2006\]](#); [Kurosawa et al. \[2011\]](#); [Verburg et al. \[2013\]](#) pour les protons, [Testa et al. \[2008\]](#) pour les ions carbone). Des mesures avec un collimateur multi-slit ont été publiées par [Min et al. \[2012\]](#) pour des protons et [Krimmer and al \[2014\]](#) pour des ions carbone. Dans une étude récente d'un groupe coréen, un système à trous parallèles bi-dimensionnel et un système à fentes parallèles ont été optimisés en utilisant des simulations MCNPX. Une étude de simulations sur l'utilisation du temps de vol à été réalisée par [Biegun et al. \[2012\]](#) pour un collimateur à fentes parallèles idéal. Une approche intéressante est proposée par [Verburg et al. \[2013\]](#), qui utilisent les profils gammas prompts de quelques lignes discrètes seulement et utilisant du blindage actif pour le détecteur.

Une version uni-dimensionnelle du concept pinhole, le collimateur knife-edge, est proposé par [Smeets \[2012\]](#). Une série de simulations a été faite afin d'optimiser la configuration, ce qui sera détaillé dans la section 8.4. Une autre configuration a été proposée par [Bom et al. \[2012\]](#). Le facteur d'agrandissement important et le fait que la caméra soit assez proche du faisceau conduisent à une résolution spatiale très bonne comparée à d'autres solutions knife-edge. Dans des simulations, la mi-hauteur de la chute du profil prompt gammas a pu être mesuré avec une précision de 0.6 mm pour  $1 \times 10^8$  protons.

**Caméras Compton** Contrairement aux systèmes de caméra collimatée, les caméras Compton n'utilisent pas de collimateur physique. Au lieu de cela, elles s'appuient sur de multiples interactions de photons à l'intérieur du détecteur pour tirer des conclusions quant à la direction d'incidence du photon. Des caméras à double diffusion ont été proposées et des lignes directrices pour la conception ont été discutées ([Seo et al. \[2007\]](#); [Peterson et al. \[2010\]](#); [Kormoll et al. \[2011\]](#); [Richard \[2012\]](#)). La configuration d'une caméra Compton à trois interactions a aussi été étudiée par simulation ([Mackin et al. \[2013\]](#)) et un prototype est actuellement en construction par [Llosá et al. \[2011\]](#).

### 8.1.4 Accélérateurs et modalités de traitement

Dans cette section seront examinées les techniques les plus usuelles utilisées pour la production d'un faisceau de protons. Des exemples numériques des propriétés d'un faisceau - tel que la structure temporelle, le courant faisceau et la taille des spots - seront examinés, afin d'étudier l'influence de ces paramètres sur la détection des gamma prompts.

Deux principaux types d'accélérateurs de particules circulaires sont utilisés pour la proton thérapie : les cyclotrons et les synchrotrons. On utilise également une approche mixte : le synchro-cyclotron.

La structure temporelle du faisceau est la conséquence directe du choix d'un type d'accélérateur. Le courant faisceau est habituellement assimilé au courant faisceau moyen des pulsations - bien que pour les faisceaux pulsés, le courant instantané puisse être bien plus grand que le courant moyen. Pour déterminer la capacité de comptage et de temps mort du détecteur désiré, il est essentiel d'examiner tant le taux de détection gamma prompt pendant un pulse, que le taux moyen. De plus, la sélection "temps de vol" pourra être affectée par le fait que, à cause de la microstructure du faisceau, les particules les plus lentes émises par un pulse soit rattrapée par les particules les plus rapides du pulse suivant (voir section 4.2 et [Biegun et al. \[2012\]](#)).

En principe, avec les cyclotrons, des particules peuvent se trouver dans chaque tour de la spirale simultanément, de sorte que le faisceau soit continuellement injecté et éjecté. Cependant, il y a en réalité une microstructure dans le temps, dû à la fréquence radio (RF pour radio frequency) utilisée pour le champ électrique accélérant. Par exemple, la RF d'un IBA C230 cyclotron s'élève à 106 MHz, ce qui correspond à un paquet de protons tous les 9,4 ns. Dans la salle de traitement du patient, la longueur des paquets est habituellement d'environ 2 ns. Cependant, dans la plupart des centres de traitement, ni la largeur ni la distribution des particules d'un paquet dans le temps n'est mesurée : les longueurs de paquets qui seront données sont donc des approximations. Avec la plupart des autres cyclotrons, les fréquences utilisées sont de 30 à 100 Mhz : on obtient alors des micro-paquets similaires (voir par exemple [Schippers \[2009\]](#)).

Pour les synchrotrons et les synchro-cyclotrons, les champs magnétiques étant synchronisés avec l'énergie des particules, on ne peut avoir des particules d'accélération différente en même temps dans l'accélérateur. Chaque paquet doit être injecté, accéléré et éjecté avant que le prochain ne puisse entrer. Il en résulte une structure faisceau où les impulsions faisceaux sont séparées par des intervalles de temps relativement longs.

Avec un synchrotron, les temps d'injection et d'accélération sont typiquement de l'ordre de quelques secondes : pendant ce temps aucun faisceau n'atteint la salle de traitement. Une éjection lente (où seulement une fraction du faisceau est éjectée à chaque tour, de telle sorte que l'accélérateur soit vidé peu à peu) peut durer jusqu'à 10 s, ce qui permet d'extraire un faisceau continue. Par exemple, le synchrotron HIT à Heidelberg présente un temps d'injection

et d'accélération de 2 s et un temps d'extraction maximum de 10 s (Cee [2012]). L'extraction peut être interrompue au besoin, par exemple pour déplacer le faisceau. Par ailleurs, un synchrotron présente également un faisceau avec une microstructure, car les petits paquets d'ions doivent pouvoir passer au travers des cavités d'accélération. Le filling factor (longueur du paquet sur période du paquet) est typiquement d'environ 10%. Avec l'énergie maximale, le temps qu'un paquet met à faire un tour est typiquement d'un ordre de grandeur plus grand que pour les cyclotrons. Cela s'explique par le plus grand radius des synchrotrons, qui entraîne une microstructure du faisceau avec des centaines de nanosecondes entre les paquets individuels (selon l'énergie d'extraction).

Les faisceaux des synchro-cyclotrons ont une macro-structure - les pulsations étant accélérées une par une - et une micro-structure - due à la RF. Par exemple, le superconducting synchro-cyclotron S2C2 d'IBA présente un taux de répétition de 1kHz, d'où une impulsion par milliseconde. La longueur de l'impulsion est actuellement estimée à 7  $\mu$ s. La micro-structure faisceau est similaire à celle d'un cyclotron, avec un paquet de l'ordre d'une à deux nanosecondes toutes les 10,9 ns (les valeurs numériques pour le S2C2 proviennent de Pearson et al. [2013]). Contrairement aux synchrotrons, les cyclotrons ont une énergie d'extraction constante et une fréquence de paquet constante à l'extraction.

Pour une vue d'ensemble des valeurs numériques des différents types d'accélérateurs, voir table 2.1.

Les modalités de livraison d'un faisceau peuvent grossièrement être séparées entre les modalités "passives" et "actives". La principale différence étant que, pour les modalités actives, la cible est balayée par le faisceau. Pour un recueil complet des méthodes de beam delivery, voir par exemple Chu et al. [1993].

Le méthodes les plus utilisés sont :

**Diffusion simple** Un seul diffuseur (le plus souvent en plomb) est utilisé pour élargir le faisceau. Seul la partie centrale, approximativement plate, est utilisé pour le traitement. Cette méthode est utilisée surtout pour les petits volumes et elle est similaire à une deuxième méthode, la

**Double diffusion** où le premier diffuseur est complété par un deuxième diffuseur conçu de telle manière que la fluence de protons est quasiment uniforme. Un collimateur et un compensateur, spécifiques au patient, sont utilisés pour rendre la forme du profil conforme à la tumeur et une roue modulatrice dans la nozzle est utilisé pour changer l'énergie du faisceau. Une vue d'ensemble très complète des méthode de double diffusion peut être trouvée dans Gottschalk [2004].

Les principaux inconvénients de la double diffusion sont le fait que le volume irradié ne peut être totalement conforme au volume de la tumeur ; que les éléments de modulation et de diffusion sont relativement proches du patient et produisent un rayonnement indésirable et qu'il y a un besoin de matériel spécifique au patient. Le principal avantage de la double diffusion est la limitation des effets d'«inter-play» pour les tumeurs mobiles.

Pour la détection de gammas prompts, la double diffusion est moins que idéale. Dowdell [2011] a comparé le dépôt de dose par des neutrons pour la double diffusion avec le pencil beam scanning et trouvé significativement plus de neutrons dans le cas de la double diffusion. Kurosawa et al. [2011] ont tenté d'imager un SOBP de 7 cm et constaté que le profil gammas prompts n'avait plus de falloff visible à cause du rayonnement de fond venant de diffusions dans les éléments de la nozzle. En outre, chaque couche irradiée est composée d'un mélange de distances de pénétration quand un compensateur est utilisé ou quand le milieu irradié est hétérogène.

**Pencil Beam Scanning (PBS)** Le PBS est une méthode en cours d'installation dans un nombre croissant de centres. Un faisceau avec une petite section transversale est balayé à travers la cible en utilisant un champ magnétique variable dans la nozzle. Chaque couche du volume à irradier est alors «peinte» avec le faisceau. Pour changer de couche,

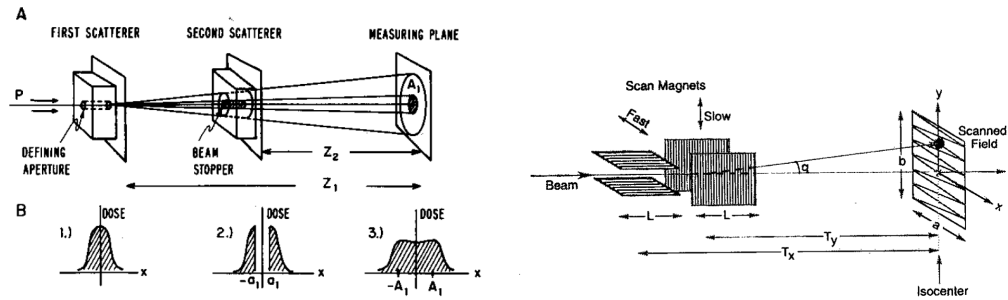


FIGURE 8.1 – Illustration of the double-scattering and pencil beam scanning beam delivery modalities. Source : [Gottschalk \[2004\]](#); [Chu et al. \[1993\]](#)

l'énergie est généralement changée en utilisant un modulateur loin en amont, avant le système de transport du faisceau.

Les avantages du PBS sont le fait que n'importe quelle forme de tumeur peut être irradiée très exactement et de manière conforme à la forme proximale de la tumeur, ainsi que la quasi-totale absence d'éléments diffuseurs dans la nozzle proche du patient. Comme l'intensité de chaque spot peut être ajustée individuellement, le PBS permet beaucoup de flexibilité dans la planification du traitement.

Dans ce manuscrit, seul le PBS va être considéré pour le développement d'un système de détection de gammas prompts. Une synchronisation avec le système de distribution du faisceau doit être mis en place afin de pouvoir acquérir un profil de gammas prompts pour chaque spot.

### 8.1.5 L'émission de gammas prompts

Le spectre en énergie des neutrons et photons émis dans la cible est montré en figure 8.2. Les photons ont une composante continue et une série de pics. Plusieurs raies d'émission listées dans [Kozlovsky et al. \[2002\]](#) peuvent être identifiés.

Regardons maintenant la distribution des points d'émission dans l'espace. La figure 8.3(gauche) montre la distribution des points d'émission de neutrons et de photons le long de l'axe d'un faisceau de 160 MeV, dans une cible de PMMA. Seules les particules avec une énergie de plus que 1 MeV sont incluses. Le profil d'émission de photons augmente doucement le long de la trajectoire du proton, présente un pic juste avant le pic de Bragg et chute ensuite. La queue de la distribution est due principalement aux interactions de neutrons dans la cible. La largeur du falloff à 95% est de 9,9 mm. Les neutrons ont eux une distribution qui décroît le long de la trajectoire du proton et s'arrête bien avant le pic de Bragg.

La figure 8.4 montre la distribution des angles d'émission. Les photons suivent une distribution isotrope, alors que les neutrons sont émis principalement vers l'avant.

## 8.2 Remarques communes aux deux géométries

### 8.2.1 Evaluation des performances

Cette section se focalise sur les méthodes d'évaluation d'un profil uni-dimensionnel, indépendamment de la façon dont le profil est obtenu. Ici, nous développons les méthodes et outils utilisés pour analyser les profils de la caméra à fentes parallèles et de la caméra à collimateur knife-edge, afin de construire les bases permettant de comprendre comment la performance évolue quand les propriétés du profil changent, en regardant des profils génériques.

**Choix des critères de performance** Afin de comparer les mérites de différents types de caméras et configurations, des critères quantitatifs doivent être choisis pour évaluer les

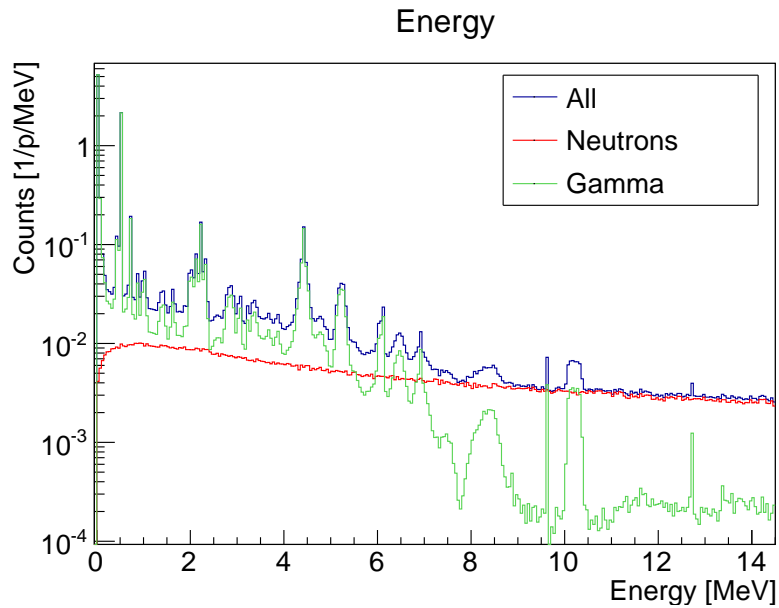


FIGURE 8.2 – Spectrum of particles emitted within the target irradiated with a 160 MeV pencil beam in simulation conducted with GATE (see section 1.3 for settings). Photons are shown in green, neutrons in red, and the sum of both in blue.

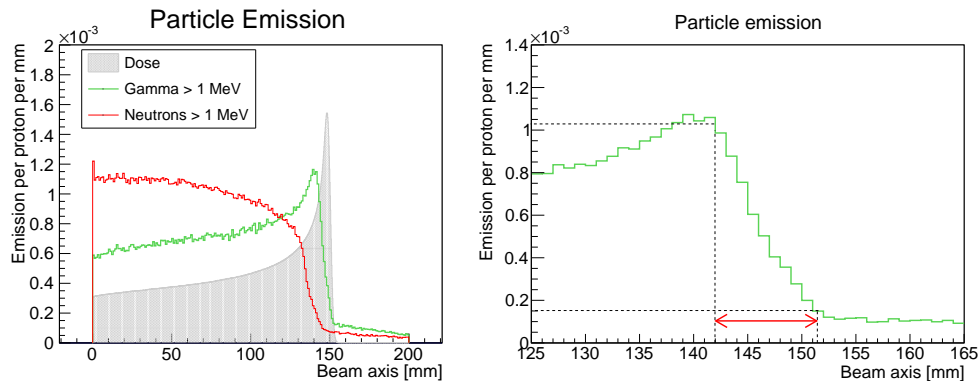


FIGURE 8.3 – Emission of particles in a PMMA target irradiated with a 160 MeV pencil beam in simulation conducted with GATE (see section 1.3 for settings).. On the left is shown the distribution along the beam axis of neutrons (red) and photons (green) superposed with the dose profile (the latter is shown in arbitrary units). On the right is shown a zoom of the prompt gamma emission profile illustrating the measurement of the 95% falloff width of 9.9 mm.

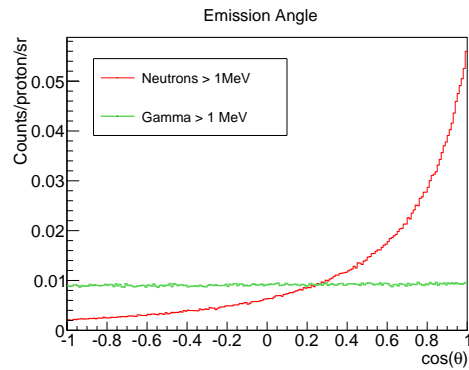


FIGURE 8.4 – Above : different distribution with regards to emission direction of neutrons (red) and photons (green) above 1 MeV.  $\theta$  is the angle between the beam direction and the movement direction of the particle. Results shown are for a PMMA target irradiated with a 160 MeV pencil beam in simulation conducted with GATE (see section 1.3 for settings).

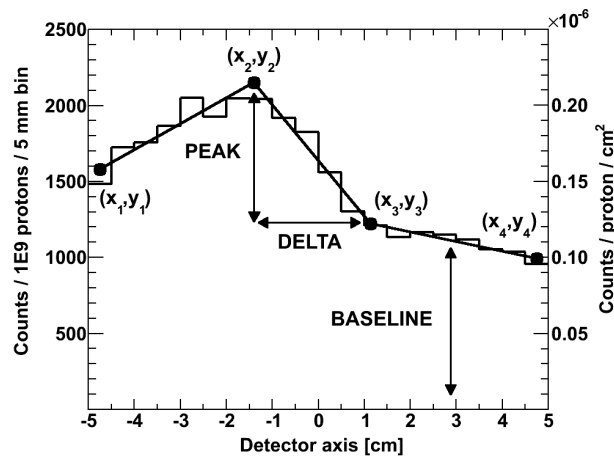


FIGURE 8.5 – Profile characteristics as defined and used in Smeets [2012] : peak, delta and baseline correspond to contrast, falloff width and background respectively. Reprinted from Smeets [2012].

performances. La plupart des qualités désirés dans un profil sont évidentes et se mesurent facilement sur le profil même : un grand contraste, peu de bruit de fond, une chute étroite. Malheureusement, des modifications de la géométrie de la caméra entraînent souvent une amélioration d'un de ces critères et une dégradation d'un autre. Si cela est le cas, comment faire pour décider de leur importance relative ? Est-il possible de trouver un critère unique qui prédit des performances optimales pour la détection d'erreurs en range ?

Afin d'estimer la capacité de mesurer les erreurs en range, nous regardons la précision avec laquelle la position de la chute du profil peut être récupérée (appelé juste «précision» par la suite). La mesure du point de la chute peut être utilisée en combinaison avec la mesure du point d'entrée du faisceau dans le patient, pour obtenir une mesure du range. La mesure du point d'entrée peut être réalisée soit avec la même caméra prompt gamma (dans ce cas, une précision similaire est attendue), soit avec un système externe, comme par exemple un système optique de positionnement du patient (dans ce cas, la précision de ce système et la précision de l'alignement entre les deux doivent être prises en compte). Nous partons du principe que l'alignement de la caméra peut être aligné avec une très bonne précision à un angle perpendiculaire au faisceau. Nous faisons également l'hypothèse que la configuration qui est optimale pour imager la chute est aussi optimale pour l'entrée dans le patient. Nous regardons uniquement la précision avec laquelle la chute peut être mesurée comme facteur de mérite.

Pour des raisons de simplification et afin de tirer les conclusions les plus générales possibles, nous ne considérons que les cibles homogènes dans un premier temps. Les erreurs sont supposées être des simples décalages du profil par rapport au profil attendu. La précision de la méthode est alors la précision avec laquelle ce décalage peut être mesuré.

En utilisant des cibles homogènes, un aspect important des gammas prompts est négligé : la densité du tissu et, dans une moindre mesure, les variations de composition atomique qui ont une influence sur l'émission de gammas prompts par proton et par unité de longueur (voir, par exemple, [De Rydt \[2013\]](#)). Pour un vrai patient hétérogène, le point d'entrée dans le patient et la chute finale du profil d'émission ne vont pas être les seules variations ou bords dans le profil. Il peut alors être avantageux d'avoir une bonne résolution spatiale afin d'être capable de séparer les différents effets. Pour cette raison, la résolution spatiale ne doit pas être négligée lors de la comparaison de profils. Une décision définitive ne peut avoir lieu qu'après une étude extensive de cas cliniques et peut dépendre de type de cas ciblé.

Si l'objectif est d'estimer le niveau de bruit des profils, le nombre de coups attendus pour un profil type lors d'une mesure doit être connu. La figure 8.6 montre un exemple d'un traitement de prostate avec les points du traitement dessinés selon l'énergie du faisceau correspondante et le nombre de protons à délivrer. Cet exemple est pris de [Grevillot \[2011\]](#) et a déjà été utilisé pour l'évaluation de la caméra knife-edge dans [Smeets et al. \[2012\]](#). Les spots les plus intéressants pour l'imagerie sont les spots les plus distaux, ayant traversés le plus de matière. De plus, les spots distaux sont ceux qui ont le plus de risque d'un «overshoot» et de déposer de la dose au-delà de la tumeur, possiblement dans un organe à risque. Heureusement, les spots distaux sont aussi ceux qui utilisent le nombre le plus important de protons. Dans l'exemple, les spots distaux s'étendent d'environ  $5 \times 10^7$  à  $2 \times 10^8$  protons. Il semble raisonnable de définir comme objectif pour la caméra le fait d'être capable d'atteindre une bonne précision pour un nombre de protons de cet ordre de grandeur.

**Analyse des profils pour une cible homogène** Afin d'estimer la précision, nous commençons avec l'hypothèse que le profil attendu est connu. Pour obtenir ce profil, que nous appellerons le «profil de référence», nous utilisons soit une mesure à très haute statistique, soit une simulation de Monte Carlo à très haute statistique. Le nombre de coups doit être suffisant pour que les fluctuations statistiques soient suffisamment basses, afin de ne pas cacher la forme du profil. En pratique clinique, ce profil devra être généré par simulations de Monte Carlo ou en utilisant un modèle analytique. Ce genre de profil consiste typiquement en un ensemble discret de points, correspondant à des pixels d'un détecteur, à des fentes d'un collimateur ou à des positions de mesure lors d'un balayage. Le profil est alors fitté avec une fonction continue, la «fonction de référence» afin d'être capable de prédire le nombre de

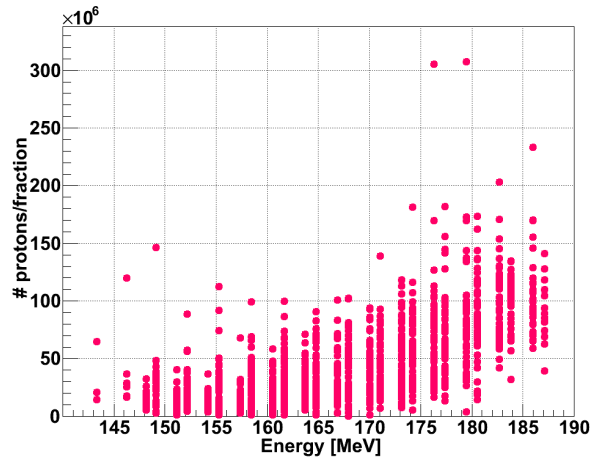


FIGURE 8.6 – Example of a prostate treatment plan : individual pencil beam spots of the treatment are plotted according to the beam energy and the number of protons per fraction delivered to the spot. Source : [Grevillot \[2011\]](#).

coups à n'importe quel point.

Ensuite, le profil «échantillon» est généré. Ceci est un profil qui représente ce qui sera réellement mesuré durant le cours d'une irradiation. Il correspond à un nombre donné de protons délivrés. Il peut être généré soit en sous-échantillonnant les données du profil de référence, soit en appliquant la loi de Poisson et un générateur aléatoire au profil de référence afin d'obtenir le bruit statistique approprié.

La meilleure correspondance entre profil échantillon et fonction de référence est alors cherchée en appliquant un décalage le long de l'axe faisceau. Les sections de la fonction qui décrivent l'entrée dans le patient et la chute sont utilisés séparément. L'idée est que lors d'une erreur dans le range et dans le cas homogène, toute la partie du profil autour de la fin du parcours sera décalée d'une quantité correspondant à l'erreur de range. Les erreurs de positionnement du patient résulteront en un décalage des deux parties.

Plusieurs méthodes peuvent être utilisées pour déterminer le décalage. La méthode utilisée ici est une simple minimisation du  $\chi^2$  (somme des carrés des différences entre le profil échantillon et la fonction de référence). Selon la forme du profil et l'amplitude du bruit statistique, la fonction objectif peut avoir de multiples minima, dont un qui correspond au «vrai» décalage, les autres correspondant à des variations aléatoires. L'occurrence de ces variations est rendue plus probable par le fait que le contraste des profils est relativement faible par rapport au bruit de fond. Pour des profils de faible statistique, les fluctuations statistiques peuvent atteindre le même ordre de grandeur que le contraste. Puisqu'il est impossible de distinguer une correspondance aléatoire de la «vraie» correspondance entre profils, le minimum global du  $\chi^2$  est toujours sélectionné. Et puisque les méthodes de descente de gradient ne trouvent pas le minimum global d'une façon fiable si plusieurs minima existent, une méthode de recherche exhaustive est utilisée.

Une valeur pour le décalage est ainsi obtenue pour le profil échantillon. Puisque le profil échantillon représente exactement le même range des protons que le profil de référence, l'espérance du décalage est zéro. Quand la procédure est répétée beaucoup de fois avec des profils échantillons générés indépendamment, la distribution de décalages obtenue donne une idée de la précision avec laquelle la caméra est capable de mesurer le décalage. Plus spécifiquement, l'écart type est une bonne mesure pour la précision avec laquelle peut être déterminé la position de la chute du profil.

Pour la procédure décrite ci-dessus, il faut être capable de trouver une fonction continue qui suit la forme du profil, la fonction de référence. Cette fonction doit satisfaire plusieurs critères. Elle doit bien suivre les variations dans le profil. Idéalement, elle devrait lisser un peu les fluctuations. Elle doit être suffisamment flexible pour être appliquée à différents profils

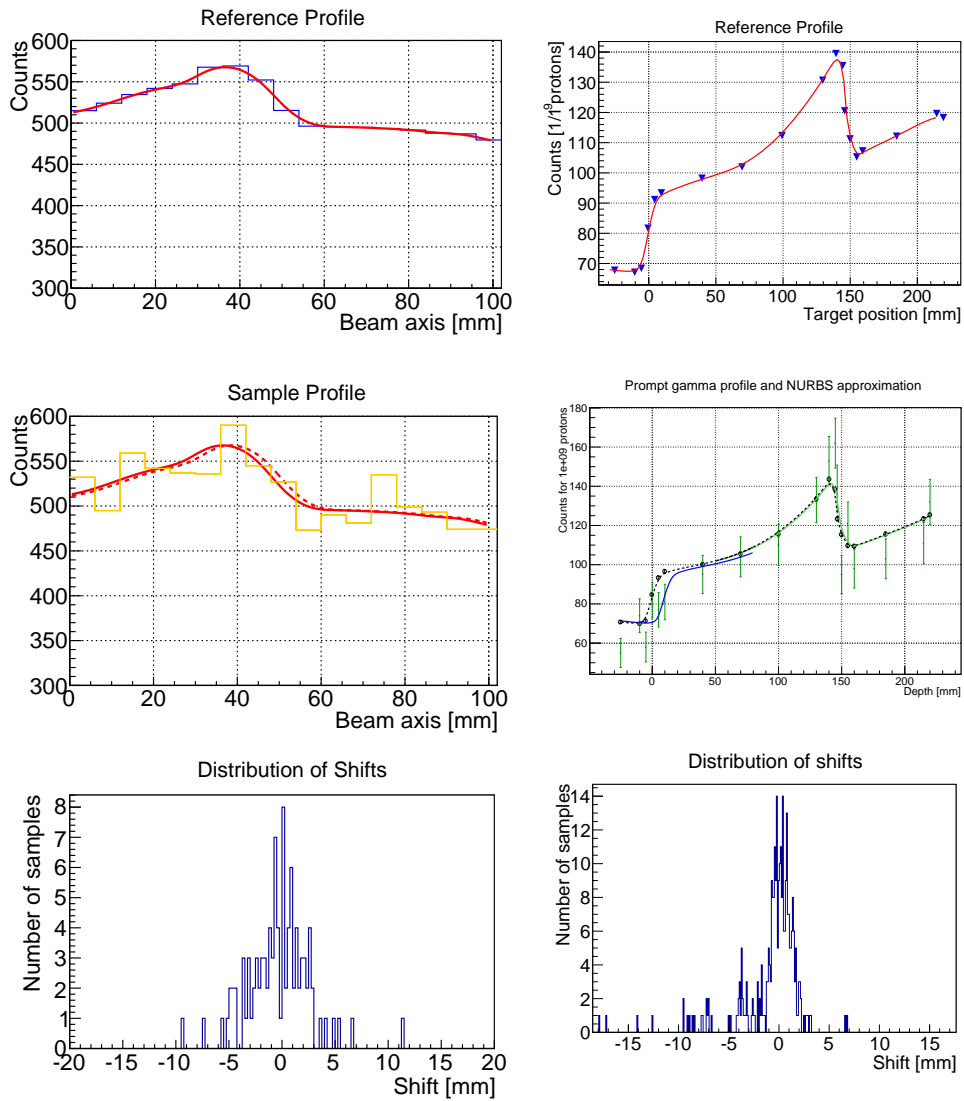


FIGURE 8.7 – The method for obtaining the falloff retrieval position as applied to a simulated multi-parallel-slit profile (left) and to a profile measured by scanning a single parallel slit (right). On the top is shown the high-statistics reference profile fitted with a continuous spline function. In the middle a sample profile generated by applying Poisson noise and the reference function shifted to match. On the bottom the distribution of shifts.

observés avec différentes géométries de caméra. La procédure doit être assez robuste, de telle sorte qu'un grand nombre de profils peuvent être traités automatiquement sans devoir être validés à la main. Idéalement, elle doit être continûment dérivable, puisque des discontinuités dans la dérivée peuvent causer des discontinuités dans la fonction  $\chi^2$  qui est utilisée pour trouver le décalage.

Plusieurs fonction ont été testées et rejetées. Des illustrations peuvent être trouvés dans le chapitre 3, figures 3.5 à 3.8, pages 35 à 38.

- De simples fonction polynomiales; ne sont pas adéquates si de grandes sections du profils sont utilisées.
- Une fonction à trois droites, avec une droite représentant le plateau, une pour la chute, et une pour le bruit de fond. Cette méthode à été utilisée dans [Smeets et al. \[2012\]](#) et a l'avantage d'utiliser directement des grandeurs «parlantes», comme les pentes, la valeur du pic, le niveau de bruit de fond. Cependant, la forme angulaire de cette fonction l'empêche de suivre le profil très exactement et elle ne s'avère pas très robuste.
- Une fonction d'erreur semble appropriée d'un point de vue théorique, puisqu'elle représente un bord. Cette fonction est utilisée dans l'étude des caractéristiques de profils généralisés (section 8.2.1). Pour les profils mesurés, cependant, nous pouvons observer que la courbure du profil juste avant et juste après la chute n'est pas la même, ce qui n'est pas modélisable avec une simple fonction d'erreur.
- Différents types de fonction spline (linéaire, cubique,...). Les splines s'adaptent bien à toute forme de profil, avec le risque de suivre aussi les variations dans le profil qui sont dues au bruit.

Finalement, une fonction NURBS (non-uniform rational B-splines) à été choisie pour un maximum de flexibilité et de robustesse. Les NURBS, à la différence des méthodes d'interpolation utilisant des splines, ne sont pas contraints de passer à travers les points de mesure et fournissent ainsi un peu de lissage.

Des NURBS d'ordre trois sont utilisés pour les fonctions de référence des profils prompt gamma puisqu'ils fournissent un peu de lissage, mais pas au point de faire disparaître le pic. Les points de mesure ou les bins des histogrammes des profils prompt gammas sont utilisés comme points de contrôle pour générer le NURBS.

**La résolution spatiale** Comme mentionné auparavant, la résolution spatiale ne doit pas être négligée comme facteur de mérite, puisqu'elle peut s'avérer utile pour résoudre des effets d'hétérogénéités dans le chemin du faisceau.

Par définition, la résolution spatiale est la capacité de séparer dans l'image, deux points source séparés d'une distance donnée dans le plan image. La résolution spatiale est souvent évaluée en regardant la fonction d'étalement du point (PSF). En analogie du critère de Rayleigh, nous pouvons utiliser un critère pour des PSF de forme Gaussienne. Deux points peuvent être séparés si les pics des deux PSF peuvent être séparés, c'est à dire qu'il y a un minimum entre les deux. Ceci est le cas si les points sont distants de plus que  $2\sigma$  de la PSF.

La même information que la PSF peut aussi être obtenue à partir d'une image d'un bord infiniment fin.

Nous décrivons la PSF de forme Gaussienne :

$$PSF(x) = G(x) = \frac{1}{\sqrt{2\pi}\sigma} \exp\left(\frac{-x^2}{2\sigma^2}\right)$$

et l'image d'un bord :

$$\begin{aligned}
 P(x) = \operatorname{erf}(bx) + c &= a \frac{2}{\sqrt{\pi}} \int_0^{bx} \exp(-t^2) dt + c \\
 &= a \frac{2}{\sqrt{\pi}} \int_0^x \exp(-b^2\tau^2) \frac{\partial t}{\partial \tau} d\tau + c \quad \text{avec } t = b\tau \\
 &= a \frac{2b}{\sqrt{\pi}} \int_0^x \exp(-b^2\tau^2) d\tau + c
 \end{aligned}$$

ce qui veut dire que le paramètre  $b$  peut être utilisé pour décrire la largeur de la PSF d'une façon équivalente :

$$\sigma \equiv \frac{1}{\sqrt{2b}}$$

Comme on peut constater ci-dessus, section 8.1.5, le profil d'émission de gammas prompts obtenu par simulations de Monte Carlo chute peu avant le pic de Bragg, avec une largeur à 95% de la chute de 9,9 mm. La largeur de la chute du profil détecté est la convolution entre la chute à l'émission et la PSF. Puisque la largeur de la chute à l'émission est connue, cela nous permet de calculer la résolution spatiale de la caméra à partir de la largeur de la chute du profil mesuré.

**Une méthode analytique pour étudier les propriétés de profil** Quand le système est optimisé par étude de Monte Carlo, chaque configuration à tester peut demander un long temps de calcul et le fait d'explorer un grand espace de paramètres aveuglement est long et inefficace. Il peut alors être très utile d'avoir un calcul analytique qui donne une première intuition de ce qui peut être attendu et qui peut servir de ligne directrice lors de l'optimisation. Il est possible de faire a minima des liens qualitatifs entre les paramètres de la géométrie de chaque caméra et l'influence attendue sur les propriétés du profil. Par exemple, il est évident que l'angle d'acceptation d'un collimateur est essentiel pour déterminer le compromis entre la résolution spatiale et l'amplitude du signal corrélé. Sachant comment ceci influe les figures de mérite dans notre cas, on peut en déduire une première idée du type de collimateur qui donnerait vraisemblablement les meilleurs résultats et quelle région de l'espace de paramètres est la plus intéressante pour nous.

La méthode utilisée est décrite section 8.2.1. Une fonction d'erreur est utilisée pour donner une approximation d'un profil prompt gamma généralisé indépendant d'une géométrie de caméra ou d'un processus d'imagerie.

Considérons les caractéristiques du profil qui pourraient avoir une influence sur les performances et qui pourraient plausiblement varier entre différentes géométries de caméra. La procédure détaillée est décrite dans la section 3.2.4 page 39 dans la partie anglaise de ce manuscrit. Les résultats sont montrés dans les graphiques de la figure 8.8 et résumés ci-dessous.

**Le contraste** est défini comme l'amplitude du signal corrélé. C'est la différence entre le nombre de coups juste avant la chute et juste après. Cette valeur est influencée par l'angle solide du détecteur, le volume du détecteur et l'angle d'acceptation du collimateur. La précision s'améliore rapidement quand le contraste est augmenté, approximativement en  $1/x$ .

**Le bruit de fond** est défini comme tous les coups qui ne sont pas corrélés à la chute. Ce sont typiquement des neutrons, des particules ayant interagis dans le collimateur et des gammas ayant traversés le collimateur sans interaction. Le bruit de fond est influencé par l'angle solide, le volume de matériel du collimateur et le volume du détecteur. La précision croît approximativement avec la racine carrée du bruit de fond.

**La largeur de la chute** est liée à la résolution spatiale du système. C'est l'espace sur lequel le profil passe du maximum au bruit de fond. La meilleure résolution spatiale est

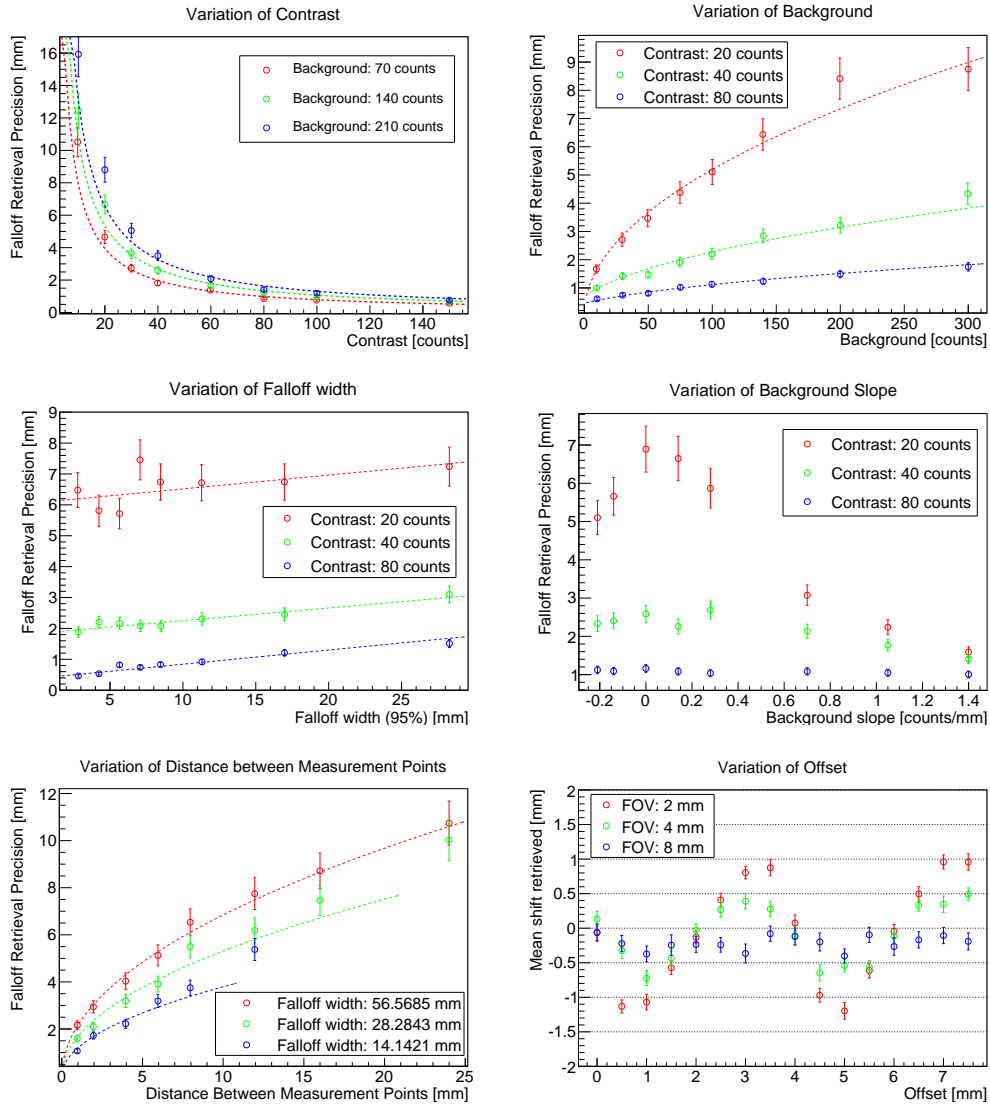


FIGURE 8.8

atteinte pour des collimateurs à faible angle d'acceptation et des pixels petits. La précision croît légèrement quand la largeur est augmentée, mais il est important de remarquer que cet effet est relativement faible par rapport à l'effet du contraste ou du bruit de fond mentionnés ci-dessus.

**Les pentes.** Des mesures ont montrés que la région du plateau et la région après le pic de Bragg ne sont pas parfaitement planes. Ceci est en partie dû à l'émission non-isotrope des neutrons, qui ajoutent un bruit de fond montant sur la longueur du profil. Une autre partie est due à la légère hausse du taux d'émission de gammas prompts vers la fin de la trajectoire des protons. Ces effets apparaissent comme des accroissements du profil approximativement linéaires dans la direction du faisceau. Ceci ne sont pas des paramètres qui peuvent être influencés de manière directe lors de la conception de la caméra. Cependant, ils doivent être pris en considération lors du design de la caméra, puisqu'ils peuvent considérablement changer le comportement du profil. Pour des contrastes faibles, une grande pente dans le bruit de fond neutrons peut en fait apporter de l'information de positionnement du pic de Bragg et mener à une précision meilleure.

**La distance entre les points de mesure** est le plus souvent liée à la taille des segments de cristal du détecteur ou par les pas utilisés lors d'un balayage. La figure 8.8 montre l'effet de différentes distances entre points de mesure dans le cas où le nombre de coups mesurés par point reste constant, comme c'est le cas lors d'un balayage où la grandeur des pas est modifiée sans changer les temps de mesure par pas. L'augmentation de la précision, pour des distances entre points de mesure plus grande, est en fait due à la diminution des coups au total sur tout le profil. Hormis cet effet, et lorsque la résolution spatiale n'est pas affectée, la distance entre points de mesure n'a pas d'effet significatif sur les performances de la caméra.

**Position des points de mesure relative** Dans certains cas, avec des collimateurs multifentes, on peut observer un effet d'ombre des septa sur l'image. Puisque les points de mesure sont discrets, la position de la chute relative à ces points peut mener à un effet systématique sur la position mesurée, comme le montre Testa [2010]. La figure 8.8f montre le décalage moyen mesuré pour différentes positions relatives des points de mesure, pour une distance de 4 mm entre points de mesure et pour des valeurs différentes de la largeur de la chute. On peut constater qu'un effet systématique existe, en particulier quand la largeur est inférieure au double de la distance entre points de mesure : la chute du profil est alors contenue dans un ou deux points de mesure. L'effet disparaît quasi totalement quand la chute est distribuée sur plus de points.

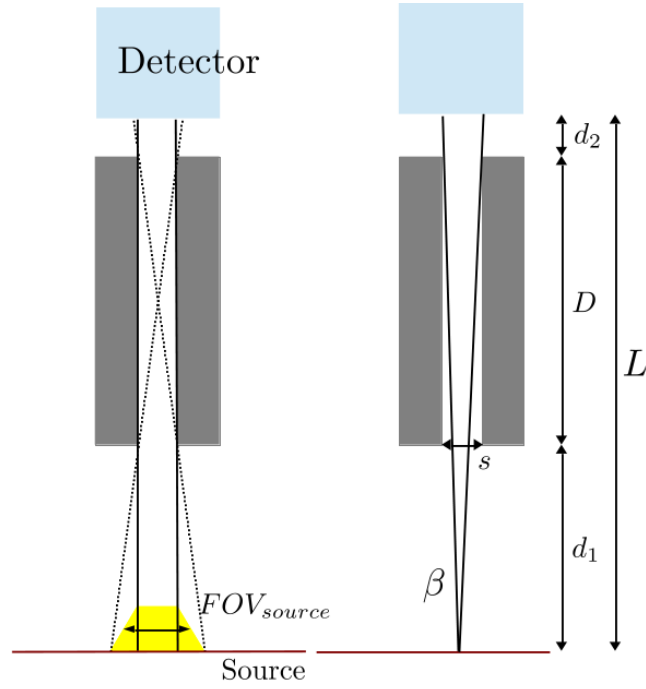


FIGURE 8.9 – Illustration of the calculation of the detector unit field of view and the detector solid angle

### 8.3 Le collimateur à fentes parallèles

#### 8.3.1 Le principe géométrique

Pour les gammas prompts des énergies discutés ici, des calculs purement géométriques ne peuvent être qu'approximatifs. Néanmoins, cela sert à interpréter les observations faites lors d'une variation d'un paramètre lors de mesures ou de simulations. Les plus importants grandeurs à considérer sont :

*Le champ de vue d'une unité de détecteur* défini comme la partie de la source linéaire qui peut être vue à travers d'une fente du détecteur. Nous le définissons comme la largeur à mi-hauteur de la fonction décrivant la probabilité qu'un photon émis à un point donné de la source atteigne le détecteur, comme illustré en figure 8.9.

$$FOV_{d.u.} = s \left( 1 + \frac{d_1}{D} \right) = p(1-f) \frac{D+d_1}{D}$$

*L'efficacité de collection du détecteur* est définie comme le nombre de gammas qui traversent le collimateur divisé par le nombre émis par la source. Elle peut être exprimée comme suit :

$$CE = \frac{Hp^2(1-f)^2}{4\pi LD} \quad (8.1)$$

L'efficacité de collection à l'unité d'une longueur pour pouvoir être utilisée avec une source linéaire. Quand elle est multiplié par l'émission par unité de longueur, on obtient le nombre de particules arrivant sur le détecteur à travers une fente.

Ces considérations géométriques nous permettent de faire certaines prédictions sur ce à quoi on peut s'attendre. Par exemple, l'on peut voir que :

- Nous nous attendons à ce que la résolution spatiale soit linéaire en  $p$ , alors que l'efficacité de collection est quadratique en  $p$ . Puisque l'efficacité de collection détermine le contraste et le contraste, comme nous avons vus précédemment dans la section 8.2.1,

détermine la précision, nous pouvons nous attendre à ce que la précision s'améliore lorsque  $p$  est grand.

- De façon similaire, un collimateur profond donne une meilleure résolution spatiale mais une moins bonne précision.
- La distance entre la source et le collimateur est le seul paramètre qui doit être choisi aussi petit que possible pour optimiser la résolution spatiale et l'efficacité de collection en même temps. Ce paramètre doit être choisi aussi petit que considéré possible en tenant compte des contraintes pratiques.

### 8.3.2 Données expérimentales

Les expériences sur lesquelles ces données sont basées ont été menées au Westdeutsche Protonentherapiezentrum à Essen (WPE) avec un collimateur à une seule fente parallèle. Les résultats ont été présentés dans Pinto [2014] et Roellinghoff et al. [2013] et une partie de cette section du texte est basée sur des extraits du dernier.

Un profil complet a été acquis en déplaçant la cible progressivement le long de l'axe faisceau. Bien que cette approche donne une approximation de l'image qui peut être obtenue avec un détecteur multi-fentes, il y a bien sûr quelques différences significatives. La différence la plus importante, sans doute, est qu'il y a des blocs solides de tungstène des deux côtés de la fente, à la place de fentes supplémentaires. Cela augmente considérablement la quantité de blindage à l'extérieur de l'angle d'acceptation de la fente. La quantité de blindage affecte aussi la probabilité d'interaction de particules avec le matériau de blindage qui peuvent causer de la radiation à leur tour.

Une autre caractéristique de cette façon d'acquérir un profil est que les distances entre les points de mesure peuvent être choisies librement et qu'elles ne sont pas limitées à un pas fixe. La distance peut même être choisie plus petite que la largeur de la fente elle-même, ce qui est évidemment impossible avec une configuration multi-fentes. Lors des expériences présentés ici, plus de points de mesure ont été acquis dans la région du fin du parcours, où le taux de comptage varie le plus.

**Montage expérimental et traitement des données** Certains des résultats de deux manipulations faits au WPE en 2011 et 2012 sont utilisés ici. Les deux montages utilisés sont décrits dans la figure 8.10, vus de dessus. En 2011, des balayages avec les deux montages avaient été réalisés, mais celui du montage B n'avait pas assez de points proche du fin de parcours pour permettre une évaluation de la précision. Les mesures avec le montage B ont été répétées en 2012, mais dû à l'occurrence de pauses irrégulières dans le faisceau, il est impossible de bien séparer les données en sous-échantillons de manière exacte. Par conséquent, une analyse de la précision atteignable n'a été faite qu'avec les données de 2011 uniquement. Les profils acquis avec les deux montages sont comparés ici surtout en vue d'étudier les effets des différentes configurations de collimateur et de blindage sur le profil.

A chaque fois, une cible cylindrique en PMMA a été irradiée avec un faisceau de protons de 160 MeV. La cible avait un diamètre de 150 mm et une longueur de 200 mm. Un collimateur en tungstène a été utilisé dans les deux cas, avec des blocs de blindage en plomb supplémentaires qui protègent le détecteur de la radiation venant de la cible et non bloquée par le collimateur. Les distances et dimensions sont indiqués dans la figure 8.10. Dans le montage A, il y a deux détecteurs LYSO derrière la fente. Les données présentées ici ont été acquises avec un seul des deux détecteurs (l'autre ayant subi un problème technique). Il s'agit de celui qui est dans la pénombre de la fente, ce qui cause une sous-estimation systématique du taux de comptage de gammas prompt corrélés. Puisque l'objectif de cette étude est surtout de démontrer la faisabilité de la méthode, l'analyse de données peut être faite malgré tout, et la sous-estimation peut être prise en compte lors de l'extrapolation des performances possibles avec un prototype clinique.

La figure 8.11 montre les profils obtenus avec et sans discrimination temps-de-vol ainsi que la différence entre les deux pour une acquisition avec la configuration A (gauche) et B

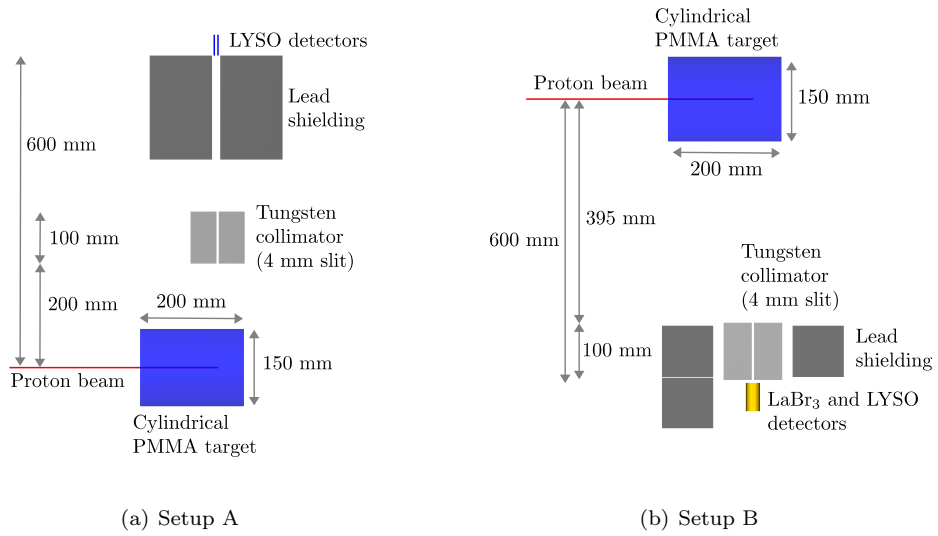


FIGURE 8.10 – Experimental setups from measurements with a single parallel slit. Both setups are shown in the way they would be seen from above and according to their orientation on the patient couch in the gantry treatment room, with the back of the gantry towards the top of the page and the beam coming from the left. The orientation may influence the observed background.

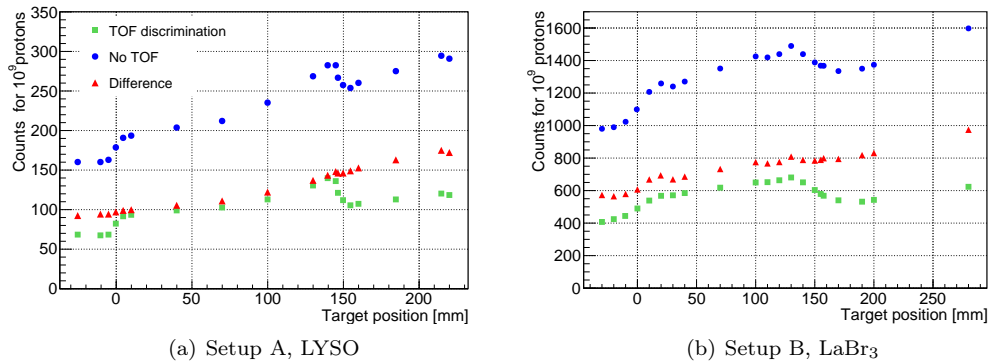


FIGURE 8.11 – Profiles acquired in 2011 with an LYSO detector and setup A (left) and profiles acquired with an LaBr<sub>3</sub> detector and setup B in 2012 (right). Profiles without any TOF discrimination shown as blue circles, With a TOF selection window of 4 ns as green squares, the difference as red triangles. A lower energy threshold of 1 MeV was set in both cases.

(droite). Notons que, suite à la façon dont le collimateur était placé, le champ de vue du détecteur et l'angle solide étaient plus grands pour la configuration B, ce qui explique les taux de comptage par proton très différents. On peut aussi observer que la largeur de la chute est plus grande pour configuration B, encore une fois dû au champ de vue plus large.

La discrimination temps-de-vol a le même effet dans les deux cas, réduisant le bruit de fond de environ 40%, correspondant à la fenêtre de temps de vol de 4 ns tous les 10 ns. La différence peut-être la plus intéressante entre les deux mesures est la pente apparente du bruit de fond. Alors que pour la configuration A, le bruit de fond double presque entre le premier point de mesure à  $-25$  mm avant la cible et le dernier point à  $220$  mm, pour la configuration B le bruit de fond augmente seulement de 50% sur le même intervalle. En général, la pente observée du bruit de fond est dû à l'émission anisotrope des neutrons. La différence observée entre les deux configurations peut être expliquée par le blindage différent utilisé dans les deux cas. D'autres simulations et, idéalement, mesures devrait être faites pour mieux comprendre ces observations.

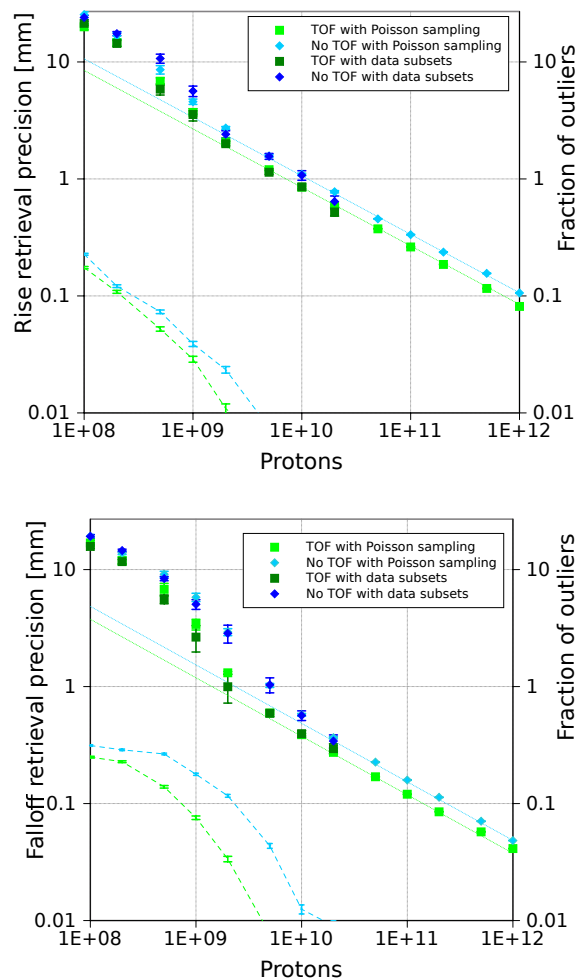


FIGURE 8.12 – Retrieval precision ( $1\sigma$ ) with and without TOF, using Poisson generation and data subsampling (full symbols and dotted lines) and corresponding fraction of outliers (dashed lines) for the entrance rise (above) and the falloff (below).

Les profils sont analysés de la façon décrite dans la section 8.2.1 et une précision de la mesure est obtenue. Les résultats de l'analyse sont décrits dans la figure 8.12 qui montre la relation entre le nombre de protons et la précision ainsi que la fraction de outliers. Ceci a été calculé à la fois à l'aide de sous-ensembles des données de mesure et en utilisant un générateur de Poisson. Les barres d'erreur représentent une estimation d'une déviation

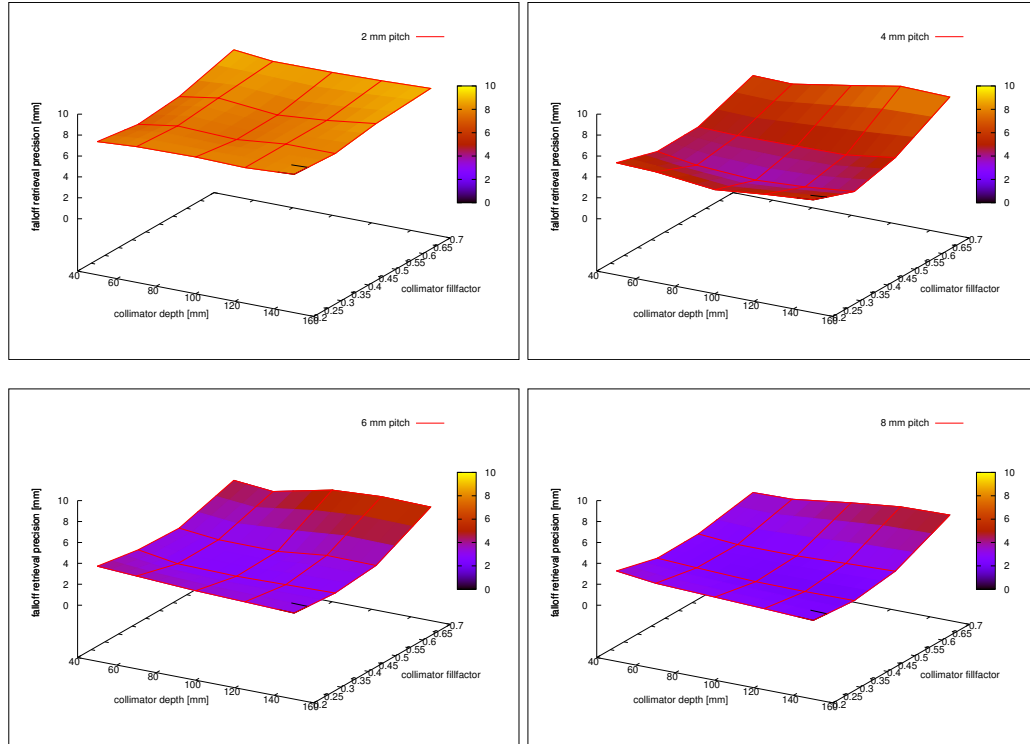


FIGURE 8.13 – Influence of the collimator properties : depth, pitch and fill factor. Simulated configurations are at the crossing of the red mesh, colors show interpolation of the FRP values. Simulation conducted with  $5 \times 10^9$  protons, subsamples corresponding to  $5 \times 10^7$  protons.

standard de valeurs.

Pour des rapports contraste-sur-bruit larges (grand nombre de protons), la précision est proportionnelle à l'inverse de la racine carrée du nombre de protons. Ceci est illustré par le comportement linéaire avec une pente de  $-1/2$  dans le graphe log-log. En d'autres termes, la précision dépend principalement du rapport contraste sur bruit. Pour un faible nombre de protons, l'apparition des outliers commence à détériorer la précision et les valeurs s'écartent du comportement inverse de la racine carrée.

### 8.3.3 Simulations pour l'optimisation du collimateur

Puisque un grand nombre de paramètres doit être optimisé et qu'ils sont a priori interdépendants, l'espace de paramètres dans lequel l'optimum doit être trouvé est multi-dimensionnel. Un essai a été fait d'utiliser une méthode de simplex pour trouver l'optimum (méthode : [Nelder and Mead \[1965\]](#)), mais dû à des régions relativement plates dans la fonction de la précision, ces méthodes atteignent rapidement une région de l'espace de paramètres où les erreurs sont plus grandes que les vraies différences dans les performances. Une approche plus systématique a alors été choisie.

En premier lieu, certains paramètres ont été fixés : la distance collimateur-patient, la hauteur de la caméra, la profondeur du cristal et le champ de vue total de la caméra. En premier aperçu de l'espace des paramètres qui définissent le collimateur (pas, profondeur, et facteur de remplissage) a été réalisé pour avoir une idée des tendances. Le résultat est présenté en figure 8.13. Quand on regarde les tendances pour les différents paramètres, on observe généralement un seul minimum est observé. En outre, le minimum semble relativement large et plat, ce qui conduit à une sorte de région optimale avec des performances très semblables dans la marge d'erreur.

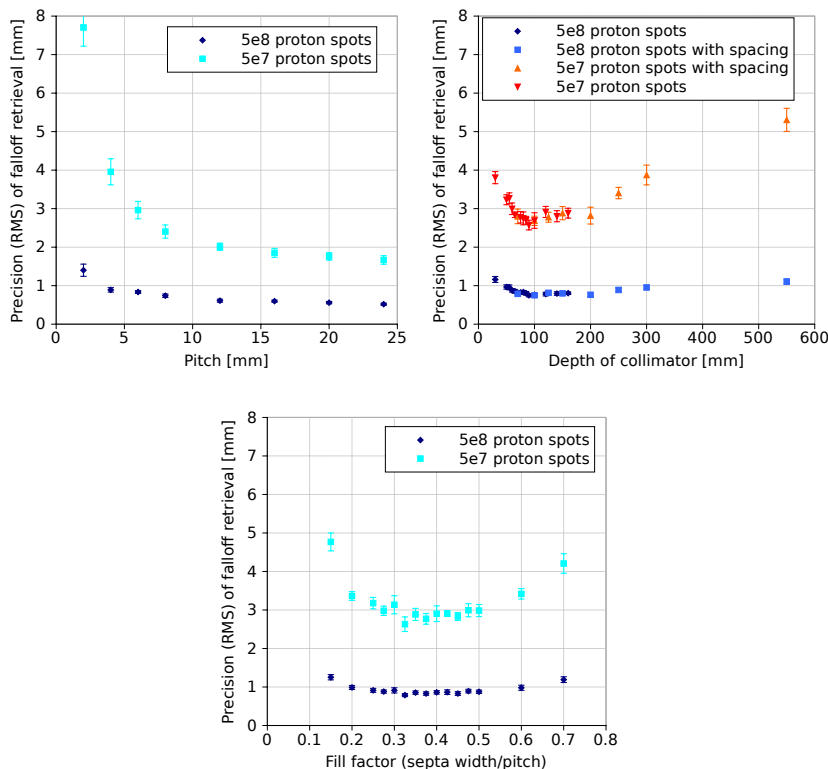


FIGURE 8.14 – Dependence of obtained precision on different parameters of the parallel-slit collimator.

Les profils ont été comparés et évalués en deux étapes. Dans un premier temps, mes propriétés du profil lui-même : le bruit de fond, le contraste, la relation contraste/bruit et la largeur de la chute (corrélé à la résolution spatiale). Dans un deuxième temps, une évaluation de la précision qui peut être obtenue avec un nombre donnée de protons. Deux points ont été choisis comme référence :  $5 \times 10^7$  et  $5 \times 10^8$  protons, en accord avec la section 8.2.1.

Afin d'évaluer les propriétés du profil, une fonction NURBS a été utilisée, comme décrit dans la section 8.2.1.

L'optimisation a été faite sans considération de la possibilité d'utiliser le temps de vol. Une autre étude d'optimisation prenant en compte la meilleure utilisation du temps de vol a été faite ailleurs (Pinto et al. [2013]). En conséquence, le choix a été fait de placer la caméra aussi proche du patient que possible sans trop d'inconvénients pour le patient afin d'avoir un angle solide large avec une quantité de cristal limitée. La valeur choisie pour cette distance est de 20 cm.

La hauteur de la caméra est fixée à 20 cm, ce qui semble un choix réaliste vu les contraintes de place.

Dans la figure 8.14 peut être vu l'influence des paramètres du collimateur sur la précision obtenue.

En premier lieu, il y a le pas du collimateur. L'influence du pas peut être comprise en regardant l'influence sur l'efficacité du collimateur, qui augmente avec le pas. Puisque le bruit de fond est peu influencé par le pas, puisque la quantité de matériel dans le collimateur reste le même, on peut s'attendre à ce que la précision s'améliore.

La profondeur du collimateur a l'effet d'améliorer la résolution spatiale du collimateur, mais limite l'efficacité. Pour des petites profondeurs, la collimation n'est pas suffisante pour avoir une bonne précision, alors que pour des très grandes profondeurs, l'efficacité moindre mène à des précisions moins bonnes. La profondeur optimale est entre les deux, autour de 70 mm à 130 mm (dans cette région, la précision varie peu).

Collimator depth	70 mm
Pitch	6 mm
Fill factor	0.35
Beam-collimator distance	200 mm
Collimator-crystal distance	0 mm
Crystal width	3.9 mm

TABLE 8.3 – Optimized configuration for the multi-parallel-slit collimator

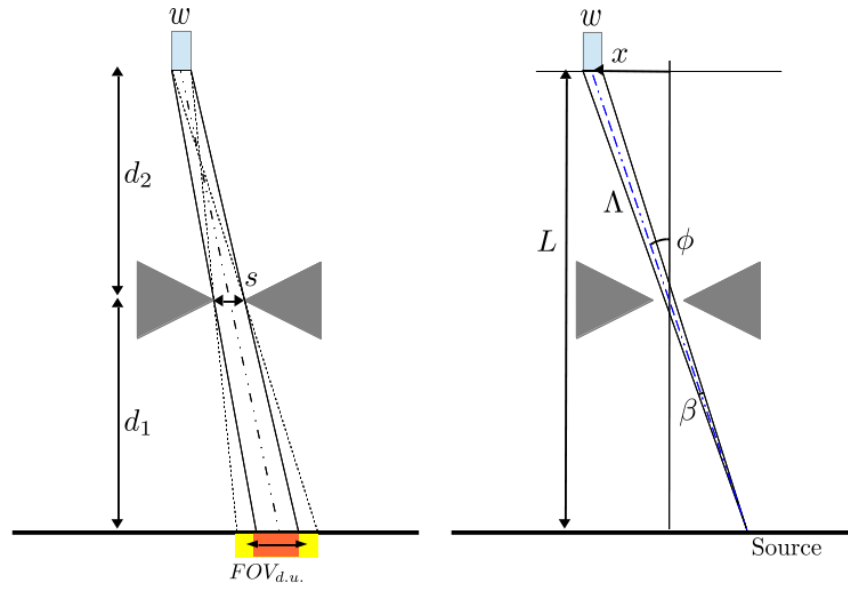


FIGURE 8.15 – Illustration of the calculation of the detector unit field of view and the detector solid angle for the knife-edge slit camera

Le facteur de remplissage optimal, de façon similaire à ce qui peut être observé pour la profondeur, constitue un compromis entre une bonne collimation (peu de pénétration des septa) et une bonne efficacité. Les meilleurs résultats sont obtenus pour des facteurs de remplissage entre 0.3 et 0.5.

Les paramètres de la configuration finale choisie peuvent être trouvés dans le tableau 8.3.

## 8.4 Le collimateur «knife-edge»

### Le principe géométrique

Le champ de vue de la source d'une unité du détecteur à travers la fente du collimateur knife-edge est défini comme la partie qui peut être vue de chaque point du cristal (en orange dans la figure 8.15) plus la moitié des deux pénombres (en jaune). Puisque les deux pénombres sont de la même taille, cela est égal à la partie centrale plus une pénombre :

$$FOV_{d.u.} = s \left( 1 + \frac{d_1}{d_2} \right) = \frac{sL}{d_2} \quad (8.2)$$

Comme pour la caméra à fentes parallèles, le champ de vue d'une unité du détecteur a une influence directe sur la résolution spatiale du système. Si un point source bouge à travers le champ de vue, le signal sur l'unité de détecteur est réduit de moitié quand le point source atteint le bord du champ de vue, ce qui veut dire que la taille du champ de vue est

en même temps la largeur à mi-hauteur de la PSF du collimateur. Les termes champ de vue et résolution spatiale du collimateur sont alors interchangeables.

Le champ de vue total de la caméra est défini comme l'espace qui peut être vu par la caméra complète et est limité par l'angle du collimateur :

$$FOV_{total} = \frac{2d_1}{\tan(\alpha)} + s \quad (8.3)$$

L'efficacité de collection d'un cristal à travers la fente peut être défini en analogie avec le collimateur à fentes parallèles comme :

$$CE = FOV_{d.u.} \times \Omega_D \quad (8.4)$$

$$\begin{aligned} &= \frac{sL}{d_2} \frac{1}{4\pi} \frac{wH}{L^2 \left(1 + \frac{x^2}{d_2^2}\right)^{3/2}} \\ &= \frac{swH}{4\pi d_2 L} \frac{1}{\left(1 + \frac{x^2}{d_2^2}\right)^{3/2}} \end{aligned} \quad (8.5)$$

et l'efficacité de collection linéaire par unité de longueur peut être obtenue en divisant par l'épaisseur du cristal,  $w$  :

$$LE = \frac{sH}{4\pi d_2 L} \frac{1}{\left(1 + \frac{x^2}{d_2^2}\right)^{3/2}} \quad (8.6)$$

**Ouverture effective de la fente** Aux énergies élevés des prompts gamma, une partie non-négligeable des particules traverse les bords de la fente du collimateur. Cet effet peut être décrit de façon approximative en introduisant une ouverture effective. Cette valeur d'ouverture effective peut être utilisée à la place de l'ouverture géométrique dans les calculs de champ de vue et efficacité. L'ouverture effective est définie comme l'ouverture d'un collimateur idéal qui laisse passer la même quantité de photons que le collimateur réel.

[Metzler \[2005\]](#) proposent une méthode pour l'estimation de l'ouverture effective prévue spécifiquement pour le calcul de la résolution spatiale. L'expression est basée sur une coupure à travers une géométrie pinhole et peut être appliqué directement à un collimateur knife-edge sans modification. Pour une source dans le centre du champ de vue, c'est :

$$s_e = s + \frac{\ln 2}{\mu \tan(\alpha)} \quad (8.7)$$

où  $\mu$  est le coefficient d'atténuation linéaire dans le matériel du collimateur et  $\alpha$  l'angle d'ouverture du collimateur.

La figure 8.16 montre une simulation de Monte Carlo des proportions de particules qui ont été détectées après avoir traversé le mur du collimateur, après avoir traversé le bord de la fente ou après être passé au travers de la fente. Les coups ayant traversé le bord de la fente montrent un profil corrélé à la dose, mais avec une largeur de la chute plus grande. La combinaison de particules ayant traversé la fente et le bord de la fente correspond au champ de vue effectif. La distribution de particules ayant traversé le mur est quasiment plate.

### 8.4.1 Optimisation par simulation de Monte Carlo

Une étude par simulation de Monte Carlo à été réalisée par [Smeets \[2012\]](#), en utilisant le code MCNPX afin d'optimiser la configuration knife-edge pour l'application à la protonthérapie. Les profils étaient estimés par une fonction à trois lignes droites et évalués sur base du contraste, du bruit de fond et de la largeur du falloff. Des paramètres optimaux ont été

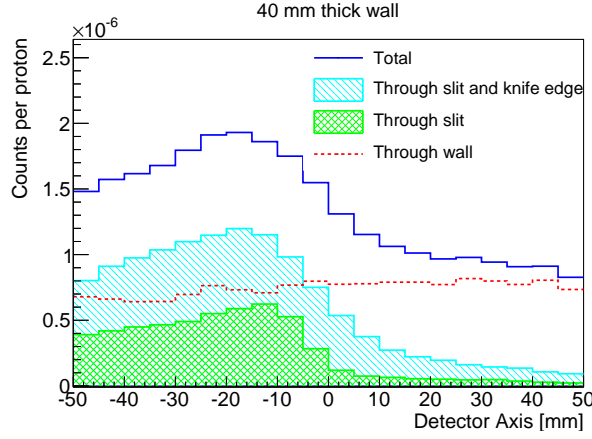


FIGURE 8.16 – Proportion of particles passing through the collimator wall, through the slit edge and through the slit itself for the final knife-edge configuration.

Symbol	Parameter	Value
$d_1$	Patient-collimator distance	150 mm
$d_2$	Collimator-Crystal distance	150 mm
$T$	Collimator wall thickness	40 mm
$s$	Slit opening	6 mm
$\alpha$	Collimator angle	$63.4^\circ$
$d_c$	Crystal depth	10 mm
$w$	Crystal width	5 mm

TABLE 8.4 – Default settings for the knife-edge collimator

choisis, en se basant sur des compromis entre ces facteurs de mérite et en utilisant des considérations pratiques comme le poids du collimateur et le taux de comptage attendus.

Afin de rendre les deux systèmes comparables, l'analyse décrite en section 8.2.1 a été appliquée aux profils obtenus par J. Smeets. Le choix des paramètres du collimateur ont été évalués sur base de la FRP et de la résolution spatiale.

Tous les paramètres de la caméra knife-edge n'ont pas été re-examinés. Quelques-uns, comme la hauteur de la caméra et la profondeur du cristal, ont des comportements facilement prévisibles analogues à ce qui a été observé pour la caméra multi-fentes dans la section 4.3.

Nous montrons ici l'effet de l'épaisseur du mur du collimateur, l'angle et l'ouverture de la fente, un par un, en gardant les autres fixés à leur valeur finale. Les valeurs par défaut sont décrites dans le tableau 8.4.

Figure 8.17 montre la dépendance de la précision et de la résolution spatiale des paramètres du collimateur, comme l'épaisseur du mur (dessus), l'angle (milieu) et l'ouverture de la fente (en bas).

Pour l'épaisseur du collimateur, il est intéressant de noter que, pour un collimateur parfait (toute particule qui touche le collimateur est absorbé), l'épaisseur n'a aucune influence sur le champ de vue et la résolution spatiale ou sur l'efficacité de collection. Par conséquent, l'épaisseur n'importe uniquement quand il y a un nombre significatif de particules qui traversent le matériau. Ces particules ne sont pas collimatées et contribuent au bruit de fond, indiquant qu'un collimateur épais est un meilleur choix de ce point de vue. D'après la figure 8.17, la précision s'améliore jusqu'à environ 40 mm d'épaisseur.

L'angle d'ouverture, comme l'épaisseur, n'influe ni la résolution spatiale ni l'efficacité dans le cas d'un collimateur parfait. L'influence principale de l'angle va être dans le nombre de gammas qui traversent le bord de la fente, et donc dans l'ouverture effective. Comme

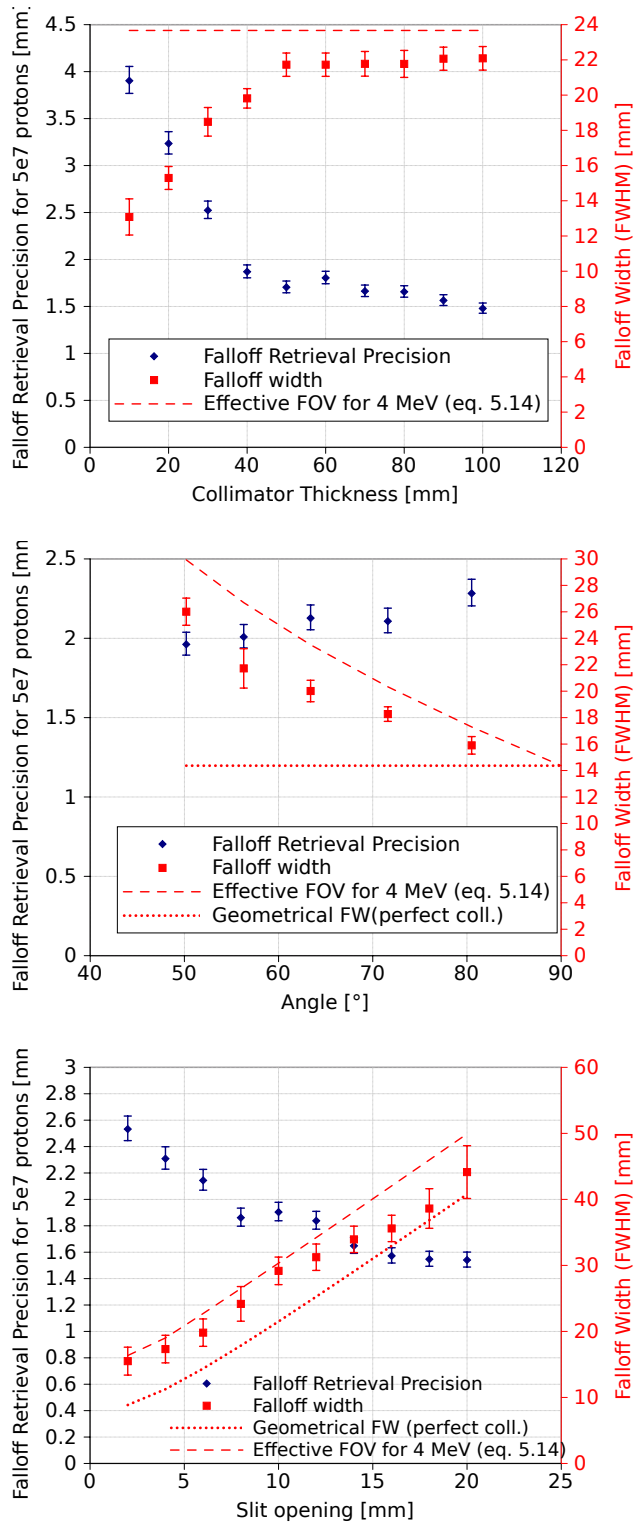


FIGURE 8.17

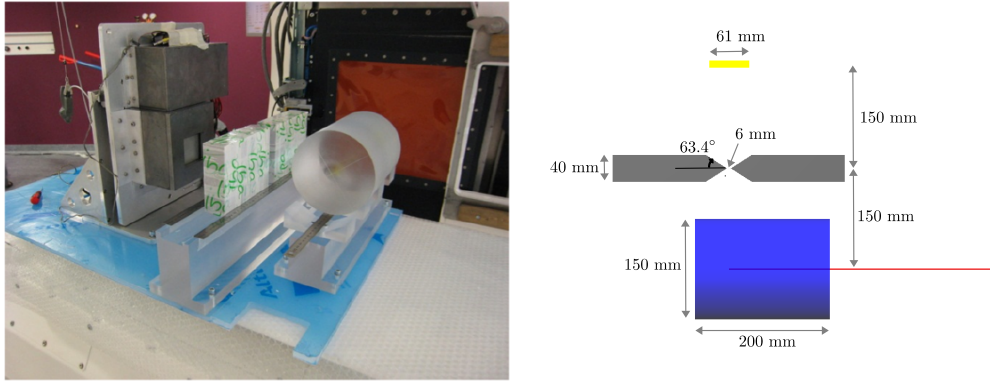


FIGURE 8.18 – Photograph of the setup of experiments with the knife-edge slit prototype and sketch as seen from above.

on peut le constater dans la figure 8.16, ce sont des gammas qui sont corrélés avec le profil de dose, mais ont une largeur de la chute plus grande. Figure 8.17 montre que le meilleur contraste dû aux photons traversant le bord de la fente mène à une précision meilleure pour de petites valeurs de l'angle, alors que la résolution spatiale se dégrade dû à l'ouverture effective plus grande.

L'ouverture du collimateur rentre de façon linéaire dans les équations (5.1) et (5.8), on peut donc s'attendre à ce que le contraste et la largeur de la chute dépendent de façon linéaire de l'ouverture. Cela correspond à une fraction croissante de photons transmis à travers l'ouverture qui contribuent au signal corrélé. D'une façon analogue à ce qui a été discuté pour le pas du collimateur à fentes parallèles, l'ouverture de la fente peut être utilisé pour ajuster le compromis entre la précision et la résolution spatiale.

#### 8.4.2 Validation expérimentale

Afin de valider la configuration de la caméra knife-edge obtenue par simulation, des expériences ont été faites sur faisceau proton aux Westdeutsche Protonentherapiezentrum à Essen (WPE) en 2011 et 2012. Une description détaillée des manipulations peut être trouvée dans Smeets et al. [2012] et Smeets [2012], chapitre 5. Une description détaillée du détecteur peut être trouvée dans Peloso et al. [2010] et Perali et al. [2012]. Les données utilisées pour l'évaluation de la précision ont été obtenues en mars 2012 et décrits dans Smeets [2012], section 5.7. Comparé aux mesures faites en 2011 et utilisés dans Smeets et al. [2012], ces acquisitions profitent d'une stabilité de faisceau améliorée, pendant que la configuration de la caméra et le traitement des données reste le même.

Nous allons que brièvement rappeler la configuration expérimentale utilisée et le traitement des données dans les pages qui suivent.

La configuration utilisée pour la manipulation avec le collimateur knife-edge est la configuration finale de l'optimisation, sauf que le détecteur était de taille plus réduite et utilisait un cristal monolithique avec une logique Anger au lieu d'un cristal segmenté. Figure 8.18 montre une photo de la manipulation à gauche et un dessin vu d'au-dessus à droite.

En plus des mesures réalisées avec une géométrie optimisée, des mesures ont aussi été faites avec un collimateur complètement fermé, en joignant les faces planes des blocs du collimateur. Cela permet de faire une mesure du bruit de fond uniquement, ce qui est utile pour la comparaison avec les simulations.

Des énergies faisceau de 100 MeV, 160 MeV et 230 MeV ont été testées pour avoir une idée de la dépendance en énergie. Pour chaque énergie du faisceau, la fente du collimateur et la caméra étaient placés face à la profondeur de parcours attendue dans la cible. Le nombre de protons était mesuré par une chambre à ionisation dans la nozzle. Puisque la caméra ne pouvait pas fonctionner aux taux de comptage élevés correspondant à des courants cliniques, le courant faisceau a été baissé de deux ordres de grandeur.

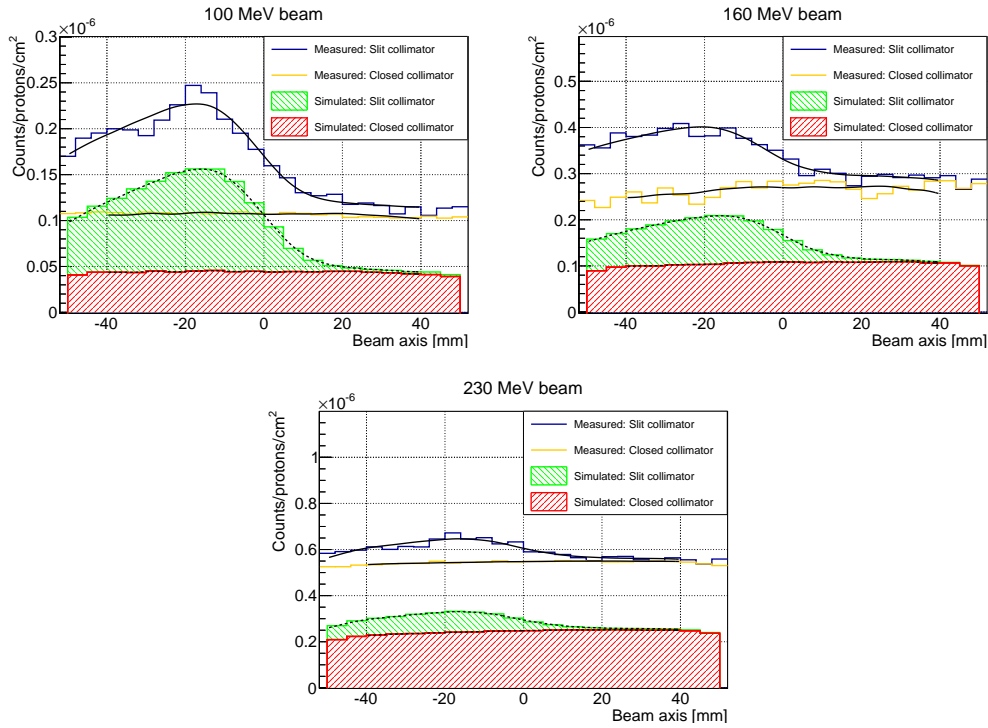


FIGURE 8.19 – Comparison of the profiles measured with HiCam for 100 MeV, 160 MeV and 230 MeV beams with the profiles predicted by simulation. Superposed as black dashed lines are NURBS fits of the simulated profiles and as black solid lines the same NURBS fits adjusted with a factor and x- and y-offsets to the measured profiles.

Beam energy	100 MeV	160 MeV	230 MeV
x-offset [mm]	1.33	4.01	0.01
factor	1.00	1.10	1.16
y-offset [counts/p/cm <sup>2</sup> ]	0.07E-6	0.17E-6	0.26E-6

TABLE 8.5 – Values of matching between the NURBS fit of the simulated profiles and the measured profiles.

Afin d'avoir des profils utilisables, plusieurs corrections et filtres ont dû être appliqués aux données. Pour compenser le nombre de coups éliminés par les filtres, un facteur de correction a été appliqué. Un facteur de correction de 1,37 pour le temps mort du système d'acquisition a aussi été utilisé.

Comme la réponse du détecteur n'était pas complètement uniforme, une correction d'uniformité a dû être appliquée. A cet effet, à la fois une acquisition «inondation» sans collimateur et une acquisition avec un mur de collimateur fermé ont été réalisées, sur la base du principe que ces images devraient conduire à des profils presque plans, où toute non-uniformité pourrait être facilement identifiée et des facteurs de correction pour chaque pixel pourrait être générés.

**Comparaison à la simulation** La figure 8.19 montre les profils mesurés pour les énergies de faisceau de 100 MeV, 160 MeV et 230 MeV avec le collimateur ouvert et fermé. Les profils sont montrés en unités de coups/proton/cm<sup>2</sup> afin d'éliminer l'influence de l'angle solide, qui est différent. Les profils mesurés ont beaucoup plus de coups que les profils simulés. Afin d'examiner l'origine des coups supplémentaires, les NURBS  $f$  des profils simulés du collima-

teur ouvert ont été adaptés aux mesures en appliquant un offset en  $x$ ,  $o_x$ , un offset en  $y$ ,  $o_y$  et une multiplication par un facteur  $m$  :  $f_{adj}(x) = m \times f(x + o_x) + o_y$ . Les valeurs obtenues sont listées dans le tableau 8.5. Après les ajustements, les formes du profil correspondent très bien, indiquant que la forme et la largeur de la chute sont très bien prédits par les simulations.

Actuellement, l'origine du offset en  $y$  est inconnue. Le même effet peut être observé pour les profils collimateur ouvert et fermé, indiquant que les simulations sous-estiment de façon significative le bruit de fond, alors qu'ils prédisent plutôt bien ce qui passe à travers la fente et donc le contraste. Fait intéressant, toutefois, de nouvelles mesures avec un nouveau prototype knife-edge (voir la section 6.5) ne semblent pas montrer de tels écarts importants avec des simulations.

## 8.5 Comparaison et conclusion

**Bruit de fond** Le bruit de fond peut essentiellement être partagé en trois contributions (si on laisse de côté le bruit de fond ambiant de la salle) : celle des gammas prompts qui ont traversé les septas du collimateur ou le mur ; celle des neutrons qui ont traversé le collimateur et celle des particules qui ont été diffusés ou ont réagi en produisant des particules secondaires dans le collimateur. La première contribution dépend de l'atténuation par le collimateur, qui dépend à son tour de l'épaisseur (effective) du collimateur. La contribution directe de neutrons dépend de l'angle solide sous lequel les neutrons «voient» le collimateur et la position du détecteur en relation à l'émission de neutrons. La dernière contribution dépend de l'angle solide du collimateur, de la quantité de matériel du collimateur (i.e.  $T_{(e)}$ ), de l'auto-atténuation du collimateur ( $T_{(e)}$ ) et de l'angle solide entre le détecteur et le collimateur.

Il est nécessaire de disposer de plus de simulations et de données expérimentales pour analyser quantitativement le bruit de fond. Cependant, des analyses qualitatives comparatives entre les deux géométries sont possibles.

Un avantage de la géométrie knife-edge est le fait que l'épaisseur  $T$  n'influence pas les autres propriétés du collimateur et peut être choisi librement afin de minimiser le bruit de fond. Pour le collimateur à fentes parallèles, l'épaisseur effective  $T_e = Df$  est conditionnée par la profondeur et le facteur de remplissage, qui influencent aussi l'efficacité et la résolution spatiale.

**Résolution spatiale** La résolution spatiale est un facteur potentiellement important dans la capacité d'observer des fluctuations dues aux inhomogénéités. En essayant d'atteindre une résolution spatiale très bonne (i.e. un champ de vue de l'unité du détecteur très petit), le collimateur à fentes parallèles a clairement un avantage. En effet, la résolution spatiale peut être réduite à une faible valeur (aussi petite qu'on le souhaite), en réduisant, par exemple, le pas du collimateur.

Pour la caméra knife-edge, une amélioration de la résolution spatiale n'est pas aussi triviale. Même avec une fente géométrique complètement fermée, l'effet de pénétration des bords de la fente conduit à avoir une ouverture effective qui entraîne une résolution spatiale plus grande que zéro. Cela veut dire qu'en pratique, la résolution spatiale a une limite inférieure. Pour le moment, il semble que ce qui soit atteignable avec la caméra knife-edge est suffisant, puisqu'il semble improbable qu'une résolution spatiale meilleure que la largeur du falloff à l'émission soit nécessaire.

**La précision** Dans les sections 4.3.5 et 5.4, nous avons vu quelle est la précision atteignable avec chacune des configurations optimisées. Toutefois, puisque le compromis entre précision et résolution spatiale n'est pas le même dans les deux cas, une comparaison directe est trompeuse. Nous allons plutôt regarder une série de configurations pour chaque concept de collimateur et voir quels sont leur performance en termes de précision et de résolution spatiale.

La première conclusion qui peut être tirée de la figure 8.20 est que les performances sont remarquablement similaires. La configuration 150 :150 de la caméra knife-edge a des

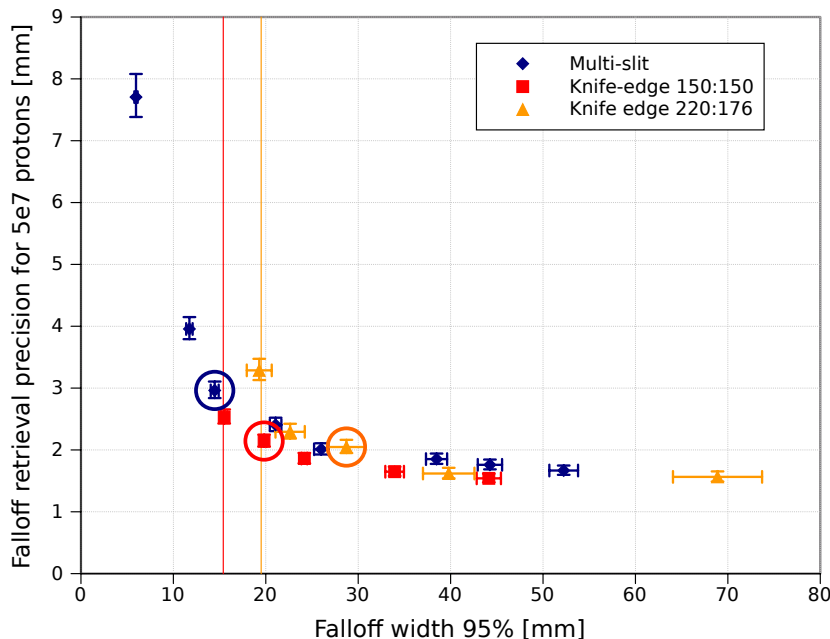


FIGURE 8.20 – Graph showing the trade-off between the falloff width and FRP for different configurations of both cameras. The parallel-slit camera is shown in blue diamonds, the optimized knife-edge configuration in red squares. In orange triangles is shown a modified knife-edge configuration with  $d_1 : d_2 = 220 \text{ mm} : 176 \text{ mm}$  to have the same beam-collimator entrance distance as the multi-slit collimator. The optimized configurations are circled and the intrinsic limit of the knife-edge collimator is indicated with a vertical line.

performances un peu meilleures que les deux autres, dû au fait qu'elle bénéficie d'un angle solide plus grand, étant plus proche du faisceau. Il y a une région, entre 20 et 30 mm de largeur de la chute, où toutes ont des performances similaires, donnant des résultats juste au-dessus de 2 mm pour la précision. Lorsqu'on va vers des valeurs plus petites de largeur de la chute, la performance du collimateur knife-edge se dégrade plus rapidement. D'un autre côté, si la priorité est à une meilleure précision, la caméra knife-edge a de meilleures performances dans cette région.

Les configurations optimisées, cerclées dans le graphe, le sont pour des compromis légèrement différents. Un choix final du compromis idéal ne peut être fait en considérant uniquement des cibles hétérogènes.

## Conclusion

Les études d'optimisation des deux caméras ont montré qu'il n'y a pas de gagnant clair entre les deux configurations. Comme le démontre la figure 8.20, les performances sont très similaires pour les configurations optimisées. Alors que la caméra à fentes parallèles peut plus facilement être configurée pour une très bonne résolution spatiale, la caméra knife-edge a un léger avantage lorsqu'une très bonne précision est désirée. Selon les qualités requises, l'une ou l'autre des caméras peut être une bonne solution. D'autres considérations comme le poids, la taille et le coût mènent également à des conclusions très similaires, comme les chapitres 4 et 5 le détaillent.

La caméra à fentes parallèles peut offrir l'avantage d'un champ de vue étendu au besoin, ce qui permet d'imager la trajectoire entière des protons, y compris l'entrée dans la cible. Considérant cet avantage et le fait qu'il n'y ait pas de distorsion vers les bords du champ de vue, la caméra ne devrait pas nécessairement être décalée en cours de mesure, ce qui est un avantage clair pour un premier prototype. Moins de distorsion signifie aussi que les effets des hétérogénéités proches des bords du champ de vue peuvent plus facilement être identifiés,

surtout si une configuration à bonne résolution spatiale est choisie.

Un risque possible pour la configuration multi-slit est le fait que la géométrie n'a pas été validée pour des faisceaux de plus haute énergie; les mesures (6.5) semblent indiquer que la performance à ces hautes énergies n'est pas idéale. Comme la caméra multi-slit est en général plus sensible au bruit de fond que la caméra knife-edge, cela peut être un problème à de plus hautes énergies, qui ont en général un bruit de fond plus élevé. Sur ce sujet, des études supplémentaires sont nécessaires.

La caméra knife-edge a été testée jusqu'à des énergies de faisceau de 230 MeV et la performance semble adéquate. Dans le cas où les mesures indiquent qu'on peut s'attendre à un bruit de fond élevé, l'épaisseur du mur peut plus facilement être ajustée.

Un nombre d'études restent à faire avant de pouvoir faire un choix clair entre les deux configurations de caméra. L'origine du désaccord entre le bruit de fond prédit par les simulations et ce qui a été mesuré n'est pas connu et mérite investigation. Un nombre cas hétérogènes typiques doivent être étudiés pour pouvoir décider du meilleur compromis entre résolution spatiale et précision dans un contexte clinique. Une étude de la caméra à fentes parallèles à plus haute énergie est nécessaire pour lever le risque de plus mauvaises performances pour tumeurs profondes. Et enfin, l'intégration dans la routine clinique doit être étudié et un logiciel permettant l'utilisation d'une telle caméra pendant les traitements doit être développé.

# Appendices



# Appendix A

## NURBS

The acronym NURBS stands for Non-Uniform Rational B-Splines. NURBS are mostly used to mathematically describe and model free-form curves or surfaces. For more details on NURBS, see for example [Piegl and Tiller \[1997\]](#); [Farin \[1992\]](#); [Rogers \[2001\]](#).

They are well suited to the problem of fitting the prompt-gamma profiles because they can be made to take any shape and will adapt to the profiles encountered for different camera types. For example, they will follow a curved background or plateau shape in a way that a three-line or erf approach do not and they can seamlessly fit the whole profile including entrance and falloff. NURBS rely on no assumptions about the shape of the profile. They inherently lead to some smoothing (depending on the degree of the NURBS), but remain vulnerable to random fluctuations in the profile.

A NURBS is described by a parametric function that is defined piecewise by polynomials joined at points called knots. The shape is determined by a set of points called control points and the degree of the NURBS, which is also the degree of the polynomials used. Each point along the curve can be described as a weighted sum of a set of control points. NURBS are described by a parametric equation, with the parameter  $u$  controlling the weight of each control point. The functions describing the weight of each control point as a function of the parameter  $u$  are polynomial and are referred to as basis functions. Only a limited number of basis functions (determined by the degree) are active at any time, the rest are set to zero. At each knot, one control point is discarded by setting its basis function to zero, and another control point is added. In this way, control points only influence the NURBS locally.

To summarize:

**Parameter  $u$**  is the variable in which the parametric basis functions are expressed.

**Control points** are the input into the function and determine the shape. Each point along the curve is a weighted sum of control points. Except for first-order NURBS, the curve does not have to go through the control points. There are  $n_c$  control points.

**Basis functions** are the polynomial functions that determine the weights used to sum the control points. They are functions of the parameter  $u$  and there is one for each control point. They are normalized so that their sum at any point is 1.

**The order** of the NURBS is the order of the basis functions. The order is denoted  $k$ .

**Knots** are the places on the curve where one control point becomes active and another is discarded. The basis functions for both these points are zero at the place of the knot. The  $k^{th}$  derivative in this point can be discontinuous. There are  $n_c + k + 1$  knots.

**Weights** can be additionally specified for each control point. The basis function is then multiplied by this weight.

A mathematical expression of the k-order NURBS is as follows:

$$C_k(u) = \frac{\sum_{i=0}^{n_c} w_i P_i N_{i,k}(u)}{\sum_{i=0}^{n_c} w_i N_{i,k}(u)} \quad (\text{A.1})$$

where:

- $u$ : parametric variable
- $k$ : order of the NURBS
- $w_i$ : weights
- $P_i$ : control points
- $N_{i,k}$ : normalized B-spline basis functions

These B-splines are defined recursively as:

$$N_{i,k}(u) = \frac{u - t_i}{t_{i+k} - t_i} N_{i,k-1}(u) + \frac{t_{i+k+1} - u}{t_{i+k+1} - t_{i+1}} N_{i+1,k-1}(u) \quad (\text{A.2})$$

$$N_{i,0}(u) = \begin{cases} 1, & \text{if } t_i \leq u < t_{i+1} \\ 0, & \text{else} \end{cases} \quad (\text{A.3})$$

where  $t_i$  are the knots forming a unit vector.

$$U = \{t_0, t_1, \dots, t_m\} \quad (\text{A.4})$$

In the most simplified case, the weights can all be set to one and the knots can be set to be equidistant with  $t_{i+k} - t_i = a$ , simplifying the above equations to

$$C(u) = \frac{\sum_{i=0}^n P_i N_{i,k}(u)}{\sum_{i=0}^n N_{i,k}(u)} \quad (\text{A.5})$$

$$N_{i,k}(u) = \frac{1}{ka} ((u - t_i) N_{i,k-1}(u) + (t_{i+k+1} - u) N_{i+1,k-1}(u)) \quad (\text{A.6})$$

$$N_{i,0}(u) = \begin{cases} 1, & \text{if } t_i \leq u < t_{i+1} \\ 0, & \text{else} \end{cases} \quad (\text{A.7})$$

which corresponds to uniform rational b-splines, which are a special case of NURBS. The splines used from now on will always be uniform, but the nomenclature of NURBS is kept as that is the term commonly used in literature.

One can easily verify that the number of control points that contribute to any one point on the curve is equal to  $k + 1$  and that the basis functions that determine the weights are polynomials of the order  $k$ . The curve is continuously derivable in  $u$   $k - 1$  times.

For the beginning and end of the NURBS, in order to have  $k$  control points contributing, there are  $k$  equal knot values to start off the first  $k$  basis functions. This is called an “open uniform” knot vector. This results in the starting point of the curve being equal to the first control point (and the end point of the curve being equal to the last control point).

NURBS of different orders are shown in figure [A.1 on the facing page](#). The first-order NURBS is simply a linear interpolation between control points. As the order increases and more control points influence each point of the curve, it becomes smoother.

**Application to prompt-gamma profiles** When applied to a prompt-gamma profile, the measured points or histogram bins are used as control points for the function. The order three was chosen, this is the first order of NURBS that has continuous first and second derivatives, which is useful for a well-behaved  $\chi^2$ -function for fitting. At the same time, third-order NURBS has a small smoothing effect, but not so much that it smoothes out the peak. An example of the used NURBS applied to a simulated falloff profile is shown in figure [A.2 on page 162](#).

The simplest possible case is used, i.e. weights of all control points are one and the knots are uniformly distributed. It would be a possibility to adjust this, for example by increasing the weights of control points in the peak for it to be less smoothed or, for example, by having more control points in the falloff (or entrance, resp.) region, where the function

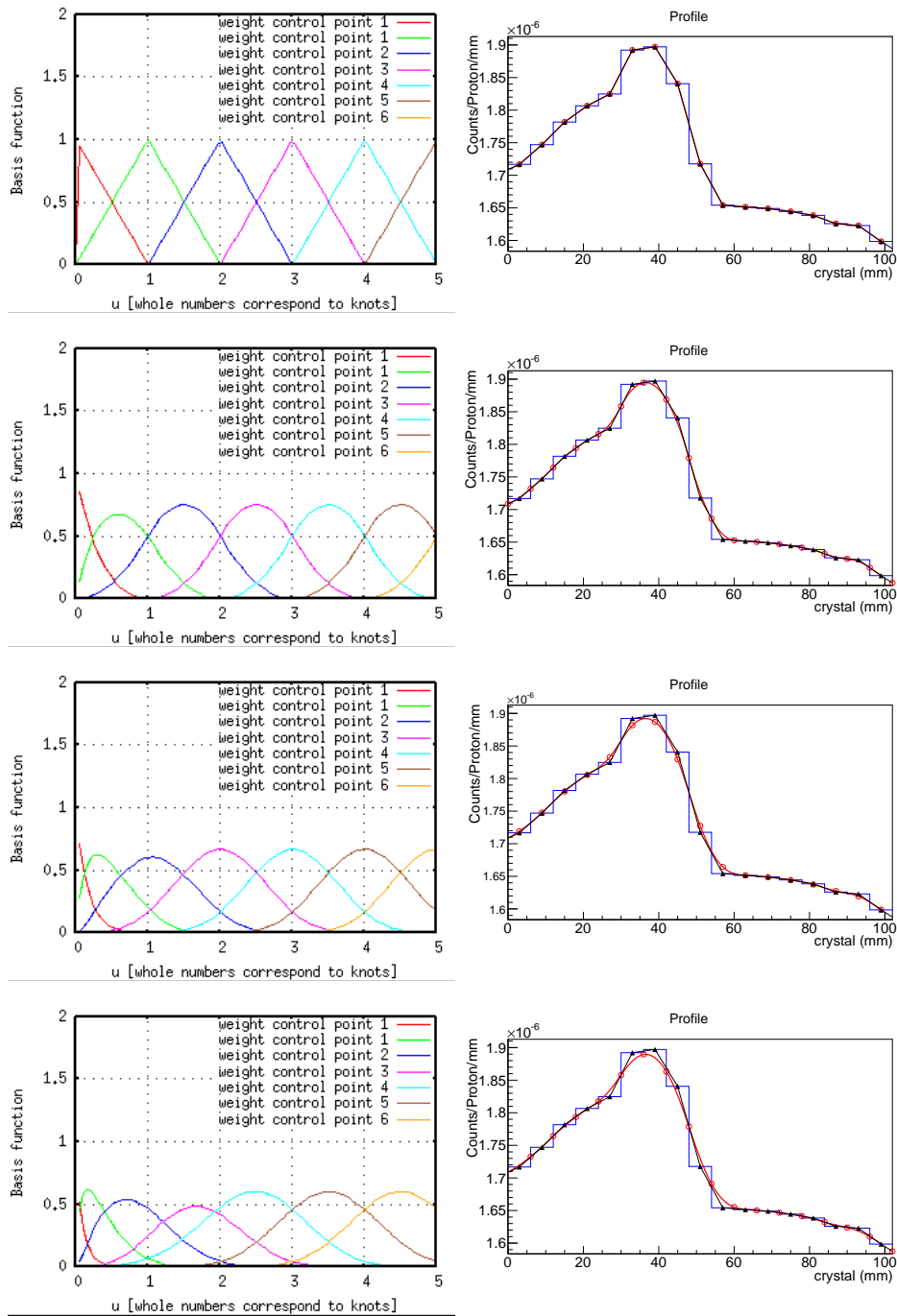


Figure A.1: NURBS of order 1, 2, 3 and 4: basis functions that give the weight for each control point (left) and application to an example profile (right). As the order increases, the area of influence of each control point increases and the curve becomes smoother.

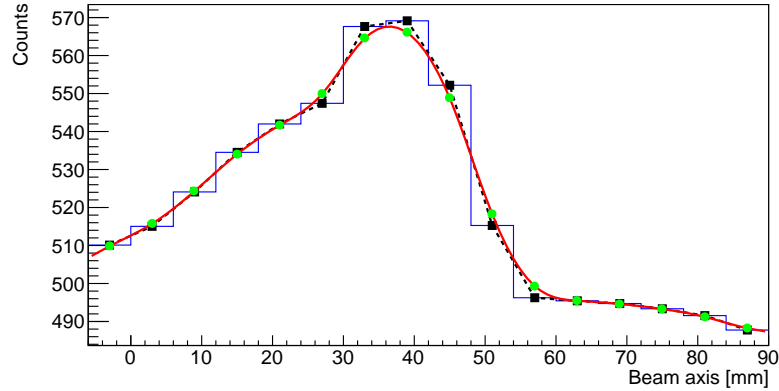


Figure A.2: Illustration of the NURBS principle as applied to a simulated prompt-gamma profile. The profile histogram is shown in blue. The centers of the profile bins are used as control points (black squares). The knots are shown as green circles and the NURBS they define as a red solid curve.

changes more quickly, while having less in the plateau region. This would lead to more smoothing in flat regions, which is desirable to get rid of statistical fluctuations. However, such a procedure would introduce a lot more adjustable parameters that would have to be optimized for each profile. For example, the distribution of control points and weights would have to be different for a low-count profile with a sharp falloff than for a high-count profile with a very smoothed-out falloff and different methods would have to be applied to measured and simulated profiles, between one camera and the other. This is the reason why, in the spirit of simplicity and comparability, the most basic settings of the NURBS were used at all times, with the weights of the individual control points all set to one and regular spacing between knots. For an analysis of the influence of these settings on the performance, see the individual sections on each profile type, for example [4.3.3 on page 71](#) on simulated profiles for the multi-slit configuration.

# Bibliography

- Anger, H. [1967], ‘Radioisotope cameras’, *Instrumentation in nuclear medicine* **1**, 485–552.
- Attanasi, F., Knopf, A., Parodi, K., Paganetti, H., Bortfeld, T., Rosso, V. and Del Guerra, A. [2011], ‘Extension and validation of an analytical model for in vivo PET verification of proton therapy—a phantom and clinical study.’, *Physics in Medicine and Biology* **56**(16), 5079–5098.
- Bentefour, E. H., Shikui, T., Prieels, D. and Lu, H.-M. [2012], ‘Effect of tissue heterogeneity on an in vivo range verification technique for proton therapy’, *Physics in Medicine and Biology* **57**(17), 5473.
- Bert, C., Grözinger, S. O. and Rietzel, E. [2008], ‘Quantification of interplay effects of scanned particle beams and moving targets’, *Physics in medicine and biology* **53**(9), 2253.
- Biegun, A., Seravalli, E., Lopes, P. C., Rinaldi, I., Pinto, M., Oxly, D. C., Dendooven, P., Verhaegen, F., Parodi, K., Crespo, P. and Schaart, D. R. [2012], ‘Time-of-flight neutron rejection to improve prompt gamma imaging for proton range verification: a simulation study’, *Physics in medicine and biology* **57**(20), 6429.
- Blomlie, V., Rofstad, E. K., Skjønberg, A., Tverå, K. and Lien, H. H. [1995], ‘Female pelvic bone marrow: serial MR imaging before, during, and after radiation therapy.’, *Radiology* **194**(2), 537–543.
- Bom, V., Joulaeizadeh, L. and Beekman, F. [2012], ‘Real-time prompt  $\gamma$  monitoring in spot-scanning proton therapy using imaging through a knife-edge-shaped slit.’, *Physics in medicine and biology* **57**(2), 297–308.
- Cambraia Lopes, P., Pinto, M., Simoes, H., Biegun, A., Dendooven, P., Oxley, D., Parodi, K., Schaart, D. and Crespo, P. [2012], Optimization of collimator designs for real-time proton range verification by measuring prompt gamma rays, in ‘Nuclear Science Symposium and Medical Imaging Conference (NSS/MIC), 2012 IEEE’, IEEE, pp. 3864–3870.
- Cee, R. [2012], ‘The HIT accelerator: A beam delivery system for a dedicated radiotherapy facility’.
- Chu, W., Ludewigt, B. and Renner, T. [1993], ‘Instrumentation for treatment of cancer using proton and light-ion beams’, *Review of Scientific Instruments* **64**(8), 2055–2122.
- Ciocca, M., Orecchia, R., Garibaldi, C., Rondi, E., Luini, A., Gatti, G., Intra, M., Veronesi, P., Lazzari, R., Tosi, G. and Others [2003], ‘In vivo dosimetry using radiochromic films during intraoperative electron beam radiation therapy in early-stage breast cancer’, *Radiotherapy and Oncology* **69**(3), 285–289.
- Crespo, P., Shakirin, G. and Enghardt, W. [2006], ‘On the detector arrangement for in-beam PET for hadron therapy monitoring’, *Physics in medicine and biology* **51**(9), 2143.
- De Rydt, M. [2013], ‘Monitoring of Hadron Therapy: Correlation between Density Variations in the Target and the Prompt-Gamma Profiles’, *submitted to Applied Physics Letters* .

- Dedes, G., Dauvergne, D., De Rydt, M., Freud, N., Krimmer, J., Létang, J.-M., Pinto, M., Ray, C. and Testa, E. [2012], Monte Carlo nuclear models evaluation and improvements for real-time prompt gamma ray monitoring in proton and carbon therapy, *in* '2012 IEEE Nuclear Science Symposium and Medical Imaging Conference Record (NSS/MIC)', pp. 2564–2565.
- Diblen, F., España, S., Van Holen, R. and Vandenberghe, S. [2012], Detector design for range monitoring in hadron therapy by means of image reconstruction, *in* 'IEEE Nuclear Science symposium and medical imaging', number 241851, pp. 3887–3889.
- Dowdell, S. J. [2011], Pencil beam scanning proton therapy : the significance of secondary particles, PhD thesis, University of Wollongong.
- Essers, M. and Mijnheer, B. [1999], 'In vivo dosimetry during external photon beam radiotherapy', *International Journal of Radiation Oncology, Biology, Physics* **43**(2), 245–259.
- Farin, G. [1992], *Courbes et surfaces pour la CGAO*.
- Frandes, M., Zoglauer, A., Maxim, V. and Prost, R. [2008], 'Compton-scattering based imaging system for hadron therapy monitoring', *2008 IEEE Nuclear Science Symposium Conference Record* pp. 4853–4859.
- Frandes, M., Zoglauer, A., Maxim, V. and Prost, R. [2010], 'A Tracking Compton-Scattering Imaging System for Hadron Therapy Monitoring', *IEEE Transactions on Nuclear Science* **57**(1), 144–150.
- Gensheimer, M. F., Yock, T. I., Liebsch, N. J., Sharp, G. C., Paganetti, H., Madan, N., Grant, P. E. and Bortfeld, T. [2010], 'In vivo proton beam range verification using spine MRI changes.', *International Journal of Radiation Oncology, Biology, Physics* **78**(1), 268–275.
- Gottschalk, B. [2004], *Passive Beam Spreading in Proton Radiation Therapy*.
- Grevillot, L. [2011], Monte Carlo simulation of active scanning proton therapy system with Gate/Geant4: Towards a better patient dose quality assurance, PhD thesis.
- Grevillot, L., Bertrand, D., Dessy, F., Freud, N. and Sarrut, D. [2011], 'A Monte Carlo pencil beam scanning model for proton treatment plan simulation using GATE/GEANT4.', *Physics in medicine and biology* **56**(16), 5203.
- Grevillot, L., Bertrand, D., Dessy, F., Freud, N. and Sarrut, D. [2012], 'GATE as a GEANT4-based Monte Carlo platform for the evaluation of proton pencil beam scanning treatment plans.', *Physics in medicine and biology* **57**(13), 4223.
- Gueth, P., Dauvergne, D., Freud, N., Létang, J. M., Ray, C., Testa, E. and Sarrut, D. [2013], 'Machine learning-based patient specific prompt-gamma dose monitoring in proton therapy', *Physics in Medicine and Biology* **58**(13), 4563–4577.
- Gunter, D. [2004], Collimator Design for Nuclear medicine, *in* 'Emission Tomography', chapter 8, p. 153.
- Jongen, Y. and Stichelbaut, F. [2003], 'Verification of the Proton Beam Position in the Patient by the Detection of Prompt gamma-Rays Emission'. 42nd Meet. Particle Therapy Co-Operative Group (PTCOG).
- Kim, C. H., Park, J. H., Seo, H. and Lee, H. R. [2012], 'Gamma electron vertex imaging and application to beam range verification in proton therapy', *Medical physics* **39**, 1001.
- Kim, D., Yim, H. and Kim, J.-W. [2009], 'Pinhole Camera Measurements of Prompt Gamma-rays for Detection of Beam Range Variation in Proton Therapy', *Journal of the Korean Physical Society* **55**(4), 1673.

- Knopf, A.-C. and Lomax, A. [2013], 'In vivo proton range verification: a review', *Physics in Medicine and Biology* **58**(15), R131–R160.
- Koehler, A. M. [1968], 'Proton radiography.'
- Kormoll, T., Fiedler, F., Schöne, S., Wüstemann, J., Zuber, K. and Enghardt, W. [2011], 'A Compton imager for in-vivo dosimetry of proton beams — A design study', *Nuclear Instruments and Methods in Physics Research Section A: Accelerators, Spectrometers, Detectors and Associated Equipment* **626-627**, 114–119.
- Kozlovsky, B., Murphy, R. J. and Ramaty, R. [2002], 'Nuclear Deexcitation Gamma Ray Lines from Accelerated Particle Interactions', *The Astrophysical Journal Supplement Series* **141**(2), 523.
- Kramer, S. L., Martin, R. L., Moffett, D. R. and Colton, E. [1977], Application of proton radiography to medical imaging, Technical report, Argonne National Lab., Ill.(USA).
- Krejcarek, S. C., Grant, P. E., Henson, J. W., Tarbell, N. J. and Yock, T. I. [2007], 'Physiologic and Radiographic Evidence of the Distal Edge of the Proton Beam in Craniospinal Irradiation', *Int J Radiation Oncol Biol Phys* **68**(3), 646–649.
- Krimmer, J. and al, E. [2014], To be published.
- Kurosawa, S., Kubo, H., Ueno, K., Kabuki, S., Iwaki, S., Takahashi, M., Taniue, K., Higashi, N., Miuchi, K., Tanimori, T., Kim, D. and Kim, J. [2011], 'Prompt gamma detection for range verification in proton therapy', *Current Applied Physics* **12**(2), 364–368.
- Le Foulher, F. [2010], Simulations Monte Carlo et mesures de l' émission de gamma prompts appliquées au contrôle en ligne en hadronthérapie, PhD thesis.
- Lee, H. R., Park, J. H., Kim, C. H. and Min, C. H. [2012], 'Design optimization of a 2D prompt-gamma measurement system for proton dose verification', *Journal of the Korean Physical Society* **61**(2), 239–242.
- Leunens, G., Van Dam, J., Dutreix, A. and der Schueren, E. [1990], 'Quality assurance in radiotherapy by in vivo dosimetry. 1. Entrance dose measurements, a reliable procedure', *Radiotherapy and Oncology* **17**(2), 141–151.
- Litzenberg, D. W., Bajema, J. F., Becchetti, F. D., Brown, J. A., Raymond, R. S., Roberts, D. A., Caraher, J., Hutchins, G., Ronningen, R., Smith, R. and Others [1992], On-line monitoring and PET imaging of proton radiotherapy beams, in 'Nuclear Science Symposium and Medical Imaging Conference, 1992., Conference Record of the 1992 IEEE', IEEE, pp. 954–956.
- Litzenberg, D. W., Roberts, D. A., Lee, M. Y., Pham, K., Vander Molen, A. M., Ronningen, R. and Becchetti, F. D. [1999], 'On-line monitoring of radiotherapy beams: experimental results with proton beams', *Medical physics* **26**, 992.
- Llosá, G., Barrio, J., Lacasta, C., Callier, S., Raux, L. and de La Taille, C. [2011], 'First tests in the application of silicon photomultiplier arrays to dose monitoring in hadron therapy', *Nuclear Instruments and Methods in Physics Research Section A: Accelerators, Spectrometers, Detectors and Associated Equipment* **648**, S96–S99.
- Lomax, A. J. [2008], 'Intensity modulated proton therapy and its sensitivity to treatment uncertainties 1: the potential effects of calculational uncertainties', *Physics in medicine and biology* **53**(4), 1027.
- Lu, H.-M. [2008a], 'A point dose method for in vivo range verification in proton therapy', *Physics in medicine and biology* **53**(23), N415.
- Lu, H.-M. [2008b], 'A potential method for in vivo range verification in proton therapy treatment', *Physics in medicine and biology* **53**(5), 1413.

- Mackin, D., Polf, J., Peterson, S. and Beddar, S. [2013], 'The effects of Doppler broadening and detector resolution on the performance of three stage Compton cameras', *Medical Physics* **40**, 012402.
- Metzler [2005], 'Resolution- versus sensitivity-effective diameter in pinhole collimation: experimental confirmation', *Physics in medicine and biology* **50**(21), 5005.
- Min, C.-H. H., Kim, C. H., Youn, M.-Y. Y. and Kim, J.-W. W. [2006], 'Prompt gamma measurements for locating the dose falloff region in the proton therapy', *Applied Physics Letters* **89**(89), 183517.
- Min, C. H., Lee, H. R., Kim, C. H. and Lee, S. B. [2012], 'Development of array-type prompt gamma measurement system for in vivo range verification in proton therapy.', *Medical physics* **39**(4), 2100–7.
- Moteabbed, M., España, S. and Paganetti, H. [2011], 'Monte Carlo patient study on the comparison of prompt gamma and PET imaging for range verification in proton therapy', *Physics in medicine and biology* **56**(4), 1063–1082.
- Mumot, M., Algranati, C., Hartmann, M., Schippers, J., Hug, E. and Lomax, A. [2010], 'Proton range verification using a range probe: definition of concept and initial analysis', *Physics in medicine and biology* **55**(16), 4771.
- Nelder, J. and Mead, R. [1965], 'A simplex method for function minimization', *The computer journal* **7**(4), 308–313.
- Nishio, T., Ogino, T., Nomura, K. and Uchida, H. [2006], 'Dose-volume delivery guided proton therapy using beam on-line PET system', *Medical physics* **33**, 4190.
- Oelfke, U., Lam, G. K. and Atkins, M. S. [1996], 'Proton dose monitoring with PET: quantitative studies in Lucite.', *Physics in medicine and biology* **41**(1), 177–96.
- Paans, A. M. J. and Schippers, J. M. [1993], 'Proton therapy in combination with PET as monitor: a feasibility study', *Nuclear Science, IEEE Transactions on* **40**(4), 1041–1044.
- Padhani, A. R., Husband, J. E. and Wardle, D. G. [1998], 'Case report Radiation induced liver injury detected by particulate reticuloendothelial contrast agent', *The British Journal of Radiology* **71**, 1089–1092.
- Paganetti, H. [2012], 'Range uncertainties in proton therapy and the role of Monte Carlo simulations.', *Physics in medicine and biology* **57**(11), R99–117.
- Paganetti, H. and Bortfeld, T. [2005], 'Proton beam radiotherapy - The state of the art', *New Technologies in Radiation Oncology (Medical Radiology Series)* (October), 3–540.
- Paix, D. [1967], 'Pinhole imaging of gamma rays', *Physics in Medicine and Biology* **12**, 489–500.
- Parodi, K., Bortfeld, T., Enghardt, W., Fiedler, F., Knopf, A., Paganetti, H., Pawelke, J., Shakirin, G. and Shih, H. [2008], 'PET imaging for treatment verification of ion therapy: Implementation and experience at GSI Darmstadt and MGH Boston', *Nuclear Instruments and Methods in Physics Research Section A: Accelerators, Spectrometers, Detectors and Associated Equipment* **591**(1), 282–286.
- Parodi, K., Crespo, P., Eickhoff, H., Haberer, T., Pawelke, J., Schardt, D. and Enghardt, W. [2005], 'Random coincidences during in-beam PET measurements at microbunched therapeutic ion beams', *Nuclear Instruments and Methods in Physics Research Section A: Accelerators, Spectrometers, Detectors and Associated Equipment* **545**(1), 446–458.
- Parodi, K., Enghardt, W. and Haberer, T. [2002], 'In-beam PET measurements of  $\beta^+$  radioactivity induced by proton beams', *Physics in medicine and biology* **47**(1), 21.

- Parodi, K., Paganetti, H., Shih, H. A., Michaud, S., Loeffler, J. S., DeLaney, T. F., Liebsch, N. J., Munzenrider, J. E., Fischman, A. J., Knopf, A. and Bortfeld, T. [2007], 'Patient Study of In Vivo Verification of Beam Delivery and Range, Using Positron Emission Tomography and Computed Tomography Imaging After Proton Therapy', **68**(3), 920–934.
- Pearson, E., Abs, M., Henrotin, S., Kleeven, W., Walle, J. V. D., Verbruggen, P. and Zaremba, S. [2013], The new IBA superconducting synchrocyclotron (S2C2): from modeling to reality, *in* 'AccApp'.
- Pedroni, E., Bearpark, R., Böhringer, T., Coray, A., Duppich, J., Forss, S., George, D., Grossmann, M., Goitein, G., Hilbes, C. and Others [2004], 'The PSI Gantry 2: a second generation proton scanning gantry', *Z. Med. Phys* **14**(1), 25–34.
- Peloso, R., Busca, P., Fiorini, C., Abba, A., Geraci, A., Manenti, A., Longoni, A., Padovini, G., Bianchi, C., Poli, G. L., Erlandsson, K., Hutton, B. F., Lechner, P., Soltau, H., Struder, L., Pedretti, A., Van Mullekom, P. and Pallaro, L. [2010], The HICAM gamma camera, *in* 'IEEE Nuclear Science Symposium & Medical Imaging Conference', IEEE, pp. 1957–1960.
- Perali, I., Celani, A., Baio, E., Fiorini, C., Frizzi, T., Clementel, E., Henrotin, S., Janssens, G., Prieels, D., Roellinghoff, F., Smeets, J. and Stichelbaut, F. [2013], Prompt Gamma Imaging of a Proton Pencil Beam at clinical Current Intensities : First Test on a Prototype and Development of a full-size Camera, *in* 'IEEE Nucl. Sci. Symp. Conf. Record', pp. 2–5.
- Perali, I., Celani, A., Busca, P., Fiorini, C., Marone, A., Basilavecchia, M., Frizzi, T., Roellinghoff, F., Smeets, J., Prieels, D., Stichelbaut, F., Vander Stappen, F., Henrotin, S. and Benilov, A. [2012], Prompt gamma imaging with a slit camera for real-time range control in proton therapy: Experimental validation up to 230 MeV with HICAM and development of a new prototype, *in* '2012 IEEE Nuclear Science Symposium and Medical Imaging Conference Record (NSS/MIC)', IEEE, pp. 3883–3886.
- Peters, A., Cee, R., Feldmeier, E., Galonska, M., Haberer, T., Höppner, K., Ripert, M., Scheloske, S., Schömers, C. and Winkelmann, T. [2010], Operational status and further enhancements of the HIT accelerator facility, *in* 'IPAC', pp. 73–75.
- Peterson, S. W., Robertson, D. and Polf, J. [2010], 'Optimizing a three-stage Compton camera for measuring prompt gamma rays emitted during proton radiotherapy.', *Physics in medicine and biology* **55**(22), 6841–56.
- Piegl, L. and Tiller, W. [1997], *The Nurbs Book*, Springer.
- Pinto, M. [2014], Absolute prompt-gamma yield measurements for ion beam therapy monitoring. unpublished.
- Pinto, M., Dauvergne, D., Freud, N., Krimmer, J., Létang, J. M., Ray, C., Roellinghoff, F. and Testa, E. [2013], 'Design optimization of a TOF-based collimated camera prototype for online hadrontherapy monitoring'.
- Polf, J. C., Panthi, R., Mackin, D. S., McCleskey, M., Saastamoinen, A., Roeder, B. T. and Beddar, S. [2013], 'Measurement of characteristic prompt gamma rays emitted from oxygen and carbon in tissue-equivalent samples during proton beam irradiation.', *Physics in medicine and biology* **58**(17), 5821–5831.
- Polf, J. C., Peterson, S., Ciangaru, G., Gillin, M. and Beddar, S. [2008], 'Prompt gamma-ray emission from biological tissues during proton irradiation: a preliminary study.', *Physics in medicine and biology* **54**(3), 731–43.
- Polf, J. C., Peterson, S., McCleskey, M., Roeder, B. T., Spiridon, A., Beddar, S. and Trache, L. [2009], 'Measurement and calculation of characteristic prompt gamma ray spectra emitted during proton irradiation', *Physics in Medicine and Biology* **54**(22), N519.

- Ramsey, R. G. and Zacharias, C. E. [1985], ‘MR imaging of the spine after radiation therapy: easily recognizable effects.’, *AJR. American journal of roentgenology* **144**(6), 1131–5.
- Richard, M., Chevallier, M., Dauvergne, D., Freud, N., Henriquet, P., Foulher, F. L., Létang, J. M., Montarou, G., Ray, C., Roellinghoff, F., Testa, E., Testa, M. and Walenta, A. H. [2010], ‘Design Guidelines for a Double Scattering Compton Camera for Prompt- Imaging During Ion Beam Therapy : A Monte Carlo Simulation Study’, *IEEE Transactions on Nuclear Science* pp. 1–8.
- Richard, M.-H. [2012], Design study of a Compton camera for prompt gamma imaging during ion beam therapy, PhD thesis, UCBL.
- Robert, C., Dedes, G., Battistoni, G., Böhlen, T. T., Buvat, I., Cerutti, F., Chin, M. P. W., Ferrari, A., Gueth, P., Kurz, C., Lestand, L., Mairani, A., Montarou, G., Nicolini, R., Ortega, P. G., Parodi, K., Prezado, Y., Sala, P. R., Sarrut, D. and Testa, E. [2013], ‘Distributions of secondary particles in proton and carbon-ion therapy: a comparison between GATE/Geant4 and FLUKA Monte Carlo codes’, *Physics in Medicine and Biology* **58**(9), 2879–2899.
- Roellinghoff, F., Benilov, A., Dauvergne, D., Dedes, G., Freud, N., Janssens, G., Krimmer, J., Létang, J. M., Pinto, M., Prieels, D., Ray, C., Smeets, J., Stichelbaut, F. and Testa, E. [2014], ‘Real-time proton beam range monitoring by means of prompt-gamma detection with a collimated camera’, *accepted by Physics in Medicine and Biology*.
- Roellinghoff, F., Benilov, A., Dauvergne, D., Dedes, G., Freud, N., Krimmer, J., Létang, J., Pinto, M., Prieels, D., Ray, C., Smeets, J., Stichelbaut, F. and Testa, E. [2013], ‘Optimization and comparison of two types of collimated camera for proton beam range monitoring’. 52nd Meet. Particle Therapy Co-Operative Group (PTCOG).
- Roellinghoff, F., Richard, M., Chevallier, M., Constanzo, J., Dauvergne, D., Freud, N., Henriquet, P., Le Foulher, F., Létang, J. M., Montarou, G., Ray, C., Testa, E., M, T. and Walenta, A. H. [2010], ‘Design of a Compton camera for 3D prompt- $\gamma$  imaging during ion beam therapy’, *Nuclear instruments and methods in physics research A*.
- Rogers, D. F. [2001], *An Introduction to NURBS: With Historical Perspective*, Vol. 8, Morgan Kaufmann.
- Romero, J., Osborne, J., Brady, F., Caskey, W., Cebra, D., Partlan, M., Kusko, B., King, R., Mirshad, I., Kubo, H., Daftari, I. and Chu, W. [1994], ‘Patient positioning for proton-therapy using a proton range telescope’, *Nuclear Instruments and Methods in Physics Research Section A: Accelerators, Spectrometers, Detectors and Associated Equipment* **356**(2-3), 558–565.
- Schippers, J. M. [2009], ‘Beam delivery systems for particle radiation therapy: Current status and recent developments’, *Reviews of Accelerator Science and Technology* **2**(01), 179–200.
- Schneider, U., Besserer, J., Pemler, P., Dellert, M., Moosburger, M., Pedroni, E. and Kaser-Hotz, B. [2004], ‘First proton radiography of an animal patient’, *Medical physics* **31**, 1046.
- Schneider, U. and Pedroni, E. [1995], ‘Proton radiography as a tool for quality control in proton therapy’, *Medical physics* **22**, 353.
- Seo, H., An, S. H., Kim, J. K. and Kim, C. H. [2007], ‘Monte Carlo study of a double-scattering Compton camera with GEANT4’, *Nuclear Instruments and Methods in Physics Research Section A: Accelerators, Spectrometers, Detectors and Associated Equipment* **580**(1), 314–317.
- Smeets, J. [2012], Prompt gamma imaging with a slit camera for real time range control in particle therapy, PhD thesis.

- Smeets, J., Roellinghoff, F., Prieels, D., Stichelbaut, F., Benilov, A., Busca, P., Fiorini, C., Peloso, R., Basilavecchia, M., Frizzi, T., Dehaes, J. C. and Dubus, A. [2012], 'Prompt gamma imaging with a slit camera for real-time range control in proton therapy.', *Physics in medicine and biology* **57**(11), 3371–405.
- Smith, S. W. [1997], Special Imaging Techniques, in 'The Scientist and Engineer's Guide to Digital Signal Processing', pp. 423–450.
- Sterpin, E., Sorriaux, J. and Vynckier, S. [2013], 'Extension of PENELOPE to protons: Simulation of nuclear reactions and benchmark with Geant4', *Medical physics* **40**(11), 111705.
- Stevens, S. K., Moore, S. G. and Kaplan, I. D. [1990], 'Early and late bone-marrow changes after irradiation: MR evaluation.', *AJR. American journal of roentgenology* **154**(4), 745–50.
- Studenski, M. T. and Xiao, Y. [2010], 'Proton therapy dosimetry using positron emission tomography.', *World journal of radiology* **2**(4), 135–42.
- Testa, E., Bajard, M., Chevallier, M., Dauvergne, D., Le Foulher, F., Freud, N., Létang, J.-M., Poizat, J.-C., Ray, C. and Testa, M. [2008], 'Monitoring the Bragg peak location of 73 MeV carbon ions by means of prompt gamma-ray measurements', *Applied Physics Letters* **93**, 093506.
- Testa, E., Bajard, M., Chevallier, M., Dauvergne, D., Le Foulher, F., Freud, N., Létang, J. M., Poizat, J. C., Ray, C. and Testa, M. [2009], 'Dose profile monitoring with carbon ions by means of prompt-gamma measurements', **267**(6), 993–996.
- Testa, M. [2010], Physical measurements for ion range verification in charged particle therapy, PhD thesis.
- Verburg, J. M., Riley, K., Bortfeld, T. and Seco, J. [2013], 'Energy- and time-resolved detection of prompt gamma-rays for proton range verification.', *Physics in medicine and biology* **58**(20), L37–49.
- Verburg, J. M., Shih, H. A. and Seco, J. [2012], 'Simulation of prompt gamma-ray emission during proton radiotherapy.', *Physics in medicine and biology* **57**(17), 5459–72.
- Vynckier, S., Derreumaux, S., Richard, F., Bol, A., Michel, C. and Wambersie, A. [1993], 'Is it possible to verify directly a proton-treatment plan using positron emission tomography?', *Radiotherapy and Oncology* **26**(3), 275–277.
- Watts, D. A., Amaldi, U., Go, A., Chang, Y.-H., Hajdas, W., Iliescu, S., Malakhov, N., Samarati, J. and Sauli, F. [2009], A proton range telescope for quality assurance in hadrontherapy, in 'Nuclear Science Symposium Conference Record (NSS/MIC), 2009 IEEE', IEEE, pp. 4163–4166.
- Wilson, R. R. [1946], 'Radiological use of fast protons.', *Radiology* **47**(5), 487–91.
- Yankelevitz, D. [1991], 'Effect of radiation therapy on thoracic and lumbar bone marrow: evaluation with MR imaging.', *American journal of roentgenology* **157**, 87–92.
- Yuan, Y., Andronesi, O. C., Bortfeld, T. R., Richter, C., Wolf, R., Guimaraes, A. R., Hong, T. S. and Seco, J. [2013], 'Feasibility study of in vivo mri based dosimetric verification of proton end-of-range for liver cancer patients', *Radiotherapy and Oncology* .



# List of Contributions

- Busca, P., Fiorini, C., Peloso, R., Basilavecchia, M., Frizzi, T., Prieels, D., Stichelbaut, F., Benilov, A. and Roellinghoff, F. [2011], ‘Development of a camera for imaging of prompt gamma rays in measurements of proton beam range’. 9th Int. Conf. on Position Sensitive Detectors (PSD) Aberystwyth.
- Peloso, R., Busca, P., Fiorini, C., Basilavecchia, M., Frizzi, T., Smeets, J., Roellinghoff, F., Prieels, D., Stichelbaut, F. and Benilov, A. [2011], Application of the HICAM camera for imaging of prompt gamma rays in measurements of proton beam range, *in* ‘2011 IEEE Nuclear Science Symposium Conference Record’, IEEE, pp. 2285–2289.
- Peloso, R., Busca, P., Fiorini, C., Basilavecchia, M., Frizzi, T., Smeets, J., Roellinghoff, F., Prieels, D., Stichelbaut, F. and Benilov, A. [2012], ‘Application of the hicamcamera for imaging of prompt gamma rays in measurements of proton beam range 13th’. 13th Int. Conf. on Nuclear Reaction Mechanisms Varenna.
- Perali, I., Celani, A., Baio, E., Fiorini, C., Frizzi, T., Clementel, E., Henrotin, S., Janssens, G., Prieels, D., Roellinghoff, F., Smeets, J. and Stichelbaut, F. [2013], Prompt Gamma Imaging of a Proton Pencil Beam at clinical Current Intensities : First Test on a Prototype and Development of a full-size Camera, *in* ‘IEEE Nucl. Sci. Symp. Conf. Record’, pp. 2–5.
- Perali, I., Celani, A., Busca, P., Fiorini, C., Marone, A., Basilavecchia, M., Frizzi, T., Roellinghoff, F., Smeets, J., Prieels, D., Stichelbaut, F., Vander Stappen, F., Henrotin, S. and Benilov, A. [2012], Prompt gamma imaging with a slit camera for real-time range control in proton therapy: Experimental validation up to 230 MeV with HICAM and development of a new prototype, *in* ‘2012 IEEE Nuclear Science Symposium and Medical Imaging Conference Record (NSS/MIC)’, IEEE, pp. 3883–3886.
- Pinto, M., Dauvergne, D., Freud, N., Krimmer, J., Létang, J. M., Ray, C., Roellinghoff, F. and Testa, E. [2013], ‘Design optimization of a TOF-based collimated camera prototype for online hadrontherapy monitoring’.
- Prieels, D., Smeets, J., Stichelbault, F., Benilov, A., Dehaes, J.-C., Dubus, A. and Roellinghoff, F. [2011], ‘Towards a practical solution for real-time measurement of the proton beam range in patients’. 50th Meet. Particle Therapy Co-Operative Group (PTCOG).
- Richard, M., Chevallier, M., Dauvergne, D., Freud, N., Henriquet, P., Foulher, F. L., Létang, J. M., Montarou, G., Ray, C., Roellinghoff, F., Testa, E., Testa, M. and Walenta, A. H. [2010], ‘Design Guidelines for a Double Scattering Compton Camera for Prompt- Imaging During Ion Beam Therapy : A Monte Carlo Simulation Study’, *IEEE Transactions on Nuclear Science* pp. 1–8.
- Richard, M.-H., Chevallier, M., Dauvergne, D., Freud, N., Henriquet, P., Le Foulher, F., Letang, J., Montarou, G., Ray, C., Roellinghoff, F. et al. [2009], Design study of a compton camera for prompt  $\gamma$  imaging during ion beam therapy, *in* ‘Nuclear Science Symposium Conference Record (NSS/MIC), 2009 IEEE’, IEEE, pp. 4172–4175.
- Richard, M.-H., Dahoumane, M., Dauvergne, D., De Rydt, M., Dedes, G., Freud, N., Krimmer, J., Létang, J., Lojacono, X., Maxim, V., Montarou, G., Ray, C., Roellinghoff, F.,

- Testa, E. and Walenta, A. H. [2012], ‘Design study of the absorber detector of a Compton camera for on-line control in ion beam therapy’, *IEEE trans. on Nuclear Science* **pp**.
- Roellinghoff, F., Benilov, A., Dauvergne, D., Dedes, G., Freud, N., Janssens, G., Krimmer, J., Létang, J. M., Pinto, M., Prieels, D., Ray, C., Smeets, J., Stichelbaut, F. and Testa, E. [2014], ‘Real-time proton beam range monitoring by means of prompt-gamma detection with a collimated camera’, *Physics in Medicine and Biology* pp. 1–14.
- Roellinghoff, F., Benilov, A., Dauvergne, D., Dedes, G., Freud, N., Krimmer, J., Létang, J. M., Prieels, D., Ray, C., Richard, M. H., Smeets, J., Stichelbault, F. and Testa, E. [2012a], ‘Proton beam range monitoring by prompt gamma detection: Experimental results for 2 types of camera’. poster presentation at 51st Meet. Particle Therapy Co-Operative Group (PTCOG).
- Roellinghoff, F., Benilov, A., Dauvergne, D., Dedes, G., Freud, N., Krimmer, J., Létang, J. M., Prieels, D., Ray, C., Richard, M. H., Smeets, J., Stichelbault, F. and Testa, E. [2012b], ‘Real-time proton beam range monitoring by means of prompt-gamma detection with a collimated camera’, presented at Int. Conf. on Translat. Res. in Radiat. Oncol. and Phys. for Health in Europe (ICTR-PHE) Geneva.
- Roellinghoff, F., Benilov, A., Dauvergne, D., Dedes, G., Freud, N., Krimmer, J., Létang, J., Pinto, M., Prieels, D., Ray, C., Smeets, J., Stichelbaut, F. and Testa, E. [2013], ‘Optimization and comparison of two types of collimated camera for proton beam range monitoring’. poster presentation 52nd Meet. Particle Therapy Co-Operative Group (PTCOG).
- Roellinghoff, F., Richard, M., Chevallier, M., Constanzo, J., Dauvergne, D., Freud, N., Henriquet, P., Le Foulher, F., Létang, J. M., Montarou, G., Ray, C., Testa, E., M, T. and Walenta, A. H. [2010], ‘Design of a Compton camera for 3D prompt- $\gamma$  imaging during ion beam therapy’, *Nuclear instruments and methods in physics research A* .
- Smeets, J., Roellinghoff, F., Prieels, D., Stichelbault, F., Benilov, A., Busca, P., Fiorini, C., Peloso, R., Basilavecchia, M., Frizzi, T., Dehaes, J.-C. and Dubus, A. [2012a], ‘Experimental evaluation of prompt gamma imaging with a slit camera for proton beam range measurement’. 27th Ann. Symp. Belgian Hosp. Physicists Ass. (BHPA) Brussels.
- Smeets, J., Roellinghoff, F., Prieels, D., Stichelbault, F., Benilov, A., Busca, P., Fiorini, C., Peloso, R., Basilavecchia, M., Frizzi, T., Dehaes, J.-C. and Dubus, A. [2012b], ‘Experimental evaluation of prompt gamma imaging with a slit camera for real time range control in proton therapy’. ESTRO 31 Barcelona.
- Smeets, J., Roellinghoff, F., Prieels, D., Stichelbault, F., Benilov, A., Busca, P., Fiorini, C., Peloso, R., Basilavecchia, M., Frizzi, T., Dehaes, J.-C. and Dubus, A. [2012c], ‘Prompt gamma imaging with a slit camera for real time range control in proton therapy’. poster presentation at Int. Conf. on Translat. Res. in Radiat. Oncol. and Phys. for Health in Europe (ICTR-PHE) Geneva.
- Smeets, J., Roellinghoff, F., Prieels, D., Stichelbault, F., Benilov, A., Busca, P., Fiorini, C., Peloso, R., Basilavecchia, M., Frizzi, T., Dehaes, J. C. and Dubus, A. [2012], ‘Prompt gamma imaging with a slit camera for real-time range control in proton therapy.’, *Physics in medicine and biology* **57**(11), 3371–405.
- Sterpin, E., Janssens, G., Smeets, J., Prieels, D., Stichelbault, F., Roellinghoff, F., Clementel, E., Benilov, A. and Vynckier, S. [2013], ‘Th-c-144-10: On the feasibility of prompt gamma imaging in heterogeneous patient anatomy’, *Medical Physics* **40**(6), 548–548.

FOLIO ADMINISTRATIFTHESE SOUTENUE DEVANT L'INSTITUT NATIONAL DES SCIENCES APPLIQUEES DE LYON

NOM : ROELLINGHOFF

(avec précision du nom de jeune fille, le cas échéant)

DATE de SOUTENANCE :

Prénoms : Frauke

TITRE : Mme

NATURE : Doctorat

Numéro d'ordre : AAAAISALXXXX

Ecole doctorale : EEA

Spécialité :

RESUME :

La protonthérapie est une technique prometteuse pour le traitement du cancer, qui se répand de plus en plus. Le pic prononcé de son profil de dose ainsi que la longueur finie du parcours des particules rendent possible un traitement plus ciblé et permettent de mieux éviter d'endommager des tissus sains. Cependant, la précision de l'irradiation s'avère également être le risque principal lors de l'utilisation de cette technique. En effet, une erreur dans la profondeur de pénétration des particules pourrait engendrer des dégâts considérables. A l'heure actuelle, aucune méthode de contrôle n'est systématiquement utilisée pour s'assurer de la qualité du traitement. Dans ce manuscrit, une méthode indirecte de mesure de la distribution de dose, basé sur la détection de gammas prompts émis le long du parcours du faisceau, est étudiée.

Deux concepts de caméra collimatée uni-dimensionnelle sont comparés à l'aune de leur utilisation potentielle : une caméra à fentes parallèles et une caméra "knife-edge". Les deux systèmes sont optimisés par simulations de Monte Carlo et des mesures sont présentés pour valider ces simulations. La comparaison se base sur la précision avec laquelle un décalage dans la chute du profil prompt gamma peut être détecté, la résolution spatiale, le coût et la taille du système. Des recommandations sont émises pour le choix de la meilleure configuration, selon différentes exigences. Des résultats similaires sont obtenus pour les deux concepts, atteignant une précision de environ 2 mm pour un seul point de "pencil beam" correspondant à  $5 \cdot 10^7$  protons.

L'étude se conclue par un tour d'horizon des pistes de recherche futures qui permettraient d'utiliser un système de détection de gammas prompts dans un contexte clinique futur.

MOTS-CLES : protonthérapie; contrôle du range; gammas prompts; Monte Carlo

Laboratoire (s) de recherche : CREATIS

Directeur de thèse: Nicolas FREUD

Président de jury :

Composition du jury : Joel Héroult, Dietmar Georg, Tony Lomax, David Sarrut, Frank Verhaegen, Denis Dauvergne, Julien Smeets